

Journal of the CERAMIC SOCIETY of Japan, *International Edition* Vol.99 Dec. 1991

■ 21 Papers from Nippon Seramikkusu Kyokai Gakujutsu Ronbunshi, Vol. 99 No.12 1991

NIPPON SERAMIKKUSU KYOKAI GAKUJUTSU RONBUNSHI Vol.99 1991

Annual
Index
Vol.99
1991



Vol.99 No.12
Dec. 1991

Editorial Board

Dr. Teruo Sakaino
Prof. Emeritus, Tokyo Institute of Technology
Dr. Nobuyasu Mizutani
Prof., Tokyo Institute of Technology
Dr. Yusuke Moriyoshi
Director, Nat. Inst. for Res. in Inorganic Materials
Dr. Kitao Takahara
Prof., Nagoya University
Yukio Endo
Chairman
Koyo-sha Co., Ltd.
Dr. Takashi Hanazawa
Executive Director,
The Ceramic Society of Japan
Seiji Iwata
Executive Director,
Japan Fine Ceramics Association
Keiji Hayashi
Managing Editor

Editors

Managing Editor	Keiji Hayashi
Associate Editor	Kohsuke Odani
Assistant Artists	Toshimitsu Irie
	Misao Tomita
Assistant	Kiyoe Kojima
Circulation	Youko Matsumoto
Publisher	Keiji Hayashi

Published Monthly by
FUJI TECHNOLOGY PRESS LTD.
7F Daini Bunsei Bldg.
11-7, Toranomon 1-chome
Minato-ku, Tokyo 105, Japan
Tel:81-3-3508-0051
Fax:81-3-3592-0648

One year subscription
Air Mail ¥200,000

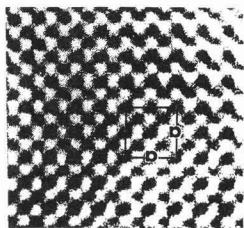
Copyright - © 1991 by
The Ceramic Society of Japan and Fuji
Technology Press Ltd. All rights reserved.

No part of this publication may be reproduced, stored in a retrieval system, or transmitted, in any form or by any means, electronic, mechanical, photo copying, recording, or otherwise, without the prior written permission of the publishers. The papers, excluding those on information and communications, reviews, etc., were originally received by Nippon Seramikkusu Kyokai Gakujutsu Ronbunshi, and translated for this journal. The responsibility for the translation lies with the publisher.

CONTENTS

Papers:

- **The Effect of Argon Addition on the Microstructure, Texture and Phases of Silicon Carbide Prepared by Chemical Vapor Deposition** 1136
Yang-Ming Lu and Min-Hsiung Hon
- **Effects of Additives on The Stacking Fault Annihilation in β -SiC Powder Compacts** 1140
Won-Seon Seo, Chul-Hoon Pai, Kunihiro Koumoto and Hiroaki Yanagida
- **Influence of Annealing on the Properties of Ca-Rich Bi-Pb-Sr-Ca-Cu-O Superconducting Thin Films** 1145
Keizou Tsukamoto, Hiromasa Shimojima, Mamoru Ishii and Chitake Yamagishi
- **Burn-out of Binder and Sintering Behavior of Powder Compacts of Bimodally Distributed Alumina Powders with Stearic Acid and Polyethyleneglycol** 1150
Seiichi Taruta, Kunio Kitajima, Nobuo Takusagawa, Kiyoshi Okada and Nozomu Ôtsuka
- **Study on the Composite Materials Consisting of $\text{Li}_2\text{O-SiO}_2$ Crystals and $\text{Na}_2\text{O-CaO-SiO}_2$ Glass** 1156
Koichi Watanabe and Shiroshi Chigira
- **Electrical Resistivity of Diamond Films Grown by Thermal Plasma CVD** 1162
Toyohiko Kobayashi
- **Improvement of Thermal Stability of SiC Fiber by CVD-C, SiC Coating** 1168
J.X. Li, Yohtaro Matsuo and Shiushichi Kimura
- **Changes in Swelling Characteristics and Structure of Na-Fluorine Micas with Ga- and Al-substitutions** 1174
Kunio Kitajima, Kazuyuki Miyake and Nobuo Takusagawa
- **Deposition of TiN Films onto Glaze of Porcelain by Reactive Sputtering** 1182
Hiromichi Ichinose, Kazuo Akamatsu, Makoto Terasaki, Hiroaki Katsuki and Masamitsu Nagano
- **Preparation of CaSiO_3 Powders by Coprecipitation Method and Their Sinterability** 1187
Shigeo Hayashi, Kiyoshi Okada and Nozomu Ôtsuka
- **Influence of Powder Characteristics on Sinterability and Mechanical Properties of Silica-Alumina Ceramics (74wt% Al_2O_3)** 1191
Takeshi Kumazawa, Shigetoshi Ohta, Takaaki Nagaoka, Masaki Yasuoka and Shuzo Kanzaki
- **Stability of Metastable Tetragonal Zirconia** 1197
Hirohiko Murakami and Hideo Ohno
- **Micro-Shirasuballoons (Hollow Glass Microspheres) from the Milled Shiras Refined by Hydrothermal Treatment** . . . 1203
Kunio Kimura, Kazuhiko Jinnai and Hiroshi Tateyama
- **Nano Composite of PZT-PMN-MnO₂-NiO Ceramics-Alumina System** 1209
Kazumasa Ohnishi, Masaru Kawarada, Takaaki Ishii, Yasuhiro Tanabe and Eiichi Yasuda



Cover:

This picture shows a high-resolution structure image of zirconia (ZrO_2) projected along the a-axis of a cubic lattice ($a=5.1$). As indicated by arrow-heads in the micrograph, both zirconium (Zr) and oxygen (O) atom positions appear as strong and weak dark dots, respectively. This is the first electron microscope data in which individual oxygen positions in inorganic compounds can be directly observed as weak dark dots.

The microgram was obtained by the ultra-high-resolution, high-voltage electron microscope (Model: H-1500) developed in 1990 as NIRIM's second high-voltage electron microscope. The device has the world's highest resolution of 1.0\AA , which was achieved by employing operating and applicable voltages of 1300kV and 1500kV , respectively. A very low spherical aberration coefficient for the objective ($C_s=1.85\text{mm}$ at 1300kV) was realized by computer-aided design of the electron-magnetic lens system. This new apparatus permits the imaging of not only metal atoms but also light atoms (such as oxygen) in many inorganic materials by means of high-resolution electron microscopy.

Technical reports:

- **Change of Surface Grinding Flaw of β -Sialon with Oxidation and Its Influence on Bending Strength** 1214
Kazushi Kishi and Seiki Umebayashi
- **Characterization of ZSM-5 Zeolite Synthesized from Silica Stone (Ioh Island, Kagoshima Prefecture)** 1219
Yoshihiro Hirata, Tadashi Kodama, Kinji Shimada and Yoshimi Ishihara
- **Corrosion Behavior of Silicon Nitride Ceramics in Aqueous Solutions (Part 1) —Effects of Testing Condition and Various Corrosive Solutions—** 1223
Akira Okada, Satoshi Iio, Tetsuo Asano, Akira Kokaji,
Hideo Takahashi and Masahiro Yoshimura

Notes:

- **Thermal and Mechanical Properties of $\text{SiC-p/Al}_2\text{O}_3$ Composite** 1228
Yoshio Akimune, Yasushi Katano, Tooru Akiba and Toshio Ogasawara
- **β -Tricalcium Phosphate Coating on Titanium** 1231
Motohiro Toriyama, Yukari Kawamoto, Takahiro Suzuki,
Yoshiyuki Yokogawa, Kaori Nishizawa and Hajime Nagae

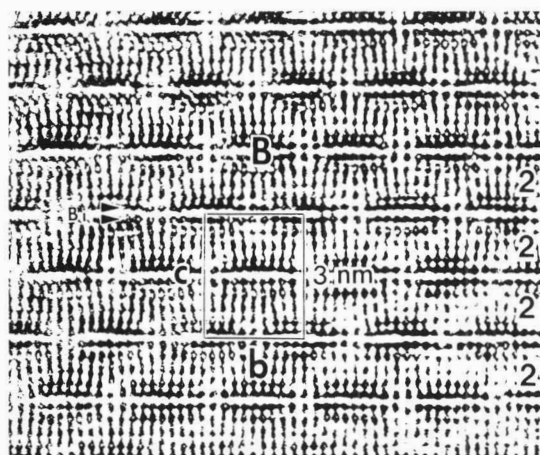
Ceramic letters:

- **Preparation of Heat and Water Vapor Resistant Composite Porous Glass Membrane Coated on Porous Alumina Tubing by Sol-Gel Method** 1234
Tetsuo Yazawa, Hiroshi Tanaka, Hiroshi Nakamichi, Kiyohisa Eguchi and Osamu Yamaguchi
- **Thermal Expansion Characteristics of Li-Replaced Type Pollucite ($\text{Cs}_{1-x}\text{Li}_x\text{AlSi}_2\text{O}_6$) Powder** 1237
Hidehiko Kobayashi, Toshihiro Terasaki, Toshiyuki Mori,
Hiroshi Yamamura and Takashi Mitamura

Information & Communications

- **News** C-95
- **Abstracts of Articles on Ceramics and Superconductivity from Selected Journal of the Academic Societies** . . . C-98
- **Keyword Index of Volume 99 (1991)** C-107
- **Author Index of Volume 99 (1991)** C-114

Papers, Letters and Notes



High resolution electron microscope photograph of the modulation doped structure of $\text{Bi}_2\text{Sr}_2\text{CaCu}_2\text{O}_y$ ($T_c=80\text{K}$) in the $[100]$ direction. Figures at right side indicate number of copper layers, symbol B indicates bismuth rich region.

The Effect of Argon Addition on the Microstructure, Texture and Phases of Silicon Carbide Prepared by Chemical Vapor Deposition

Yang-Ming Lu and Min-Hsiung Hon

Department of Materials Engineering, National Cheng Kung University
Tainan, Taiwan, R.O.C.

Silicon carbide was chemically deposited on the (111) surface of silicon single crystal and isotropic pyrolytic graphite by using methyltrichlorosilane as source gas. The deposits were examined by X-ray diffractometry and electron scanning microscopy (SEM) and found to be composed of β -SiC, free Si and a trace of 2H-SiC. The coatings yielded less free silicon in it using graphite as substrate and at a higher argon flow rate. X-ray analysis indicated that the degree of preferred orientation varied with the kinds of substrate materials and the amount of argon added. A film with $\langle 111 \rangle$ preferred orientation was obtained on silicon substrate compared to the $\langle 220 \rangle$ orientation on the graphite substrate. Increasing the flow rate of argon decreases the probability of the $\langle 111 \rangle$ orientation but enhances the $\langle 220 \rangle$ one on graphite substrate, whereas the deposition rate was greatly lowered by adding argon. The morphologies of deposits obtained by the CVD process were dependent on the input fraction of argon at 1400°C.

[Received February 12, 1991; Accepted August 22, 1991]

Key-words: β -SiC, Free Si, Preferred orientation, CVD, Morphology

1. Introduction

Silicon carbide (SiC) prepared by chemical vapor deposition (CVD) is a material with some outstanding properties such as high hardness, good oxidation resistance at high temperatures and inertness in acids or other corrosive media. Chemically vapor deposited SiC can be obtained by the thermal decomposition of gaseous compounds containing both Si and C, or a combination of gaseous species containing either Si or C, respectively.¹⁾ The most conventional known way to deposit SiC is to decompose organosilane compounds. Such a procedure was especially studied for methyltrichlorosilane (CH_3SiCl_3), because of its 1:1 ratio of silicon to carbon content.²⁾ The kinetics of the deposition process and the surface morphology of deposited SiC have been examined by many investigators.³⁻⁵⁾ Since CVD involves a nucleation and growth process,⁶⁾ the structural perfection of the deposited SiC films is strongly dependent on the deposition parameters such as temperature, total system pressure, and the input fraction of reactants. The purpose of the present work is to understand the morphology, the preferred orientations, the growth rates, the chemical compositions and the structural changes of deposited β -SiC from the pyrolysis of $\text{CH}_3\text{SiCl}_3 + \text{H}_2$ onto different substrates in the

presence of argon. The deposition mechanism was also discussed as it related to the experimental results.

2. Experimental

Silicon carbide was deposited on isotropic graphite (22mm \times 20mm \times 6mm) and (111) silicon single crystal (10mm \times 10mm \times 0.3mm) substrates, heated by rf, using a gaseous mixture of methyltrichlorosilane (MTS) (CH_3SiCl_3), hydrogen and argon. A quartz tube reactor (50mm diameter by 700mm length) was used for deposition in a horizontal open-flow-type. The temperature of the substrate was measured by an optical pyrometer. In order to maintain at constant vapor pressure of MTS, the bubbler was cooled to 0°C. When the substrate reached the deposition temperature, the gaseous mixtures of MTS, argon and hydrogen was introduced into the reaction chamber to begin deposition. In the present work, a silicon single crystal wafer with (111) orientation was used as substrate which was deposited at 1300°C. On the other hand, pyrolytic graphite substrates with no preexist preferred orientation were also used for deposition at 1300°C and 1400°C respectively. The parameters of the experiment were as follows: substrate temperature: 1300°C and 1400°C; total flow rate of hydrogen: 21/min; CH_3SiCl_3 : 15c.c./min; deposition pressure: 40Torr; the flow rate of argon: 0–285c.c./min. The surface morphology of the deposits was observed using a scanning electron microscope; an X-ray powder diffractometer was employed to determine the preferred orientation of the film and the relative content of free silicon in the deposited SiC films. The relative content of free silicon was determined by the ratio of the strongest X-ray diffraction peak of silicon to the strongest one of silicon carbide. The growth rate of SiC was estimated by measuring the weight gain of depositions.

3. Results and Discussion

CH_3SiCl_3 was thermally decomposed into intermediate gaseous species of hydrocarbon and silicon chloride. According to pyrolysis mechanisms reported by Gyarmati and Nickel,⁸⁾ the SiC bond in CH_3SiCl_3 is broken in the gas phase and then SiC is formed on the substrate surface by the reaction between silicon and carbon which are independently deposited from chlorosilane radicals and hydrocarbon radicals, respectively. Since silicon and carbon deposit individually, there was a possibility to form ex-

cess carbon or silicon on the substrate under certain gas phase conditions. Silicon-rich SiC deposits were usually observed at high ratio of H_2 to CH_3SiCl_3 , at higher pressure and lower temperature.⁹⁾ The deposits contain a lot of free silicon which were prepared at 1300°C and 1400°C by the reaction of silane and hydrogen without argon. The amount of excess carbon is greater in argon than that in the hydrogen,¹⁰⁾ i.e., the formation of carbon progressed in the presence of argon.

Figure 1 shows the relationship between the argon flow rate and the free silicon content in the deposits. The free silicon content decreases with increasing argon flow rate in the deposition system with silicon as substrate. It was considered that excess argon suppressed the dechlorination of chlorosilane radicals and then decreased the content of free silicon in the deposits. With increased the argon flow rate to 285 c.c./min, no detectable free silicon was found on the films deposited on graphite substrate, whereas some free silicon still remained on the films deposited on silicon substrate. This implied that silicon atoms were readily rearranged on silicon substrates compared with graphite substrates.

Figure 2 shows X-ray powder diffraction patterns of deposits on the graphite substrate. It is clear that 2H-SiC is partially formed in the β -SiC (3C-SiC) film. The supersaturation of MTS in gas phase increased with decreasing deposition temperature, and the rate of the chemical reaction: $C_{(s)} + 2H_{2(g)} \rightarrow CH_{4(g)}$ decreased as temperature decreased. The concentration of carbon in the gas phase was then increased above the substrate. This may lead to the enlargement of the 2H-SiC formation region.¹¹⁾

Figure 3 shows the X-ray powder diffraction patterns of deposits on the Si substrate. A considerable degree of structural anisotropy was found in the deposits on comparing the intensity of the (111) peak with that of the (220) and (200) peaks. The preferred orientation of a certain crystal plane (hkl) in a polycrystalline film can be estimated by the texture coefficient (TC) using the Harris method¹²⁾:

$$TC = \frac{(I/I_0)}{(1/n) \sum_n (I/I_0)_i}$$

where I is the measured XRD intensity, I_0 is the ASTM standard intensity and n is the number of reflections. As shown in **Fig. 4**, the texture coefficient for the (111) orientation was changed from 1.4 to 1.3 as the argon flow rate increased. **Figure 5** indicates that the preferred crystallographic orientation of β -SiC films, which are deposited on graphites at 1300°C in a pure hydrogen atmosphere, is observed on the (111) plane and changes to the (220) plane as the argon flow rate increase. On the other hand, it is found that the preferred orientation of the films deposited at 1400°C is always (220) plane with increased input flow fraction of argon as shown in **Fig. 6**. As a result, the excess of argon was available for changing the preferred orientation of deposits from (111) to (220). As the same as pointed in ref.¹³⁾ stacking faults were frequently observed on the (111) crystal planes of the β -SiC film. With increasing the input flow fraction of argon, the growth rate of deposits remarkably decreased as shown in **Fig. 7**. The partial pressures of

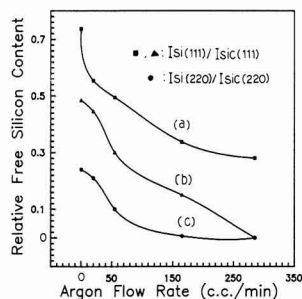


Fig. 1. Effects of argon flow rate on the content of free silicon in the films (a) at 1300°C, with silicon substrates (b) at 1300°C, with graphite substrate (c) at 1400°C, with graphite substrate, I is the X-ray intensity.

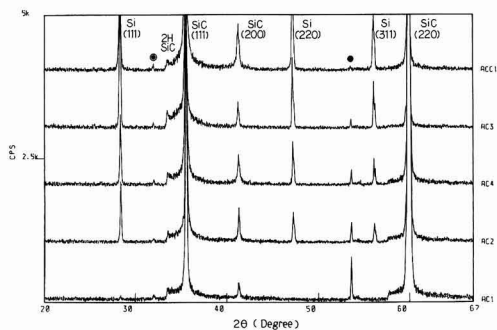


Fig. 2

Fig. 2. X-ray diffraction patterns obtained from deposits grown on graphite substrates at 1300°C. The flow rate of argon in each run was: (a) ACC1: 0 c.c./min (b) AC3: 20 c.c./min (c) AC4: 55 c.c./min (d) AC2: 165 c.c./min (e) AC1: 285 c.c./min. The diffraction peaks denoted by (●) are produced by $CuK\beta$ radiation of SiC (220), while (○) are from $CuK\beta$ radiation of SiC (111).

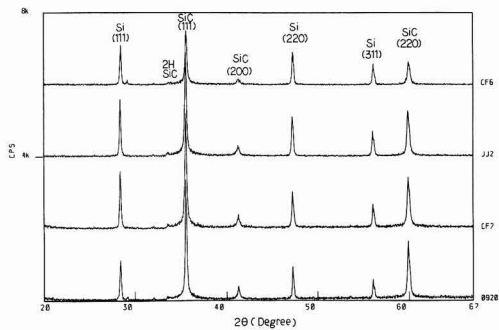


Fig. 3

Fig. 3. X-ray diffraction patterns obtained from deposits grown on <111> silicon substrate at 1300°C. The flow rate of Ar in each run is: (a) CF6: 0 c.c./min (b) JJ2: 20 c.c./min (c) CF7: 55 c.c./min (d) 09207: 165 c.c./min.

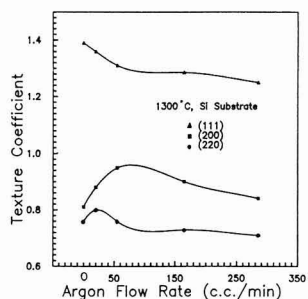


Fig. 4

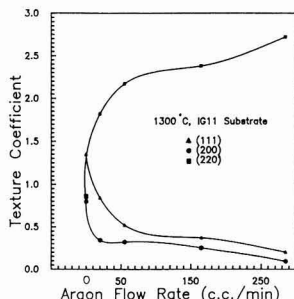


Fig. 5

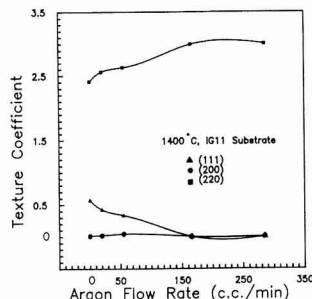


Fig. 6

Fig. 4. Dependence of texture coefficient of the films on the flow rate of argon deposited on $\langle 111 \rangle$ silicon substrates, at 1300°C .

Fig. 5. Dependence of texture coefficient of the films on the flow rate of argon deposited on graphite substrates, at 1300°C .

Fig. 6. Dependence of texture coefficient of the films on the flow rate of argon deposited on graphite substrates, at 1400°C .

hydrocarbon and silicon-chloride were decreased by introducing argon into the reaction zone. Accordingly, the growth rate of SiC deposition also decreased.

By varying the argon input fraction, three different types of morphology were obtained. The variation of the argon addition governed the domain sizes of β -SiC in which fine grains were randomly distributed. An increase in the argon flow rate resulted in the growth of the domain sizes in the films deposited on silicon at 1300°C as shown in Fig. 8. The SEM photographs of the as-deposited β -SiC surface on graphite in Fig. 9 show a change of small rounded hillocks to larger ones as the argon flow rate increased at 1300°C . Figure 10 shows a surface morphology of the deposits grown on graphite substrate at 1400°C . As argon flow rates increased, the surface morphologies changed from a smaller and more loosely faceted crystal structure to a larger and more densely faceted one, and then to a structure with multistar twin tips and intersected twin configurations extending in the radial direction. The resulting morphologies of β -SiC films were substantially affected by the argon input fraction at the only higher temperature. At lower deposition temperatures, Si and C atoms were expected to have some restriction of surface mobility on the substrate. Restrictive diffusion of atoms depresses crystal growth at energetically favorable sites and promotes atoms to nucleate at new sites which results in a structure of small rounded hillocks. At higher deposition temperatures, both atoms had enough energy to diffuse to the preferred nucleation sites of the substrate. Ease of propagation of atoms arises through the

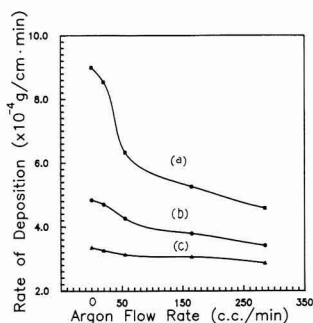


Fig. 7. The effect of flow rate of argon on the deposition rate with (a) $\langle 111 \rangle$ silicon substrates, at 1300°C (b) graphite substrates, at 1400°C (c) graphite substrates, at 1300°C .

formation of reentrant corners at the intersection of twin planes,¹⁴⁾ which make this location a favorable site for nucleation and growth and results in developing a strong faceted crystal with the preferred orientation. The SEM observations indicated that the growth of β -SiC films was attributed to ledge movement associated with twin planes. Increasing the argon input fraction reduced the partial pressure of MTS and suppressed the preferential nucleation probability on the substrate. Consequently, the grain size of β -SiC increased with the amount of argon.

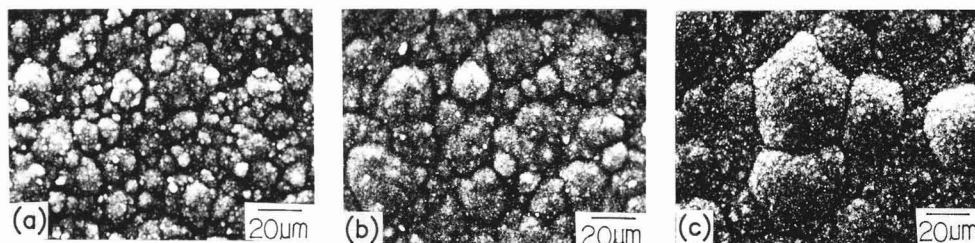


Fig. 8. The effect of the argon flow rate on the surface morphologies of deposits grown on $\langle 111 \rangle$ silicon substrates at 1300°C . The Ar flow rate were (a) 0 c.c./min (b) 55 c.c./min (c) 285 c.c./min.

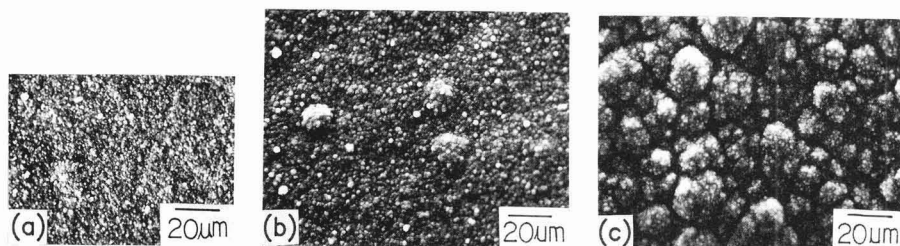


Fig. 9. The effect of argon flow rate on surface morphologies of deposits grown on graphite substrate at 1300°C. (a) Ar: 0c.c./min (b) Ar: 55c.c./min (c) Ar: 285c.c./min.

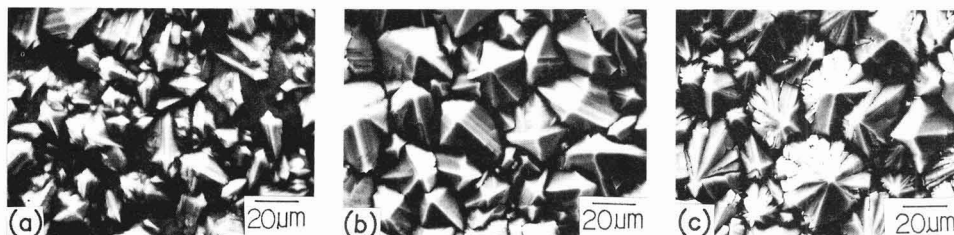


Fig. 10 The effect of the argon flow rate on surface morphologies of deposits grown on graphite substrate at 1400°C. The Ar flow rates were (a) 0c.c./min (b) 55c.c./min (c) 285c.c./min.

4. Conclusion

In summary,

- 1) The deposits were predominantly found to be β -SiC with a trace of 2H-SiC.
- 2) Addition of argon suppressed the formation of free silicon.
- 3) Increasing the flow rate of argon decreased the (111) but promoted the (220) preferred orientation.
- 4) The grain size of the polycrystalline β -SiC became larger as the flow rate of argon was increased at 1300°C. The morphologies changed from faceted crystals to structures with multistar twin tips and intersected twin configurations extending in the radial direction with increasing argon flow rate at 1400°C.
- 5) The growth rate of the deposits also decreased with increasing the input fraction of argon.

Acknowledgments

This study was supported by National the Science Council, (NSC 79-0405-E006-37), Taiwan, R.O.C.

References:

- 1) J. Schlichting, Powder Metall. Int., 12, 141 (1980).
- 2) M.J. Chappell and R.S. Millman, J. Mater. Sci., 9, 1933 (1974).

- 3) J. Chin, P.K. Gantzel, and R.G. Hudson, Thin Solid Films, 40, 57 (1977).
- 4) K. Kuroiwa and T. Sugano, J. Electrochem. Soc., 120, 138 (1973).
- 5) H. Matsunami, S. Nishino, and T. Tanaka, J. Crystal. Growth, 45, 138 (1978).
- 6) J.M. Blocher, Jr., J. Vac. Sci. Technol., 11, 680 (1974).
- 7) E. Gyarmati and H. Nickel, Kernforschungsanlage Jülich Tech. Rept. No.Jül-900-RW, November (1972).
- 8) E. Gyarmati and H. Nickel, Jül-900-RW, KFA Jülich, Germany (1972).
- 9) A.I. Kingon, L.J. Lutz, P. Liaw and R.F.Davis, J. Am. Ceram. Soc., 66, 558 (1983).
- 10) F. Kobayashi, K. Ikawa and K. Iwamoto, J. Cryst Growth, 28, 395 (1975).
- 11) M.S. Saidov, Kh. a. Shamuratov and M.A.Kadyrov, J. Cryst Growth 87, 519 (1988).
- 12) C. Barret and T.B. Massalski, Structure of Metals, Pergamon, Oxford (1980) 204.
- 13) D. Pandey and P. Krishna, in: Silicon Carbide 1973, ed. by R.C. Marshall, J.W. Faust, Jr. and C.E. Ryan, Univ. of South Carolina Press, Columbia (1974) 198.
- 14) D.J. Cheng, W.J. Shyy, D.H. Kuo and M.H. Hon, J. Electrochem. Soc., 134, 3245 (1987).

This article appeared in English in Nippon Seramikkusu Kyokai Gakujutsu Ronbunshi (Japanese version), Vol.99, No.12, 1991.

Effects of Additives on The Stacking Fault Annihilation in β -SiC Powder Compacts

Won-Seon Seo, Chul-Hoon Pai, Kunihito Koumoto and Hiroaki Yanagida

Department of Industrial Chemistry, Faculty of Engineering, The University of Tokyo
7-3-1 Hongo, Bunkyo-ku, Tokyo 113 Japan

Effects of the addition of B, Al, Fe and C on the annihilation of stacking faults (S.F.) in β -SiC powder compacts were investigated. The separability of the X-ray diffraction lines, $K\alpha_1$ and $K\alpha_2$, was applied to the qualitative evaluation of the lattice strain to elucidate the annihilation phenomena. Dissolution of B or Al (rapid heating condition) into SiC grains enhanced the lattice strain suppressing both grain growth and S.F. annihilation. The second phases formed in Al (slow heating condition) and Fe addition to β -SiC promoted both grain growth and S.F. annihilation, while the residual free carbon in C-added β -SiC impeded the grain boundary movement and hence suppressed grain growth and S.F. annihilation. [Received June 7, 1991; Accepted September 19, 1991]

Key-words: β -SiC, Stacking fault, Additives, Grain growth, Lattice strain, Second phase

1. Introduction

Silicon carbide is a highly useful material for both electronic and mechanical applications. When a powder compact of SiC is heat-treated at high temperatures in a normal sintering process, various changes such as grain growth, pore elimination, phase transformation, etc. occur.^{1,2)} Among those changes the annihilation process of stacking faults initially present within the grains is interesting and should be understood because they greatly affect the properties of a final product.³⁻⁵⁾

We have already reported³⁾ that the stacking fault annihilation in a nominally pure (undoped) β -SiC powder compact occurs simultaneously with the grain growth which is supposedly controlled by surface diffusion and/or vapor transport. Incorporation of nitrogen into the SiC grains during firing in N_2 atmosphere was found to enhance the lattice strain, which was considered to be the most important factor to suppress the mass transport rate.

For the pressureless sintering or even for the hot-pressing various sintering aids (usually boron and carbon) are added to the starting SiC powder because of its low sinterability.^{6,7)} Behavior and roles of these sintering aids have been controversial for many years but are not yet fully understood. Therefore, studying the effects of sintering aids on the annihilation of stacking faults is considered to be significant from this point of view.

In the present study, boron (B), aluminum (Al), carbon (C), and iron (Fe) were chosen as additives. The former three elements are known to be the typical sintering aids, but the effect of Fe addition is unknown. Boron and aluminum are known to dissolve into the SiC lattice to make solid

solutions,⁸⁾ while carbon and iron do not apparently form solid solutions. Hence, we thought that the effects of dissolution of additives and chemical reaction, ex. second phase formation, on the stacking fault annihilation could be examined separately through the systematic addition of these elements.

2. Experimental Procedure

2.1. Heat Treatment of β -SiC Powder Compact

Beta-SiC powder (Centgral glass Co., Ltd.) having 15.0% stacking fault density synthesized by carbothermal reduction of SiO_2 was employed as a starting material. BET surface area, average particle size, and impurity contents of the powder are shown in Table 1. The powder was isostatically pressed in a rubber mold after prepressing in a unidirectional mold, and was annealed at 1775°-2000°C for 0-1 h in an Ar or a N_2 atmosphere.

2.2. Analysis

Gold was evaporated onto the fractured surface, and SEM observations were conducted to examine the microstructure. The average grain size was calculated from the micrographs. X-ray diffraction (XRD) measurements of the crushed powders were conducted using $CuK\alpha$ radiation with a Ni filter and a graphite monochromator under the following conditions; scanning speed=1/8° (in 2θ) min⁻¹, time constant=5 s, receiving slit=0.15mm. The intensities of the peaks at 33.6° and 41.4° (2θ) were measured and stacking fault density was calculated using the following equation:⁴⁾

$$A = \frac{33.6^\circ \text{ peak intensity } (2\theta)}{41.4^\circ \text{ peak intensity } (2\theta)}$$

Stacking fault =

$$\frac{A}{6.82 \times 10^{-2} A + 2.27 \times 10^{-2}} + 1.7 A^3 (\%)$$

The half-width of the (111) reflection peak (33.6°) was also measured and the Scherrer equation was used to calculate the crystallite size. Lattice parameter was calculated from the observed peak positions of (331), (420) and (422)

Table 1. Properties of the β -SiC powder.

BET surface area (m ² /g)	average particle size (μ m)	impurity (ppm)				
		Fe	Al	Ca	Mg	Na
17.4	0.60	144	212	90	12	12

reflections precisely determined by an internal method using high-purity silicon as a standard. The computer program which could separate $K\alpha_1$ from $K\alpha_2$ by Rachinger method was used to calculate the precise lattice parameters of β -SiC which showed only poor crystallinity.

3. Results and Discussion

3.1. Simple Method to Evaluate the Lattice Strain

Our previous study revealed that the dissolution of nitrogen into the SiC grains during firing in a N_2 atmosphere induces the lattice strain and hence reduces the mass transport rate suppressing the annihilation of stacking faults.⁴⁾ This phenomenon was also confirmed for the powder employed in the present study as shown in Fig.1, where the stacking fault density measured after annealing the powder compacts for 0.5 h is plotted as a function of annealing temperature. It is evident that the stacking fault density decreases with increasing annealing temperature and that rate of stacking fault annihilation is suppressed in a N_2 atmosphere.

The enhanced lattice strain introduced by the incorporation of nitrogen has already been verified by the direct measurement according to the hall method.^{4,9)} However, this method is rather complicated and time consuming, so that it is not suitable to the evaluation of lattice strain for a large number of specimens. As an alternative simple method, the measurement of the separability of X-ray diffraction lines, $K\alpha_1$ and $K\alpha_2$, is proposed here.

In general, the width of an X-ray diffraction line is associated fundamentally with the structural factors such as crystallite size, stacking fault density, and lattice strain. If the

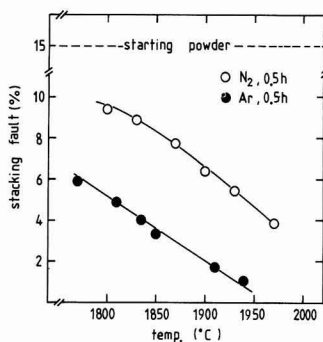


Fig. 1. Temperature dependence of the stacking fault density for the β -SiC compacts annealed for 0.5 h in N_2 and Ar atmospheres.

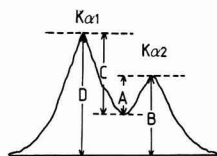


Fig. 2. X-ray diffraction profile in which the values for defining the separability are shown.

separability of the X-ray diffraction lines, $K\alpha_1$ and $K\alpha_2$, is defined to be either A/B or C/D as shown in Fig.2, it must have close relationships with those structural factors. In order to judge if the separability is applicable to evaluate the lattice strain, both undoped and nitrogen-doped β -SiC specimens were employed.

The β -SiC powder compact having 15% stacking fault density was annealed at various temperatures in either N_2 or Ar atmosphere, and then crystallite size and stacking fault density were measured. The results are shown in Fig.3. It is very interesting to note that the relation between the crystallite size and the stacking fault density is expressed by a "master" curve in a limited range irrespective of the annealing conditions.

We have further chosen the two specimens having approximately the same stacking fault density, ~3.6%, and the same crystallite size, ~810 Å, and the separabilities were calculated for the various diffraction planes in terms of either A/B or C/D. Figure 4 shows the calculated separability vs. the diffraction angle. It is clearly seen that the difference in A/B or C/D between the Ar- and N_2 -annealed specimens increased with increasing diffraction angle and A/B gives larger differences than C/D. In either case, separability is

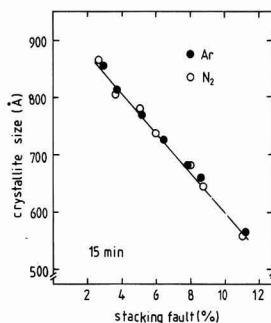


Fig. 3. Relation between the crystallite size and the stacking fault density for the specimens annealed at various temperatures for 15 min in N_2 and Ar atmospheres.

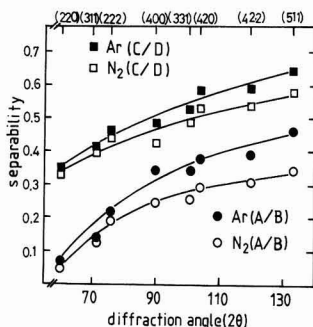


Fig. 4. Variations of the separability defined as either A/B or C/D with the diffraction angle for the specimens which have similar crystallite sizes (810 Å) and stacking fault densities (3.6%). Difference in the separability according to the firing atmospheres is clearly seen for all diffraction angles.

always larger in an Ar-annealed specimen than in a N₂-annealed specimen, which firmly indicates the nitrogen dissolution further introduces the lattice strain (the existence of lattice strain leads to a decrease in separability).

As a result, the separability of the X-ray diffraction lines, K α_1 and K α_2 , can be easily measured and is judged to be applicable to evaluate, though qualitatively, the lattice strain introduced into β -SiC grains. Therefore, the separability was utilized in the present study to elucidate the effect of lattice strain on the stacking fault annihilation in β -SiC.

Before explaining the detailed experimental results, separabilities of the specimens with various kinds of additives measured using the (422) diffraction lines are presented here. **Figure 5** shows the relationships between the separability and the stacking fault density for the specimens annealed at 1800°C for 0.5 h in Ar. As has been expected, the separability decreases with increasing stacking fault density. The most significant feature to be noted in the figure is that the separabilities for the Fe- and C-added specimens are generally larger than those for the B- and Al-added specimens, when compared at the same stacking fault density. This fact indicates that the dissolution of B or Al into SiC grains enhances the lattice strain, while undissolved Fe or C has little effect on the lattice strain, as will be verified from the lattice parameter variations described in the following sections.

3.2. Effects of Soluble Additives on the Stacking Fault Annihilation

3.2.1. Boron (B)

Boron is known as an additive for solid state sintering and is commonly added with carbon. The effects of boron on the sintering behavior or β -SiC have been widely studied by many researchers. Greskovich and Rosolowski¹⁰⁾ showed that boron inhibits surface diffusion during heating up and so reduces particle coarsening. Murata and Smoak¹¹⁾ reported that the formation of solid solution between SiC and boron composite (BN, BP, B₄C) occurred during densification, and the maximum density of SiC body was obtained at the maximum solubility of additives. It is also

expected that the addition of boron to β -SiC should have great effects on the annihilation of stacking faults.

Figure 6 shows the stacking fault density and lattice parameter for the β -SiC specimens with various boron contents after annealed at 1800°C for 0.5h in Ar. It appears that the stacking fault density increases with increasing boron content, indicating that the annihilation of stacking faults become more suppressed as increasing B content. Lattice parameter decreases with increasing boron content, exhibiting a high correlation with the change in the stacking fault density.

It is postulated from Fig.6 that the substitutional solid solution may be formed when boron is incorporated into β -SiC lattice. Since the difference in covalent radii between B(0.082nm) and C(0.077 nm) is smaller than that between B and Si (0.111 nm), it may be expected that B is incorporated into C site in SiC. However, it is considered from

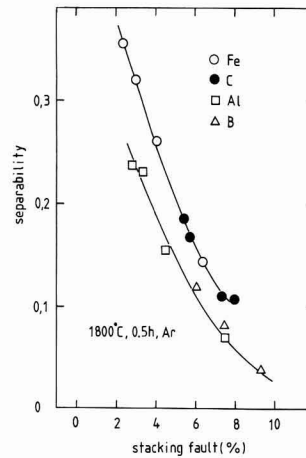


Fig. 5. Relation between the separability and the stacking fault density for the specimens with additives annealed at 1800°C for 0.5 h in Ar.

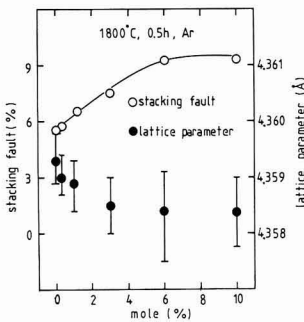


Fig. 6

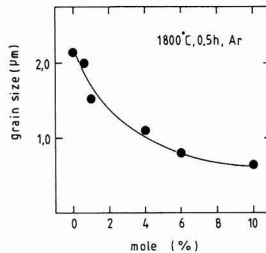


Fig. 7

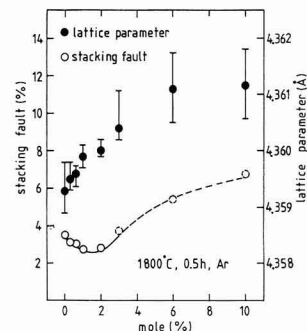


Fig. 8

Fig. 6. Stacking fault density and lattice parameter as functions of the amount of B addition for the specimens annealed at 1800°C for 0.5 h in Ar.

Fig. 7. Average grain size as a function of the amount of B addition for the specimens annealed at 1800°C for 0.5 h in Ar.

Fig. 8. Variations in the stacking fault density and lattice parameter with the Al additive concentration for the specimens annealed at 1800°C for 0.5 h in Ar. Specimens were slowly heated up to 1800°C at the rate of 4°C/min.

decreasing lattice parameter that the added B dissolves into Si sites, or C and Si sites concurrently. It may be explained from the stability of chemical bonding. Both B-C and Si-B systems form binary compounds having the same structure, B_4C and SiB_4 . The B-C system is chemically and thermally much more stable than Si-B system above $\sim 1400^\circ\text{C}$.^{8,12)}

Figure 7 shows the average grain size as a function of B content. Grain size decreases with increasing B content. It should be noted that the change in grain size after annealing is closely related to the annihilation of stacking faults and the lattice parameter change. Dissolution of B into SiC grains enhances the lattice strain as mentioned in the previous section and hence decreases the rate of grain growth owing to the suppression of surface diffusion and/or vapor transport, just as the case for nitrogen-doped β -SiC.⁴⁾ Stacking fault annihilation always takes place simultaneously with the grain growth, and hence the inhibition of grain growth causes the suppression of stacking fault annihilation.

3.2.2. Aluminum (Al)

Figures 8 and 9 show stacking fault densities and lattice parameters in the β -SiC specimens with various Al contents obtained after annealing at 1800°C for 0.5 h in Ar. The specimens in Fig. 9 were heated at the rate of $30^\circ\text{C}/\text{min}$ which is eight times as rapid as that for the specimens in Fig. 8 ($4^\circ\text{C}/\text{min}$). In both cases, lattice parameter increased with increasing Al content. Regardless of the heating schedule, the solid solubility limit of Al is found to be about 6 mol% (in an amount of addition) and the maximum value of lattice parameter is about 4.361\AA . However, the difference in the rate of annihilation of stacking faults is remarkable between the two heating schedules. In Figs. 8 and 9, symbols at 0 mol% may be due to the difference in the heating rate, since annihilation of stacking faults starts at about 1600°C in an Ar atmosphere.

It is widely accepted that thin Al-containing grain boundary films exist in Al- and C-doped SiC,¹³⁾ and that aluminum

powder reacts with SiC to give Al_4C_3 , Al_4SiC_4 , and ternary (Al-C-Si) liquid phase at $700^\circ\text{--}1700^\circ\text{C}$.¹⁴⁾ Fig. 8 shows that annihilation of stacking faults is enhanced by the addition of a small amount (below 2 mol%) of Al under the slow heating condition. Therefore, in the case of slow heating, Al-containing second phase may be formed on the grain surfaces and grain boundaries at relatively low temperatures before the added Al dissolves into the grains. Then the mass transport rate is increased through the Al-containing second phase which becomes a liquid phase at higher temperatures.¹⁴⁾ The existence of Al-containing second phase must further have a large effect on the formation and growth of intergranular neck and the grain coarsening during annealing. Because annihilation of stacking faults occurs simultaneously with the grain growth, the existence of the second phase would enhance the stacking fault annihilation.

Under a rapid heating condition, annihilation of stacking faults is suppressed more than under a slow heating condition. It is assumed that the most of the added Al may directly dissolve into grains at high temperatures (1800°C) without forming the second phase because of the rapid heating rate. It is considered from lattice parameter change that the lattice strain is introduced by solid solution formation owing to the different atomic radius of solute atoms. Under the high strain energy field, annihilation of stacking faults may be more difficult than under the low strain energy field.

In the case of adding more than 3 mol% of Al, $3C \rightarrow 4H$ phase transformation occurs as shown in Figs. 8 and 9. The precise calculation of stacking faults is impossible due to the superimposition of the (100) diffraction peak of the 4H phase on the 33.6° peak (2θ) of the 3C phase which is important for the calculation of stacking fault density. However, if the diffraction intensity of $(100)_{4H}$ is 25% of that of $(101)_{4H}$ according to the JCPDS card, the approximate calculation is possible. The results of the approximate calculation are shown by the broken lines in Figs. 8 and 9 for the specimens added with more than 3 mol% Al. Though the

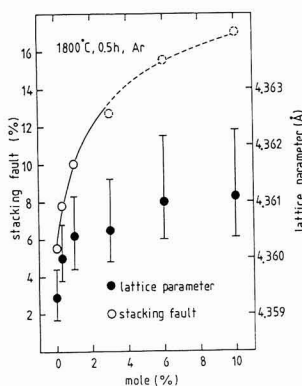


Fig. 9

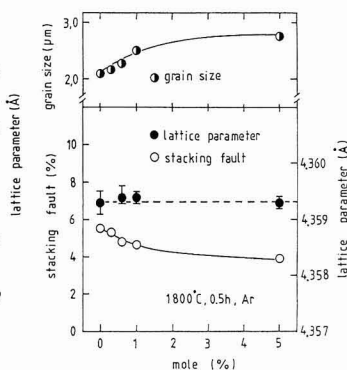


Fig. 10

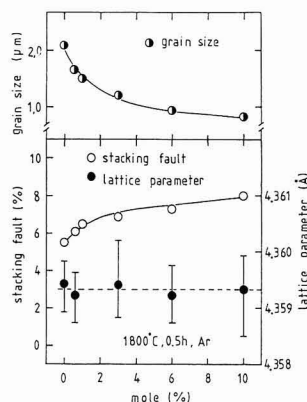


Fig. 11

Fig. 9. Variations in the stacking fault density and lattice parameter with the Al additive concentration for the specimens annealed at 1800°C for 0.5 h in Ar. Specimens were rapidly heated up to 1800°C at the rate of $30^\circ\text{C}/\text{min}$.

Fig. 10. Variations in the stacking fault density, lattice parameter and the average grain size with the Fe additive concentration for the specimens annealed at 1800°C for 0.5 h in Ar.

Fig. 11. Variations in the stacking fault density, lattice parameter and the average grain size with the C additive concentration for the specimens annealed at 1800°C for 0.5 h in Ar.

phase transformation occurs, the stacking fault density increases with increasing content of added Al. Moreover, in the case of adding more than 6 mol% for rapid heating, the stacking fault density appears to become larger than that of the starting powder (15% stacking fault density). Also, 4H content increases with increasing content of the added Al. Consequently, it is considered that the degree of 3C→4H phase transformation is closely related to the annihilation and formation of stacking faults. However, the effects of stacking faults on the phase transformation are fairly complicated, and our investigation on this problem will be published separately.

3.3. Effects of Insoluble Additives on the Stacking Fault Annihilation

3.3.1. Iron (Fe)

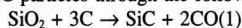
Because good intrinsic properties of the sintered body of SiC cannot be expected under the existence of Fe and other metal impurities, the powder prepared by a conventional method is usually passed through the acid treatment to remove metal impurities. Hence, there have been few reports on the behavior of Fe in SiC, in contrast with the number of reports on the sintering additives, such as Al, B and C. Allegro only reported that 3 mol% addition of Fe was the most effective in promoting the densification of β -SiC by hot pressing.¹⁵⁾

However, by the present pressureless sintering, the relative density of the annealed body did not practically change with an increase in the amount of Fe addition, while the average grain size increased as shown in Fig.10. Fig.10 also shows the changes in stacking fault density and lattice parameter for the Fe-added β -SiC specimens. It is evident that increasing amount of Fe-addition promotes the annihilation of stacking faults and that the lattice parameter remains unchanged within experimental errors. Because there is no change in lattice parameter, lattice strain occurring from the dissolution of Fe atoms would never exist in the Fe-added β -SiC. Therefore, the promotion of stacking fault annihilation must have been caused by other microstructural factors.

An increase in the grain size as increasing Fe content is due to the enhancement of surface diffusion and/or vapor transport rate which controls the initial stage of sintering in β -SiC at relatively low temperatures. The added Fe powders could form a liquid phase, since α -FeSi whose melting point is 1410°C¹⁶⁾ is always detected by XRD when more than 1 mol% of Fe is added. Then, Fe-based melt covers the grain surfaces and possibly grain boundaries, which would promote the grain growth through the liquid phase transport and hence disappearance of small grains leads to the enhancement of stacking fault annihilation according to the previously proposed mechanism.⁴⁾

3.3.2. Carbon (C)

The addition of carbon to β -SiC as a sintering additive has been reported by many researchers.^{6,17-19)} The added carbon probably removes the oxygen from the surface of SiC particles through the following reaction:^{17,18)}



The removal of surface oxide causes an increase in the surface area and thus in the surface energy of a particle.⁶⁾

An increase in the surface energy is expected to promote the grain growth. However, the grain size of β -SiC decreased with increasing content of carbon as shown in Fig.11. Although the surface oxide turns into the newly formed SiC and exhausted CO gas according to the reaction (1), the residual unreacted carbon would impede the grain growth by pinning the grain boundary movement.¹⁹⁾

Fig.11 shows the changes in stacking fault density and lattice parameter for the C-added β -SiC specimens. Stacking fault density increases but lattice parameter remains unchanged with increasing C content. As the amount of the added C is increased, the annihilation of stacking faults becomes suppressed. Since lattice strain introduced by the dissolution of C in β -SiC grains does not exist, the suppression of stacking fault annihilation must be attributed to the inhibition of grain growth.

Acknowledgements

The authors express their sincere thanks to Mr. T. Ono and Mr. R. Tanaka of Central Glass Co., Ltd. for supplying the specially ordered β -SiC powders.

References:

- 1) W.F. Knoppenberg, Phillips Res. Rep., 18, 161-274 (1963).
- 2) S. Prochazka, Ceramics for High Performance Applications, J. Burk, A.E. Gorun and R.M. Katz, Brook Hill, Chestnut Hill, MA, (1974) pp.239-52.
- 3) K. Koumoto, S. Takeda, C.H. Pai, T. Sato and H. Yanagida, J. Am. Ceram. Soc., 72, 1985-1987 (1989).
- 4) W.S. Seo, C.H. Pai, K. Koumoto and H. Yanagida, J. Ceram. Soc. Jpn., 99, 443-447 (1991).
- 5) K. Koumoto, C.H. Pai, S. Takeda and H. Yanagida, Proc. 8th Int. Conf. on Thermoelectric Energy Conservation and 2nd Europe Conf. Thermoelec., ed. by H. and S. Scherrer, Nancy, France, (1989) pp.107-112.
- 6) S. Prochazka, Special Ceramics 6, British Ceramic Research Association, (1975) pp.171-82.
- 7) F.F. Lange, J. Mater. Sci., 10, 314-320 (1975).
- 8) Y. Tajima and W.D. Kingery, J. Am. Ceram. Soc., 65, C27-29 (1982).
- 9) W. H/Hall, Proc. Phys. Soc., A62, 741-743 (1949).
- 10) C. Greskovich and J.H. Rosolowski, J. Am. Ceram. Soc., 59, 336-343 (1976).
- 11) Y. Murata and R.H. Smoak, Proc. Int. Symp. of Factors in Densification and Sintering of Oxides and Non-Oxide Ceramics, ed. by S. Somiya and S. Saito, Hakone, Japan, (1978) pp.382-399.
- 12) R.D. Allen, J. Am. Chem. Soc., 75, 3582-3583 (1953).
- 13) R. Hamminger, G. Grathwohl and F. Thummler, J. Mater. Sci., 18, 3154-3160 (1983).
- 14) J.C. Viala, P. Fortier and J. Bouix, *ibid.*, 25, 1842-1850 (1990).
- 15) R.A. Allegro, L.B. Coffin and J.R. Tinklepaugh, J. Am. Ceram. Soc., 39, 386-389 (1956).
- 16) R. Schmid, CALPHAD, 4, 101-108 (1980).
- 17) H. Tanaka, Y. Inomata, K. Hara and H. Hasegawa, J. Mater. Sci. Lett., 4, 315-317 (1985).
- 18) P. Elder and V.D. Krstic, J. Mater. Sci. Lett., 8, 941-943 (1989).
- 19) E.R. Maddrell, J. Mater. Sci. Lett., 6, 486-488 (1987).

Influence of Annealing on the Properties of Ca-Rich Bi-Pb-Sr-Ca-Cu-O Superconducting Thin Films

Keizou Tsukamoto, Hiromasa Shimojima, Mamoru Ishii and Chitake Yamagishi

Central Research Laboratory, Nihon Cement Co. Ltd.
1-2-23 Kiyosumi Koutoku Tokyo 135 Japan

Bi-Pb-Sr-Ca-Cu-O superconducting thin films with various Ca contents were prepared by rf-magnetron sputtering method using multi targets. The influence of the annealing on the obtained films was investigated. Ca-rich films compared to the high T_c phase did not show zero resistivity after the annealing. The C-axis length of the high T_c phase in these films was in a range of 3.710–3.720 nm. Moreover, as the annealing time was increased, the orientation of the grains was improved and the film was composed of the stacking layer structure of the thin and platelike crystals. These results suggest that the liquid phase between platelike crystals produced by the annealing had a negative influence on the superconductive properties of the annealed films because the grain was isolated and grain boundary works as insulator.

[Received June 12, 1990; Accepted September 19, 1991]

Key-words: Bi-Pb-Sr-Ca-Cu-O thin film, Rf magnetron sputtering, Multi target, High T_c phase, Stacking layer structure, Isolated grain

1. Introduction

The Bi-Sr-Ca-Cu-O and Bi-Pb-Sr-Ca-Cu-O system superconductors consist of the polymorphism of 110K (high T_c phase), 80K (low T_c phase) and semiconductor phase.¹⁻³⁾ It is well known, in order to form the high T_c phase that the partial melting conditions (low T_c phase and the liquid phase around it) are very important. The partial melting conditions, therefore, are kept for a long time in the production of the single, high- T_c phase in the bulk body. A number of researchers have been attempting to make Bi-system superconductive thin films to apply to electronic materials and devices. The as-deposited films with a high critical temperature are rarely obtained, and the high T_c superconductive films are normally obtained by the annealing the deposited films.

It is possible to produce, a Bi-system superconductive thin film by the short time annealing, which has a critical temperature above 100K.⁴⁻⁶⁾ However, the film, unlike the bulk, may be badly affected by the long time annealing for an extended period of time.⁴⁾ Particularly for the Ca-rich composition, when the resistivity curves have the tailing for a long time.⁷⁾

In this study, thin films annealing with various Ca content, which are greatly influenced by the annealing, were prepared to investigate the effects of the morphology, particle orientation and lattice constant on critical temperature, and thereby to investigate the effects of heat treatment on

the thin film properties.

2. Experimental Procedure

The Bi-Pb-Sr-Ca-Cu-O film was prepared on the commercial substrate of MgO single crystal by a rf magnetron sputtering (supplied by Tokki), using multi targets. The three targets are

- ① $\text{Bi}_{10.5}\text{Pb}_{0.5}\text{O}_x$ (mixed powder of Bi_2O_3 and PbO)
 - ② $\text{CaCu}_{0.75}\text{O}_x$ (powders of CaCO_3 and CuO fired at 950°C)
 - ③ $\text{SrCu}_{0.75}\text{O}_x$ (powders of SrCO_3 and CuO fired at 950°C)
- The Bi-Pb-O, Ca-Cu-O and Sr-Cu-O compositions were deposited, consecutively in this order, over the MgO substrate to form the multi-layered film by sputtering (Table 1 gives the sputtering conditions). In this study, deposition time for each target was set at: Thin Film A ... ① 8sec, ② 63.5sec ③ 28.5sec, and Thin Film B ... ① 8sec, ② 58.5sec ③ 33.5sec.

A total of 100sec was allocated to each sputtering cycle covering the three targets, and the sputtering cycles were repeated 400 times. Each sputtering cycle gave a thickness of 5nm, and thus a total of 2 μm thickness was obtained.

The thin film, prepared while keeping the substrate at 200°C, was amorphous. It was annealed at 850°C for 15, 24 or 65hr for crystallization. Each film was heated to a given temperature in approximately 3hr, and then allowed to cool in the furnace, after having been held at that temperature for a given time.

During the annealing process, the film was placed in an alumina boat, along with 1.0g of pelleted $\text{Bi}_{0.96}\text{Pb}_{0.24}\text{SrCaCu}_{1.6}\text{O}_x$ (fired at 850°C for 50hr), where the boat was sealed by another alumina boat, to prevent vaporization of PbO from the film.

The chemical composition of the thin Bi-Pb-Sr-Ca-Cu-O film was determined by EPMA (hitachi). The crystalline

Table 1. Sputtering conditions.

rf power	100W
substrate temperature	200°C
sputtering gas	100% Ar
gas pressure	10mTorr
target-substrate spacing	60mm
substrate	MgO (100)
film thickness	2 μm

phases and c-axis length of the annealed film were determined by a X-ray diffractometer (Rigaku Denki), using Cuk α X-ray. Volume of the high T_c phase, relative to that of the low T_c phase, was determined by Equation (1):

Volume ratio of the high T_c phase = $\frac{H(002)}{H(002) + L(002)}$ (%)

..... (1)

where,

- $H(002)$: intensity of (002) reflection of the high T_c phase
- $L(002)$: intensity of (002) reflection of the low T_c phase

Orientation of the superconducting particles was determined from the half maximum intensity breadth of the rocking curve.

Resistance of the thin film was determined by the 4-probe method, using a cryostat (Sumitomo Heavy Industries), which was cooled at a rate of 2°C/min. The morphology of the thin film were determined by a scanning electron microscope (SEM, Hitachi).

3. Results and Discussion

3.1. Critical Temperature of Thin Films

Two types of thin films were prepared; Film A and Film B, the former having Ca in excess of the stoichiometric composition of the high T_c phase composition, and the latter having a smaller quantity of Ca than the former, represented by the compositions of Bi_{0.85}Pb_{0.85}Sr_{1.00}Ca_{1.17}Cu_{1.87}O_x and Bi_{0.74}Pb_{0.74}Sr_{1.00}Ca_{0.92}Cu_{1.80}O_x, before annealing. Their Pb content was higher than that in the bulk composition, in consideration of its evaporation during the annealing process.

These thin films were annealed at 850°C for 15, 24 or 65hr. **Figures 1(A) and (B)** show the temperature dependence of resistivity of these films. Critical temperature of the thin films was greatly affected by annealing time at 850°C.

The resistivity of Film A, when annealed for 15hr, decreased from around 110K to zero at 99K, showing no phenomenon in which resistivity trailed down, frequently observed with the Bi-system superconductors. The resistivity of the film annealed for 24hr began to decrease from

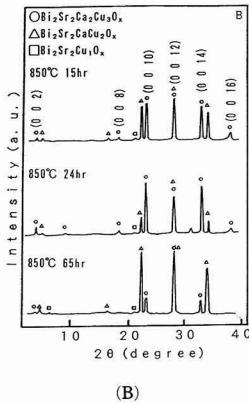
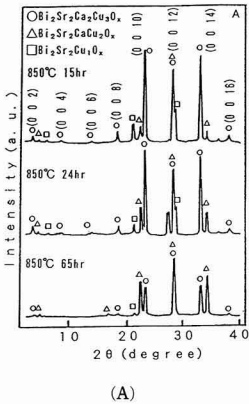
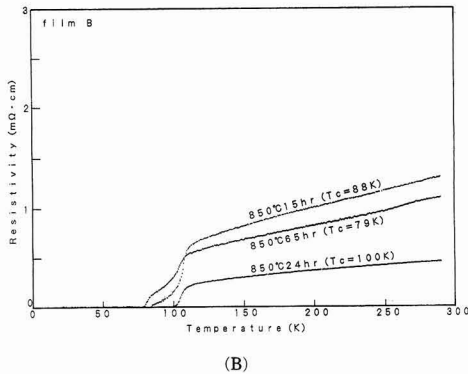
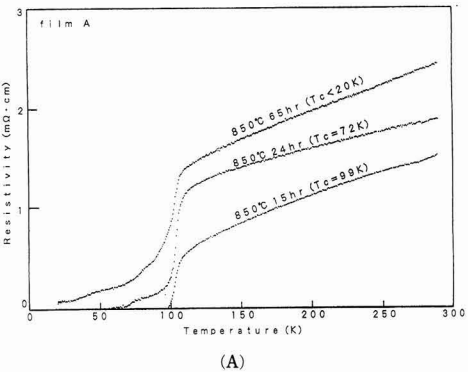


Fig. 1. Temperature dependence of the resistivity for the annealed films A and B.

Fig. 2. XRD patterns of the annealed films A and B.

around 110K, which trailed slightly to attain zero at 77K. On the other hand, the resistivity of the film annealed for 65hr showed trailing down slowly to 20K, at which it was still not zero.

Film B attained zero resistance at 88K with the film annealed for 15hr and at 100K with the film annealed for 24hr. With the one treated for 65hr, on the other hand, resistivity showed a trailing tendency to some extent, but attained zero at 79K.

Endo et al discuss that resistance of the Ca-rich composition trails down as temperature decreased, because of the formation of the semiconductor phase during annealing process,⁸⁾ and such a phenomenon was also observed with the thin films annealed for 24 and 65hr in this study. On the other hand, the film annealed for 15hr showed no such phenomenon.

It was also observed that decreasing Ca content tended to diminish the trailing phenomenon, even when increasing annealing time.

3.2. Crystalline Phases of the Thin Films

Figures 2(A) and (B) show the XRD patterns of each sample. Each composition consisted of the high T_c phase ($\text{Bi}_2\text{Sr}_2\text{Ca}_2\text{Cu}_3\text{O}_x$) oriented to the c-axis, the low T_c phase ($\text{Bi}_2\text{Sr}_2\text{Ca}_1\text{Cu}_2\text{O}_x$) and the semiconductor phase ($\text{Bi}_2\text{Sr}_2\text{Cu}_1\text{O}_x$). The volume ratio of the high T_c phase accounted for 91, 77 and 42% in the compositions treated for 15, 24 and 65hr, respectively, as determined by eq.(1); decreasing in quantity as annealing time increased.

It was also noted that the semiconductor phase decreased in quantity with annealing time. The Ca-richer composition favors formation of the semiconductor phase, as pointed out by Endo et al,⁸⁾ which was also observed in this study. It had been considered that resistance of the superconductor was greatly affected by the presence of the semiconductor phase, and that resistivity followed the semiconductor behavior. However, both showed the metallic behavior. Critical temperature decreased with annealing time, as was the case with proportion of the high T_c phase, from which it can be postulated that it is affected by the crystalline phases. The film annealed for 65hr consisted essentially of the high and low T_c phases, judging from its XRD patterns; nevertheless, however, its resistance trailed to 20K. This indicates that the crystalline phase is not the sole factor that

determines resistance-related behavior of the film.

It was also observed that the high T_c phase increased in quantity as Ca content increased, and its contents were 50, 75 and 24% in the films annealed for 15, 24 and 65hr, respectively.

Therefore, length of the c-axis in the high T_c phase, degree of orientation of the superconducting particles and film structures were analyzed, to investigate their effects on critical temperature.

3.3. Length of the C-axis of the Thin Film

Length of the c-axis in the high T_c phase in Films A and B were measured with Si powder as the reference. The diffraction lines used to determine the length were of (002), (008), (0010), (0014), (0016), (0018), (0024), (0024), (0026), (0032) and (0034). The results are given in Table 2.

The c-axis length of both films changed with annealing time, and that of the film having a higher critical temperature was 3.710 to 3.720nm. Kozono et al, on the other hand, discuss that critical temperature of the film (composition: $\text{Bi}_2\text{PbSr}_{2.2}\text{Ca}_{2.2}\text{Cu}_{3.7}\text{O}_x$) increases as its c-axis length approaches 3.71nm.⁹⁾ The results observed in this study, coupled with Kozono et al's, suggest that c-axis length in a certain range gives a high critical temperature.

It is discussed that the layers of the Bi-system superconductor are not only irregularly configured but also distorted.^{10,11)} The changed c-axis length of the high T_c phase as a result of heat treatment, observed in this study, suggests that the annealing changes the lamination conditions. The three-layer structure of the Cu-O plane may be contaminated with the one-, two- or four-layer structure, to change the calculated c-axis length.

3.4. Orientation of the Thin Film

Degree of orientation of the particles in the high and low T_c phases in Film A was determined from the half maximum intensity breadth of the rocking curves, using the (0014) and (0012) diffraction lines of the high and low T_c phases, respectively (see Fig. 3). The rocking curve became sharper with annealing time, by which is meant that degree of orientation of the c-axis of the high T_c phase increases with annealing time. The thin film annealed for 65hr and a high degree of orientation of 1° or less. It was observed with the

Table 2. C-axis length of film A and B.

Film	Annealing Process	C-axis length
A	850°C×15hr	3.711±0.003nm
A	850°C×24hr	3.708±0.001nm
A	850°C×65hr	3.694±0.002nm
B	850°C×15hr	3.713±0.003nm
B	850°C×24hr	3.710±0.002nm
B	850°C×65hr	3.737±0.003nm

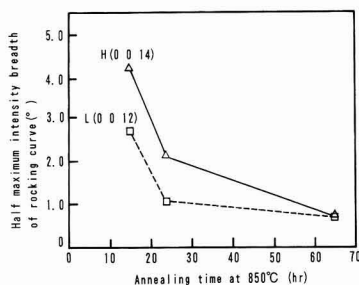


Fig. 3. Relationship between half maximum intensity breadth of rocking curve and annealing time at 850°C for the film A.

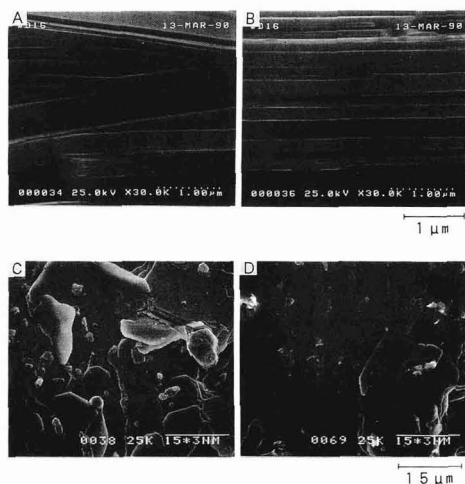


Fig. 4. SEM photographs of the film A.

(A) cross section morphology of the film annealed at 850°C for 15 hr.

(B) cross section morphology of the film annealed at 850°C for 65 hr.

(C) surface morphology of the film annealed at 850°C for 15 hr.

(D) surface morphology of the film annealed at 850°C for 65 hr.

bulk superconductor that the superconducting characteristics (critical temperature and critical current flux) increases as degree of orientation of the c-axis increases. The thin film having an improved degree of orientation prepared in this study, however, is characterized by resistance which trails down but is not converged to zero until temperature is decreased to 20K.

On the other hand, the thin film annealed for 15 hr, showing a high T_c (99K), had a relatively low degree of orientation of 4.2°.

The half maximum intensity breadth of the rocking curve was measured also for the low T_c phase, showing that degree of orientation of the c-axis increased as annealing time increased, as was the case with the high T_c phase.

3.5. SEM Observation of the Thin Films

Figure 4 shows the SEM photographs of the cross-sections and surfaces of the Films A annealed for 15 and 65 hr. The former film had more blurred surface structures than the latter.

The photographs of the cross-sections indicated that relatively thick plate-like crystals, which were randomly oriented, were bonded to each other in the thin film annealed for 15 hr, whereas the thin plate-like crystals were laminated regularly to form the layered structure, in which the crystals were completely separated from each other, in the film annealed for 65 hr. These results are in good agreement with those showing that degree of orientation of the c-axis increases as annealing time increases.

The results of the SEM observation and orientation of the c-axis suggest that the structural changes with annealing

time result from reduced quantity of the high T_c phase, the Ca-O and Cu-O driven off from the phase forming the liquid phase together with Ca and Cu not included in the superconducting crystals, which cover the plate-like crystals. As a result, the plate-like crystals become sufficiently slippery to be regularly configured. The liquid phase present in the grain boundaries will remain as the glassy phase around the plate-like crystals, after the film is cooled, to weaken the electrical bond between the crystals. As a result, resistance trails with temperature, on account of retarded flow of superconducting current.

4. Conclusions

The effects of annealing on behavior of the Bi-Pb-Sr-Ca-Cu-O superconductor with varying Ca content were investigated.

1) Resistance of Films A and B depended on annealing time.

In particular, resistance of the film contained Ca in excess of the stoichiometric content of high T_c phase showed a trailing trend and was not converged to zero, when the films were annealed for an extended period. Lengths of the c-axis of these films were measured. The results indicated that those films with a high critical temperature had a c-axis length within a certain range, 3.710 to 3.720 nm for the film prepared in this study.

2) Increasing annealing time increased degree of orientation of the high and low T_c phases, allowing the thin plate-like crystals to be regularly laminated, to form the layered structure. These results suggest that the liquid phase, formed as a result of annealing for an extended period, covers the plate-like crystals, making them slippery and regularly configured.

It is therefore considered, based on these results, that heat treatment of the Ca-rich composition for an extended period reduces quantity of the high T_c phase, with the result that the Ca-O and Cu-O bonds driven off from the phase form the liquid phase together with excess elements such as Ca and Cu (which are not included in the crystals); the liquid phase remains as the glassy phase, after the film is cooled, to cover the plate-like crystals. This weakens the electrical bond between these crystals, as a result of which resistance of the film trails with temperature on account of retarded flow of superconducting current.

References:

- 1) H. Maeda, Y. Tanaka, M. Fukutomi and T. Asano, *Jpn. J. Appl. Phys.*, 27, L209-210 (1988).
- 2) M. Takano, J. Takada, K. Oda, H. Kitaguchi, Y. Miura, Y. Ikeda, Y. Tomii and H. Mazaki, *ibid.*, 27, L1041-1043 (1988).
- 3) U. Endo, S. Koyama and T. Kawai, *ibid.*, 27, L1476-1479 (1988).
- 4) A. Tanaka, T. Machi, N. Kamehara and K. Niwa, *Appl. Phys. Lett.*, 54 (14) 3, 1362-1364 (1989).
- 5) A. Tanaka, N. Kamehara and K. Niwa, *ibid.*, 55 (12) 18, 1252-1254 (1989).
- 6) Y. Hakuraku, Y. Aridome and T. Ogushi, *Jpn. J. Appl. Phys.*, 27, L2091-2093 (1989).
- 7) S. Nagai, N. Fujimura and T. Itoh, *Powder and Powder Metallur.*, 37, 99-102 (1990).
- 8) U. Endo, S. Koyama and T. Kawai, *Jpn. J. Appl. Phys.*, 28, L190-192 (1989).
- 9) Y. Kozono, T. Ohono, M. Kasai, M. Hanazono and Y. Sugita, *ibid.*, 28, L646-649 (1989).

- 10) Y. Matsui, H. Maeda, Y. Tanaka, E.T. Muromachi, S. Takekawa and S. Horiuchi, *ibid.*, 27, L827-829 (1988).
- 11) Y. Matsui, H. Maeda, Y. Tanaka and S. Horiuchi, *ibid.*, 27, L372-375 (1988).
- 12) K. Tsukamoto, H. Shimojima, M. Ishii and C. Yamagishi, *Seramikkusu Ronbunshi*, 99, 68-72 (1991).

This article is a full translation of the article which appeared in *Nippon Seramikkusu Kyokai Gakujutsu Ronbunshi* (Japanese version), Vol.99, No.12, 1991.

Burn-out of Binder and Sintering Behavior of Powder Compacts of Bimodally Distributed Alumina Powders with Stearic Acid and Polyethleneglycol

Seiichi Taruta, Kunio Kitajima, Nobuo Takusagawa, Kiyoshi Okada* and Nozomu Ôtsuka**

Department of Chemistry and Material Engineering, Faculty of Engineering, Shinshu University
500, Wakasato, Nagano-shi, 380 Japan

*Department of Inorganic Materials, Faculty of Engineering, Tokyo Institute of Technology
2-12-1, O-okayama, Meguro-ku, Tokyo, 152 Japan

**Department of Materials, Faculty of Science and Engineering, The Nishi Tokyo University
2525, Yatsusawa, Uenohara-machi, Kitatsuru-gun, Yamanashi, 409-01 Japan

In order to achieve high green density of alumina powder compacts of particles with bimodal size distribution, stearic acid and polyethleneglycol were used as forming aids. Burn-out of binder and sintering behavior of these powder compacts were investigated. The forming aids melted at 50°C and concentrated on contact points of particles where a large capillary force acts, and became difficult to burn out. Therefore, the forming aids in compacts containing a large amount of fine particles tended to burn out at higher temperature. Powder compacts containing 40-100% fine particles expanded prior to burn-out of forming aids and began to contract simultaneously with burn-out of forming aids at 170°C. Powder compacts containing 0-30% fine particles did not expand but began to contract at 300°C. As forming aids burn-out, small pores in compacts shrank, whereas large pores grew. The sintered densities of compacts that were high green density with forming aids were also higher than those of compacts that were low green density without forming aids, until the relative density reached 95%. However, the effect of green density on the densification decreased when the relative density exceeded 95% due to remarkable grain growth.

[Received January 30, 1991; Accepted August 22, 1991]

Key-words: Bimodal alumina powder, Stearic acid, Polyethleneglycol, Thermal analysis, Capillary force, Burn-out, Sintering

1. Introduction

In the previous paper,¹⁾ changes in open pore size distribution were mainly studied among the sintering behavior of alumina powder mixtures with different particle size. As a result, it was found that the pores of green compacts of the powder mixtures grow by sintering. Moreover, this suggested that the control of pore growth by preparing compacts with denser structures allows densification at lower temperatures. There are lubricants²⁾ as forming aids to reduce the sliding friction of particles or to assist mold release. The addition of these lubricants to powder is considered to provide denser compacts. However, when organic matter is used as a forming aid, it burns during firing and may cause

defects such as cracks or deformation in compacts. Consequently, it is important to know the behavior of a compact while the organic matter burns from the standpoint of preventing defects. But very few works have dealt with its relation to the particle size of powder, though some have reported on the thermal analysis of forming aids in terms of removal behavior.³⁻⁸⁾

In this study, stearic acid was added as a lubricant in order to increase the density of compacts of alumina powder mixtures with different particle size. However, compaction was not able to be performed so that polyethylene glycol was added to provide plasticity with stearic acid. These powder mixtures were compacted by isostatic pressing. And thermal properties, density after forming aids removal and sintering and pore size distributions of obtained compacts were measured, microstructures were observed. These results were examined to study the influences of blending ratios of alumina powder with different particle size, the amount of added molding aids and heating rate on the behavior of compacts during lubricant removal, as well as a relation between the packing state of compacts and sintering properties.

2. Experimental Procedure

2.1. Alumina Raw Materials and Forming Aids

The two kinds of alumina powder, the same as in the previous report,¹⁾ were employed as raw materials. Their average particle diameters were 6.3µm and 0.52µm. The powder with coarse particles was spherical polycrystalline alumina. Both polyethylene glycol (average molecular weight: 2000) and stearic acid were first-class reagents (Wako Pure Chemical Industrial, LTD.) Hereafter, coarse particles are referred as c particles, fine particles as f particles, polyethylene glycol as PEG, stearic acid as SA, and a PEG/SA mixture (1:1 in weight ratio) as SP.

2.2. Preparation of Specimens

Magnesium nitrate corresponding to 0.02wt% MgO was added to coarse and fine powders, each of which was mixed in wet with a plastic ball mill. They were dried, calcined at 550°C for 1h, weighed out to prepare specimens with the specified weight ratios (c:f particles) from 10:0 to 0:10, and mixed in wet with the plastic ball mill. The liquid medium

was ethanol dissolving a certain amount of PEG and SA. The resulting slurry was dried, mixed again in dry with the plastic ball mill, and screened by a 100-mesh sieve. The prepared powder mixtures were compacted by uniaxial pressing at 12MPa and isostatic pressing at 98MPa to provide compacts 10φ×3mm in size, which were sintered at 1500°C or 1600°C for 2h. **Table 1** shows the amount of added PEG and SA. SP4% represents a specimen with 2wt% of PEG and 2wt% of SA, SPX% that with less PEG and SA than SP4% reduced according to the specific surface area of each powder mixture with the value of c:f=0:10 (7.6m²/g) as 1, and SP0% that without addition.

2.3. Thermal Analyses of Compacts

In order to investigate the behavior of compacts during lubricant removal, the following instruments were used for thermal analyses: a thermal gravimetric analyzer (TGA; Shimadzu Seisakusho Ltd., TGC-40), a differential thermal analyzer (DTA; Shimadzu Seisakusho Ltd., DT-40), and a differential thermal expansion meter (TMA; Rigaku Denki, CN8098D2). Specimens used in TGA and DTA were about 50mg of pieces cut out of compacts prepared as in Clause 2.2, while those in TMA were stick compacts 20×4.5×3mm in size formed by isostatic pressing as in 2.2. A standard sample was α-Al₂O₃, load 1g, and heating at a rate of 2°C/min. or 10°C/min in air.

2.4. Evaluation of Compacts and Sintered Bodies

The green density was calculated from the volume of a green compact and weight after heating up to 800°C. The sintered density was obtained by an Archimedeian method. The open pore size distribution of compacts and sintered bodies was measured with Hg porosimeter (Shimadzu Seisakusho, pore sizer type 9310). Their microstructures were observed with a scanning electron microscope (SEM; JEOL, Ltd., JSM-T20). The surfaces of specimens of sintered bodies were polished and etched thermally before observation.

3. Results and Discussion

3.1. Green Density

Figure 1 shows the relative density which were experimental values of SP0%, SP4%, and SPX% compacts and calculated values of SP4%. However, SP0% and SPX% samples with c:f=10:0 and 9:1 could not be formed. The relative density of SP4% was 3-5% higher than that of SP0%, proving that the addition of SP was effective to improve density. However, as in the case of the previous report,¹⁾ the experimental values of SP4% was lower than calculated values based on Furnas' relationship.⁹⁾ When

the density was compared between SP4% and SPX% with less addition, they were almost equal with all mixing ratios except that SPX% with c:f=7:3 had slightly higher density.

3.2. Burnout Behavior of Forming Aids

Figure 2 shows DTA curves of SP2%, PEG4%, and SP4% with c:f=0:10. Specimens were powder and a heating rate was 10°C/min. In the case of SA2%, there was an endothermal peak caused by the melting of forming aids near 70°C, and PEG4% near 40°C. Moreover, SA2% had two large exothermal peaks by the combustion of the forming aids at 250-400°C, and PEG4% three such peaks at 160-400°C. SP4% had an endothermal peak by SP melting near 50°C, and exothermal peaks at 140-210°C and 250-400°C. With the results of SA and PEG, the exothermal reaction at 140-210°C is considered to have been caused mainly by the burnout of PEG, while that at 250°C-400°C by the burnout of organic contaminants to be stated later.

Figure 3 shows the SEM photos of SP4% green compacts with c:f=10:0, and heated to 160°C or 350°C. SP in green compact is dispersed almost uniformly on the particles. In the case of 160°C, molten SP is concentrated mainly between particles or near the contact points of particles by capillary force (arrows in the figure). As for 350°C, SP is observed only at the above parts, and almost nowhere else. Consequently, as in the photos, SP is considered to be hard to burn by capillary force among particles.

Figure 4 shows the TGA results of SP4% compacts. The heating rate was 10°C/min. T₅, T₅₀, and T₉₅ represent the temperatures at which 5%, 50% and 95% of SP in compacts burned respectively. The figure shows that T₅ is almost

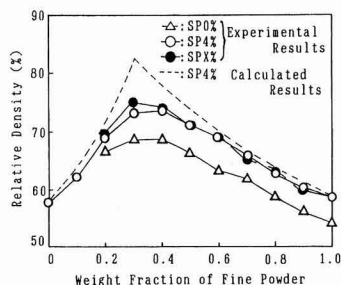


Fig. 1. Experimental green densities for various ratios of binary alumina mixtures with SP0%, SP4% and SPX% and calculated densities for SP4% which were obtained from Furnas packing model.⁹⁾

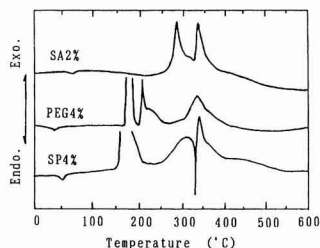


Fig. 2. DTA behavior of c:f=0:10 powders with SA2%, PEG4% and SP4% heated at 10°C/min.

Table 1. Content of stearic acid and polyethyleneglycol.

c:f	10:0	9:1	8:2	7:3	6:4	5:5	4:6	3:7	2:8	1:9	0:10
SP4% Stearic Acid(wt%)	2	2	2	2	2	2	2	2	2	2	2
PEG (wt%)	2	2	2	2	2	2	2	2	2	2	2
SPX% Stearic Acid(wt%)	0.1	0.3	0.5	0.7	0.9	1.0	1.2	1.4	1.6	1.8	2
PEG (wt%)	0.1	0.3	0.5	0.7	0.9	1.0	1.2	1.4	1.6	1.8	2

constant at 170°C even with different c:f mixing ratios, while the greater the amount of f particles, the harder SP is to burn. The probable reason for this is that the greater the amount of f particles, the larger the amount of SP under great capillary force. However, the TGA curves of powder and compacts are similar with the same c:f mixing ratios; therefore, it is surmised that the burnout of SP is affected not only by capillary force on particle contacts but by the size of the mass of SP under capillary force and the diffusion distance of SP to be removed.

Figure 4(b) shows the TGA curves of SP0%, SP4%, and SPX% with c:f=7:3 measured at a heating rate of 10°C/min, as well as those of SP4% measured at 2°C/min. The weight loss of SP0% is probably due to the removal of organic matter entering from the plastic ball mill and residual alcohol in mixing. T_{50} of SPX% and SP4% is 315°C and 245°C respectively, and that of SPX% is higher than SP4%'s because the proportion of SP free from capillary force is low. However, the temperature where SP of both burns almost completely is nearly equal (about 600°C), which indicates that if the c:f mixing ratio is the same, almost the equal amount of SP hard to burn remains up to 600°C between particles and near particle contact points, regardless of the amount of SP added. From the results of different heating rates (2°C/min and 10°C/min), it was found that SP burns at lower temperatures with slower heating rate.

3.3. Expansion and Contraction of Compacts During

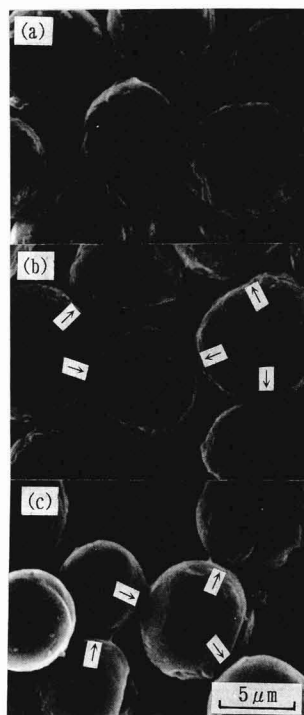


Fig. 3. SEM microphotographs.

(a) Green compacts and heated compacts at 10°C/min up to (b) 160°C and (c) 350°C for c:f=10:0 with SP4%.

Burnout of Forming Aids

Figure 5 shows the typical results of TMA with SP4% compacts with c:f=10:0~0:10. The heating rate was 10°C/min. These results showed a difference in expansion and contraction between compacts with ① c:f=10:0~7:3 and ② 6:4~0:10.

First, ① showed almost no change at r.t. ~ 170°C while ② expanded. This expansion would have been caused by the process that SP migrating between particles or near particle contacts by capillary force underwent greater thermal expansion than alumina, and particle distance was prodded. However, in the case of adding only PEG with c:f=0:10, no expansion occurred, and when SA, PEG and SP were heated while placed on alumina sintered bodies polished to mirror face, SA and SP were harder to extend than PEG though each molten liquid had a contact angle of less than 90° exhibiting no visual change (the absolute value of Work of Spreading Wetting⁽¹⁰⁾ was great). These facts suggest that the expansion of compacts is affected also by affinity between alumina and the molten liquid of forming aids (especially Work of Spreading Wetting). Consequently, it is surmised that in ② the greater the amount of f particles with great capillary force, the greater the expansion while in ① compacts did not expand because c particles constituting the skeleton in compacts had low capillary force, allowing the expanded molten liquid to extend in space formed by particles.

At 170° ~ 200°C, ① showed little change while ② contracted rapidly. This contraction would have been due to the abrupt burnout of chiefly PEG existing on particles with low capillary force, thereby reducing SP between particles and attracting particles which had been parted by the expansion of SP. Especially, the reason for large contraction in the case of c:f=4:6 and 3:7 is considered to be due to plenty

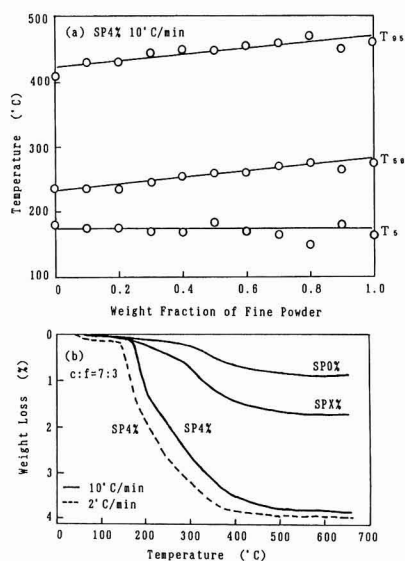


Fig. 4. TGA behavior of green compacts for (a) various ratios of binary alumina mixtures with SP4% heated at 10°C/min and (b) c:f=7:3 with SP0%, SP4% and SPX% heated at 10°C/min and with SP4% at 2°C/min.

of f particles as well a greater SP burnout than the case of $c:f=2:8-0:10$.

At 200 ~ 300°C, no substantial expansion or contraction was observed with any mixing ratio. In this temperature range, SP chiefly near particle contacts burned gradually so that the force of attracting particles was probably in rough balance with that of SP expansion.

At 300 ~ 800°C, gentle contraction was observed with any mixing ratio. In this temperature range, SP remaining near particle contacts or between particles burned almost completely, which would have allowed the attraction of particles to show contraction. For this reason, the amount of contraction in this temperature range would have been larger with increase of particles in the case of ②, and with $c:f=10:0$ having more contact between c particles in ①. In the latter, ①, expansion was recognized from 600°C, and the cause is under study.

As has been stated above, the thermal expansion and contraction of compacts can be classified into ① and ② groups, depending on the arrangement of c and f particles.¹⁾ In the group ①, c particles with small capillary force constitute a skeleton, so that expansion or abrupt contraction does not occur, except for contraction only when SP between particles or near particle contacts burns. In ②, f particles with large capillary force comprise matrix allowing expansion, and contraction occurs at the same time as forming aids removal. The extent of this change depends on the amount of f particles and the burnout rate of SP. However, the cases of 5:4 and 5:5 which show intermediate arrangement between ① and ②¹⁾ are considered to exhibit the behavior of both ① and ②.

Figure 6 shows the TMA curves of SP0%, SP4% and SPX% measured at a heating rate of 10°C/min. and that of SP4% measured at 2°C/min. The amount of expansion and contraction was smaller in the case of SPX% with low addition than in SP4%, but the former showed the behavior of expansion and contraction similar to the latter. The contraction of SP0% is probably due to the burnout of organic contaminants. Moreover, in comparison between 2°C/min. and 10°C/min., the amount of expansion and contraction was almost the same in both cases, but it occurred at lower

temperatures in the case of 2°C/min.

3.4. Change in Pore Size Distribution of Compacts During Burnout of Forming Aids

Figure 7 shows the pore size distribution of SP4% green compacts with $c:f=4:6$ and heated compacts to 165°C, 350°C and 800°C. The pore diameter of the 165°C case was greater than that immediately after molding. This is considered to have been caused by the expansion of compacts. The pore diameter of the 350°C case was almost as large as the 165°C case. The reason is probably that an increase in pore diameter by SP combustion counterbalanced a decrease in that by compact contraction. Further heating to 800°C contracted compacts but enlarged pore diameter compared with that of the 350°C case. The cause was discussed referring to Fig.8.

Figure 8 shows the pore size distribution of SP0%, SP4%, and SPX% with $c:f=4:6$ and 7:3 heated to 800°C at a rate of 10°C/min. and that of SP4% heated to the same temperature at 2°C/min. In the case of $c:f=4:6$, the order of pore diameters after forming aids removal were $SP0\% > SP4\% > SPX\%$. SP0% had the lowest green density, which would have resulted in the largest pore diameter.

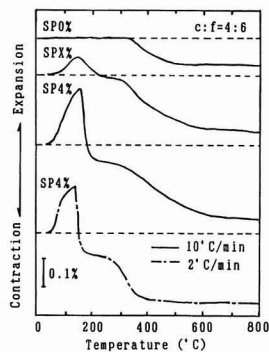


Fig. 6. TMA behavior of green compacts for $c:f=4:6$ with SP0%, SP4% and SPX% heated at 10°C/min and with SP4% at 2°C/min.

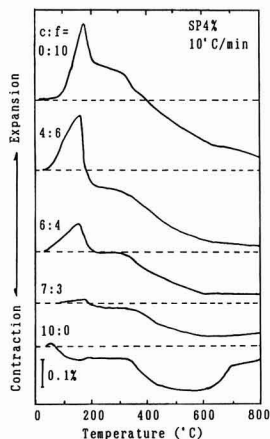


Fig. 5. TMA behavior of green compacts for various ratios of binary alumina mixtures with SP4% heated at 10°C/min.

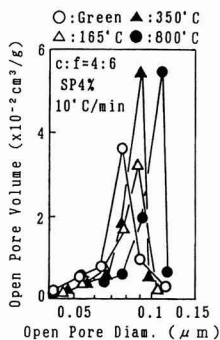


Fig. 7. Open pore size distribution of green compacts and heated compacts at 10°C/min up to 165°C, 350°C and 800°C for $c:f=4:6$ with SP4%.

Since the green density of SP4% was almost equal to that of SPX% with less addition, it was first predicted that the pore diameter of SPX% compacts with small contraction after forming aids removal was larger than that of SP4%, but the experimental results were quite the opposite. This suggests that pore growth after forming aids removal is promoted not only by SP burnout but by the process that during the contraction of a compact by forming aids removal, nonuniform rearrangement of particles occurs to permit small pores to be smaller and large ones to be larger.

In the case of $c:f=7:3$, pore diameters after forming aids removal were $SP4\% > SP0\% > SPX\%$. The smallest pore diameter of SPX% is probably due to the highest green density. But SP4% with higher green density than SP0% had larger pore diameter. This suggests that the contraction compacts with $c:f=7:3$ was small after forming aids removal and the degree of rearrangement of c particles constituting skeletons was small, but f particles in the space formed by c particles undergo local nonuniform rearrangement by melting and removal of SP, thus resulting in large pores.

As stated above, it was found that the pore diameter increases by SP removal and nonuniform particle rearrangement also in the process where a compact contracts by forming aids removal. Considering the state of arrangement of c and f particles in the compact,¹⁾ it is surmised that the cases of $c:f=4:6-0:10$ allow f particles constituting matrix to undergo nonuniform rearrangement, those of $10:0-7:3$ allow f particles among c particles to undergo nonuniform rearrangement, and those of $6:4$ and $5:5$ allow the behavior of both to coexist. The nonuniformity of this rearrangement is considered to increase with greater SP addition and higher heating rate.

3.5. Sintering Properties

1) Densification

Figure 9 shows the relative density of SP0%, SP4%, and SPX%, sintered at 1500°C or 1600°C for 2h. In comparison between specimens with the same $c:f$ mixing ratios, sintered density had the same tendency as green density ($SP0\% < SP\% < SPX\%$) when the relative density of sintered bodies was less than 95%. However, with high mixing ratio of f particles and relative sintered density greater than 95%, sintered density was almost equal even though there was a difference of 3~5% in relative green density.

2) Pore size distribution

Figure 10 shows the open pore size distribution of SP0%, SP4%, and SPX% with $c:f=4:6$ and $7:3$. The order of the pore size of sintered bodies with $c:f=7:3$ was $SPX\% < SP4\% < SP0\%$, which agreed with that of the pore size after forming aids removal. That is, the smaller the pore size after lubricant removal, the smaller the pore size of sintered bodies. The order of the pore size of sintered bodies with $c:f=4:6$ was $SP4\% = SPX\% < SP0\%$, since SP0% had the largest pore size after forming aids removal, so did after sintering. However, SP4% had larger pore size than SPX% after forming aids removal, and yet both were almost equal after sintering. The probable reason is that when the addition of SP increases green density and raise packing ratio of f particles, the pore size after sintering is affected more greatly by the sinterability of c and f particles than by the pore size distribution of compacts.

3) Microstructures of sintered bodies

Figure 11 shows SEM photos of SP4% sintered bodies with $c:f=0:10, 4:6$, and $7:3$ heated at 1600°C for 2h. SP4%

with $c:f=0:10$ had large spherical pores several micron meters in size as in Fig.11(a). Such pores were spherical and hardly observed in SP0%, so that they would have been caused by the process where a part of the pyrolytic products of SP remained till sintering advanced to form closed pores. In SP4% with $c:f=4:6$, as in Fig.11(b), notable grain growth was observed as transgranular pores were formed. This remarkable grain growth was encountered in SP0% and SPX% as well. In SP4% with $c:f=7:3$, the grain growth was also observed as in Fig.11(c), but it was not as active as the case of $c:f=4:6$ because f particles were few. These results suggest that the reason why sintered density becomes almost equal when it approaches 95% even with high green density is violet grain growth in the form of trans-granular pores.

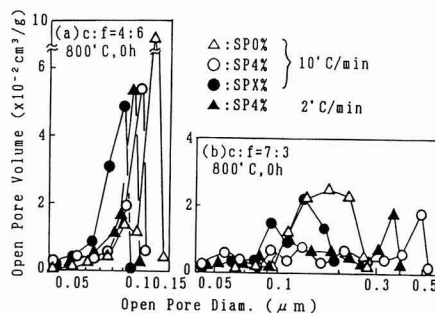


Fig. 8. Open pore size distribution.

(a) $c:f=4:6$ and (b) $c:f=7:3$ with SP0%, SP4% and SPX% heated at 10°C/min and with SP4% at 2°C/min up to 800°C.

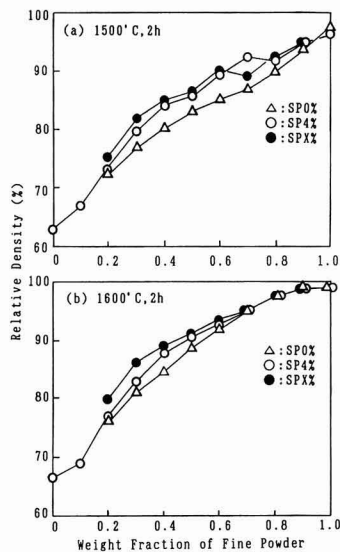


Fig. 9. Relative densities for various ratios of binary alumina mixtures with SP0%, SP4% and SPX% fired (a) at 1500°C for 2h and (b) at 1600°C for 2h.

5. Conclusion

When stearic acid and polyethyleneglycol(SP) was added to alumina powder mixtures with different particle size, the relative green density became 3~5% higher than the case without SP addition. Compacts were examined for forming aids removal and sintering properties. The following results were obtained.

1) SP in compacts becomes hard to burn due to the capillary force of particles. During this process, the compacts undergo expansion and contraction affected by the capillary force of particles along with affinity between alumina

and molten forming aids, and the particles undergo non-uniform rearrangement.

- 2) The combustion of SP in compacts begins at higher temperatures with higher mixing ratio of fine particles (f particles). The behavior of compacts in the above process differs with different mixing ratios of coarse and fine particles (c:f):(a) c:f=10:0~7:3, (b) 6:4~5:5, and (c) 4:6~0:10. In the case (a), coarse particles (c particles) with small capillary force constitute a skeleton and neither expansion nor abrupt contraction occurs, while in the case (c) f particles with great capillary force constitute matrix to allow such changes. Additionally, nonuniform rearrangement is undergone by f particles in the skeleton in (a) and by those constituting matrix in (c). In the case (b), the behavior of (a) and (c) coexists.
- 3) When SP addition is less than 4%, the degree of expansion and contraction of compacts becomes low and the degree of rearrangement of particles is small though the temperature where SP burns completely hardly changes. Moreover, with slower rate of forming aids removal the burnout of SP occurs at lower temperatures, and particle rearrangement becomes more uniform though the amount of expansion and contraction of compact is unchanged.
- 4) In specimens with the same c:f mixing ratios, it was found that SP-added compacts with high green density have higher sintered density than SP-nonadded compacts until the relative density reaches 95%.
- 5) In specimens with the same c:f mixing ratios, notable grain growth occurs when the relative sintered density approaches 95%, vanishing the effect of particle packing in compacts. Consequently, to densify powder mixtures at low temperatures the control of grain growth requires as well as higher green density.

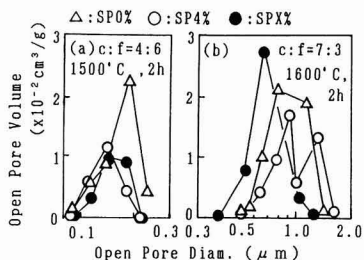


Fig. 10. Open pore size distribution.

(a) c:f=4:6 with SP0%, SP4% and SPX% fired at 1500°C for 2h and (b) c:f=7:3 with SP0%, SP4% and SPX% fired at 1600°C for 2h.

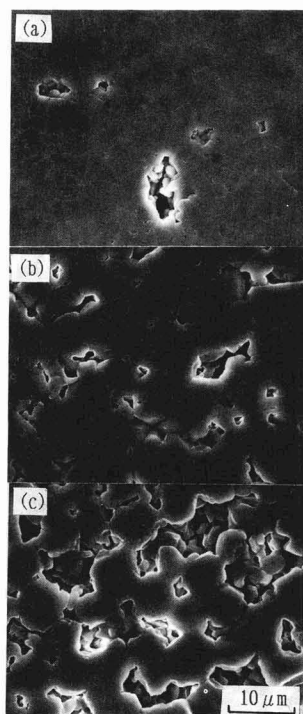


Fig. 11. SEM microphotographs.

(a) c:f=0:10, (b) 4:6 and (c) 7:3 with SP4% fired at 1600°C for 2h.

Acknowledgements

The authors are grateful to Prof. M. Hirao and Associate Prof. S. Oishi, Department of Chemistry and Material Engineering, Faculty of Engineering, Shinshu University, for the measurement of thermal expansion and preparation of compacts, and Mr. T. Yamada, Industrial Research Institute of Nagano, for the measurement of pore size distribution.

References

- 1) S. Taruta, K. Okada and N. Ôtsuka, *Seramikkku-Ronbun-Shi*, 98, 29-35 (1990).
- 2) K. Saito, *Fain Seramikkusu Kinzoku Funtai Seikei-Yo Baida-Rui no Kiso to Oyo Gijutsui*, Ai Shi Pi (1988).
- 3) C. Dong and H.K. Bowen, *J. Am. Ceram. Soc.*, 72, 1082-1087 (1989).
- 4) M.J. Cima, M. Dudziak and J.A. Lewis, *ibid.*, 72, 1087-1090 (1989).
- 5) M.J. Cima, J.A. Lewis and A.D. Devoe, *ibid.*, 72, 1192-1199 (1989).
- 6) V.N. Shukla and D.C. Hill, *ibid.*, 72, 10 1797-1803 (1989).
- 7) J.K. Wright, J.R.G. Evans and M.J. Edirisinghe, *ibid.*, 72, 10 1822-1828 (1989).
- 8) P. Calvert and M. Cima, *ibid.*, 73, 575-579 (1990).
- 9) C.C. Fumas, *U.S. Bur. Mines, Rep.*, No.2984 (1928).
- 10) Chem. Soc. Jpn. (ed.), *Jikken Kagaku Koza* 7, Kaimen Kagaku, Maruzen (1956) 67-69.

This article is a full translation of the article which appeared in *Nippon Seramikkusu Kyokai Gakujutsu Ronbunshi* (Japanese version), Vol.99, No.12, 1991.

Study on the Composite Materials Consisting of $\text{Li}_2\text{O-SiO}_2$ Crystals and $\text{Na}_2\text{O-CaO-SiO}_2$ Glass

Koichi Watanabe and Shiroshi Chigira

Department of Material Chemistry, Faculty of Technology, Gunma University

1-5-1, Tenjin-cho, Kiryu-shi, 376 Japan

The composite materials consisting of crystals and glasses were prepared by heat-treating the mixtures of $\text{Li}_2\text{O-ASiO}_2$ (LS) and $\text{Na}_2\text{O-caO-SiO}_2$ (NCS) glass powders. In the specimens in which the proportion of $\text{Li}_2\text{O-SiO}_2$ glass content decreases, other crystals such as α -quartz, β -cristobalite, and wollastonite were detected. The differential thermal analysis, thermal expansion coefficient, softening temperature, apparent density, porosity, compressive strength and bending strength were measured. The relations between the strengths and the mixing ratio of LS and NCS glass were analyzed based on the crystal content and the porosity. The crystallization behavior and the composite reaction process were also discussed.

[Received April 2, 1991; Accepted September 19, 1991]

Key-words: $\text{Li}_2\text{O-SiO}_2$ glass, $\text{Na}_2\text{O-CaO-SiO}_2$ glass, Composite material, Porosity, Mechanical strength, Crystallization behavior, Thermal expansion

1. Introduction

It is known that the characteristics of composite materials are greatly affected by 1) the properties of raw materials, 2) composite structures (the proportion of dispersed to matrix, morphology, distribution state etc.), 3) interfacial conditions, and others. Among these, factor 3) is the most important in preparing composite materials and involves miscellaneous problems such as

wettability of both materials and chemical reactivity at the interface; a difference in the coefficients of thermal expansion that will cause strain and cracks inside materials as well as invite a decrease in strength; surface conditions before reaction (rough or smooth); and surface structures including matching of lattice constants of both materials, number of protruded dislocation sources, and condition of interfacial layers. The composite reinforcement of ceramic materials is classified into two types according to used raw materials and forms-fiber reinforcement and particle dispersion reinforcement.¹⁾ Moreover, the particle dispersion reinforcement type is grouped into the following two types: precipitated particle reinforcement which controls crystals precipitation and particle diameter by heat treatment to obtain reinforcement, and mixed particle reinforcement that crack pinning, the control of crack development and the generation of prestress²⁾ provides reinforcement.

Some examples of the preparation of composite ceramic materials include an early work of $\text{Li}_2\text{O-Al}_2\text{O}_3\text{-nSiO}_2\text{-Li}_2\text{O-SiO}_2$ glass composites,³⁾ of a precipitation particle reinforcement type intended to improve mechanical strength

and thermal shock resistance, and recent works of cordierite ($2\text{MgO} \cdot 2\text{Al}_2\text{O}_3 \cdot 5\text{SiO}_2$ - mullite ($6\text{Al}_2\text{O}_3 \cdot 2\text{SiO}_2$)) composite sintered bodies by Mussler⁴⁾ and Ikawa et al.⁵⁾ aimed at application for substrates for electronic materials, cordierite-mullite glass composite of a mixed particle reinforcement type by Ushifusa et al.,⁶⁾ and fiber-reinforced ceramics (FRC) using SiC fiber.⁷⁾

The authors attempted the reacted-composition glass ceramics consisting of a precipitated particle dispersion type and mixed particle dispersion type, employing $\text{Li}_2\text{O-SiO}_2$ crystalline glass with well-studied crystallization behavior⁸⁾ and ordinary $\text{Na}_2\text{O-CaO-SiO}_2$ glass powder, while taking chemical reactivity and a difference in the coefficients of thermal expansion into consideration. The obtained composites were subjected to measurement for mechanical properties such as compressive and flexural strength, porosity, and thermal expansion, as well as to discussion on precipitated crystal phases resulting from different mixing ratio of the two glass materials and heat treatment temperatures and their reaction processes. This paper describes some basic knowledge obtained in this study.

2. Experimental Procedure

2.1. Preparation of Glass

The commercial special-grade reagents of SiO_2 , Li_2CO_3 , Al_2O_3 , Na_2CO_3 , CaCO_3 , and $\text{Mg}(\text{OH})_2$ were used as starting raw materials to prepare $\text{Li}_2\text{O-SiO}_2$ and $\text{Na}_2\text{O-CaO-SiO}_2$ glass. Each starting raw material was weighed out in the specified batch composition, mixed fully, charged in a 300-cc platinum crucible, and melted at 1500°C for 3h in an electric furnace. The molten matter was allowed to flow onto the iron plate to form glass, which was ground into powder samples less than $30\mu\text{m}$ in particle size for experiment. For simplification, $\text{Li}_2\text{O-SiO}_2$ glass to obtain crystalline glass is referred to as "LS," and $\text{Na}_2\text{O-CaO-SiO}_2$ glass (soda lime glass) as "NCS." In the case of the latter glass, some SiO_2 was added in excess compared with composition of practical glass,⁹⁾ taking differences in heat treatment temperature and coefficients of thermal expansion with crystalline glass into consideration. Table 1 shows the results of chemical analysis by an ICP method of these glass samples as well as their batch compositions.

2.2. Reaction Processes and Precipitated Crystal Phases of LS and NCS Glass

In order to observe crystallization and its process of LS glass when mixed with NCS glass, about 0.5 grams of a powder sample was charged in a Pt capsule and underwent differential thermal analysis (DTA) at a heating rate of $5^\circ\text{C}/\text{min}$. In addition, quenching experiment was performed

with samples packed in Pt tubes at temperatures somewhat higher and lower than peak temperatures in DTA curves, and precipitated crystal phases and the disappearing processes were examined by X-ray diffraction. In the same manner, the identification and semiquantitative analysis of crystal phases precipitated in formed samples after heat treatment were conducted by X-ray diffraction using the $\text{CuK}\alpha$ ray. In the semiquantitative analysis, Si metal was adopted as a standard sample, and values were estimated roughly from the peak intensity of 2SiO_2 (130) diffraction line ($2\theta=23.7$) (ASTM Card 17-447). To determine the coefficient of thermal expansion of each mixed sample, a thermal expansion curve was obtained using a quartz pushing rod type dilatometer (1/1000mm). The shape of a specimen was a rectangular parallelepiped $5\times 5\times 25\text{mm}$ in size after heat treatment at 700°C for 3h. Specimens of 100% of LS and NCS glass were cylinders 10mm in diameter and 20mm in length. The coefficients of thermal expansion were corrected using quartz glass and a pure silver rod as standard samples. The heating rate was $5^\circ\text{C}/\text{min}$.

2.3. Mechanical Strength, Porosity, and Microstructures

In order to prepare specimens for the measurement of compressive strength, 1.5 grams of mixed glass with the specified proportion was formed into a cylinder $10\times 10\text{mm}$ in size at a pressure of about $370\text{MPa}/\text{m}^2$. As for specimens for the measurement of flexural strength, 2 grams of mixed glass was molded into a stick $5\times 3\times 50\text{mm}$ in size at about $130\text{MPa}/\text{m}^2$. The specimens for flexural strength were hard to mold so that 1% of a polyvinylalcohol solution was added as a binder. The formed specimens were placed in the nichrome wire electric furnace, heated at a rate of $5^\circ\text{C}/\text{min}$., held at 650, 700, and 800°C for 3h and cooled in the furnace. In the preparatory experiment, the amount of precipitated crystals of crystalline glass employed in the main experiment saturated in about an hour at each treatment temperature. Consequently, heat treatment for 3h was judged to be sufficient. The temperature deviation in the electric furnace was $\pm 3^\circ\text{C}$. The compression test (loading vertical to a cylinder axis) of specimens after reaction and a four-point bending test (loading in the direction of 3mm thickness) were carried out using an Amsler-type compression tester and a universal testing machine.²⁾ The crosshead speed was $0.75\text{mm}/\text{min}$. and $0.5\text{mm}/\text{min}$. respectively. As for the bending test, the lower support span was 30mm and upper load span 10mm. Each measurement was performed with 5 specimens, and the average was adopted as a representative. In ordinary testing for mechanical strength, the surface

of a specimen should be polished to mirror flat to minimize the influence of its surface. Yet, in the preparatory experiment with specimens in this study, polishing tended to cause greater deviation in strength values, so that mirror flat polishing was omitted in this case and specimens directly after heat treatment were adopted in the testing. On the other hand, mechanical strength is affected greatly by the porosity of a specimen. Accordingly, each specimen formed and heat-treated under the same conditions as that for compressive strength was subjected to the measurement of apparent density and porosity by the ordinary method (JIS Z2505, 1979). Moreover, the SEM observation of fracture surfaces of specimens after compression tests was conducted to examine a relation between their microstructures and mechanical strength.

3. Experimental Results

3.1. Reaction process and Precipitated Crystal Phases

Generally, the crystallization of glass tends to start in the surface rather than inside.¹⁰⁾ However, heat treatment after mixing with non-crystalline glass as in this experiment may vary its surface condition as well as precipitated crystal phases, crystallization rate, and reaction process. **Figure 1** is a DTA curve of a LS-NCS glass mixture (weight ratio-LS80: NCS 20). The shift of the base line by glass transition is noticed at 450°C along with a large exothermal peak by crystal precipitation at $565\sim 660^\circ\text{C}$. The height of this peak by crystal precipitation decreased with an increase in the mixing ratio of NCS glass, and yet the initiation temperature of crystallization at a peak rise was almost constant (565°C) regardless of mixing ratios. The X-ray diffraction spectrum of a quenched specimen proved that this exothermal peak near 600°C is attributed to the precipitation of $\text{Li}_2\text{O}\cdot\text{SiO}_2$ crystals in the main phase and a small amount of Li_2OSiO_2 crystals.

The small exothermal peak near 700°C was not recognized in the case of monolithic LS glass, and proved to be caused by the precipitation of α -quartz (ASTM Card 33-1161) and β -cristobalite ($27\text{-}605$) crystal phase. The small exothermal peak near 800°C was attributed to β -spodumene ($2\text{Li}_2\text{O}\cdot\text{Al}_2\text{O}_3\cdot 4\text{SiO}_2$) (35-797). in addition, two endothermal peaks at 963°C and 987°C appeared probably owing to

Table 1. Chemical composition (mol%) of the LS glass-ceramics and NCS glass. The parenthesized values are batch composition.

	$\text{Li}_2\text{O}\cdot\text{SiO}_2$ system (LS)	$\text{Na}_2\text{O}\cdot\text{CaO}\cdot\text{SiO}_2$ system (NCS)
SiO_2	65.64 (67.54)	76.23 (77.61)
Al_2O_3	2.56 (3.14)	1.19 (1.49)
HgO	-----	4.47 (3.70)
CaO	-----	8.52 (8.42)
Na_2O	-----	9.59 (8.78)
Li_2O	31.80 (28.32)	-----
	100.00 (100.00)	100.00 (100.00) (mol %)

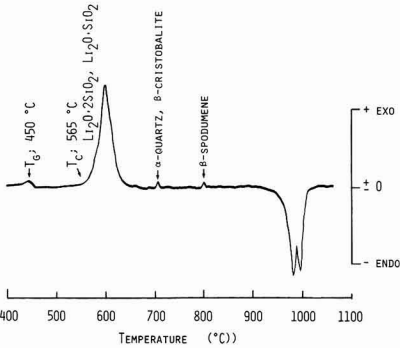


Fig. 1. DTA curve of the mixture (80 : 20 in wt%) of LS glass and NCS glass powders. Heating rate: $5^\circ\text{C}/\text{min}$.

the melting of crystal phases. The height of both peaks decreased with an increase in the mixing ratio of NCS glass as in the case of the large exothermal peak near 600°C. However, no change was encountered in the initiation temperature of the peak. **Figure 2** presents the typical changes of X-ray diffraction patterns. The figure shows that the crystal phases precipitating in the case of monolithic LS glass are $\text{Li}_2\text{O}\cdot\text{SiO}_2$ and Li_2OSiO_2 , and β -spodumene precipitates with increasing treatment time and temperature. However, the mixing of NCS glass led to the precipitation of the following three phases in addition to the above phases: α -quartz and β -cristobalite, both transformation phases of SiO_2 , and wollastonite (CaSiO_3) (29-372). The precipitation amount of these phases tended to increase as the mixing ratio of NCS glass increased, while β -spodumene and Li_2O crystal phase decreased, and the main $\text{Li}_2\text{O}\cdot\text{SiO}_2$ phase finally disappeared. **Figure 3** shows hypothetical composite reaction process in composite of LS glass and NCS glass. **Table 2** lists precipitated crystal phases obtained by the heat treatment of specimens with various mixing ratios for 3h at 650, 700, and 800°C. The wollastonite phase precipitated with a mixing ratio of LS60 : NCS40 by heat treatment at 650 and 700°C, whereas it was not encountered by heat treatment at the highest 800°C.

Figure 5 gives compressive strength, apparent density

and porosity at various heat treatment temperatures of specimens with different mixing ratios of LS and NCS glass. The optimum mixing ratio to provide a maximum strength was found at each treatment temperature. Such a ratio was LS glass 80 : NCS glass 20 at 800°C, 60:40 at 700°C and 10:90 at 650°C. Additionally, the maximum value of strength obtained in this experiment was about 7 times (690MPa/m^2) as much as monolithic LS glass (about 100MPa/m^2), and the mixing ratio was LS80:NCS20. The strength values of specimens of monolithic LS glass are hardly affected by treatment temperature, while some mixed specimens are affected greatly. For instance, in the case of LS80 : NCS20 the specimen treated at 800°C exhibited a maximum strength value, followed by that treated at 700°C and 650°C in this order. However in the case of 60 : 40, this was opposite and treatment at 700°C provided a maximum, then at 650°C and 800°C in this order. Moreover, the porosity of monolithic LS glass was not virtually affected by treatment temperature, showing almost constant values (17.7 ~ 18.8%). Yet, porosity decreased with an increase in the addition of NCS glass, and especially a porosity of less than 1% was achieved by LS60 : NCS40 at 800°C, 40 : 60 at 700°C and 20 : 80 at 650°C, thus proving that porosity is affected not only by treatment temperature but by mixing ratios. Further, in a relation between compressive strength

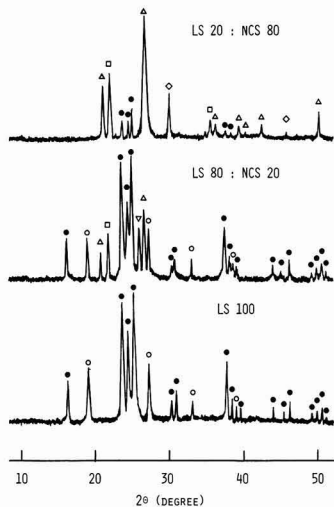


Fig. 2. Typical X-ray diffraction patterns. Heat treatment: 650°C, 3h.
●: $\text{Li}_2\text{O}\cdot 2\text{SiO}_2$, ○: $\text{Li}_2\text{O}\cdot\text{SiO}_2$, △: α -quartz, ▽: β -spodumene, □: β -cristobalite, ◇: wollastonite.

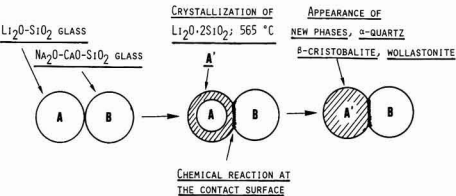


Fig. 3. Hypothetical composite reaction process in the composite of LS glass and NCS glass.

Table 2. Relationship between crystalline phases and heat-treatment temperatures.

L2S; $\text{Li}_2\text{O}\cdot 2\text{SiO}_2$, LS; $\text{Li}_2\text{O}\cdot\text{SiO}_2$, Q; α -quartz, C; β -cristobalite, S; β -spodumene, W; wollastonite.

MIXED RATIO (wt%)	HEAT TREATMENT TEMPERATURE (°C)		
	650	700	800
LS 100 : NCS 0	L2S, LS	L2S, LS, s	L2S, LS, s
LS 80 : NCS 20	L2S, LS, s, q, c	L2S, LS, s	L2S, s
LS 60 : NCS 40	L2S, LS, q, c, w	L2S, LS, q, c, w	L2S, s
LS 40 : NCS 60	L2S, q, c, w	L2S, q, c, w	-----
LS 20 : NCS 80	L2S, q, c, w	L2S, q, c	-----
LS 0 : NCS 100	-----	-----	-----

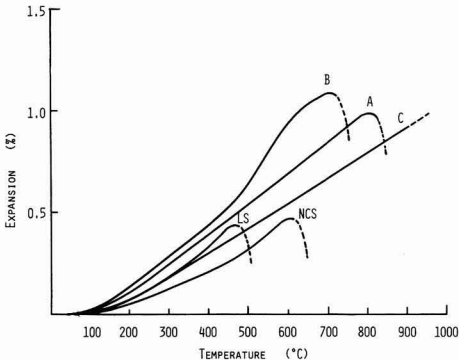


Fig. 4. Thermal expansion curve of the respective specimens which were heat-treated at 700°C for 3h. A ; LS80 : NCS20, B; LS20 : NCS80, C; LS100 : NCS0, LS; 100% LS glass rod, NCS; 100% NCS glass rod.

and porosity, the strength increased with decreasing porosity when the mixing ratio of NCS glass was low. By contrast, with higher mixing ratio of the glass, the strength tended to decrease in spite of decreasing porosity, and it was difficult to express a relation between compressive strength and porosity in a simple proportional function. The apparent density was 2.42 for monolithic LS glass, and increased by degrees with the increasing mixing ratio of NCS glass until it reached 2.47 for monolithic NCS glass. **Figure 6** plots a relation between flexural strength and mixing ratio. At each heat treatment temperature, flexural strength varied with mixing ratios in the same manner as compressive strength, but the maximum value tended to shift to a specimen with higher mixing ratio of NCS glass than the case of compressive strength. Maximum flexural strength at each tempera-

ture was obtained by a specimen with LS60 : NCS40 at 800°C, 10 : 90 at 700°C, and 20 : 80 at 650°C, and the maximum value was about 70MPa/m² (800°C), about 1/10 as much as compressive strength. The maximum flexural strength was achieved by the specimen treated at 800°C as in the case of compressive strength, and yet the values of specimens treated at 650 and 700°C were not so distinct as the case of compressive strength. As shown in Figs.4 and 6, compressive and flexural strength is greatly affected by heat treatment temperature and mixing ratios. With regard to the precipitation amount of Li₂O₂SiO₂ crystals, semi-quantitative analysis was carried out using specimens after the measurement of compressive strength by an X-ray method. The results are shown in **Fig.7**. The Li₂O-SiO₂ crystals decreased almost linearly with a decrease in the mixing ratio of LS glass at each heat treatment temperature, and the slight influence of treatment temperature was noticed in specimens with some kinds of mixing ratios.

The mechanical strength of particle dispersion type composites is greatly affected by particle diameter, pore size, its distribution, and the microstructure of matrix at particle interfaces or others. In general, smaller pores and finer particles will provide higher strength, and in the case of oval or formless voids, greater curvature of their corners is con-

Table 3. Variations of the thermal expansion coefficient and the softening temperature with a mixed ratio. Mark LS 100 and NCS 100 denote each rod specimen of LS glass-ceramics and NCS glass.

Mixed Ratio (wt%)	Thermal Expansion Coefficient (K ⁻¹)		Softening Temp. (°C)
	200~450(°C)	450~550(°C)	
LS 100 : NCS 0	9.4 × 10 ⁻⁶	10 × 10 ⁻⁶	> 900
LS 80 : NCS 20	14 × 10 ⁻⁶	14 × 10 ⁻⁶	805
LS 60 : NCS 40	14 × 10 ⁻⁶	19 × 10 ⁻⁶	760
LS 40 : NCS 60	14 × 10 ⁻⁶	28 × 10 ⁻⁶	725
LS 20 : NCS 80	14 × 10 ⁻⁶	35 × 10 ⁻⁶	710
NCS 100	7.0 × 10 ⁻⁶	8.1 × 10 ⁻⁶	610
LS 100	13 × 10 ⁻⁶	-----	475

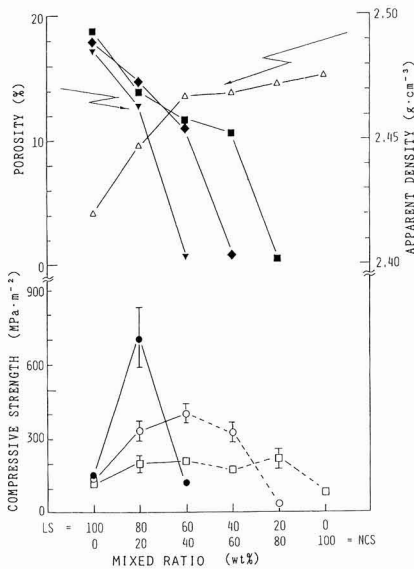


Fig. 5. Relationships between the compressive strength, porosity, and apparent density and a mixed ratio of LS glass-ceramics and NCS glass. —●—, —▼—: specimens which were heat-treated for 3h at 800°C, —○—, —◆—: at 700°C, —□—, —■—: at 650°C, —△—: density of specimens which were heat-treated at 650°C for 3h. The regime denoted by a dotted line included three new crystal phases.

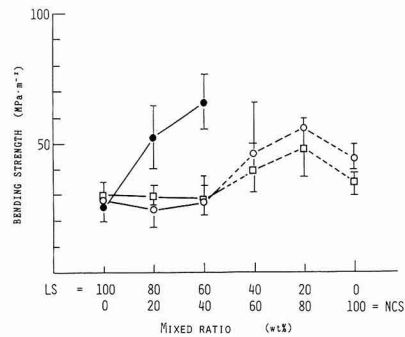


Fig. 6. Bending strength as a function of the mixed ratio. —●—: 800°C, —○—: 700°C, —□—: 650°C.

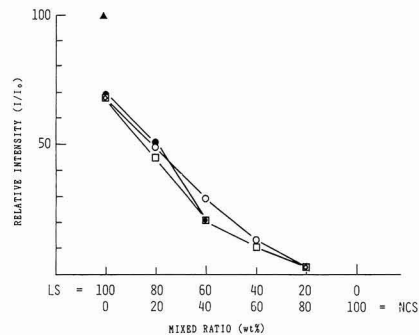


Fig. 7. Relative intensity of X-ray diffraction peak Li₂O₂SiO₂ with a mixed ratio. The diffraction peak height of (130) plane was calibrated by comparing with that of the pure Li₂O₂SiO₂ crystal. The specimen was heat-treated at the respective temperatures: —●—: 800°C, —○—: 700°C, —□—: 650°C, —▲—: Li₂O₂SiO₂ crystal.

sidered to be desirable.²⁾ Figure 8 gives the observation results of fracture surfaces of specimens providing maximum compressive strength at corresponding treatment temperatures. Figure 8(a) is the case of monolithic LS glass in which the lack of NCS glass to act as a binder causes insufficient bonding among LS glass particles, thus forming plenty of small voids and peeled thin flakes. In the specimen treated at 800°C (b) there are considerable bonding among particles, and spherical pores are observed with relatively large diameter (8 ~ 9µm). On the other hand, specimens treated at 700°C (c) and 650°C (d) have small spherical pores 3 ~ 4µm in diameter along with relatively large formless voids, so that bonding seems to be insufficient.

4. Discussion

According to the equilibrium diagram of an $\text{Li}_2\text{O}-\text{Al}_2\text{O}_3-\text{SiO}_2$ system,¹¹⁾ the eutectic temperature of the three phases of $\text{Li}_2\text{O}-\text{SiO}_2$, Li_2OSiO_2 , and β -spodumene is 975°C, and that of $\text{Li}_2\text{O}-\text{SiO}_2$, SiO_2 , and β -spodumene is 980°C. The two endothermal peaks at 963°C and 987°C in the DTA curve in Fig.1 is attributable to the melting phenomenon at the eutectic temperature of a crystal phase consisting of each of the above-stated three phases. There are slight differences in melting temperatures between the results of this experiment and the equilibrium diagram; the reason is probably that the mixing of NCS glass in this experiment leads to the precipitation of the new crystal phases of α -quartz, β -cristobalite, and wollastonite, thus affecting the results. Table 2 lists the mixing ratios of LS and NCS glass as well as precipitated crystal phases at various heat treatment temperatures. The precipitated crystal phases of monolithic LS glass are $\text{Li}_2\text{O}-\text{SiO}_2$, Li_2OSiO_2 , and β -spodumene, while those resulting from the mixing of NCS glass are α -quartz, β -cristobalite, and wollastonite, which are probably due to the result of a fusion reaction between LS and NCS glass.

The initiation temperature of an exothermal peak near 565°C accompanying the crystallization of $\text{Li}_2\text{O}-\text{SiO}_2$ in the DTA curve in Fig.1 was almost constant even with varied mixing ratios of NCS glass. The above results including DTA (Fig.1) and the changes of X-ray diffraction patterns (Fig.2 and Table 2) suggest that a fusion reaction to form LS-NCS composite glass is as follows (Fig.3). A mixture of LS and NCS glass in the vitreous state is heated and softening begins at the surface of the A particle made of LS glass with lower softening temperature (400°C) in the early step, followed by an interfacial fusion reaction with the B particle made of NCS glass through this softened surface. In parallel to the fusion reaction, the crystals of $\text{Li}_2\text{O}-\text{SiO}_2$ and Li_2OSiO_2 (565°C), the main phase, as well as β -spodumene (800°C) precipitate in the surface of and inside the LS glass particle. As the fusion reaction proceeds, the mutual diffusion of ions becomes active between A and B particles, and with a rise in temperature the reaction further advances to trigger the precipitation of the new crystal phases of α -quartz, β -cristobalite and wollastonite.

As in Fig.5, the compressive strengthened porosity of specimens of 100% LS glass was not affected by treatment temperature, showing almost constant values. Nevertheless, when NCS glass was mixed, substantial differences in compressive and flexural strength were caused by different heat treatment temperature, mixing ratios and porosity. As shown in Fig.7, the precipitated amount of $\text{Li}_2\text{O}-\text{SiO}_2$ crystals decreased at each treatment temperature almost linearly with a decrease in the mixing ratio of LS glass. Yet, with some specific mixing ratios, slight differences were noticed by heat treatment temperature, and in the case of LS60 : NCS40 the precipitated amount of a specimen treated at 700°C was the greatest. With this mixing ratio, compressive strength was also the highest at 700°C despite high porosity. Moreover, the porosity of a specimen with a mixing ratio of LS60 : NCS40 was the lowest (0.06%) after heat treatment at 800°C, 10.92 at 700°C, and 11.80 at 650°C, while compressive strength was the lowest in the case of 800°C treatment with the lowest porosity. Generally, mechanical strength is high when a specimen has low porosity and fine particles, or formless or oval voids having corners with layer curvature. Figure 8 shows the fracture surfaces of specimens treated at various temperatures. The specimen treated at 800°C (b) with the highest compressive strength has relatively large spherical pores and thus high porosity, whereas the specimens treated at 700°C (c) and at 650°C (d) have small pores and low porosity. However, compressive strength is low despite low porosity compared with the specimen treated at 800°C. The probable reason is that the 700- and 650-°C-treated specimens have plenty of nearly oval voids with sharp corners (small curvature), at which compressive stress localizes to allow failure by relatively low stress. Consequently, as in Fig.5, it is surmised that when the mixing ratio of NCS glass is low, compressive strength is affected by porosity, but when the mixing ratio exceeds a certain limit, it is affected rather by the precipitated amount of crystals such as $\text{Li}_2\text{O}-\text{SiO}_2$, or the form and distribution of voids than porosity. In addition, the flexural strength of a specimen with a mixing ratio of LS60 : NCS40 treated at 800°C showed a maximum, as opposed to the case of compressive strength. It is not clear whether this is due to the different forms of specimens, a difference in the mechanism of stress generation, or other factors. At any rate, when the mixing ratio of LS glass becomes 60% or

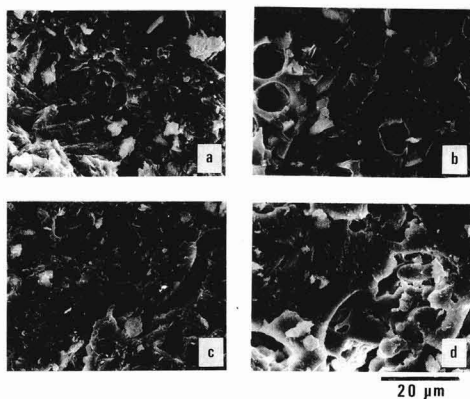


Fig. 8. SEM photographs of the fracture surface. (a): the specimen of LS 100 : NCS 0 which was heat-treated at 800°C for 3h., (b): the specimen of LS 80 : NCS 20 which was treated at 800°C for 3h., (c): LS 60 : NCS 40 at 700°C for 3h., (d): LS60 : NCS40 at 650°C 3h.

less, a change in the precipitated amount of other crystal phases than $\text{Li}_2\text{O-SiO}_2$, the main phase, is encountered as in Fig.2 and Table 2. Hence, in the discussion of mechanical strength of composites with an LS glass mixing ratio of 60% or less, these new precipitated phases should fundamentally be taken into consideration in addition to the crystallization amount of $\text{Li}_2\text{O-SiO}_2$, and yet details are unknown at present.

In general, the destruction energy of particle dispersion type composite materials is expressed as follows¹²⁾:

$$\Gamma = \Gamma_m + \tau\delta \quad \dots \dots \dots (1)$$

where Γ : destruction energy, Γ_m : the destruction energy of matrix, τ : the linear tensile force of a crack front, and δ : a distance between particles. According to formula (1), greater destruction energy Γ can be obtained either by reducing δ or by increasing Γ_m . In this experiment, NCS glass is mainly used as matrix, Γ_m will not show much variation. Therefore, increasing the destruction energy Γ on the left side of formula (1) will be achieved by reducing distance between $\text{Li}_2\text{O-SiO}_2$ crystal particles, that is, raising the mixing ratio of LS glass. However, in this experiment (as shown in Fig.5), when the mixing ratio of LS glass was low, strength increased with its increase, but when the ratio exceeded a certain limit, strength showed a decrease. Below the limit, as stated above, a distance between $\text{Li}_2\text{O-SiO}_2$ crystal particles decreased in the NCS matrix glass, which is considered to be the same behavior as the case of mixed-particle-reinforced composites with the increased effect of crack prevention. In the case of exceeding the limit, the influence of porosity and precipitated crystal phases to greatly affect the strength of conventional glass or other ceramics with coexisting crystals will become dominant, shifting the structure to a precipitated-particle-reinforced composite type.

5. Conclusion

- 1) $\text{Li}_2\text{O-SiO}_2$ (LS) and $\text{Na}_2\text{O-CaO-SiO}_2$ (NCS) glass powder materials were mixed and underwent heat treatment to prepare composites consisting of crystal particles and glass phases. The precipitated major crystal phase was $\text{Li}_2\text{O-SiO}_2$. Yet, under some conditions of heat treatment temperature or the mixing ratio of NCS glass, various crystal phases were observed such as $\text{Li}_2\text{O-SiO}_2$, β -spodumene, α -quartz, β -cristobalite, and wollastonite. The three phases of α -quartz, β -cristobalite, and wollastonite would have been formed by the fusion reaction of both glass materials.
- 2) The initiation temperature of crystallization of LS glass was constant (about 565°C) regardless of the mixing ratio of NCS glass. Moreover, the coefficients of thermal expansion of specimens after heat treatment were 1.4×10^{-5}

($200 \sim 450^\circ\text{C}$) and $1.4 \sim 3.5 \times 10^{-5}$ ($450 \sim 550^\circ\text{C}$), and the softening point became higher by the addition of LS glass than monolithic NCS glass.

- 3) Compressive strength varies with the mixing ratios of two glass materials or heat treatment temperature. With treatment at the same temperature, a maximum mechanical strength depends on the mixing ratio; for instance, LS80 : NCS20 (wt%) at 800°C , 60 : 40 at 700°C , and 10 : 90 at 650°C . In addition, with the same mixing ratio, strength tended to become higher as treatment temperature rose.
- 4) As for flexural strength, there were optimum mixing ratios: LS60 : NCS40 at 800°C , 10 : 90 at 700°C and 20 : 80 at 650°C . With the same mixing ratio, treatment at 800°C provided the highest strength, and no distinct difference was detected between 700°C and 650°C .
- 5) From the qualitative viewpoint, compressive and flexural strength was associated with porosity when the mixing ratio of NCS glass was low, and yet as the ratio exceeded a certain value, the strength tended to depend on the amount of crystal precipitation along with the form and distribution of voids. However, the mixing of NCS glass caused the precipitation of new crystal phases, and a quantitative relation cannot be discussed owing to complicated changes in the crystal phases.

References:

- 1) Y. Motoki, *Ceram. Soc. Jpn. ed.*, *Seramikkusu Kogaku Handbook*, Gihodo (1989) 2293-2312.
- 2) T. Hanazawa, H. Abe, S. Udagawa, K. Yoneya and G. Toda ed., *Seramikkusu no Kikaiteki Tokusei*, Yogyo Kyokai (1984) 25-56.
- 3) H. Tashiro and T. Maki, *Yogyo Kyokaishi*, 70, 102-119 (1962).
- 4) B.H. Mussler and M.W. Shafer, *Am. Ceram. Soc. Bull.*, 63, 705-710 (1984).
- 5) H. Igawa, T. Watanabe, K. Urabe and S. Udagawa, *Yogyo Kyokaishi* 93, 762-767 (1985).
- 6) N. Ushibusu, K. Sakamoto, K. Nagayama and S. Hagiwara, *Seramikkusu Ronbunshi*, 98, 377-383 (1990).
- 7) M. Ashizuka, M. Watanabe and N. Ikeyama, *ibid.*, 98, 408-411 (1990).
- 8) K. Matsushita and S. Sakka, *J. Non-Cryst. Solids*, 38&39, 741-746 (1980).
- 9) S. Sakka, T. Sakaino and K. Takahashi ed., *Garasu Handbook*, Asakura Shoten (1975) 530.
- 10) K. Watanabe, E.D. Giess and M.W. Shafer, *J. Mater. Sci.*, 20, 508-515 (1985).
- 11) E.M. Levin, C.R. Robbins and H.F. McMurdie, *Phase Diagrams for Ceramists*, *Am. Ceram. Soc.* (1964) 166.
- 12) F.F. Lange, *Phil. Mag.*, 22, 983-992 (1970).

This article is a full translation of the article which appeared in Nippon Seramikkusu Kyokai Gakujutsu Ronbunshi (Japanese version), Vol.99, No.12, 1991.

Electrical Resistivity of Diamond Films Grown by Thermal Plasma CVD

Toyohiko Kobayashi

Ishinomaki Plant, Tokai Carbon Co., Ltd.
1-10, Shigeyoshi-cho, Ishinomaki-shi, 986 Japan

Electrical resistivity of diamond films grown by a thermal plasma chemical vapor deposition technique was measured from room temperature to 870°C at 3×10^{-5} – 1×10^{-6} Torr. The surface-treatments of the films were carried out in the following ways, i.e. 1) immersing in an aqua regia at 75°C for a week, 2) immersing in a solution of CrO_3 in H_2SO_4 for a day, 3,4) heat treating at 400 and 550°C respectively in air for two hours. Electrical contacts on the resultant films were made by gold electrodes deposited by an ion sputtering technique in air at 0.2 Torr and argon gas at 0.2 Torr, respectively. The films with gold electrodes deposited in air had peaks in electrical resistivity at temperature of 400–530°C, but the peaks did not appear with the gold electrodes deposited in argon gas and without gold electrode. It can be explained that this phenomenon was caused by the desorption of oxygen molecules, which were adsorbed from an air plasma generated by the ion sputtering, from the diamond surface and the diamond/electrode interface, further by subsequent reconstructions of the diamond surfaces.

[Received May 1, 1991; Accepted September 19, 1991]

Key-words: Electrical resistivity, Surface treatment, Diamond films, Thermal plasma chemical vapor deposition, Desorption, Oxygen, Diamond surface.

1. Introduction

Diamond film prepared by the CVD method has been already commercialized as coating for cutting tools.^{1,2} More recently, many researchers are interested in its electrical properties to commercialize it for electrical devices. At present, P- and N-type semiconductor films of diamond have been prepared by doping boron and phosphorus, respectively.^{3,4} It is known that a Schottky junction is formed by providing diamond film having semiconductor characteristics with metallic electrodes of specific metal.⁵⁻⁷ Mori et al discuss that the characteristics of metal/diamond interface depend on electronegativity of the metal, and that the I-V characteristics at the interface will no longer depend on the metal by adsorbing oxygen on the diamond surface.⁵⁻⁷ A number of researchers discuss adsorption of oxygen and hydrogen on the diamond surface and their desorption, and accompanied changes in the surface conditions.⁵⁻²⁸ In this study, the author has measured effects of temperature on electrical resistance of the diamond films²⁹⁻³² prepared by the thermal plasma method, some of which are surface-treated, under a vacuum to find that their resistance changes, conceivably as a result of desorption of the adsorbed gas.

2. Experimental Procedure

The as-grown and surface-treated diamond films were measured for their electrical resistance under the conditions of pressure in a range from 3×10^{-5} to 1×10^{-6} Torr and temperature in a range from room temperature to 870°C.

2.1. Sample Preparation

The diamond film was grown on a molybdenum substrate from a methane/hydrogen mixture, using high-frequency thermal plasma. No impurity was doped for the preparation of the film. **Figure 1** shows the plasma torch^{30,32} used for the formation of the film, and **Table 1** the film deposition conditions. Temperature at the back side of the substrate, determined by a photo sensor, decreased during the deposition process as film thickness increased, because of de-

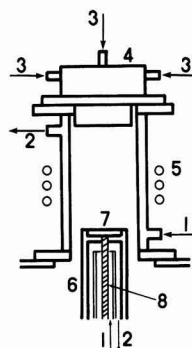


Fig. 1. Schematic view of the rf plasma torch: (1) cooling water inlet, (2) cooling water outlet, (3) gas inlet, (4) gas supply, (5) induction coil, (6) substrate holder, (7) substrate, and (8) optical sense.

Table 1. Deposition conditions of diamond films.

CH_4/H_2	0.033
Initial temperature of substrate	850 - 840°C
Final temperature of substrate	790 - 720°C
Pressure	1 atm
Deposition time	120 - 720 min

creased quantity of heat transferring from the front surface.^{30,32)}

2.2. Analytical Procedure

Electrical resistance of the diamond film was measured, after the substrate was separated from the film by the chemical treatment with aqua regia (Table 2, for Samples A, B, D and E) or mechanical exfoliation (Table 2, for Sample C). It took 2 days to dissolve the substrate with aqua regia at room temperature.

Resistance was measured basically using the following procedure: At first, the 20mm-diameter film separated from the substrate was crushed into pieces, to prepare the specimen. It was provided with electrodes for the measurement of resistance; ion-sputtered onto the edges, while the central portion was covered with a strip of paper for wrapping medicines, to grow golden layers. The sputtering was conducted under three different conditions; (1) Air: 0.15-0.2 Torr, Powder: 8-11 W, held for 4min (SC-1), (2) Air: 0.2 Torr, Powder: approximately 10 W, held for 10min (SC-2), and (3) Air: 0.2 Torr, Powder: approximately 7 W, held for 2min (SC-3). Platinum lines as the leads were drawn on the golden electrodes with platinum paste. The assembly was held at 110°C for 1hr to dry the platinum paste, and then placed in a vacuum oven.

The vacuum oven consisted of a transparent quartz tube as the specimen chamber surrounded by the heater, oil-circulating pump and turbo-molecular pump. Resistance of the film placed in the specimen chamber was measured, via

the platinum lead, by an external multimeter (IWATSU VDAC 7412), and temperature by the thermocouples attached to a place near the specimen. Resistance of the platinum lead increased with temperature to 25Ω at 870°C, which, however, was lower by several digits than that of the film, and the effect of lead resistance was not taken into consideration. Resistance of the film was measured, after pressure inside the specimen chamber was reduced to 3×10⁻⁵ Torr or below, while changing the chamber temperature. Temperature was increased from room temperature to 870°C in 90min, at which the specimen was held for a given time, and then allowed to decrease by cutting the power source.

2.3. Treatment of Film Surface

The film surface was treated by the following procedure:

- 1) The specimens were held at 400, 550, 650 or 750°C for 2hr in air, and those treated at 400 and 550°C were measured for their resistance.
- 2) They were treated with aqua regia at 75°C for 2hr.
- 3) They were then treated with chromic acid for 24hr, where chromic acid was prepared by dissolving 26.7g of chromium oxide (CrO₃) in 23ml of concentrated sulfuric acid and 40ml of pure water and diluting the mixture with pure water to 100ml.

All the samples, Samples A through E (Table 2), were treated by the above procedure. Table 2 summarizes the surface treatment conditions, sputtering conditions, storage period from film formation to resistance measurement, and film thickness.

Table 2. Treatment conditions of sample films.

No	Sample 1)	Treatment of surface	Retention period 2) (day)	Electrode	Ion sputtering 3)	Film thickness (μm)
1	A1		91	Au	SC-1	360
2	B1		31	Au	-1	100
3	B2	Aqua regia	4)	Au	-1	
4	C1	As-grown	0.5	Au	-1	150
5	C2	Remeasurement	5)	Au	-1	
6	B3	Heat at 400°C	6)	Au	-1	
7	C3	Heat at 550°C	7)	Au	-1	
8	C4	CrO ₃	8)	Au	-1	
9	C5		41	Au	SC-2	
10	C6		37	Pt		
11	C7		38	Pt		
12	B4	Heat at 400°C	6)	Pt		
13	D1	Heat at 550°C	7)	Pt		100
14	E1	CrO ₃	8)	Pt		75
15	C8		58	Au	SC-3	
16	E2	Heat at 400°C	6)	Au	-3	
17	E3	Heat at 550°C	7)	Au	-3	
18	E4	CrO ₃	8)	Au	-3	

1) Substrates of sample A, B, D, and E were removed by an aqua regia treatment but that of sample C was peeled off mechanically.

2) Retention period between the day of depositing a diamond film and that of measuring its resistivity.

3) Ion sputtering conditions.
SC-1: Air 0.15-0.2Torr, Power: 8-11W, and Holding time : 4min.
-2: Air 0.2Torr, Power: 10W, and Holding time : 10min.
-3: Argon 0.2Torr, Power: 7W, and Holding time : 2min.

4) Kept in an aqua regia for a week.

5) Measurement of resistivity of sample C1 again after being exposed to air in the furnace at room temperature for a day.

6) Heat treatment at 400°C for two hours.

7) Heat treatment at 550°C for two hours.

8) Kept in (CrO₃+H₂SO₄) solution for a day.

3. Results and Discussion

3.1. Sample Preparation

Figure 2 shows the SEM (scanning electron microscopy) photograph of the cross-section of the film, grown on the substrate and then treated with aqua regia to remove the substrate. Figure 3 is the Raman spectral pattern of the cross-section of the film, measured with laser beams having a spot size of approximately $60\mu\text{m}$, showing Raman light of diamond at 1332cm^{-1} and the fluorescence-induced rise-up of the background in the short wavelength region. The Raman spectrum of the film surface had similar shape. No change in the spectral pattern was observed with the film treated at 870°C (the as-grown film and the film treated with aqua regia to remove the substrate).

The film was measured by the thermoelectric power method³³⁾ for its conduction type, and judged to be of P-type. Al and B present in the film were analyzed as the impurities considered to make the film P-type. The SIMS (secondary ion mass spectrometry) was used. As a result, 2×10^6 atoms/cc of Al and 1×10^{15} atoms/cc of B were detected. The activation energy was estimated at 0.07 to 0.1eV for the sample provided with golden electrodes under the SC-1 conditions from its resistance-temperature curve (Fig.6) during the cooling process.

3.2. Heat-Treated Samples

Figures 4 and 5 show the SEM photographs of the films held at 650°C and 750°C in air, respectively. No abnormalities were found on the film treated at 650°C or less, but that

treated at 750°C was covered with a carbon film, as shown in Fig.5A.^{22,34)} The grain boundaries and the portion facing the substrate were particularly oxidized (Fig.5B), as noted by Hata et al in the diamond films oxidized by air or oxygen plasma,³⁵⁾ indicating the presence of non-diamond component or microparticles of diamond in these portions.

3.3. Changes in Film Resistance

First, the as-grown and surface-treated films were provided with golden electrode under the SC-1 sputtering conditions in air, following the procedure described in Section 2.2, to measure their resistance. Next, three types of the specimens were prepared and measured in a similar manner; films provided with golden electrodes under the SC-2 conditions, with platinum paste as electrode and these with golden electrodes, under the SC-3 conditions in an argon atmosphere. It should be noted that gold and platinum show similar I-V characteristics as diamond.⁶⁾ The results are given in Fig.6. Unit of resistivity is Ωcm for all the specimens, except that provided with platinum electrodes, for which Ω is used because of its unstable shape (distance between the electrodes: 1 to 2cm). Resistance of the films generally decreased as temperature increased, and continued to decrease while they were held at 870°C . However, some specimens showed rapidly increasing resistance while they were being heated.

The rapid increase in resistance, starting at around 300 to 500°C , was found during the heating process with the as-grown, aqua-regia-treated, chromic-acid-treated and heat-treated (at 400°C) specimens out of those provided with golden electrodes in air. But no such trend was observed with the specimen treated at 550°C and that measured for its resistance at varying temperature (870°C at the highest) and then exposed to air for 24hr in the specimen chamber for the second resistance measurement (here in after referred

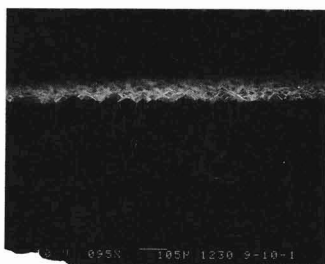


Fig. 2. SEM photograph of the cross section of a diamond film.

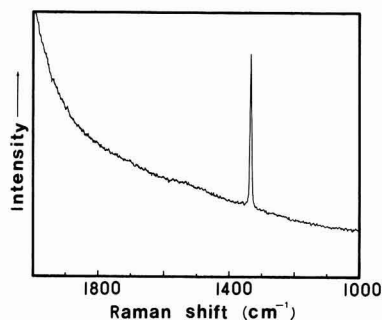


Fig. 3. Raman spectrum of the cross section of a diamond film.



Fig. 4. SEM photograph of the surface of diamond film heat-treated at 650°C for two hours.

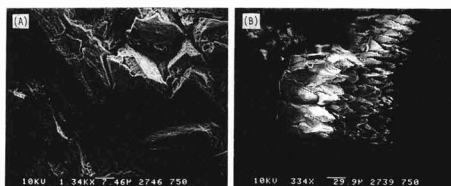


Fig. 5. SEM photographs of (A) surface and (B) rear face of the diamond film after heat treatment at 750°C .

to as the retested specimen or film). The specimens provided with electrodes in an argon atmosphere, and those with the electrodes of platinum paste also showed no such trends.

Those showing rapid increase in electrical resistance had the following characteristics:

- 1) Comparing resistance (R_d) during the heating process at from room temperature to T_r (at which resistance started to increase) with resistance (R_u) during the cooling process:

These specimens fell into the two general categories:

- ① $R_d - R_u \geq 0$, for the as-grown, aqua-regia-treated and heat-treated (at 400°C) specimens, and
 - ② $R_d - R_u \leq 0$, for the chromic-acid-treated and retested specimens
- 2) For the specimens showing the tendency of $R_d - R_u \geq 0$, bringing the sputtering conditions from the SC-1 to SC-2

by increasing sputtering time in air and pressure caused:

- ① T_r to shift to the higher-temperature side,
 - ② the value $R_d - R_u$ to increase, and
 - ③ the difference between the highest resistance during the heating process and resistance at the same temperature during the cooling process to decrease.
- 3) The temperature level T_r at which resistance started to increase rapidly was the lowest at around 300°C with the as-grown specimen (C1) provided with the golden electrodes under the SC-1 conditions, and the highest at around 500°C with the specimen (C5) provided with the golden electrodes under the SC-2 conditions, in place of the SC-1 conditions. This level was around 400°C with the other specimens. It is however not clear whether or not the difference in the T_r level at around 400°C was attributable to the treatment conditions, because the SC-1 conditions were not strictly controlled.

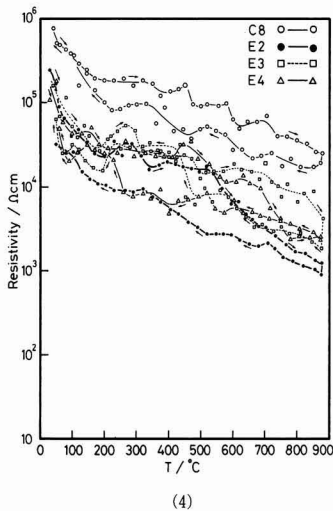
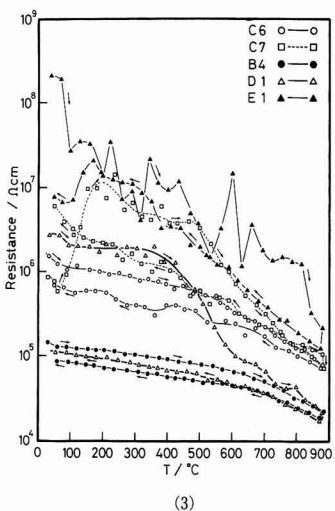
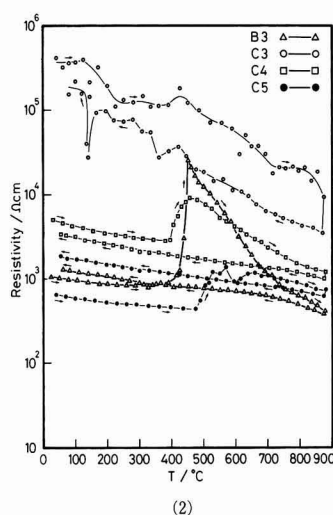
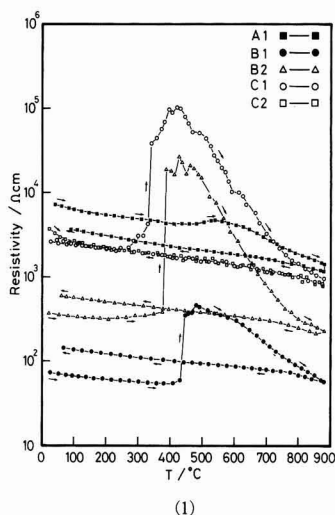


Fig. 6. Resistivity and resistance of diamond films A1 - E4 plotted as a function of temperature. Data was taken along by the arrow.

Those specimens which showed no tendency of starting rapid increase in resistance at 300 to 500°C during the heating process had the following characteristics:

- 1) The specimens generally had a higher resistance during the heating process than during the cooling process, except specimen (C7) described later and those specimens showing rapid fluctuations in resistance readings, whose resistance was partly lower during the heating process than during the cooling process.
- 2) The specimens provided with the electrodes of platinum paste, but not with the golden electrodes, had resistance sharply fluctuating during the measurement. No such fluctuations, however, were observed with those treated at 400° and 550°C.
- 3) Of the specimens provided with no surface treatment (C6 and C7), one (C7) showed increased resistance at from around 80°C during the measurement with the platinum electrodes. It was also noted, though not shown here, that the specimen (A) treated with aqua regia to remove the substrate and (C) provided with no surface treatment and not dried at 110°C after having been coated with platinum paste showed similar resistance changes as the specimen (C6).
- 4) The specimen provided with the golden electrodes in an argon atmosphere had resistance sharply fluctuating during the measurement.

A number of unsaturated bonds (dangling bonds) are found on the surface of a semiconductor, because it serves as the terminal of the regularly configured atoms that constitute the crystal. This results in many local levels formed on the surface, and they are referred to as surface levels. The terminal is not the sole cause for the surface level, and it is known to result also from surface roughness, adsorbed impurity and surface reconfiguration.

It was found in this study that resistance of the films prepared under different conditions, i.e., the as-grown, surface-treated and those provided with electrodes under different conditions, changed differently with temperature. Most of the samples showed rapid increase in resistance during the heating process, but exhibited semiconductor behavior during the cooling process, because their resistance increased gradually with temperature. No change in Raman spectral pattern was observed with the specimens heated to 870°C, from which it was judged that these resistance changes were related to desorption of the gases adsorbed on the diamond surfaces and diamond/electrode interfaces.

A number of attempts have been made to adsorb oxygen on diamond surfaces by various methods, including treatment with chromic acid,⁶⁻⁸⁾ treatment with hydrochloric and nitric acids,¹⁵⁾ thermal treatment in air, and treatment with oxygen plasma^{6-8, 15)} and NO plasma.¹⁵⁾ In the case of the treatment with NO plasma, it is reported that oxygen is the only adsorbed species and nitrogen is not adsorbed. On the other hand, treatments in a hydrogen atmosphere and with hydrogen plasma have been attempted, after the system atmosphere is degassed, in order to adsorb hydrogen on a sample.^{7,8,36)} Some researchers observe that hydrogen is adsorbed on the as-polished specimen with olive oil.²⁵⁻²⁷⁾ Essentially no oxygen is found on the film synthesized from the vapor phase, even it is from CO/H₂ as the starting mixture, as far as the X-ray photoelectron spectroscopy (XPS) results indicate,⁵⁻⁷⁾ suggesting the presence of hydrogen. The groups that are possibly present on the surface, together with hydrogen or oxygen, include carbonyl, carboxylic, lac-

tone, tertiary alcohol, cross-linked oxygen and epoxide.²³⁾ The diamond surface will be reconfigured by the adsorption/desorption of these gases.^{9,10,25-27)} The 1×1 surface having the same symmetry as the crystal can be kept intact when oxygen or hydrogen is adsorbed, but will be reconfigured into the 2×1/2×2 surface on desorption of hydrogen. On the other hand, it is discussed that strength of the LEED pattern of the diamond film oxidation-treated with nitric acid or aqua regia increases slightly with temperature up to 450°C, at which it starts to rapidly decrease, and is diminished completely at 800° to 1000°C.⁹⁾ It is considered, based on these results, that oxygen is adsorbed on the films treated in this study with aqua regia, chromic acid or heat in air, and hydrogen on the as-grown film. It is also considered that oxygen is adsorbed on the films provided with the electrodes under the SC-1 and -2 conditions, as is the case with the previously discussed treatment with NO plasma, because of the formation of plasma in the gases in which the ion-sputtering was conducted. Changes in resistance observed during the heating or cooling process result conceivably from desorption of these adsorbed gases. It is particularly noted that behavior of resistance, starting to increase rapidly at 300° to 500°C during the heating process, is similar to the spectral pattern associated with thermal desorption of the diamond power treated with oxygen, observed by Matsumoto et al.,^{14,19,21,34)} in that the spectra of the specimens treated at 25° to 554°C in an atmosphere containing 10⁻² Torr of oxygen start to rise at the treatment temperature and attain a peak at 500° to 600°C. The researchers also discuss that adsorbed oxygen is desorbed in the form of CO or CO₂, adsorption of oxygen falls into two general categories (α the β), and the α type is further subdivided into α -1 through α -4 types. Adsorbed oxygen, when desorbed massively from the diamond surface in the form of CO or CO₂, will leave behind a number of unsaturated bonds, which will trap the carriers, to increase resistance. These unsaturated bonds cannot stably exist in large quantities on the surface, and the surface is reconfigured, to decrease resistance. Marsh et al discuss, as described earlier, that the LEED pattern is eventually diminished by desorption of oxygen. The results of this study, on the other hand, indicate that unsaturated bonds are possibly reconfigure, though not regularly, but to an extent sufficiently to change resistance. In addition, changed conditions of adsorbed oxygen as a result of surface treatment will change temperature at which resistance starts to increase rapidly and surface conditions after desorption.^{14,19,21,34)} The examples are the shift of T_r to the higher-temperature side and the increased R_d-R_u value as a result of the changed golden electrode depositing conditions from the SC-1 to SC-2. It is considered that the adsorbed gases would not be desorbed rapidly from those samples showing no tendency of rapid increase in resistance during the heating process. In such samples, formation of the unsaturated bonds caused by desorption of the gases and reconfiguration would occur orderly, with the result that resistance decreased uniformly. It is considered, for the specimen provided with the golden electrodes under the SC-1 conditions and treated with chromic acid, that oxygen present in the vicinity of the film surface is adsorbed under two or more different adsorption conditions, judging from different behavior of resistance changes; for example, oxygen adsorbed during the surface treatment would exert effects different from that adsorbed during the golden electrode deposition process.

For the specimens heat-treated in air, that treated at 400°C showed rapid increase in resistance at around 400°C, when it was provided with the golden electrodes, and showed behavior similar to that of the retested specimen (C2), when it was provided with the platinum electrodes. On the other hand, the specimen treated at 550°C had resistance sharply fluctuating during the measurement, when it was provided with the golden electrodes, and that provided with the platinum electrodes was characterized by its resistance which was relatively unaffected by temperature up to 400°C, at which it started to decrease, and increased gradually with temperature during the cooling process. Such differences result conceivably from the diamond surface modified by the treatment at 550°C, and oxygen from the air plasma selectively adsorbed on the diamond film.

Treatment with the argon ion has been used to clean the diamond surface,¹⁵⁾ and some researchers discuss that it tends to transform the diamond surface into graphite.¹⁷⁾ The deposition of the electrode in an argon atmosphere will make the adsorbed gases unstable, which may account for rapid fluctuations of resistance.

Landstrass et al discuss that desorption of hydrogen adsorbed on the as-grown film and the film treated with hydrogen plasma starts at around 100°C, which causes resistance to increase by several digits.³⁶⁾ It was observed in this study that one of the specimens provided with the platinum electrodes has resistance starting to increase at around 80°C, which might result from desorption of oxygen adsorbed while the film was held at 110°C for 1hr.

4. Conclusions

The as-grown diamond films prepared using high-frequency thermal plasma and those provided with surface treatment were measured for their resistance under the conditions of pressure in a range from 3×10^{-5} to 1×10^{-6} Torr and temperature in a range from room temperature to 870°C. Changes in resistance with temperature varied, depending on the surface treatment conditions, suggesting that these changes resulted from desorption of the gases adsorbed on the surfaces. Oxygen adsorbed on the surfaces, when desorbed in the form of CO and CO₂, will leave the unsaturated bonds, which is accompanied by the reconfiguration (probably having no regularity) of these bonds to change resistance. It is also suggested, from the changes in resistance of the treated films, that there are two or more different adsorption conditions.

Reference:

- 1) S. Matsumoto, Y. Sato, M. Kamo and N. Setaka, *Jpn. J. Appl. Phys.*, 21, L183-85 (1982).
- 2) M. Kamo, Y. Sato, S. Matsumoto and N. Setaka, *J. Cryst. Growth.*, 62, 642-644 (1983).
- 3) N. Fujimori, H. Nakahata and T. Imai, *Jpn. J. Appl. Phys.*, 29, 824-827 (1990).
- 4) T. Iwasaki, T. Okano, H. Kiyota, Y. Akiba, T. Kurosu and K. Nakamura, *Proc. 37th Appl. Phys. Symp.* (1990) 388.
- 5) Y. Mori, H. Kawarada and A. Hiraki, *Proc. Mat. Res. Soc.*, 162 (1990) 353-358.
- 6) Y. Mori, C.Ma., H. Kawarada and A. Hiraki, *Proc. 4th Diamond Symp.* (1991) 77-78.
- 7) Y. Nishibayashi, T. Tsukino, J. Kimura, H. Shiomi and N. Fujimori, *ibid.*, 63-64 (1991).
- 8) J.B. Marsh and H.E. Farnsworth, *Surf. Sci.*, 1, 3-21 (1964).
- 9) J.J. Lander and J. Morrison, *ibid.*, 4, 241-246 (1966).
- 10) R. Sappok and H.P. Boehm, *Carbon*, 6, 283-295 (1968).
- 11) R. Sappok and H.P. Boehm, *ibid.*, 6, 573-588 (1968).
- 12) R.C. Bansal, F.J. Vastola and P.L. Walker, Jr., *ibid.*, 10, 443-448 (1972).
- 13) S. Matsumoto, Y. Sato, N. Setaka and M. Goto, *Chem. Lett.*, 1247-1250 (1973).
- 14) J.M. Thomas and E.L. Evans, *Diamond Res.*, 2-8 (1975).
- 15) P.G. Lurie and J.M. Wilson, *ibid.*, 26-32 (1976).
- 16) S. Evans and J.M. Thomas, *Proc. R. Soc. Lond.*, A. 353, 103-120 (1977).
- 17) P.G. Lurie and J.M. Wilson, *Surf. Sci.*, 65, 453-475 (1977).
- 18) S. Matsumoto, H. Kanda, Y. Sato and N. Setaka, *Carbon*, 15, 299-302 (1977).
- 19) S. Evans and J.M. Thomas, *Diamond Res.*, 31-36 (1978).
- 20) S. Matsumoto and N. Setaka, *Carbon*, 17, 485-489 (1979).
- 21) Y. Sato and M. Kamo, *Hyomen*, 19, 197-205 (1981).
- 22) H.L. Shergold and C.J. Hartley, *Int. J. Miner. Process.*, 9, 219-233 (1982).
- 23) S.V. Pepper, *J. Vac. Sci. Technol.*, 20, 213-216 (1982).
- 24) B.B. Pate, M.H. Hecht, C. Binns, I. Lindau and W.E. Spicer, *J. Vac. Sci. Technol.*, 21, 364-367 (1982).
- 25) B.J. Wacławski, D.T. Pierce, N. Swanson and R.J. Celotta, *ibid.*, 21, 368-370 (1982).
- 26) B.B. Pate, *Surf. Sci.*, 165, 83-142 (1986).
- 27) H. Namba, M. Masuda and H. Kuroda, *Appl. Surf. Sci.*, 33/34, 187-192 (1988).
- 28) S. Matsumoto, H. Hino and T. Kobayashi, *Appl. Phys. Lett.*, 51, 737-739 (1987).
- 29) T. Kobayashi, *J. High Temp. Soc. Jpn.*, 17, 42-45 (1991).
- 30) T. Kobayashi, *Seramikkusu Ronbunshi*, 99, 119-123 (1991).
- 31) T. Kobayashi, *Seramikkusu Ronbunshi*, in printing.
- 32) Denki, *Denshi Zairyo Hand book*, Asakuma Shoten, (1987) 242.
- 33) NIRIM Report, 20, 49-63 (1979).
- 34) C. Hata, M. Kamo and Y. Sato, *New Diamond*, 5, 12-17 (1989).
- 35) M.I. Landstrass, *Appl. Phys. Lett.*, 55, 1391-1393 (1989).
- 36) M.I. Landstrass, *ibid.*, 55, 975-977 (1989).

This article is a full translation of the article which appeared in *Nippon Seramikkusu Kyokai Gakujutsu Ronbunshi (Japanese version)*, Vol.99, No.12, 1991.

Improvement of Thermal Stability of SiC Fiber by CVD-C, SiC Coating

J.X. Li, Yohtaro Matsuo and Shiushichi Kimura

Department of Inorganic Materials, Tokyo Institute of Technology
2-12-1, Ookayama, Meguro-ku, Tokyo, 152 Japan

The effects of CVD conditions, thickness and composition of CVD-C, SiC coating on the mechanical properties, microstructure and thermal stability of Nicalon-SiC fibers were studied. Tensile strength of fibers coated at 1300°C was lower than that of as-received fiber, because large flaws were formed on the fiber surface during the heating stage of the CVD process. When a fiber was treated at elevated temperatures, the coating layer acted as an effective fiber-coating interfacial diffusion barrier, and resisted the gas (CO, SiO) evolution from the fiber surface, which improved thermal stability of coated fibers. Thicker coating layer was more effective to prevent decomposition of Nicalon fiber at higher temperatures. The fibers coated at 1200°C possessed high values of strength, though these decreased due to the interface reaction in the heat treatment process.

[Received May 22, 1991; Accepted July 18, 1991]

Key-words: Nicalon-SiC fiber, CVD-Coating, Thermal Stability, Tensile strength

1. Introduction

Fiber-reinforced ceramic matrix composite materials have been noted recently as high temperature structural materials having high strength, high elastic modulus and high toughness. The characteristics of fiber-reinforced ceramic matrix composite materials depend on the respective characteristics (especially at elevated temperatures) of reinforcing fibers and matrix, and on the behavior at the interface between fiber and matrix. Ceramics materials themselves used as the matrix possess a good thermal stability, but most of the reinforcing fibers commercially available are short of thermal stability. For instance, carbon fibers have a problem of oxidation in an oxidizing atmosphere, and alumina fibers have various problems at elevated temperatures of coarsening and deformation of crystal grains, and of reaction with glass matrix.^{1,2)} SiC based fibers like Tyranno fibers³⁾ and Nicalon fibers,⁴⁻⁶⁾ which are both produced by pyrolysis process of organic materials, have the problems of decomposition of fiber and of coarsening of crystal grains at elevated temperatures beyond 1000°C. Nicalon fiber itself is chemically unstable, thereby, when it is heated at the temperature beyond 1000°C, the fiber surface is generated with microvoids by the chemical reaction of fiber itself. As a result, stresses are concentrated at these microvoids under a given tensile stress.⁸⁾ While in the case of composite materials, a stress to work to the fiber surface becomes larger than that to work inside the fiber, because an interfacial shearing stress is added. Therefore, fibers tend to be

failed from the surface flaws, instead of from the internal ones.⁹⁾ Consequently, it is important to control the reinforcing fibers in terms of surface state, surface flaws at the surface, and composition at the surface. A coating on the fiber surface can be one of the practical methods for the control of the interface between fiber and matrix in the fiber-reinforced composite materials.

The objectives of fiber coating usually include the improvements of oxidation resistance and thermal stability of fibers, the prevention of reaction between fiber and matrix, and the optimization of interfacial bonding.¹⁰⁻¹⁴⁾ In our current study, we studied the effects of fiber coating on thermal stability of fiber. In the first place, we coated Nicalon fibers by CVD process, and measured tensile strength of the coated fibers. In the second place, we heat-treated at elevated temperatures as-received Nicalon fibers and CVD-coated ones, and investigated the effects of various factors as thickness, composition, and so forth of the coating on the thermal stability and the microstructure of Nicalon fibers at elevated temperatures, and, based on these results, we discuss the optimum CVD process condition for the coating of Nicalon fibers.

2. Experimental Procedure

Fibers used in our experiments were Nicalon-NL200, produced by Nihon Carbon Co., Ltd.. They had an average fiber diameter of 15μm, an average strength of 2910MPa, and an average elastic modulus of 203GPa (according to the catalogue data). Surface coating of the fibers was carried out using a CVD apparatus of high temperature and low pressure type. The fibers were put in a reaction furnace of the CVD process. After the furnace was heated to the specified temperatures under the argon atmosphere at a pressure of 1atm, the pressure was reduced and CVD reaction gases were introduced into the furnace. A heating rate of 6°C/min was applied. The reaction gases were composed of SiCl₄ and CH₄, and the carrier gas used was H₂. The CVD reaction was processed at the respective temperatures of 1200°C and 1300°C and at the pressure of 20Torr. Gas flow rates of SiCl₄ and CH₄ were 40 and 40SCCM respectively, and that of H₂ was either 120 or 170SCCM. (1SCCM means a gas flow rate of 1CC/min of gas at 0°C and at 1atm.) Nicalon fibers are known to degrade at elevated temperature. Therefore, in order to assess the degradation of Nicalon fibers during the heating period in the CVD process, we treated the as-received Nicalon fibers by heating at 1300°C under the argon atmosphere at a pressure of 1atm (then by holding them under the argon atmosphere at a reduced pressure of 20Torr), and by cooling without CVD-coating the fibers. In order to investigate the effect of heat

treatment on the strength of fiber, we heat-treated both the as-received fibers and the fibers coated at 1300°C (by holding for 6h under the argon atmosphere at a pressure of 1atm), and at 1500°C (by holding for 5h under the vacuum of 10^{-3} Torr), and then observed the surface state of respective fibers using an SEM. We carried out tension test of the fibers treated in various conditions as afore-mentioned in accordance with the testing method for carbon fibers specified by JIS-R7601 using a gauge length of 25mm. Then we observed the fractured fibers to find out the fracture origin using an SEM, and measured the diameter of fiber and the thickness of coating layer also using an SEM. We calculated the tensile strength of a single fiber from the fiber diameter measured and the maximum load recorded in the tension test.

3. Test Results and Discussion

3.1. Structure of CVD-coating Layer

As proven in our previous report,⁽⁵⁾ coating layers in thickness of 0.1 to 0.5 μ m were formed on the fiber surface in the CVD reaction time of 5 to 30min. The coating layer exhibited a very smooth surface, but SiC grains in domelike shape were observed to be deposited in the layer, though their number was very few. Elementary compositions of the CVD-coating layer were found to be carbon (C) (in thickness of about 0.1 to 0.5 μ m) in the initial coating layer on the fiber surface, and to be Si and C in the outer coating layer, which ranges several dozen nm depthwise from the surface of coating layer. As the mechanism of CVD coating on the surface of Nicalon fibers, carbon particles are deposited initially on the fiber surface by thermal decomposition of CH₄ at elevated temperature, and subsequently Si is deposited in such manner as to disperse in the C layer initially formed, and with the gradual increase of Si deposition amount, a mixed coating layer of SiC and C is formed, and a coating layer of pure SiC is eventually formed.

3.2. Mechanical Properties of CVD-coated Fibers

In order to clarify the effect of thickness of coating layer on tensile strength of fiber, we carried out a tension test using Nicalon fibers coated in various CVD process conditions. For comparison purposes, we also measured respective tensile strengths of the as-received Nicalon fiber and the same fiber after heat treatment in the same condition (at 1300°C for 10min) as in the heating period in the CVD coating process. It was revealed that the as-received Nicalon fibers exhibited an average tensile strength of

2450MPa, and the heat-treated ones exhibited an average tensile strength of 1220MPa. That is, tensile strength of Nicalon fibers was reduced to half by the heat treatment. Fracture origin of the as-received fibers was the flaws existing at the surface of fiber, and that of the heat-treated ones was the surface flaws containing a lot of micro-voids caused by abnormal SiC grain growth in the fibers. **Figure 1** shows SEM micrographs of the fracture surface of CVD-coated fibers after the tension test. It is seen in Fig.1(a) that the structure of the fracture surface of coated fibers contained a typical fracture origin, which consisted of various zones of mirror-mist-hackle-crack-brachings,^(16,17) in the same manner as in the case of tension fracture of the as-received Nicalon fibers, and the fracture origin was surface flaws. All of the coated fibers fractured due to similar surface flaws. Some time during the fracture of fibers, coating layers debonded from the fiber surface (as seen in Fig.1(b)). This phenomenon suggests a weak bonding between fiber and coating layer, and, as a reverse interpretation, a toughening effect of fiber-reinforced composite materials can be expected due to a pull-out of fiber from the composite matrix. **Figure 2** shows the relationship between tensile strength of CVD-coated fiber at 1300°C and coating layer thickness. In the case of coating thickness in the range of 0.1 and 0.5 μ m, average tensile strengths of the fibers were nearly constant at about 1470MPa, but in the case of coating thickness beyond 0.5 μ m, average strengths of the fibers decreased with the increase of coating thickness. As shown in Fig.2, tensile strength of CVD-coated fibers is lower than that of as-received fiber, even when the coating thickness is thin. This phenomenon is attributed to the decreased tensile strength of fiber itself caused during the heating period in the CVD process. In other words, SiO₂, free carbon and SiC contained in Nicalon fiber reacted with each other during the heating period because of instability of the fiber itself, and the evolution of reaction products of SiO and CO gases and the grain growth of SiC in the fiber caused large flaws on the fiber surface. These flaws are found to exist in the region, in which SiC crystal grains grew abnormally and a lot of micro-cavities were generated.⁽⁸⁾ These surface flaws remain on the surface of fiber (at the interface between fiber and coating layer) without being modified during CVD-coating process, thereby, we assume the strength of coated fiber decreased.

As observed in Fig.2, tensile strength of coated fiber having a coating thickness of 5 μ m decreased to a half of

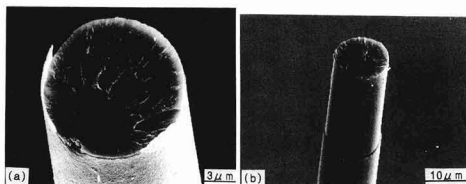


Fig. 1. Fracture surface of fibers coated at 1300°C (H₂ 120SCCM, 20torr) with tensile strength of (a) 1640MPa, (b) 1695MPa.

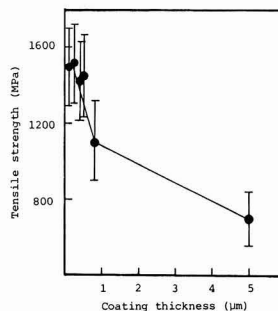


Fig. 2. The relationship between the coating thickness and the tensile strength of CVD-coated fiber.

that of coated fiber having a thin coating (in thickness of 0.1 to 0.5 μm). As mentioned in our previous report,¹⁵⁾ composition of coating layer changes from carbon to a mixture of carbon and SiC, and eventually to pure SiC along with the increase of coating layer thickness. As the growing rate of SiC grain is high, grain boundaries remain between the grains. Flaws such as micro-void and others exist in those grain boundaries, and when a tension stress is given, a stress concentration takes place around these flaws, resulting in the decreased strength of fiber.^{18,19)} When a coating layer was formed in as high thickness as 25 μm , the coated fiber became so brittle that we could not measure its tensile strength. We suppose it was because SiC grains in the coating layer were accompanied with the weaker boundaries.

When the CVD-coating treatment was applied at 1200°C for 30min, a coating layer in thickness of 0.3 μm was formed on the fiber. The coating layer was observed to be composed of carbon in the neighborhood of fiber surface, and of SiC in the outside. The coated fibers exhibited an average tensile strength of 2380MPa, which was close to that of as-received Nicalon fibers. **Figure 3** shows an SEM micrograph of the fracture surface of this coated fiber after tension test. This fracture surface appears similar to that shown in Fig.1, but the fracture origin is observed to be smaller in size than that in Fig.1.

Table 1 gives average tensile strengths (σ) and estimated Weibull parameters (m) of as-received Nicalon fibers, heat-treated Nicalon fibers at 1300°C for 10min without coating, and coated Nicalon fibers at respective CVD process temperatures of 1300°C and 1200°C. Here, we presumed a two-parameter system Weibull's distribution as applicable in the statistic analysis of tensile strength, because the fracture origin consisted of a single kind (surface flaws), and, based on this presumption, we estimated m values by a maximum likelihood estimation method. As-received

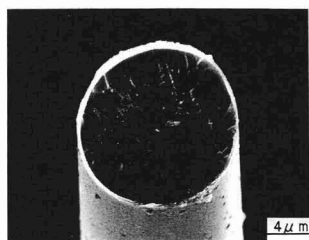


Fig. 3. Fracture surface of fiber coated at 1200°C (H₂ 120SCCM, 20torr) with tensile strength of 2345MPa.

Table 1. Average tensile strengths (σ) and Weibull's parameters (m) of Nicalon fibers with different treatments (N: number of specimens).

	N	σ	m
as-received fiber	50	2450	4.5
heat-treated fiber	12	1220	5.0
CVD-coated at 1300°C			
coating thickness(μm)			
0.12	27	1495	7.9
0.25	19	1510	7.5
0.40	12	1420	6.8
0.50	22	1455	6.8
CVD-coated at 1200°C			
coating thickness(μm)			
0.30	16	2380	4.4

Nicalon fibers and heat-treated Nicalon fibers exhibited the m values of around 5. The coated fibers at 1300°C exhibited the larger m values of around 7. The reason why the coated fibers exhibited such large m values is thought to be that the large flaws generated on the fiber surface during the heating period in the CVD process were distributed relatively uniformly over the whole fiber surface, thereby, fluctuation of the flaws decreased conversely. Meanwhile, the coated fibers at 1200°C exhibited m values similar to those of the as-received fibers and the heat-treated ones. The reason for such similar m values is believed to be that these coated fibers had similar surface flaws in their size and distribution as the non-coated fibers. Judging from the experimental results and the reasoning, we deem a CVD-coating temperature of 1300°C and a coating thickness in the range of 0.1 and 0.5 μm as the optimum CVD process conditions for Nicalon fibers.

3.3. Effect of Heat Treatment on Mechanical properties and Microstructure of Coated Fibers

In the preparation process of fiber-reinforced ceramics matrix composite materials, reinforcing fibers are exposed to an elevated temperature for a long time. Therefore, it is necessary to clarify the effect of heat treatment at elevated temperatures on the characteristics of fibers, even though they are coated on the surface. We accordingly experimented to expose the as-received Nicalon fibers and the coated ones to the two different temperatures of 1300°C and 1500°C, and investigated the effect of the heat treatments on the mechanical properties and the microstructure of respective fibers.

In the first place, we heat-treated the as-received fibers and the coated fibers at a treatment temperature of 1300°C (in the argon atmosphere of a pressure of 1atm for 6h). **Figure 4** shows the bar graphs comparing the tensile strengths of the respective fibers before and after the heat treatment. In the case of the as-received fibers, average strength decreased greatly from 2450MPa to around 900MPa by the heat treatment for 6h. In the case of the CVD-coated fibers at 1200°C, the strength also decreased greatly from 2380MPa to 1060MPa by the same heat treatment. In the case of the CVD-coated fibers at 1300°C, however, the strength did not change so much as to be kept at around 1450MPa after the heat treatment, compared to 1470MPa before. After carrying out the tension test, we observed their fracture surface using an SEM. In the case of the CVD-coated fibers at 1300°C, fracture surface and external surface of the fibers after heat treatment appeared similar to those of the same coated fibers before heat treat-

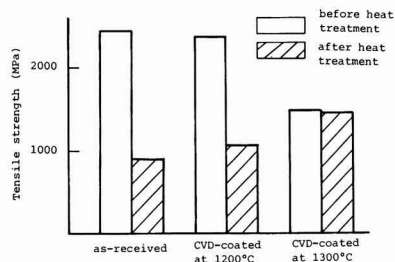
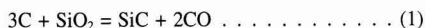


Fig. 4. Variation of fiber tensile strengths, heat treated at 1300°C in Ar (6hrs).

ment. In the cases of the as-received fibers and the CVD-coated fibers at 1200°C, however, both fracture surface and external surface changed greatly by the heat treatment. That is, in the case of the as-received fibers after the heat treatment, the fracture surface was observed to contain a large fracture origin, in which the zones of mirror and mist were enlarged, compared to those in the fibers before the heat treatment, and the zones of hackle and crack-branching disappeared, as if these fibers were low strength and brittle materials. In addition, a reacted layer was observed to be in the depth-wise range of about 1μm from the external surface of the fiber, and was identified as a region in which SiC crystal grains grew abnormally and a lot of micro-voids were generated.²⁰⁾

Figure 5 shows an SEM micrograph of the external surface of the CVD-coated fiber at 1200°C after the heat treatment at 1300°C. We can observe in this figure a trace of a reaction taken place between coating layer and fiber. As mentioned in our previous report,¹⁵⁾ when fibers are CVD-coated at 1200°C, a coating layer in thickness of 0.3μm is formed, and it is composed of carbon and SiC. Since Nicalon fibers are composed of C, SiC and SiO₂, we assume that a reaction as expressed by equation (1) below took place between C in the coating layer and SiO₂ in the fiber during the heat treatment at 1300°C.



We accordingly assume that the large surface flaws as observed in Fig.5 were caused by this reaction, which took place at the interface between fiber surface and coating layer. Figure 6 shows an SEM micrograph of the fracture surface of the same CVD-coated and heat-treated fiber after tension test. A large fracture origin is observed in this figure in the same manner as in the case of the as-received fiber after heat treatment. We assume that this fracture origin was caused by the development of the region, in which SiC grains grew abnormally and a lot of micro-voids were generated, to the center part of fiber, and the strength of fiber decreased thereby. In addition, a reacted layer, in which SiC grain grew abnormally, was observed to have been formed by the heat treatment in the neighborhood of the surface of the CVD-coated fiber at 1200°C (as seen in Fig.7). This observed result suggests that the reaction of equation (1) took place not only at the interface, but also in the inside of fiber. On the contrary, in the case of CVD-coated fibers at 1300°C, neither the abnormal growth of SiC crystal grains in the neighborhood of the fiber surface nor the reaction

between fiber and coating layer took place by the heat treatment.

As-received Nicalon fibers are existed with an oxygen-rich layer in their surface region, and when they are heat-treated at 1300°C in argon atmosphere, oxygen amount at the fiber surface region decreases gradually as the result of internal reaction of the fiber itself. The reaction products are SiC in solid state and SiO and CO in gas state, so oxygen amount at the surface of fiber tends to become smaller than that in the inside of fiber with the increase of treatment time and treatment temperature.^{3,8)} We therefore assume that this reaction behavior resulted a smaller oxygen amount in the neighborhood of fiber surface in the case of Nicalon fiber CVD-coated at 1300°C than in the case of that at 1200°C. When this CVD-coated Nicalon fiber at 1300°C is heat-treated at 1300°C, the oxygen amount in the neighborhood of fiber surface is small (SiO₂ content is small), thereby, the afore-mentioned reaction of equation (1) takes place less at the interface between fiber and coating layer, and, as the result, coating layer acts as an effective barrier for preventing the evolution of reaction products (CO and SiO gases), and for the result suppressing of the additional progress of the reaction of fiber. On the contrary, when the CVD-coated Nicalon fiber at 1200°C is heat-treated at 1300°C, oxygen remains in a high concentration in the neighborhood of fiber surface, therefore, we assume that the said reaction took place actively at the interface between fiber and coating layer, and as a result the continuous coating layer was broken and the reaction of fiber itself was not suppressed.

In the second place, we heat-treated both as-received nicalon fibers and CVD-coated Nicalon fibers at 1300°C in a more severe condition (at 1500°C in vacuum for 5h). As Nicalon fibers themselves are thermally unstable, evaporation of the reaction products (CO and SiO gases) becomes more vigorous in the heat treatment condition of higher temperature and lower atmosphere pressure (vacuum).^{21,22)} Figure 8 shows SEM micrographs of the fractured fibers heat-treated in the above-mentioned condition. In the case of as-received Nicalon fiber (Fig.8(a)), the fiber was thermal-decomposed completely to consist of micro-voids and crystal grains of β-SiC and α-SiC. In this state, the strength of the fiber was almost negligible. In the case of coated fiber with a coating of 0.1μm thick (Fig.8(b)), a similar reaction took place inside the fiber and similar texture of fiber resulted, as in the case of as-received fiber, but most of the coating layer remained in the as-coated state. However, some of the coating layer indicated a trace of reaction

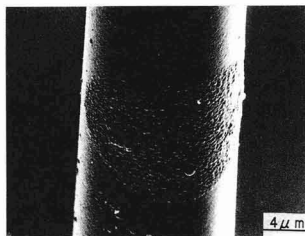


Fig. 5

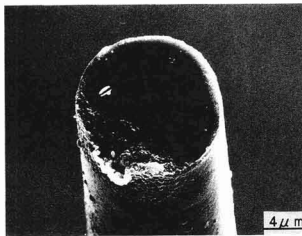


Fig. 6

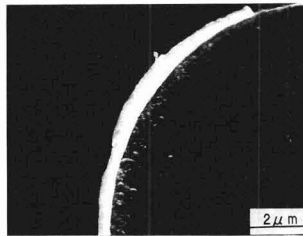


Fig. 7

Fig. 5. SEM micrograph of coated fiber, heat treated at 1300°C in Ar.

Fig. 6. Fracture surface of coated fiber, heat treated at 1300°C in Ar with tensile strength of 610MPa.

Fig. 7. SEM micrograph of coated fiber, heat treated at 1300°C in Ar, showing a reaction zone around fiber surface.

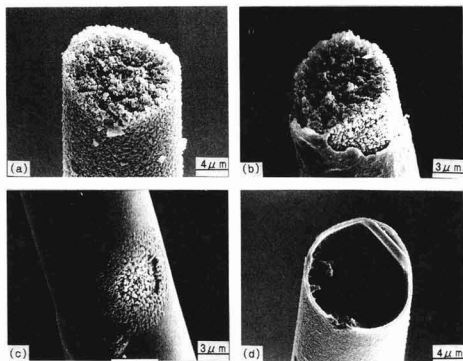


Fig. 8. SEM micrographs of coated and uncoated fibers heat treated at 1500°C in Vacuum: (a) uncoated fiber, (b) and (c) fiber with coating (0.1μm), (d) with coating (0.5μm).

with the fiber (Fig.8(c)). Through the heat treatment tests of Nicalon fibers at an increased temperature of 1500°C, we noticed some different interfacial reactions taking place which did not take place in the heat treatment at 1300°C. These are, in the case of a coating layer as thin as 0.1μm, large surface flaws generated at the fiber surface during the heating period in CVD process which were not covered completely with the coating layer, thereby, the reaction of equation (1) proceeded in the surface flaw region during the heat treatment, and the interfacial reaction took place simultaneously, and, as the result, the reaction propagated radially along the surface flaws. We suppose that the surface flaws served as a passage for the evolution of the reaction products of CO and SiO gases to the outside, and as a result had the effect of accelerating the reaction inside the fiber, therefore, thermal decomposition of fiber was not suppressed by the coating layer.

While, in the case of a thick coating layer as 0.5μm (Fig.8(d)), both the reaction of the fiber itself and the interfacial reaction between coating layer and fiber were much suppressed during the heat treatment, but the coated fiber became brittle, so that its strength could not be measured. We suppose that the thick coating layer covered all surface flaws, which otherwise might have served as a passage for the evolution of the reaction products of CO and SiO gases, as previously mentioned, and as a result contributed to suppress further progress of the reaction. We further suppose that, even if the reaction between C and SiO₂ takes place at the interface between fiber and coating layer, it is prevented from further progress because the outside coating layer is constructed with a dense structure composed of C and SiC, thereby, the CVD coating becomes effective for the improvement of thermal stability of Nicalon fibers. Judging from the results mentioned above, we conclude that a thicker coating is more effective to be applied on Nicalon fibers, as far as the fibers are used at a higher temperature.

4. Conclusion

Nicalon fibers coated with SiC by a CVD process were studied in terms of their mechanical properties and thermal stability. When the fibers were coated at 1300°C, large

flaws were generated on the fiber surface due to the evolution of the reaction products of CO and SiO gases from the fiber surface during the preliminary heating period in the argon atmosphere at a pressure of 1 atm in the CVD process. As a result, the CVD-coated fibers (with coating of 0.1 to 0.5μm thick) exhibited an average tensile strength (around 1470MPa), which was much lower than that of as-received Nicalon fibers (2450MPa). When a thicker coating layer in thickness beyond 0.5μm was formed at the same CVD-process temperature of 1300°C, flaws like micro-voids were generated at the boundary of SiC grain which grew abnormally at a high rate. As a result, strength of the coated fibers decreased rapidly with the increase of coating thickness. Meanwhile, when the fibers were CVD-coated at 1200°C, the reaction of the fiber itself was not so vigorous that the strength of the as-received fibers was almost maintained as to exhibit an average tensile strength of the coated fibers of 2380MPa.

When Nicalon fibers variously prepared were heat-treated at 1300°C, both the as-received fibers and the CVD-coated ones at 1200°C were deteriorated in their structures and decreased their strengths rapidly down to 1000MPa, but the CVD-coated fibers at 1300°C maintained the strength in the similar level to that before the heat treatment. In the former case of CVD-coating at 1200°C, oxygen remains in a high concentration in the neighborhood of the fiber surface after the coating, thereby, a reaction between C and SiO₂ takes place at the interface between fiber and coating layer during the heat treatment at 1300°C, resulting in the decrease of fiber strength. In the latter case of CVD-coating at 1300°C, oxygen concentration in the neighborhood of the fiber surface is reduced, thereby, the reaction at the interface is suppressed during the heat treatment, and the strength of the fiber does not decrease so much. The coating layer composed of C or C + SiC acts as an effective barrier to diffusion of the reaction products of CO and SiO gases at elevated temperature, suppressing the progress of thermal decomposition of fiber, and further resulting in the improvement of thermal stability of Nicalon fibers.

When heat treatment temperature was increased to 1500°C, both the reaction at the interface between coating layer and fiber and the reaction inside the fiber took place even in the case of the CVD-coated fibers at 1300°C. However, an increase of thickness of the coating layer was found as effective for the reduction of these reactions.

Acknowledgements

The authors wish to thank messrs. Atsushi Kimura (presently working for Tokyo Electric Power Co., Ltd.), Kazuhiro Fueda (presently working for Ube Industries Co., Ltd.) and Katsuya Kuboyama, who were all students at the Department of Inorganic Materials of Tokyo Institute of Technology, for their help with the CVD coating experiments in our current study.

References:

- 1) R.A.J. Sambell, A. Briggs, D.C. Phillips and D.H. Bowen, *J. Mater. Sci.*, **7**, 676-681 (1972).
- 2) T. Mah, M.G. Mendiratta, A.P. Katz and K.S. Mazdiyashi, *J. Am. Ceram. Soc. Bull.*, **66**, 304-308 (1987).
- 3) D.B. Fischbach, P.M. Lemoine and G.V. Yen, *J. Mater. Sci.*, **23**, 987-993 (1988).
- 4) G. Simon and A.R. Bunsell, *ibid.*, **19**, 3649-3657 (1984).
- 5) T.J. Clark, M. Jaffe and N.R. Langley, *Ceram. Eng. Sci. Proc.*, **7**, 901-913 (1986).
- 6) L.C. Sawyer, R.T. Chen, F. Haimbach, P.J. Harget, E.R. Prack and M. Jaffe, *ibid.*, **7**, 914-930 (1986).

- 7) T.J. Clark, E.R. Pack, M.I. Haider and L.C. Sawyer, *Ceram. Eng. Sci. Proc.*, 8, 717-731 (1987).
- 8) J.X. Li, Y. Matsuo and S. Kimura, *Advanced Composite materials*, to be published.
- 9) M. Sutcu, *J. Mater. Sci.*, 23, 928-933 (1988).
- 10) J. Avenston, *Nature*, 226, 146-147 (1970).
- 11) M.W. Lindley and B.F. Jones, *ibid.*, 255, 474-475 (1975).
- 12) K.D. McHenry and R.E. Tressler, *J. Comp. Mater.*, 9, 73-76 (1975).
- 13) R.N. Singh and M.K. Brun, *Ceram. Eng. Sci. Proc.*, 8, 636-643 (1987).
- 14) A.J. Caputo, D.P. Stinton, R.A. Lowden and T.M. Bessmann, *Am. Ceram. Soc. Bull.*, 66, 368-372 (1987).
- 15) J.X. Li, Y. Matsuo and S. Kimura, *Seramikkusu Ronbunshi*, 99, 1129-1134 (1991).
- 16) L.C. Sawyer, R. Arons, F. Haimbach, M. Jaffe and K.D. Rappaport, *Ceram. Eng. Sci. Proc.*, 6, 567-575 (1985).
- 17) R.W. Rice, ASTM STP 827, ed. by J.J. Mecholsky and S.R. Powell, 5-103 (1984).
- 18) T.F. Foltz, *Ceram. Eng. Sci. Proc.*, 9-10, 1206-1220 (1985).
- 19) S.S. Shinozaki and H. Sato, *J. Am. Ceram. Soc.*, 9, 425-429 (1978).
- 20) J.X. Li, A. Kimura, Y. Matsuo and S. Kimura, *Proc. Japan-U.S. CCM-V, Tokyo* (1990) 395-401.
- 21) S.M. Johnson, R.D. Brittain, R.H. Lamoreaux and D.J. Rowcliffe, *J. Am. Ceram. Soc.*, 71, C132-C135 (1988).
- 22) K.L. Luthra, *ibid.*, 69, C231-C233 (1986).

This article is a full translation of the article which appeared in *Nippon Seramikkusu Kyokai Gakujutsu Ronbunshi* (Japanese version), Vol.99, No.12, 1991.

Changes in Swelling Characteristics and Structure of Na-Fluorine Micas with Ga- and Al-substitutions

Kunio Kitajima, Kazuyuki Miyake and Nobuo Takusagawa

Department of Chemistry and Material Engineering, Faculty of Engineering, Shinshu University
500, Wakasato, Nagano-shi, 380 Japan

Series of Ga- and Al-substituted Na-fluorine micas $\text{NaMg}_{2-x}\text{Li}_{1-x}(\text{T}_x\text{Si}_{4-x-y}\text{Ge}_y\text{O}_{10})\text{F}_2$ and $\text{NaMg}_{2+x}\text{Li}_{1-x}(\text{T}_x\text{Ge}_{4-x-y}\text{Si}_y\text{O}_{10})\text{F}_2$; $x=0.0-1.0$, $\text{T}=\text{Ga}, \text{Al}$, $y=0, 1, 2, 3$, were synthesized. Variations of infrared spectra, lattice constants and swelling properties were studied, and compared with those of corresponding K-series micas. Continuous changes in basal spacing ($c\text{-sin}\beta$) with increasing Ga- and Al-contents proved that there were complete series of solid solutions between the end member micas with an exception of $\text{NaMg}_3(\text{AlSi}_3\text{O}_{10})\text{F}_2$. Linear relations between $c\text{-sin}\beta$ or b-axis values and mean radius of tetrahedral cation were obtained for Ga- and Al-substituted Na-micas having x-value of 1.0. However, the b-axis values of Na-micas are far smaller than those of corresponding K-analogues, demonstrating that the degree of distortion in tetrahedral rotation angle α and octahedral flattening angle ψ is determined by the size of interlayer cation as well as that of tetrahedral cation. The values of α for Na-micas increased with the amounts of Ga- and Al-substitution. Na-micas lose also their swelling ability with increasing Ga- and Al-substitution. The loss of hydration property of interlayer cation results from the increase of α and the change of charge balancing, which increase the stability of interlayer structure.

[Received June 19, 1991; Accepted August 22, 1991]

Key-words: Na-mica, Swelling, Ga-substitution, Al-substitution, Tetrahedral rotation angle, Basal spacing

1. Introduction

Isomorphic substitution in fluorine micas takes place with various kinds of ions, because the structure of fluorine micas has a "flexibility" of allowing large distortions.¹⁾ This structural flexibility makes chemistry of fluorine micas complicate on one hand, but contributes to give various materials characteristics to fluorine micas on the other hand. Therefore, it is important to study systematically the relationships between chemical composition, structure and properties of fluorine micas. In our current study, the authors paid our attention to the swelling characteristics of fluorine micas, and, using Na-taeniolite [$\text{NaMgLi}(\text{Si}_4\text{O}_{10})\text{F}_2$]²⁾ and its analogues with Ge-substitution as the basic compositions of mica samples, we investigated the changes of structure and swelling characteristics of micas in accordance with the isomorphic substitution with Ga^{3+} and Al^{3+} ions at the four-coordination sites. Swelling characteristics of micas are closely related with such important properties as ion exchangeability³⁾ and complex formation,⁴⁾ therefore,

the clarification of the causes for swelling behavior of micas in this study is expected to be useful for designing synthetic fluorine micas as the functional materials. We previously reported^{5,6)} our study results on the effects of Ga- and Al-substitutions at the four-coordination sites to infrared absorption spectra and lattice parameters in the case of K-taeniolite [$\text{KMg}_2\text{Li}(\text{Si}_4\text{O}_{10})\text{F}_2$] and its analogues. So we examined our current study results by comparing them with those obtained in our previous study as much as necessary.

2. Experimental Procedure

2.1. Synthesis of Fluorine Micas

Na-fluorine micas are expressed by two series of general formulas as $\text{NaMg}_{2+x}\text{Li}_{1-x}(\text{T}_x\text{Si}_{4-x-y}\text{Ge}_y\text{O}_{10})\text{F}_2$ and $\text{NaMg}_{2+x}\text{Li}_{1-x}(\text{T}_x\text{Ge}_{4-x-y}\text{Si}_y\text{O}_{10})\text{F}_2$, [$\text{T}=\text{Al}$ and Ga ; $x=0.0, 0.2, 0.4, 0.6, 0.8$ and 1.0 ; $y=0, 1, 2$ and 3], and have 16 compositional series. We measured guaranteed reagents of SiO_2 , GeO_2 , MgO , MgF_2 , LiF , NaF , Al_2O_3 and Ga_2O_3 in such respective amounts as to agree with the respective mica compositions (in total amount of 2g), and mixed them together respectively. Then we put and sealed each sample in a platinum container (in size of $9\times 9\times 40\text{mm}$), fused it for 2h at 1400°C in the case of high SiO_2 content, and at 1300°C in the case of high GeO_2 content, and cooled it slowly down to 800°C at a cooling rate of 2 to $3^\circ\text{C}/\text{min}$. After that, we further cooled it naturally at the outside of furnace, obtaining a crystalline mica aggregate. In the following description, we abbreviate the compositions of 16 series of Al- and Ga-substituted Na-fluorine micas by the respective tetrahedral compositions, for instance, $\text{NaMg}_{2+x}\text{Li}_{1-x}(\text{Ga}_x\text{Si}_{4-x}\text{O}_{10})\text{F}_2$ series by $\text{Ga}_x\text{Si}_{4-x}$ series.

2.2. Microscopic Observation

Mica samples prepared by the procedure described in section 2.1 were observed visually as well as with a microscope, and the size of mica crystals precipitated and the presence of foreign minerals were examined.

2.3. Measurement of Infrared Absorption Spectrum

Mica crystal aggregates synthesized were crushed into fine size of minus 325mesh using an agate mortar. Infrared absorption spectra of the micas were measured with these fine particles as test sample by KBr pellet method using an infrared spectrometer (model IR-430), made by Shimadzu Seisakusho Ltd. Wavenumber of absorption band was corrected using polystyrene.

2.4. X-ray Diffraction

Mica crystal aggregates synthesized were crushed into fine size of minus 325mesh. X-ray powder diffraction

analysis was carried out with these fine samples, and the presence of foreign minerals other than mica was examined. When these mica samples did not have swelling characteristics, we measured 12 to 16 diffraction lines appeared in the conditions of room temperature and $24^\circ \leq 2\theta(\text{CuK}\alpha) \leq 74^\circ$, and determined the lattice parameters of the micas by means of least-squares method. While, when the samples had swelling characteristics, we dehydrated them at a temperature of 120°C , and, immediately after that, we measured only basal spacing values ($c \cdot \sin\beta$) of the micas. Diffraction angle of mica was corrected based on that of silicon.

2.5. Swelling Characteristics and Thermal Analysis

We also measured basal spacing values of micas by X-ray diffraction analysis of respective mica samples in the wetted state with water, and determined the type of maximum hydration phase of respective micas from the measured data. In addition, after dried these wet mica samples at room temperature (R.H. $\approx 60\%$) in air, we measured DTA and TA curves, from which we determined the dehydration amount and the temperature for dehydration of single-layer hydrated type mica.

3. Results and Discussion

3.1. Synthesis of Na-fluorine Micas

Based on the results obtained by microscopic observation and X-ray powder diffraction analysis, we classified the conditions of forming micas, and plotted the classified results on the ternary composition system diagram for tetrahedral layer, as shown in Fig.1. In both cases of Al- and Ga-substitution series micas, the sample having other composition than in the regions circled by dotted line in Fig.1 were composed of mica only, or of mica accompanied with a trace of by products. This result suggests that the compositions of synthesized micas herewith almost agree with those of batch materials, thereby, Al^{3+} or Ga^{3+} ions are proved to substitute Si^{4+} or Ge^{4+} ions at the tetrahedral sites in the case of Na-fluorine micas, in the same manner as in the case of K-fluorine micas in our previous report. While, in the case of the samples having composition in the regions

circled by dotted line on the Ge-rich side in both Al- and Ga-substitution series diagrams, mica was coexisted with MgGeO_3 , but since its formed amount was very small, we judged that the compositions of synthesized micas could be approximated by those of batch materials. In the case of the samples having composition in the region circled by dotted line on the Si-rich side in Al-substitution series diagram, mica was coexisted with amphibole and norbergite in a considerable amount. Therefore, we excluded these samples from the following measurements.

3.2. Infrared Absorption Spectrum

As the typical examples, Fig.2 shows the infrared absorption spectra of four kinds of Na-fluorine micas of $\text{Ga}_x\text{Si}_{4-x}$, $\text{Ga}_x\text{Ge}_{4-x}$, $\text{Ga}_x\text{Si}_{3-x}\text{Ge}$ and $\text{Ga}_x\text{Ge}_{3-x}\text{Si}$ series.

The composition of $\text{Ga}_x\text{Si}_{4-x}$ series micas with $x=0.0$, which is given in Fig.2(1), is equal to that of Na-taeniolite [$\text{NaMg}_2\text{Li}(\text{Si}_4\text{O}_{10})\text{F}_2$]. All of absorption bands at various wave-numbers 1110, 980 and 706cm^{-1} in the spectra of this series micas are assigned to stretching vibration of Si-O, and a band at wavenumber 462cm^{-1} in this spectrum is assigned to deformation vibration of Si-O. Especially when judged from the assignments based on lattice vibration of $(\text{Si}_2\text{O}_5)_n$ of talc⁷⁾ and mica,⁸⁾ absorption bands at 1110, 980, 706 and 462cm^{-1} can be respectively assigned to modes a_1^1 , e_1^1 , a_1^2 and e_1^2 .⁹⁾ Infrared absorption spectra of Na-taeniolite were found to be similar to those of corresponding K-taeniolite [$\text{KMg}_2\text{Li}(\text{Si}_4\text{O}_{10})\text{F}_2$],⁵⁾ because the absorption band assigned to mode a_1^1 shifted toward the lower

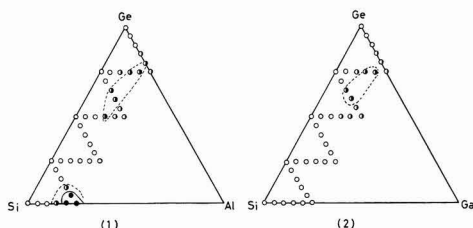


Fig. 1. Formation region of Na-micas and other phases shown by the ternary systems of tetrahedral composition for $\text{NaMg}_{2-x}\text{Li}_{1-x}(\text{T}_4\text{Si}_{4-x-y}\text{Ge}_y\text{O}_{10})\text{F}_2$ and $\text{NaMg}_{2-x}\text{Li}_{1-x}(\text{T}_4\text{Ge}_{4-x-y}\text{Si}_y\text{O}_{10})\text{F}_2$: (1): T=Al, (2): T=Ga.
○: mica
○: mica + trace of MgGeO_3
◐: mica + small amount of MgGeO_3 or richterite
●: mica + richterite and norbergite

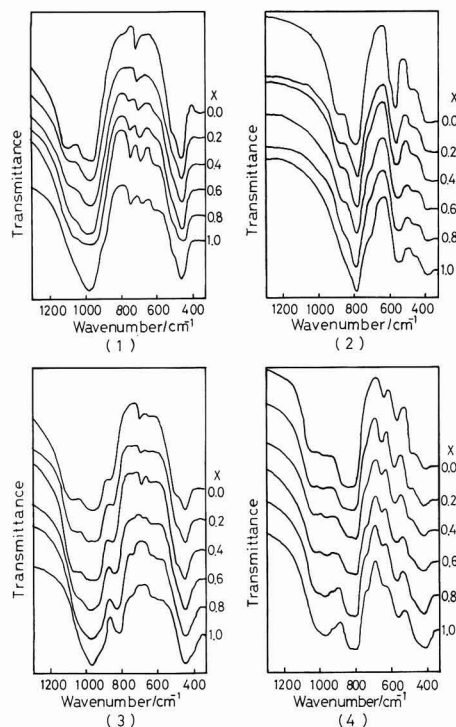


Fig. 2. Infrared spectra of Ga-substituted fluorine micas. (1) $\text{Ga}_x\text{Si}_{4-x}$, (2) $\text{Ga}_x\text{Ge}_{4-x}$, (3) $\text{Ga}_x\text{Si}_{3-x}\text{Ge}$, (4) $\text{Ga}_x\text{Ge}_{3-x}\text{Si}$

wavenumber side only by about 5cm^{-1} and band assigned to mode e_1^1 shifted toward the higher wavenumber side only by about 18cm^{-1} in the case of Na-taeniolite, compared to the corresponding bands in the case of K-taeniolite. These slight differences in the position of respective absorption bands suggest the effect of interlayer ions on lattice vibration of $(\text{Si}_2\text{O}_5)_n$. Two absorption bands at 1110 and 980cm^{-1} were apparently separate in the case of $x=0.0$ in $\text{Ga}_x\text{Si}_{4-x}$ series micas, but shifted toward the direction as to come closer with each other in accordance with the increase of value x , until they joined into a broad absorption band at $x=1.0$. In addition, with the increase of value x , a new absorption band appeared at around 740cm^{-1} and its absorption intensity increased. This new absorption band is assigned to lattice vibration of $\text{Ga}^{\text{IV}}\text{-O}$.⁵⁾

Fig.2(2) shows infrared absorption spectra of $\text{Ga}_x\text{Ge}_{4-x}$ series Na-fluorine micas. The sample with $x=0.0$ is equal to a Na-analogue of Ge-substituted K-taeniolite [$\text{KMg}_2\text{Li}(\text{Ge}_4\text{O}_{10})\text{F}_2$], and exhibits similar spectra to those of Ge-substituted K-taeniolite. Absorption bands at 880 and 780cm^{-1} in these spectra are respectively assigned to the absorption bands, which are respectively assigned to modes a_1^1 and e_1^1 , based on $(\text{Ge}_2\text{O}_5)_n$ lattice vibration. In the case of $\text{Ga}_x\text{Ge}_{4-x}$ series micas, these two absorption bands assigned to respective modes a_1^1 and e_1^1 , shifted toward the direction as to come closer with each other with the increase of value x , until they joined into a broad absorption band at $x=1.0$, as they did in the case of $\text{Ga}_x\text{Si}_{4-x}$ series micas.

Both $\text{Ga}_x\text{Si}_{3-x}\text{Ge}$ series and $\text{Ga}_x\text{Ge}_{3-x}\text{Si}$ series micas,

respectively shown in Figs.2(3) and 2(4), have tetrahedral composition in ternary system. Infrared absorption spectra of these two series micas exhibited the same major absorption bands as exhibited in the spectra of $\text{Ga}_x\text{Si}_{4-x}$ series and $\text{Ga}_x\text{Ge}_{4-x}$ series ones. Both spectra of these two series micas changed continuously with the increase of value x , as they did in Figs.2(1) and 2(2). Intensity ratio between two absorption bands, which were respectively assigned to vibration of Si-O and Ge-O, and which appeared in the wave-number range of 800 and 1100cm^{-1} , changed with the change of content ratio between Si and Ge. Other micas of $\text{Ga}_x\text{Si}_{2-x}\text{Ge}_2$, $\text{Ga}_x\text{Si}_{1-x}\text{Ge}_3$, $\text{Ga}_x\text{Ge}_{2-x}\text{Si}_2$ and $\text{Ga}_x\text{Ge}_{1-x}\text{Si}_3$ series exhibited the similar spectra to those shown in Figs.2(3) and 2(4).

Figure 3 shows infrared absorption spectra of typical Al-substituted Na-fluorine micas, namely, $\text{Al}_x\text{Si}_{4-x}$, $\text{Al}_x\text{Ge}_{4-x}$, $\text{Al}_x\text{Si}_{3-x}\text{Ge}$ and $\text{Al}_x\text{Ge}_{3-x}\text{Si}$ series. Fig.3(1) shows the absorption spectra of $\text{Al}_x\text{Si}_{4-x}$ series micas. Absorption bands at 1110 and 980cm^{-1} were apparently separated at $x=0.0$, but shifted as to come closer with each other with the increase of value x , and joined into a broad band with an accompanied shoulder at $x=0.6$. It was additionally observed that a new absorption band at around 810cm^{-1} came to appear in a shoulder with the increase of value x . This new band is assigned to lattice vibration of $\text{Al}^{\text{IV}}\text{-O}$.⁶⁾

Figure 3(2) shows the absorption spectra of $\text{Al}_x\text{Ge}_{4-x}$ series micas. Absorption bands assigned to respective modes a_1^1 and e_1^1 also shifted as to come closer with each other until they joined into a broad band at $x=1.0$.

Figures 3(3) and 3(4) show the respective absorption spectra of $\text{Al}_x\text{Si}_{3-x}\text{Ge}$ series and $\text{Al}_x\text{Ge}_{3-x}\text{Si}$ series micas. They both exhibited the same major absorption bands, which appeared in the spectra of $\text{Al}_x\text{Si}_{4-x}$ series and $\text{Al}_x\text{Ge}_{4-x}$ series micas. With the increase of value x , the spectra of both series micas changed continuously, as they did in Figs.3(1) and 3(2). Absorption intensity ratio between two absorption bands, which were respectively assigned to vibration of Si-O and that of Ge-O and appeared in the wavenumber range of 800 and 1100cm^{-1} , changed with the change of content ratio between Si and Ge. Other micas of $\text{Al}_x\text{Si}_{2-x}\text{Ge}_2$, $\text{Al}_x\text{Si}_{1-x}\text{Ge}_3$, $\text{Al}_x\text{Ge}_{2-x}\text{Si}_2$ and $\text{Al}_x\text{Ge}_{1-x}\text{Si}_3$ series exhibited the similar spectra to those shown in Figs.3(3) and 3(4). All of the spectra of Na-fluorine micas of any substitution series were similar to those of corresponding K-analogues. As above mentioned, infrared absorption spectra of synthesized micas of both Ga- and Al-substitution series changed continuously with the change of value x , that is, Ga and Al contents in the synthesized micas, and a new absorption band at 740cm^{-1} in the case of Ga-substitution series, and that at 810cm^{-1} in the case of Al-substitution ones, which respectively appeared with the increase of value x , were judged to be assigned to respective lattice vibrations of $\text{Ga}^{\text{IV}}\text{-O}$ and $\text{Al}^{\text{IV}}\text{-O}$. Consequently, the change of infrared absorption spectra indicates the continuous change of chemical composition of synthesized fluorine micas of respective substitution series with the change of value x .

3.3. Lattice Parameters of Na-fluorine Micas

Table 1 shows the lattice parameters of various end member Na-fluorine mica series, which do not exhibit swelling characteristics as described later in section 3.6, together with those of Na-taeniolite and its Ge-substituted analogues. The figures given in parentheses indicate the last figure of standard deviation of respective parameter. Table 2 shows

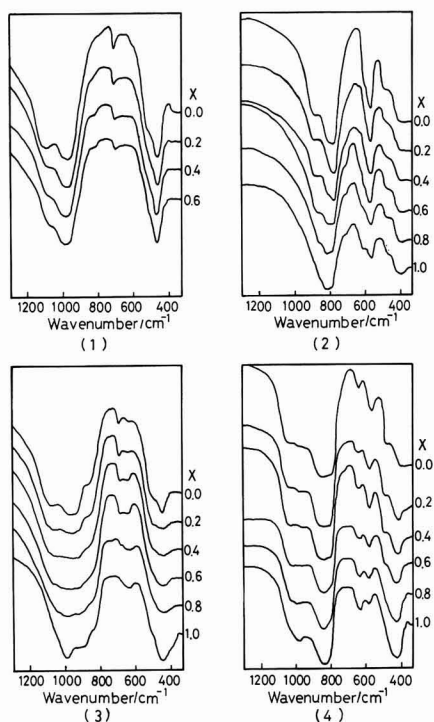


Fig. 3. Infrared spectra of Al-substituted fluorine mica. (1) $\text{Al}_x\text{Si}_{4-x}$, (2) $\text{Al}_x\text{Ge}_{4-x}$, (3) $\text{Al}_x\text{Si}_{3-x}\text{Ge}$, (4) $\text{Al}_x\text{Ge}_{3-x}\text{Si}$

X-ray powder diffraction data of two typical end member Na-fluorine micas. **Figure 4** shows the relationship between value x and lattice parameters of $\text{Ga}_x\text{Ge}_{1-x}$ series Na-fluorine micas, which turn to be non-swelling micas when x is 0.2 or larger than that. As seen in Fig.4, the respective values of a -axis, b -axis and axial angle β increased linearly and the value of c -axis decreased almost linearly with the increase of value x . Such continuous change of respective lattice parameters with the change of value x suggests that these respective substitution series micas take complete series of solid solution between the end member micas. However, chemical expansion¹⁰⁾ caused by isomorphic substitution exhibited a remarkable anisotropy, which was indicated by the change of lattice parameters. Content ratio between Mg^{2+} and Li^{2+} ions at octahedral sites of respective substitution series micas changes with the change of value x , but, since respective ionic radii of Mg^{2+} and Li^{2+} are 0.72

and 0.76\AA ,¹¹⁾ and differ only a little with each other, we assume that the effects of different size of these cations at octahedral sites to the changes of a -axis value and basal spacing value are small. While, respective ionic radii of Ge^{4+} and Ga^{3+} at tetrahedral sites are 0.39 and 0.47\AA , so radius of Ga^{3+} is considerably larger than that of Ge^{4+} . Therefore, respective increases of a -axis value and b -axis value in the case of Ga-substitution are explained as to be mainly due to the larger size of Ga ion at tetrahedral sites, but the decrease of basal spacing value is not explained only by the size of this ion. These anisotropic behaviors in expansion and contraction of lattice parameters can be explained if we take account of structural distortion, which is expressed by a coordination polyhedral model of mica structure described in the following, as it was explained in the case of analogous substitution series K-fluorine micas.^{5,6)}

It has been well known that mica structure is caused of structural distortion in both tetrahedral and octahedral sheets in order to cancel the misfit of the size between these two sheets. As illustrated in **Fig.5**, structural distortion in tetrahedral sheet is expressed by tetrahedral rotation angle α , and that in octahedral sheet is expressed by octahedral flattening angle ψ .^{1,10)} Angles α and ψ are related to b -axis value, as respectively expressed by equations (1) and (2).^{1,10)}

$$\alpha = \cos^{-1}(b/2\sqrt{3} \cdot e_b) \dots \dots \dots (1)$$

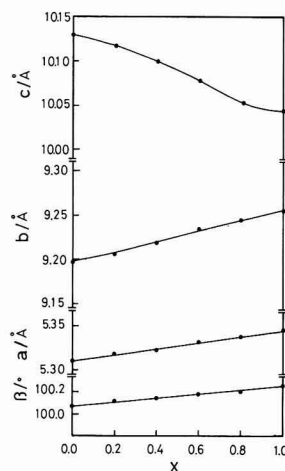


Fig. 4. Lattice constants of $\text{NaMg}_{2-x}\text{Li}_{1-x}(\text{Ga}_2\text{Ge}_{2+x})\text{F}_2$ series fluorine micas

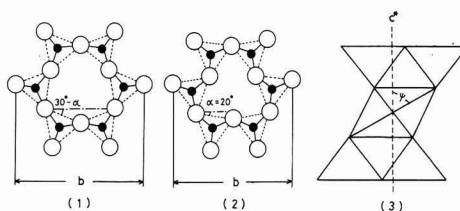


Fig. 5. Schematic illustration of tetrahedral rotation angle (α) and octahedral flattening angle.

The value α for (2) is much larger than that for (1), forming nearly six-coordination around interlayer cation.

Table 1. Lattice constants for various end-member Na-fluorine micas. Standard deviations are given in parentheses.

Composition of micas	a (/Å)	b (/Å)	c (/Å)	β (°)
$\text{NaMg}_2\text{Li}(\text{Ge}_2\text{O}_5)\text{F}_2$	5.310 (2)	9.199 (2)	10.129 (3)	100.07 (3)
$\text{NaMg}_2(\text{GaGe}_2\text{O}_5)\text{F}_2$	5.346 (3)	9.256 (3)	10.045 (3)	100.26 (3)
$\text{NaMg}_2(\text{GaSiGe}_2\text{O}_5)\text{F}_2$	5.318 (2)	9.210 (2)	9.994 (4)	100.22 (4)
$\text{NaMg}_2(\text{GaSi}_2\text{GeO}_5)\text{F}_2$	5.292 (2)	9.163 (2)	9.941 (2)	100.07 (2)
$\text{NaMg}_2(\text{AlGe}_2\text{O}_5)\text{F}_2$	5.325 (4)	9.234 (5)	10.006 (5)	100.13 (5)
$\text{NaMg}_2(\text{AlSiGe}_2\text{O}_5)\text{F}_2$	5.304 (5)	9.185 (5)	9.948 (5)	100.10 (6)
$\text{NaMg}_2\text{Li}(\text{Si}_2\text{O}_5)\text{F}_2$	5.228 (5)	9.045 (6)	9.766 (6)	100.02 (6)

Table 2. X-ray powder diffraction data of Al- and Ga-substituted Na-micas [$\text{NaMg}_3(\text{AlSiGe}_2\text{O}_{10})\text{F}_2$ and $\text{NaMg}_3(\text{GaSiGe}_2\text{O}_{10})\text{F}_2$], showing 1M mica structure.

$\text{NaMg}_3(\text{AlSiGe}_2\text{O}_{10})\text{F}_2$			$\text{NaMg}_3(\text{GaSiGe}_2\text{O}_{10})\text{F}_2$		
d / Å	I/I ₁	hkl	d / Å	I/I ₁	hkl
9.79	70	001	9.84	25	001
4.897	55	002	4.918	75	002
4.593	3	020	4.605	4	020
4.540	3	110	4.550	4	110
4.381	1<	111	4.396	3	111
3.898	3	111	3.907	1<	111
3.615	2	112	3.631	4	112
3.350	6	022	3.361	16	022
3.265	100	003	3.279	100	003
3.102	6	112	3.109	9	112
2.866	4	113	2.879	8	113
2.661	2	023	2.671	7	023
2.641	5	201, 130	2.648	7	201, 130
2.610	6	200, 131	2.616	9	200, 131
2.493	2	202, 131	2.501	4	202, 131
2.449	4	004	2.459	9	004
2.419	3	201, 132	2.424	6	201, 132
2.240	4	203, 132	2.249	7	203, 132
2.152	1<	202, 133	2.157	1<	202, 133
1.959	45	005	1.967	35	005
1.718	3	205, 134	1.726	4	205, 134
1.647	7	204, 135	1.652	8	204, 135
1.632	30	006	1.639	3	006
1.531	3	060, 331	1.535	4	060, 331
1.508	7	206, 135	1.515	8	206, 135
1.399	9	007	1.472	2	116
1.335	4	207, 136	1.405	6	007
			1.341	4	207, 136

Intensities are probably affected by preferred orientation which enhances (001) reflections.

$$\psi = \sin^{-1}(b/3\sqrt{3} \cdot d_o) \dots \dots \dots (2)$$

Here, *b* indicates *b*-axis value we measured, *e_b* does basal O-O distance, and *d_o* does average octahedral cation-anion distance. By applying the values *e_b* and *d_o*, which we estimated in our previous study on analogous substitution series K-fluorine micas, into equations (1) and (2), we calculated α and ψ , which are larger in both cases of Ga- and Al-substituted Na-fluorine micas with increasing Ge content, thereby, the structural distortion is larger (see Table 3). It is also revealed that the values α and ψ of Ga-substituted micas are larger than those of corresponding Al-substituted ones. The reason for this difference in values α and ψ is assumed to be that Ga³⁺ ion has a larger ionic radius than Al³⁺ ion has, thereby, a misfit between tetrahedral sheet and octahedral one became larger in the case of Ga-substitution and the values α and ψ increased in order to cancel the larger misfit.

The values α of these various Na-fluorine micas are larger by about 2 degree than those of the corresponding K-fluorine micas. As seen in Fig.5(2), interlayer Na cations are coordinated in a closer state to six-coordination with the increase of value α . This larger rotation angle value of Na-fluorine mica series is attributed to the small ionic radius of Na⁺, which allows the tetrahedron rotate in a wider angle range, in contrast to the case of K-fluorine mica series, in which the tetrahedron is allowed to rotate in a certain limit, because K⁺ ion is larger in radius and touches the basal oxygen.

Table 3. Predicted values of $\alpha^{(1)}$ and $\psi^{(2)}$ for some Na-fluorine micas and *e_b*⁽³⁾ and *d_o*⁽⁴⁾ values used for calculation

Composition of micas	<i>e_b</i> (/Å)	<i>d_o</i> (/Å)	α (°)	ψ (°)
NaMg ₂ Li(Ge,O ₆)F ₂	2.773	2.092	16.7	57.8
NaMg ₂ (GaGe,O ₆)F ₂	2.846	2.076	20.1	59.1
NaMg ₂ (GaSiGe,O ₆)F ₂	2.798	2.072	18.1	58.8
NaMg ₂ (GaSi ₂ GeO ₆)F ₂	2.748	2.066	15.7	58.6
NaMg ₂ (AlGe,O ₆)F ₂	2.811	2.076	18.5	58.9
NaMg ₂ (AlSiGe,O ₆)F ₂	2.767	2.070	16.7	58.6
NaMg ₂ Li(Si,O ₆)F ₂	2.617	2.061	3.9	57.6

⁽¹⁾ α ; tetrahedral rotation angle
⁽²⁾ ψ ; octahedral flattening angle
⁽³⁾ *e_b*; the basal O-O distance
⁽⁴⁾ *d_o*; the average octahedral cation to anion distance

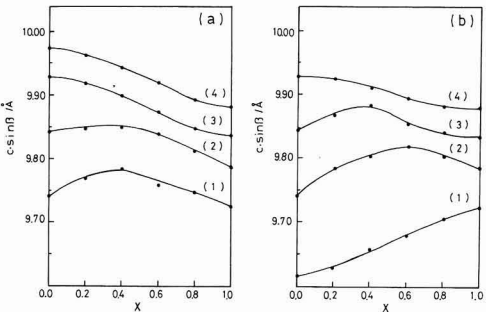


Fig. 6. Basal spacings plotted against *x* (tetrahedral Ga-substitution).
(a): NaMg_{2+1-x}Li_{1-x}(GaGe_{4-x-y}Si_{3y}O₁₀)F₂ series micas
(1) Ga₁Ge_{1-x}Si₃, (2) Ga₁Ge_{2-x}Si₂, (3) Ga₁Ge_{3-x}Si, (4) Ga₁Ge_{4-x}
(b): NaMg_{2+1-x}Li_{1-x}(GaSi_{4-x-y}Ge_{3y}O₁₀)F₂ series micas
(1) Ga₁Si_{4-x}, (2) Ga₁Si_{3-x}Ge, (3) Ga₁Si_{2-x}Ge₂, (4) Ga₁Si_{1-x}Ge₃

While, the values ψ of various Na-fluorine micas are smaller by 1 to 1.2 degree than those of corresponding K-analogues. This smaller ψ value suggests that structural distortion of Na-fluorine micas is cancelled relatively more by the rotation of tetrahedron than by the flattening of octahedron. It shall be noted for reference that, according to a study report¹²⁾ on the similar cancellation mechanism of structural distortion in the case of biotite, the temperature factor for basal oxygen (O_b) was larger than that for apical oxygen (O_a), thereby, the rotation angle value α was not affected so much by the composition of octahedral sheet.

3.4. Relationship Between Basal Spacing (*c*·sinβ) and Amount of 3-valence Ion Substitution

Figure 6 shows the relationship between *c*·sinβ and tetrahedral Ga-substitution amount in the case of Ga-substituted series Na-fluorine micas. It was found that *c*·sinβ and Ga-substitution amount were related with each other not in a linear line like Vegard law, but in a curve having a maximum point or a turning point. Fig.6(a) concerns the series of substituting Ge⁴⁺ with Ga³⁺. Among them, Ga_xGe_{1-x}Si₃ and Ga_xGe_{2-x}Si₂ series respectively exhibited a maximum *c*·sinβ value at a certain *x* value, and Ga_xGe_{3-x}Si and Ga_xGe_{4-x} series respectively exhibited a simple decrease of *c*·sinβ value with the increase of value *x*. The difference of value *c*·sinβ (value Δ*c*·sinβ) between the end members at *x*=0.0 and *x*=1.0 was negative in any series, and the value Δ*c*·sinβ was larger with the increased Ge content. While, Fig.6(b) concerns the series of substituting Si⁴⁺ with Ga³⁺. Among them, Ga_xSi_{4-x} series exhibited a simple increase of value *c*·sinβ with the increase of value *x*, and Ga_xSi_{3-x}Ge and Ga_xSi_{2-x}Ge₂ series respectively exhibited a maximum *c*·sinβ value at a certain *x* value, and the *x* value, at which the maximum *c*·sinβ value is exhibited, shifted toward the lower *x* value side with the decrease of Si content and the increase of Ge content. Ga_xSi_{1-x}Ge₃ series exhibited a simple decrease of *c*·sinβ value with the increase of value *x*. The value Δ*c*·sinβ between the end members was positive in the case of Ga_xSi_{4-x} and Ga_xSi_{3-x}Ge series, and was negative in the case of Ga_xSi_{2-x}Ge₂ and Ga_xSi_{1-x}Ge₃ series. Therefore, although Si⁴⁺ ion was substituted with Ga³⁺ ion having a larger ionic radius, the value *c*·sinβ decreased when Ge

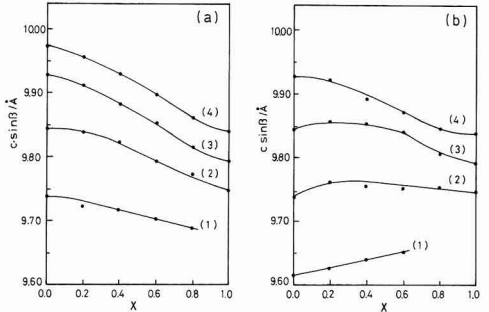


Fig. 7. Basal spacings plotted against *x* (tetrahedral Al-substitution).
(a): NaMg_{2+1-x}Li_{1-x}(AlGe_{4-x-y}Si_{3y}O₁₀)F₂ series micas
(1) Al₁Ge_{1-x}Si₃, (2) Al₁Ge_{2-x}Si₂, (3) Al₁Ge_{3-x}Si, (4) Al₁Ge_{4-x}
(b): NaMg_{2+1-x}Li_{1-x}(AlSi_{4-x-y}Ge_{3y}O₁₀)F₂ series micas
(1) Al₁Si_{4-x}, (2) Al₁Si_{3-x}Ge, (3) Al₁Si_{2-x}Ge₂, (4) Al₁Si_{1-x}Ge₃

content was high in the Ga-substituted mica series.

Figure 7 shows the relationship between value $c\text{-sin}\beta$ and tetrahedral Al substitution amount in Al-substituted series Na-fluorine micas. Fig.7(a) concerns the series of substituting Si^{4+} with Al^{3+} , and Fig.7(b) does those of substituting Ge^{4+} with Al^{3+} . In both series, this relationship changed in a similar manner to those in the Ga-substituted series above mentioned, but the value $\Delta c\text{-sin}\beta$ was smaller when it was positive, and was larger when it was negative, compared to the respective ones in the Ga-substituted series, because of the effect of a smaller ionic radius of Al^{3+} than Ga^{3+} .

The value $c\text{-sin}\beta$ is related to interlayer thickness (IL), tetrahedral sheet thickness (TL) and octahedral sheet thickness (OL), as expressed in the equation given below.

$$c\text{-sin}\beta = IL + 2TL + OL$$

In the series of substituting Si^{4+} with Ga^{3+} , TL increases as the effect of substitution of a smaller radius ion with a larger radius one, thereby, the increase of value $c\text{-sin}\beta$ in the lower x value region has been caused by the effect of increased TL value. However, in the higher x value region, in which Ga-substitution to Si increases and TL further increases, the misfit between a tetrahedral sheet and an octahedral sheet is compensated by the flattening of octahedral sheet, thereby, the decreasing effect of flattening and the increasing effect of TL to $c\text{-sin}\beta$ is assumed to cancel with each other, resulting to make the value $c\text{-sin}\beta$ turn to decrease. In the series of substituting Ge^{4+} with Al^{3+} having the same ionic radius, the value $\Delta c\text{-sin}\beta$, which is negative, become larger with the increase of Ge content. This phenomenon suggests that both thicknesses of OL and IL are affected by the charge balancing in mica structure in such way as to contract more by the substitution of 4-valence ion with 3-valence one. (Here, the charge balancing means a system of indicating which positive charge deficiency generated in an octahedral sheet or in a tetrahedral sheet is compensated by an interlayer cation in a mica structure.) These additional contractions of OL and IL are caused by the change of the tetrahedral structure into a structure having a larger rotation angle α , because not only the ionic radius of Na^+ is too small to fit the interlayer spacing, but also the larger substitution amount of 4-valence ion with 3-valence one effects to more

localize negative charges to basal oxygen O_b . In the case of K-fluorine micas, IL increased with the increase of rotation angle α ,^{5,6)} but, in the case of Na-fluorine micas, IL is supposed to decrease instead when the effect of aforementioned localized negative charges to O_b is given, because Na^+ ion is small in radius. Although the change of value $c\text{-sin}\beta$ caused by the Ga- and Al-substitution is not simple as mentioned above, it is systematic and continuous, therefore, the afore-mentioned series Na-fluorine micas are implied to have a complete series of solid solution.

3.5. Relationship Between b -axis Dimension and Basal Spacing Value ($c\text{-sin}\beta$) and Mean Four-coordination Ionic Radius

Figure 8 shows the relationship between b -axis dimension and mean tetrahedral ionic radius (R_m) for the end member Na-fluorine micas¹¹⁾ and the same for the corresponding K-analogues. It is seen that both 3-valence substituted Na-mica and K-mica series have respective linear relationships between b and R_m , and these two lines are nearly parallel with each other. This result suggests that not only the size of tetrahedral ion determines the dimension of b -axis, but also the size of interlayer ion gives a decisive effect to the determination of b -axis dimension. In other words, when Al- and Ga-substituted Na-fluorine micas are compared to the corresponding K-analogues, the b -axis dimension is smaller in the former than in the latter, and this smaller b -axis dimension indicates that Na-micas have a larger rotation angle (α) of the tetrahedron, as shown in Fig.5(2), thereby, they have a more-distorted structure.

Figure 9 shows the relationship between $c\text{-sin}\beta$ and R_m for the end member Na-fluorine micas and the same for the corresponding K-fluorine micas. It is seen that the relationship between $c\text{-sin}\beta$ and R_m is linear in the case of Na-mica series in the same manner as it was in the case of K-mica series, but the values $c\text{-sin}\beta$ are much smaller in the former than in the latter. This difference of value $c\text{-sin}\beta$ is attributed to the smaller dimension of interlayer Na^+ ion, compared to that of K^+ ion, and the difference of value $c\text{-sin}\beta$ between these two mica series increased with the increase of R_m . These much larger $c\text{-sin}\beta$ values in the case of K-

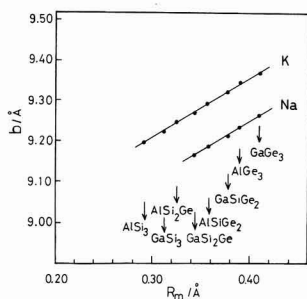


Fig. 8. Relationship between b -axis dimension and mean tetrahedral ionic size for Na-micas (Na) and corresponding K-micas (K; after Kitajima et al., 1989, 1990). Tetrahedral composition of micas is shown in abbreviated symbols.

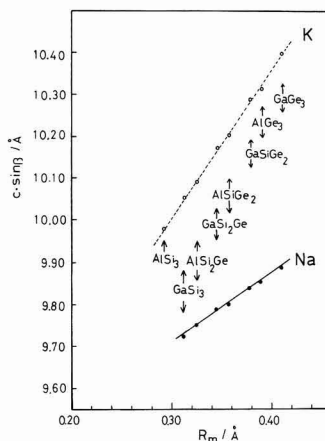


Fig. 9. Relationship between $c\text{-sin}\beta$ and mean tetrahedral ionic size for Na-micas (Na) and corresponding K-micas (K).

mica series are caused by the increase of α value with the increase of R_m and the resultant elongation of the thickness of coordination polyhedron of interlayer K^+ ions along the c^* -axis direction. In other words, hexagonal holes formed with O_b are transformed to ditrigonal holes having a smaller dimension with the increase of α value, as shown in Fig.5, thereby, when K^+ ions having a larger radius are filled into the interlayer sites, the interlayer is assumed to be necessarily expanded in the c^* -axis direction.⁵⁾

3.6. Swelling Characteristics

In the case of mica samples having swelling characteristics, all of the TG curves showed one-stage weight loss. It was revealed that this weight loss was attributed to dehydration of interlayer water, and that the dehydration amount decreased and the swelling characteristics decreased with the increase of x value. It was also revealed that both Al- and Ga-substitution series micas did not contain interlayer water when Ge content was higher and x value was higher, when the TG data were compared to the corresponding X-ray diffraction data. We determined the water contents of the mica samples, which were equilibrated in air (R.H. \approx 60% at 20°C), from the TG curves, and classified them into four categories, obtaining Fig.10. In both Al- and Ga-substitution series micas, water content decreased with the increase of 3-valence ion substitution amount (x), and was less than 0.5% in the compositional region, which is indicated on the right-hand side to the dotted line in Fig.10. This implied that the micas in this region lost swelling characteristics and contained only free water adhered on their surfaces. From the X-ray diffraction data of micas wetted with water, we classified the maximum-hydrated phases into three cases of double-layer hydrated phase observed, single-layer hydrated phase observed, and no hydrated phase observed. Figure 11 shows the classified results. It is seen in both Al- and Ga-substitution series micas that, when Ge content in mica is high, swelling characteristics are lost completely by the increase of 3-valence ion substitution amount.

3.7. Causes for Loss of Swelling Characteristics by 3-valence Ion Substitution

With the increase of Al- or Ga-substitution amount, rotation angle value α increases, therefore, tetrahedral layer

changes from the structure illustrated in Fig.5(1) to that illustrated in Fig.5(2), so the coordination of interlayer Na^+ ions changes to be closer to a six-coordination state. Furthermore, as the result of substitution of four-coordination sites with 3-valence ions, effective negative charge of basal oxygen (O_b) increases, thereby, $Na-O_b$ bond is strengthened. Both of these changes are judged to contribute to stabilize the interlayer structure, resulting to make the hydration of interlayer ions unnecessary in terms of energy balance. The substitution of four-coordination sites with 3-valence ions additionally effects to accelerate rotation of tetrahedron, as the result of the increase of effective negative charge of O_b afore-mentioned. In other words, this substitution gives a synergetic effect to the stabilization of interlayer region because of both the increase of value α and the change of charge distribution. This effect can explain the loss of swelling characteristics of micas in the lower x value range with the increase of Ge content in mica. It is also supposed that a remarkable contraction of basal spacing $c\text{-sin}\beta$ by the 3-valence ion substitution in the case of Na-fluorine micas containing a high Ge content is closely related to the loss of swelling characteristics.

4. Conclusion

Series of Ga- and Al-substituted fluorine micas $NaMg_{2+x}Li_{1-x}(T_xSi_{4-x}Ge_yO_{10})F_2$ and $NaMg_{2+x}Li_{1-x}(T_xGe_{4-x}Si_yO_{10})F_2$ [$T=Ga, Al$; $x=0.0$ to 1.0; $y=0, 1, 2, 3$], which were based on the end member micas of Na-taeniolite [$NaMg_2Li(Si_4O_{10})F_2$] and its Ge-analogues, were synthesized, and using these mica samples, the changes of infrared absorption spectra and of lattice parameters in relation to the isomorphic substitution were studied, the changes of swelling characteristics of these substituted mica series were studied, and the causes for the loss of swelling characteristics were examined. The results are summarized in the followings.

- 1) Infrared absorption spectra of Na-fluorine mica series changed continuously with the change of amount of Ga- and Al-substitution at four-coordination site, and the absorption bands of Si-O and Ge-O were observed to shift, and new absorption bands caused by the Ga- and Al-sub-

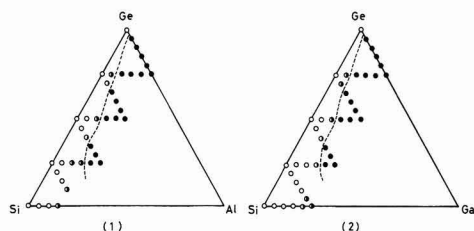


Fig. 10. Water content shown by ternary systems of tetrahedral composition for (1) Al-substituted micas $NaMg_{2+x}Li_{1-x}(Al_xGe_{4-x}Si_yO_{10})F_2$, $NaMg_{2+x}Li_{1-x}(Al_xSi_{4-x}Ge_yO_{10})F_2$ and (2) Ga-substituted micas $NaMg_{2+x}Li_{1-x}(Ga_xGe_{4-x}Si_yO_{10})F_2$, $NaMg_{2+x}Li_{1-x}(Ga_xSi_{4-x}Ge_yO_{10})F_2$.
●: < 0.5wt%, ◐: 0.5–3wt%, ○: > 5wt%
The samples were equilibrated in air at 20°C, R.H. \approx 60%

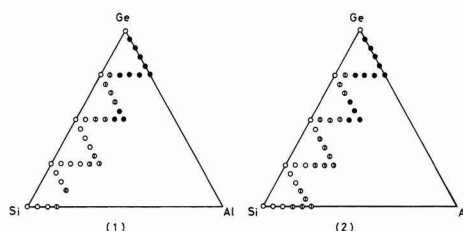


Fig. 11. Swelling tendency represented by the highest hydration phase under wetted conditions with water. The results are shown for Al-substituted micas (1) and Ga-substituted micas (2) in the same ternary systems as in Fig.10.

- : anhydrous phase,
- ◐: single-layer hydrated phase,
- : double-layer hydrated phase

stitution were observed to appear in the substitution series containing larger Si contents.

- 2) Basal spacing value ($c \cdot \sin \beta$) changed continuously with the change of Ga- and Al-substitution amount. This behavior proved the presence of a complete series of solid solution between the end member mica series.
- 3) Basal spacing value changed simply in some cases, and changed as to have a maximum at a certain x value in other cases. These complicated changes of basal spacing value could be explained by the respective changes of structural distortions (α and ψ) and of interlayer structure.
- 4) The respective structural distortions (α and ψ) of tetrahedral sheet and octahedral sheet increased with the increase of Ga- and Al-substitution amount. When structural distortions were compared between the corresponding analogues Ga-substituted micas were found to exhibit larger α and ψ value than Al-substituted ones did.
- 5) b -axis values and $c \cdot \sin \beta$ values were plotted against mean ionic radii (R_m) of four-coordination cations for the end member Na-fluorine micas, which included Al- and Ga-substitution series micas, together with those for the corresponding K-fluorine mica series. Both plots for Na- and K-fluorine mica series gave respective linear relation lines. These linear relationships indicated that the distortion of coordination polyhedron was determined not only by the dimension of four-coordination ions, but also by the dimension of interlayer ions.
- 6) In the case of Na-fluorine micas, interlayer structure changed to be closer to the ideal six-coordination state, which is a more stabilized structural arrangement, with the increase of α value, thereby, swelling characteristics

were lost.

Acknowledgements

The authors wish to thank Mr. Junichi Sano for his assistance to us in the experiments in this study.

References:

- 1) G. Donnay, J.D.H. Donnay and H. Takeda, *Acta Crystallogr.*, 17, 1734-1781 (1964).
- 2) K. Kitajima, K. Sugimori and N. Daimon, *J. Chem. Soc. Jpn.*, 1973, 1885-1892.
- 3) K. Kitajima, A. Murata and N. Takusagawa, *ibid.*, 1990, 746-752.
- 4) K. Kitajima, M. Matsukura and N. Takusagawa, *ibid.*, 1989, 1038-1040.
- 5) K. Kitajima, T. Inada and N. Takusagawa, *Seramikkusu Ronbunshi*, 97, 649-655 (1989).
- 6) K. Kitajima, T. Inada and N. Takusagawa, *ibid.*, 98, 476-482 (1990).
- 7) J.D. Russell, V.C. Farmer and B. Velde, *Mineral Mag.*, 37, 869-879 (1970).
- 8) M. Ishi, T. Shimanouchi and M. Nakahira, *Inorg. Chim. Acta*, 1, 387-392 (1967).
- 9) K. Kitajima and N. Takusagawa, *Clay Minerals*, 25, 235-241 (1990).
- 10) H. Takeda and B. Morosin, *Acta Crystallogr.*, B31, 2444-2452 (1975).
- 11) R.D. Shannon, *Acta Crystallogr.*, A32, 751-767 (1976).
- 12) M.F. Brigatti and P. Davoli, *Am. Miner.*, 75, 305-313 (1990).

This article is a full translation of the article which appeared in *Nippon Seramikkusu Kyokai Gakujutsu Ronbunshi* (Japanese version), Vol.99, No.12, 1991.

Deposition of TiN Films onto Glaze of Porcelain by Reactive Sputtering

Hiromichi Ichinose, Kazuo Akamatsu, Makoto Terasaki,* Hiroaki Katsuki* and Masamitsu Nagano

Department of Applied Chemistry, Faculty of Science and Engineering, Saga University
1, Honjou-machi, Saga-shi, 840 Japan

*Ceramics Industrial Research Institute of Saga Prefectural Government
3100-5, Chubu, Arita-machi, Nishimatsuura-gun, Saga 844 Japan

In an attempt to develop a new method for decorating porcelain, TiN films were deposited onto the glaze of porcelain by reactive DC magnetron sputtering of Ti in NH_3 discharge gas. For comparison with the glaze, effects of other substrates such as Si, Ti, Al_2O_3 , ZrO_2 and MgO on the formation of TiN films were examined. A pleasing gold-like appearance was obtained under the following sputtering conditions: pressure of 0.007Torr, discharge power below 40W and substrate temperature above 300°C. At higher pressures, higher discharge powers, or lower substrate temperatures, the hue of TiN films changed gradually to reddish gold and then dark red. The degradation in color is ascribed to the increasing oxygen contamination as well as the deviation of the nitrogen content from the stoichiometry. XPS analysis revealed the existence of a considerable amount of O-H bonds in the film when the substrate temperature was below 200°C. In the case of oxide substrates such as glaze, gray diffusion layers with a thickness less than 100nm were formed between TiN films and the substrates. The layers contained more Ti-O bonds and less nitrogen than those on Si or Ti substrate. TiN films with a similar hue and reflection to gold over-glaze were obtained on the glaze with surface roughness of 0.25 μm . [Received June 24, 1991; Accepted August 22, 1991]

Key-words: TiN film, Reactive sputtering, Glaze of porcelain, Color, Diffusion layer, Surface roughness, Reflection.

1. Introduction

TiN films are featured by an extremely high chemical stability, a high hardness, a high abrasion resistance and a very beautiful golden color. Therefore, they are being put to various industrial (such as cutting tools and press molds) and decorative uses.¹⁾ Regarding the formation of TiN films, a good number of study reports have been made available, and TiN films are currently formed by various methods such as ion-plating,²⁾ reactive sputtering,³⁻¹⁰⁾ thermal CVD,¹¹⁾ and, more recently, plasma CVD.¹²⁻¹⁴⁾ However, very few study reports are available on the effect of mutual diffusion of atoms at the interface between substrate and TiN film to the hue of the film.

Gold over-glaze of porcelain is prepared by using paints made of gold powder which was mixed with flux of bismuth bride or bismuth oxide, or of gold chloride which was dissolved in oils, and by baking at 800°C as to be fixed on the

porcelain glaze. However, the gold over-glaze of porcelain thus prepared has poor abrasion resistance and poor adhesion to the glaze, so that it is worn and exfoliated during use, or it is discharged and changes in color by microwave in an electron range, resulting in less commercial value. Accordingly, an attempt to develop a new technique of the abrasion resistant and exfoliation resistant decoration on ceramic wears, to authors applied a coating of TiN film on the surface of porcelain glazes which were ordinarily used on porcelains in the Arita district in Saga prefecture, and investigated the effect of the deposition condition of TiN film and that of the diffusion layer formed between TiN film and substrate to the hue of film. In order to compensate for the drawback of low reflectance of TiN compared to that of gold, we also attempted to improve the hue of TiN film by increasing the apparent reflectance of TiN film by giving some appropriate surface roughness to the substrate.

2. Experimental Procedure

We used a flat-type DC magnetron sputtering apparatus for the deposition of TiN films. The electrodes were disk shaped of diameter 10cm made with Ti metal (in purity of 99.5%, made by Nippon Denkyu Kogyo), and the distance between the electrodes was set as 5cm. Permanent magnets of cylindrical shape and of columnar shape were set equiaxially behind the electrodes so as to make the electric field and the magnetic field cross perpendicularly in the neighborhood of the anode. Nitrogen source we used was NH_3 gas (commercially available). We did not refine this NH_3 gas, because the handling of reagents for dehydration and deoxidation was complex and expensive. Using various discharge voltages in the range of 200 and 510V and various discharge currents of 50, 100 and 200mA, we deposited TiN films on the substrates, which were located at 1.5cm above the cathode, and preheated. The substrates used were either fired porcelain glaze at 1300°C for 30min (chemical composition of the glaze: $\text{SiO}_2=75.94\%$, $\text{Al}_2\text{O}_3=12.71\%$, $\text{Fe}_2\text{O}_3=0.31\%$, $\text{TiO}_2=0.05\%$, $\text{CaO}=6.37\%$, $\text{MgO}=0.15\%$, $\text{Na}_2\text{O}=1.98\%$, $\text{K}_2\text{O}=2.48\%$, Total=100.0%, or plates of single crystals of Si (100) and Ti, and of sintered bodies of Al_2O_3 , ZrO_2 (stabilized with 9.8mol% of Y_2O_3) and MgO, all of which were polished to a mirror finish. We not only observed the TiN films deposited using a scanning electron microscope (SEM), but also determined the composition and the hue of the films and the elements contained in the films by measuring powder X-ray diffraction, surface roughness, reflection spectrum of light in the range of visible

wave length, and X-ray photoelectron spectrography (XPS). Reflection spectrum of light in the range of visible wave length was measured by sending a light at an incidence angel of 30 degrees against the perpendicular direction to the substrate surface and by receiving the reflected light at the same angle. Surface roughness of substrate was adjusted by polishing the substrate using water-proof polishing papers or SiC abrasive grains. The surface roughness was determined by the largest surface roughness (R_{max}) measured in the measured distance of 50 μ m. Adhesion strength between film and substrate was measured using a strength tester of SEBASTIAN-V model, made by Quad Group, in which aluminum stands in diameter of 0.106 inch were attached to the film at a perpendicular angle using an adhesive reagent of epoxy system. As an additional evaluation method for adhesion strength between film and substrate, we made a Vickers indent onto the film using a micro-Vickers hardness tester, and examined the presence of exfoliated film using an SEM.

3. Experimental Results and Discussion

3.1. Effects of Reaction Gas Pressure, Substrate Temperature and Discharge Current

TiN films were formed at the respective rates of about 5, 7 and 2nm/min under the reaction gas pressures of 0.007, 0.06 and 0.5Torr, when the fixed process conditions of discharge current of 200mA and substrate temperature of 300°C were applied. SEM observation revealed that the texture of TiN films was a dense columnar structure, which grew perpendicular to the substrate, and had a flat surface. **Figures 1 and 2** show a $L^*a^*b^*$ color coefficient diagram, recommended by CIE (International Committee on Illumination),¹⁵⁾ of TiN films formed on porcelain glaze. Here, L^* corresponds to lightness, and a^* and b^* respectively correspond to hue and saturation, based on the original point without color. When gas pressure was 0.007Torr and substrate temperature was higher than 300°C in the sputtering, the films exhibited gold-like color almost consistently, but when substrate temperature was lower than 200°C, they ex-

hibited various colors in the range from reddish gold to gray. When gas pressure was 0.06Torr, a higher substrate temperature was required to obtain gold-like color. As seen in **Fig.2** on the effect of discharge current, when discharge current was higher than 100mA, the film color tended to change toward the red side, and this tendency was especially remarkable when gas pressure was 0.06Torr. **Figure 3** shows the relationship between substrate temperature and lattice parameter of TiN films. When processed in the conditions of gas pressure of 0.06Torr and discharge current of 100mA, lattice parameters of the TiN films formed were constant regardless of substrate temperature as to be nearly equal to that of stoichiometric TiN.⁵⁾ When discharge current was increased to 200mA under the same gas pressure of 0.06Torr, lattice parameter decreased remarkably from 0.425nm to 0.420nm along with the decrease of substrate temperature from 400°C to 200°C. According to the X-ray diffraction patterns observed, when a low gas pressure of 0.007Torr, a low substrate temperature of 210°C and the same discharge current of 200mA were applied, diffraction peaks of cubic δ -TiN phase were no longer observed, but broad peaks of tetragonal ϵ -Ti₃N (002) came to be observed clearly.

Table 1 shows the results of XPS analysis of TiN films formed on the glazes for pottery and porcelain. TiN film No. 1, which exhibited a bright gold-like color, had a Ti/N atomic ratio of nearly 1. While, other TiN films, which exhibited reddish golden color or dark golden color, had a decreased nitrogen content and an increased oxygen content. **Figure 4** shows O_{1s} photoelectron spectra of four kinds of

Table 1. Sputtering condition and atomic ratios in the film determined by XPS.

No.	sputtering condition				hue	etching with Ar (min)	atomic ratio	
	P(Torr)	Ts(°C)	Id(mA)	time(h)			N/Ti	O/Ti
1	0.007	300	100	1	G	6	0.99	0.20
2	0.06	300	100	2	RG	5	0.78	0.61
3	0.06	300	200	2	DR	5	0.82	0.62
4	0.007	120	100	2	DR	5	0.92	0.93

G : gold, RG : reddish gold, DR : dark red.

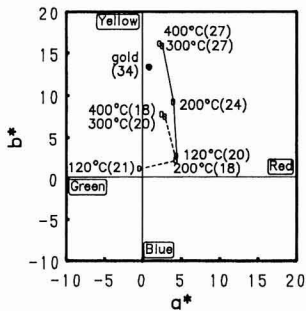


Fig. 1

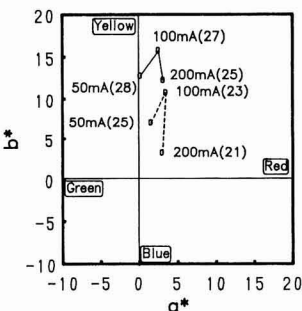


Fig. 2

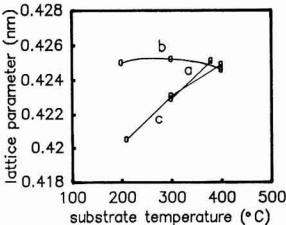


Fig. 3

Fig. 1. Effect of substrate temperature on color coefficients a^* and b^* of TiN film. Lightness (L^*) is shown in parentheses. Solid line: 0.007Torr, 100mA; dotted line: 0.06Torr, 100mA.
Fig. 2. Effect of discharge current on color coefficients a^* and b^* of TiN film. Lightness (L^*) is shown in parentheses. Solid line: 0.007Torr, 300°C; dotted line: 0.06Torr, 300°C.
Fig. 3. Effect of deposition condition on lattice parameter of TiN film. a) 0.007Torr, 200mA, b) 0.06Torr, 100mA, c) 0.06Torr, 200mA.

TiN films listed in Table 1. In the case of TiN films, which exhibited degraded colors, the peaks, which were assumed to correspond to O-H bond, were observed in addition to those to Ti-O bond, and especially in the case of TiN films (NO.4) formed on an unpreheated substrate at 120°C, hydrogen was recognized to reside in a considerable amount.

We assumed that the following might be some of the reasons for the degradation of color of TiN films. Impurity matters such as O_2 and H_2O are contained in the reaction gases. Sputtering rate of Ti increases with the increase of discharge current. When nitriding rate is low, excessive Ti remained unnitrided in the gas phase reacts with oxygen component at an increased probability. While, when sputtering rate of Ti is increased and NH_3 gas pressure is increased, over-saturation degree for TiN formation is supposed to be increased, resulting to accelerate the nucleation of TiN in the gas phase and the growth of these nuclei.¹⁵⁾ During this process of nucleation and nucleus growth, oxygen components in the gas phase are trapped in the TiN particles. These TiN particles deposit onto a substrate, thereby, TiN films involved with these particles are assumed to be more contaminated with oxygen than the TiN films grown on the substrate.

Compared to the lattice parameter of TiN of 0.424nm determined by JCPDS (6-0642), the parameter we obtained in our current experiment was a slightly larger value of 0.425nm. We assume that this difference was not caused by the change of lattice parameter due to the difference of thermal expansion coefficient between porcelain glaze ($6.35 \times 10^{-6}/^\circ C$) and TiN ($9.35 \times 10^{-6}/^\circ C$), but was mainly caused by the contamination of oxygen in TiN crystal lattice,⁵⁾ since the presence of oxygen in the lattice was detected by XPS. When substrate temperature is lower than 300°C, at which nitriding reaction rate on a substrate is assumed to decrease, the amount of Ti sputtered onto the substrate increases with the increase of discharge current density. Therefore, we assume that TiN of nitrogen-defective type became easier to be formed and the lattice param-

eter became smaller resultantly.⁵⁾ When substrate temperature was further decreased to lower than 200°C, we assume that degassing reaction at substrate surface did not take place sufficiently, thereby, hydrogen remained in the TiN deposited, resulting in a remarkably degraded hue of TiN films.¹³⁾

3.2. Effect of Substrate

In the case of substrates made of pottery and porcelain ceramics, TiN films deposited by reactive sputtering in the process conditions of 0.007Torr, 100mA and 300°C exhibited a golden hue when the treatment time was longer than 1h, but exhibited a gray hue when it was shorter than 30min. Since the hue of TiN film seemed to be effected by the chemical composition of substrate used, we experimented to deposit TiN films onto various kinds of substrate as metals and oxides in the same sputtering condition as above described. Figure 5 shows the hues resulted. In the case of substrates made of metals such as Si and Ti used, the hues of the TiN films formed were concentrated in the same region as that formed onto a substrate of gold, although the reflectance of the films was low, even when the treatment time was as short as 30min. However, in the case of substrates made of oxides used, the hues of TiN films formed were concentrated in the region of gray color. When TiN films were formed in a higher thickness than 100nm onto oxide substrates, the effect of the kind of substrate disappeared, and the hues of TiN films formed were almost con-

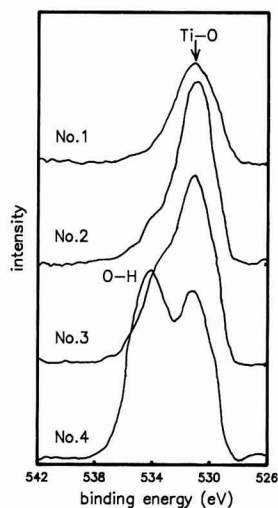


Fig. 4. O_{1s} electron spectra of TiN film. See Table.1 for No.1, 2, 3 and 4.

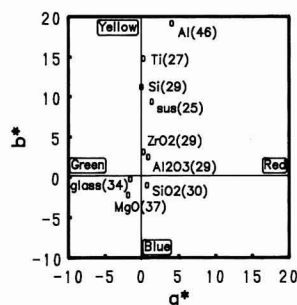


Fig. 5. Color coefficients a^* and b^* of films deposited onto various substrates. Lightness (L^*) is shown in parentheses. 0.007Torr, 300°C, 100mA, 30min.

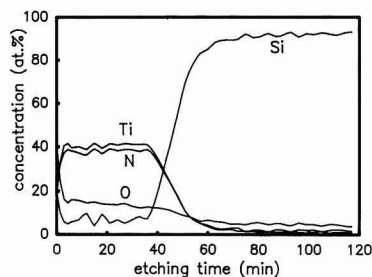


Fig. 6. XPS depth profile of film deposited onto silicon substrate. Etching time by Ar is assumed to be responsible to the depth from film surface.

centrated in the region of yellow color as to exhibit golden color. In the case of substrate made of Si, we examined the concentration profile of elements in the depth-wise direction of TiN film by XPS, the results of which are shown in Fig. 6. Oxygen content in the bulk of film were in the range of 10 and 15at.% when they were corrected only by the analysis result of Si substrate. While, in a diffusion layer formed at the interface between TiN film and substrate, the contents of Ti, N and O gradually decreased in the direction toward the substrate, and the content of Si increased in the same direction. The diffusion layer was estimated to range in a thickness of about 40nm, judging from the thickness of TiN film over 100nm, and contained Ti and N in an atomic ratio of nearly 1. In the case of substrate made of porcelain glaze, we obtained concentration profile of elements in the depth-wise direction of TiN film by XPS as shown in Fig. 7, and the O_{1s} photo-electron spectra also in the depth-wise direction of TiN film as shown in Fig. 8. Oxygen content in the diffusion layer increased along with the direction toward substrate surface, which was a reverse behavior to the case of TiN film deposited onto Si substrate, as seen in Fig. 7, and O_{1s} spectrum peak, which is assumed to be attributed to Ti-O bond, gradually increased in the diffusion layer on the side of TiN film, and reached a maximum intensity, as seen in Fig. 8. This spectrum peak started to decrease gradually

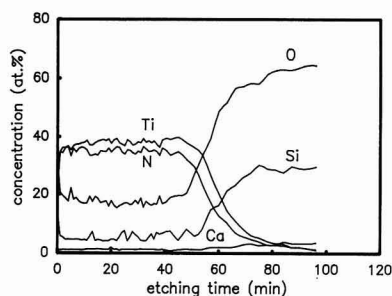


Fig. 7. XPS depth profile of film deposited onto glaze substrate. Etching time by Ar is assumed to be responsible to the depth from film surface.

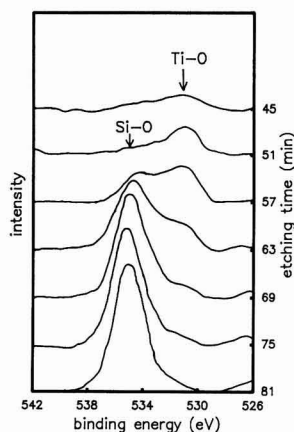


Fig. 8. Change in O_{1s} electron spectra of films deposited onto glaze with etching times.

after reaching the maximum, and another O_{1s} spectrum peak, which is assumed to be attributed to Si-O bond, increased. Al and Ca were recognized to diffuse from the porcelain glaze substrate into the diffusion layer. In the case of porcelain glaze substrate used, we assume that the chemical composition changes more gradually in the region from substrate to diffusion layer than in other regions in the film, and that the width of this region is broader than that in the case of Si substrate used. Atomic ratio of Ti and N in this diffusion layer was determined as to range from 0.63 to 0.80.

The experimental results and examinations above suggest that, in the case of oxide substrates like pottery and porcelain ones, oxygen contained in the substrates diffused into the TiN films and increased the Ti-O bond in the diffusion layer, resulting in degraded hue of the film. Porcelain glaze is composed of glass phase by more than 90%, thereby, both of atomic bonds between Si and O and between Al and O are relatively weak so as to allow a high diffusion rate of oxygen, therefore, we assume the diffusion layer was formed in a greater thickness in the case of porcelain glaze substrate.

3.3. Effect of Surface Roughness of Substrate

In the $L^*a^*b^*$ color coefficient diagram shown in Fig. 1, color coefficient values a^*b^* of TiN films are close to that of gold, but are lower in lightness and are less lustrous, compared to over-glaze gold. Furthermore, color difference $(E^*ab)^{16}$ calculated by the equation given below is larger than 10 between these TiN films and over-glaze gold.

$$\Delta E^*ab = \sqrt{(\Delta L^*)^2 + (\Delta a^*)^2 + (\Delta b^*)^2}$$

Surface roughness (R_{max}) of TiN films deposited onto porcelain glaze was less than $0.1\mu\text{m}$, which differed greatly from that of gold over-glaze of more than $0.5\mu\text{m}$ manufactured in the Arita ceramic industrial district in Saga Prefecture. The TiN films formed in our current experiments were given with a smooth surface and a uniform film thickness, thereby, the surface pattern of the substrate was exactly reproduced on the film surface. We therefore attempted to modify the hue of TiN film by changing surface roughness of the porcelain glaze substrate. Figure 9 shows the visible reflection spectra of the TiN films deposited onto the glaze substrates given with various surface roughnesses. Figures in parentheses indicate the color difference between TiN

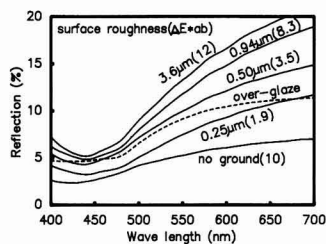


Fig. 9. Effect of surface roughness of glaze substrate on reflective spectrum of TiN film. Difference of color (ΔE^*ab) from gold over-glaze is shown in parentheses. 0.007Torr , 100mA , 300°C , 1h.

film and gold over-glaze. With the increase of surface roughness of TiN film, reflectance increased especially on the longer wavelength side, and situation also increased. When the surface roughness of TiN film was about 0.25 μ m, color difference ΔE^*_{ab} exhibited was a minimum value of 1.9, and the hue was nearly equal to that of gold over-glaze. Color difference was measured by injecting light in a specified incident angle, which was close to the naked eye visual angle, therefore, the increased surface roughness accelerated the irregular reflection of light, thereby, it effected to the apparent reflectance.

Concerning the adhesion strength of TiN film with substrate, we deposited TiN films onto porcelain glaze substrates having a surface roughness of 0.25 μ m in the sputtering condition of gas pressure of 0.007Torr, discharge current of 100mA, and substrate temperature of 300°C, and took the films having a film thickness of less than 4 μ m among them for the tension strength test, in which the samples of TiN film deposited onto glaze substrate were attached with aluminum stands using epoxy system adhesive reagents. The test results revealed that all of the films together with the glaze substrates peeled off at a fracture strength of about 60 to 155kgf/cm². Therefore, adhesion strength between film and substrate could not be measured, but could be evaluated so high as to exceed the fracture strength recorded. When a Vickers' indenter was indented vertically onto the TiN films having a film thickness of around 0.4 μ m under a load of 25gf, the films deposited onto substrates made of alumina, silicon or magnesia exfoliated, but those deposited onto porcelain glaze substrates did not exfoliate even under an increased load of 500gf. Compared to the case of TiN films deposited onto non-oxide substrates like silicon, the composition of TiN films deposited onto porcelain glaze substrates changes more gradiently in the region between substrate and TiN film, and this region is broader, as we mentioned previously. Therefore, we assume that stresses caused between substrate and film were dispersed without being concentrated in this limited region, thereby, a high adhesion strength was obtained at the interface between substrate and film.

4. Conclusion

Aiming to obtain a colored coating having abrasion resistant and exfoliation resistant properties on porcelain glazes, the authors experimented to deposit golden TiN films onto porcelain glaze substrates by means of a reactive sputtering process using a tangent of Ti and a reactive gas of NH₃. The test results are summarized in the following.

- 1) In the process condition of gas pressure of 0.007Torr and substrate temperature of higher than 300°C, TiN films were obtained to exhibit color coefficient values a*b* closer to golden color with the decrease of discharge power, but the lightness of the golden color was slightly lower.
- 2) When gas pressure and discharge power were increased respectively, oxygen components in the process atmosphere were trapped in the films deposited, thereby, the hues of the film changed from reddish gold to gray.
- 3) When discharge current was increased and substrate temperature was decreased to lower than 300°C, TiN films of nitrogen-defective type were formed and the golden hue of the film was degraded.
- 4) When substrate temperature was decreased, dehydrogenation reaction at the substrate surface took place insufficiently, thereby, a considerable amount of hydrogen remained in the TiN films deposited, which resulted in degrading the golden hue remarkably.
- 5) When deposited onto oxide substrates, TiN films formed in thickness of over 100nm exhibited a pleasing golden color. However, when they were formed in thickness of less than 100nm, Ti-O bond increased in the diffusion layer due to the diffusion of oxygen out of the oxide substrates, thereby, the golden hue was degraded.
- 6) When surface roughness of porcelain glaze substrate was prepared as around 0.25 μ m, the TiN films deposited were given with increased apparent reflectance and exhibited a golden hue very close to that of porcelain gold over-glaze. In addition, TiN films deposition onto porcelain glaze has a superb adhesion strength in terms of exfoliation resistance because of gradient composition in the interface layer.

Acknowledgements

The authors wish to thank the personnel of both Yamazoe Seminar and Arai Seminar of Science and Engineering Seminar of Post-Graduate Course of Kyushu University for their assistance in the XPS measurement in our study.

References:

- 1) For instance, Y. Doi, R and D report on Teion Plasma Ouyou-Gijutsu, ed. by T. Higaki, C.M.C. (1983), 143-159.
- 2) D.D. Wang, H. Murata and T. Oki, Hyomen-Gijutsu, 41, 382-387 (1990).
- 3) A. Mumtaz and W.H. Class, J. Vac. Sci. Technol., 20, 345-348 (1981).
- 4) J.E. Sundgren, B.O. Johansson and S.E. Karlsson, Thin Solid Films, 105, 3530366 (1983).
- 5) J.E. Sundgren, B.O. Johansson, S.E. Karlsson and H.T.G. Hentzell, Thin Solid Films, 105, 367-384 (1983).
- 6) J.E. Sundgren, B.O. Johansson, H.T.G. Hentzell and S.E. Karlsson, Thin Solik Films, 105, 385-393 (1983).
- 7) W.D. Sproul, Thin Solid Films, 107, 141-147 (1983).
- 8) J. Danroc, A. Aubert and R. Gillet, Surface and Coatings Technology, 33, 83-90 (1987).
- 9) R.C. Ellwanger and J.M. Towner, Thin Solid Films, 161, 289-304 (1988).
- 10) M.Y. Al-Jaroudi, H.T.G. Hentzell and A. Bengtson, Thin Solid Films, 170, 293-307 (1989).
- 11) B. Karlsson, R.P. Shmshock, J.C. Haygarth and B.O. Seraphin, Physica Scripta, 25, 775-79 (1982).
- 12) N.J. Ianno, A.U. Ahmed and D.E. Englebert, J. Electrochem. Soc., 136, 276-280 (1989).
- 13) P. Mayr and H.R. Stock, J. Vac. Sci. Technol., A4, 2726-2730 (1986).
- 14) K. Oguri, H. Fujita and T. Arai, Hyomen-Gijutsu, 40, 539-542 (1989).
- 15) R.F. Strickland-Constable, "Kinetics and Mechanism of Crystallization," Chapt. 1, Academic Press London (1968) pp.7-43.
- 16) A. Morimoto, Hyomen-Gijutsu, 41, 1033-1037 (1990).

Preparation of CaSiO_3 Powders by Coprecipitation Method and Their Sinterability

Shigeo Hayashi, Kiyoshi Okada and *Nozomu Ôtsuka

Department of Inorganic Materials, Faculty of Engineering, Tokyo Institute of Technology
2-12-1, O-okayama, Meguro-ku, Tokyo, 152 Japan

*Department of Material Engineering, Faculty of Science and Technology, The Nishi Tokyo University
2525, Yatsuzawa, Uenohara-machi, Kitatsuru-gun, Yamanashi, 409-01 Japan

Fine CaSiO_3 powders were prepared by the coprecipitation method using an ethanol solution of calcium nitrate and tetraethyl orthosilicate. The powder composed of only β - CaSiO_3 was synthesized by adding NH_4OH to the solution and firing the precipitates at 1000°C for 2 hours. Addition of oxalic acid in this precipitates process suppressed the formation of β - CaSiO_3 , and the powders composed mainly of α - CaSiO_3 were prepared. The primary particle sizes were under $1\mu\text{m}$, but particles agglomerated to several microns in diameter. These powders were sintered to around 90% theoretical density by firing at 1400°C for 1 hour without sintering additives. The sintered bodies did not absorb water.

[Received June 26, 1991; Accepted September 19, 1991]

Key-words: Powder preparation, CaSiO_3 , Coprecipitation, Sinterability

1. Introduction

CaSiO_3 is a silicate compound belonging to sub-pyroxene group; its three polymorphs are known: pseudowollastonite (α - CaSiO_3), which is high-temperature phase, wollastonite (β - CaSiO_3), which is low-temperature phase, and parawollastonite for which stable regions are not defined. In the industrial sector, this material is used as filler for paper and resins, a material for white paint, a substitute for asbestos,¹⁾ a material for tile base²⁾ and so on. It has been reported that its addition to pottery base reduces shrinkage due to drying or firing, decreases the firing temperature, and increases the strength.^{3,4)} Also, an example of its use as a high-frequency insulating material has been reported.⁷⁾ Recently, it has been suggested that CaSiO_3 may be used as machinable ceramics¹⁾ or it may be useful as a substrate material for superconductive substances.⁸⁾

CaSiO_3 is synthesized by solid state reaction using calcite or quartz or by crystallization via the melting process.⁹⁾ These methods require a relatively high temperature and cannot easily provide fine powder. CaSiO_3 must be synthesized at a temperature lower than the temperature for these methods. One synthesizing method that seems suitable for fulfilling this purpose is the coprecipitation method. This method has a possibility of synthesizing fine powder in which target components are uniformly mixed, but whether good powder can be synthesized or not depends on the synthesizing conditions. Therefore, this problem must be studied. In this study, we tried synthesizing CaSiO_3 powder by the coprecipitation method using ammonia by using cal-

cium nitrate and Si alkoxide. Since it was expected that it was difficult to rapidly deposit Ca during coprecipitation by the use of ammonia only, the effect of addition of oxalic acid in the preparation process on the preparation of CaSiO_3 was also investigated. In addition, the sintering experiment was performed by using powders prepared by these different methods for study the sinterability.

2. Experiment

2.1. Preparation of Samples

$\text{Ca}(\text{NO}_3)_2 \cdot 4\text{H}_2\text{O}$ and $\text{Si}(\text{OC}_2\text{H}_5)_4$ (Wako Pure Chemical Industries, Ltd., guaranteed reagent) were dissolved in ethanol of 100ml so that 0.4mol/l was obtained in CaSiO_3 composition. The quantity of water in the solution was adjusted so that $\text{H}_2\text{O}/\text{SiO}_2$ was 6. These solutions were mixed for 2 hours with a stirrer, and then a hot aqueous solution (40°C) of oxalic acid ($\text{H}_2\text{C}_2\text{O}_4 \cdot 2\text{H}_2\text{O}$) of 100ml was added in the following proportions:

- 1) Not added (sample name CS-0)
- 2) Addition of half mole of Ca (sample name CS-0.5)
- 3) Addition of the same mole as Ca (sample name CS-1)
- 4) Addition of double mole of Ca (sample name CS-2)

Then, the coprecipitate was prepared by adding concentrated ammonia water (25%) of 100ml. The coprecipitate was dried together with the solution in a water bath, then dried for 24 hours in a 110°C constant temperature bath. These materials were calcined at 500°C for 2 hours in the air to use as starting materials.

2.2. Characterization

The differential thermal analysis (DTA, high-temperature micro type manufactured by Rigaku) was performed on each sample. The samples were heat-treated at a specified temperature between 800°C and 1300°C for 2 hours and the change of crystalline phase was investigated by powder X-ray diffraction (XRD, Geigerflex manufactured by Rigaku). Heatings were all performed in the air.

For CS-0 and CS-1 sample, the observation by means of a transmission electron microscope (TEM, JEM-2000EX manufactured by JEOL Ltd.) and the measurement of composition distribution in powder by means of energy dispersive X-ray spectroscopy (EDX, TN-2000 manufactured by Tracor Northern) were performed.

In addition, the samples fired at 1000°C for 2 hours were wet ground in a mortar, and the observation by means of a scanning electron microscope (SEM, MSM-9 manufactured by ABT) and the particle size analysis by means of laser diffraction particle size analyzer (Micortrack manufactured

by Nikkiso Co., Ltd.) were performed.

2.3. Preparation of Sintered Bodies

After being calcined at 1000°C for 2hours, CS-0 and CS-1 samples were ground by a wet vibration mill using zirconia ball (2mm in diameter) for 4hours with ethanol being used as a medium. One percent of polyvinyl alcohol was added in a form of aqueous solution. After being passed through a 100-mesh screen, the sample of about 1g was compacted into a 20mm-dia disk under a pressure of 98MPa. The compact was fired at a specified temperature for 1hour in an electric furnace using an Mosi_2 heating element.

The bulk density and water absorption of the sintered body were measured by the Archimedeian method. The polished and thermally etched surface of the sintered body was observed by a SEM. Thermally etching was performed by holding the sample at a temperature 100°C lower than the sintering temperature for 30minutes.

3. Results and Discussion

3.1. Coprecipitation

For CS-0 sample, the addition of ammonia water produced white precipitate. For this sample, Ca remains in the solution, but it seems to be deposited by the subsequent drying process. For other samples, the precipitation occurred when oxalic acid was added and increased when ammonia water was added. The latter reaction may be the same process as that in which the precipitation of component other than raw material is deposited into the raw material solution in which powder is dispersed.

3.2. Formation Process of CaSiO_3

Figure 1 shows the results of DTA measurement. The measurement was made in the air. For CS-0 sample, an exothermic peak appeared at 876°C, which seemed to accompany the crystallization. As the added oxalic acid increases, the exothermic peak temperature shifted to the high-temperature side, and the peak height decreased. For CS-0.5 to CS-2 samples, endothermal peaks appeared near 700-800°C. This is probably because the oxalate generated in the sample during coprecipitation was changed into carbonate by calcination, which was pyrolyzed in the above-

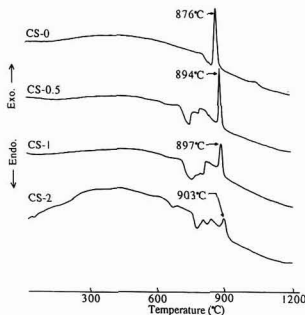


Fig. 1. DTA curves of the samples in air.

described temperature range.

Table 1 gives crystalline phase in the samples obtained by the XRD measurement results for heated samples. Figure 2 shows the change of XRD pattern for CS-0 and CS-1 samples. For CS-0 sample, $\text{Ca}_3\text{Si}_2\text{O}_7$ and some unidentified phases were produced from 800°C, and $\beta\text{-CaSiO}_3$, a low-temperature phase, was formed. When the sample was heated to 1000°C, the crystalline phases other than β phase disappeared, and single phase remained. When the sample was heated to higher temperatures, $\alpha\text{-CaSiO}_3$ began to form at 1200°C. At 1300°C, the sample became almost only α phase, though peaks that seemed to be $\beta\text{-Ca}_2\text{SiO}_4$ remain a little. For CS-0.5 to CS-2 samples, it was found that the increase in added oxalic acid suppressed the formation of β phase; instead, the formation temperature of α phase decreased. For CS-1 and CS-2 samples, the amount of β -phase was very small independent of the heating temperature.

Figure 3 shows the distribution of SiO_2 concentration in CS-0 and CS-1 samples heated at 800°, 1000° and 1300°C. This result was obtained by the EDX measurement. The variations in concentration at 800° and 1000°C were smaller in CS-0 powder than CS-1. At 1300°C, the variation in concentration in CS-1 powder was nearly equal to that in CS-0 powder. Figure 4 shows the TEM micrographs of CS-0 and CS-1 samples heated at 800°C for 2 hours. The EDX analysis value of the portion denoted by A through D were as follows: A: CaO 44.19, SiO_2 55.80, B: CaO 41.03,

Table 1. Crystalline phases in the samples heated in air at various temperatures. ●: $\beta\text{-CaSiO}_3$, ○: $\alpha\text{-CaSiO}_3$, □: $\beta\text{-Ca}_2\text{SiO}_4$, △: $\text{Ca}_3\text{Si}_2\text{O}_7$, ? : unidentified. The phase enclosed with the parenthesis is trace.

	800°C	900°C	1000°C	1200°C	1300°C
CS-0	● △ ?	● △ ?	●	● ○	○ (□)
CS-0.5	?	● ○ △	● ○ (□)	○ (□)	○ (□)
CS-1	?	(●) ○ □ △	● ○ □	○ (□)	○ (□)
CS-2	○ (□)	(●) ○ □ △	(●) ○ □	○ (□)	○ (□)

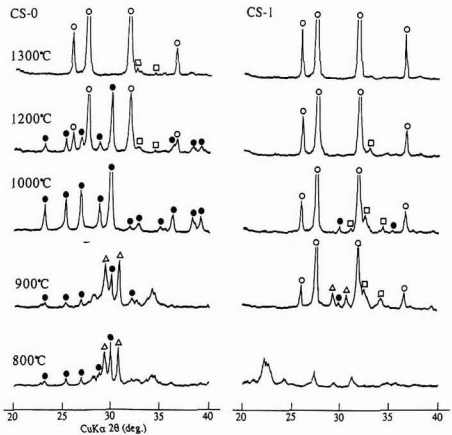


Fig. 2. XRD patterns of CS-0 and CS-1 samples heated in air at various temperatures: ●: $\beta\text{-CaSiO}_3$, ○: $\alpha\text{-CaSiO}_3$, □: $\beta\text{-Ca}_2\text{SiO}_4$, △: $\text{Ca}_3\text{Si}_2\text{O}_7$, no mark: unidentified.

SiO₂ 58.96, C: CaO 94.79, SiO₂ 5.20, D: CaO 80.03 SiO₂ 19.96 (wt%). For CS-1 sample, Ca component apparently separated significantly from Si component as compared with CS-0 sample. The portion where Si concentration was high had finer particles than the portion where Ca concentration was high.

From the above results, it is supposed that Ca and Si are mixed more uniformly in CS-0 sample than in other samples, resulting in rapid formation of β phase by heating. The exothermic peaks of DTA seem to accompany this crystallization. By adding oxalic acid in synthesis, the Ca component in the coprecipitate separates from the Si component because the Ca component deposited as oxalate. It is therefore thought that the formation reaction of CaSiO₃ in which these powders are precursors is similar to the solid state reaction between the raw material powder of Ca component and that of Si component. In these samples, the exothermic peaks of DTA are present a little and β phase is formed in the powder. This suggests that some portions where Ca and Si components are uniformly mixed lie in the coprecipitate

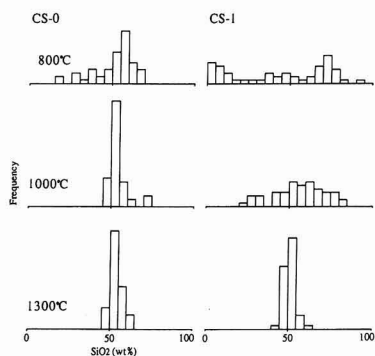


Fig. 3. Distribution of SiO₂ concentration in CS-0 and CS-1 samples heated in air at various temperatures.

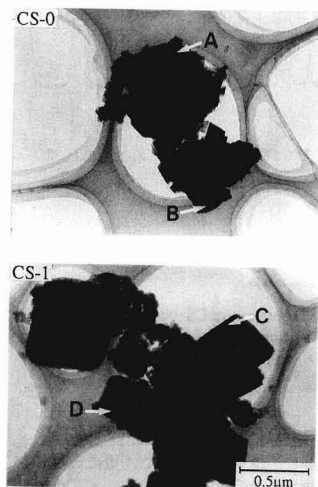


Fig. 4. TEM micrographs of CS-0 and CS-1 samples heated in air at 800°C for 2 hours. The compositions of A-D points were measured by EDX.

to which oxalic acid is added.

The crystalline phase of CaSiO₃ formed by heating varies with its relation path. It has been reported that the solid state reaction from the mixed powder of CaCO₃ and SiO₂ generates α phase, and the glass crystallization of the same composition generates β phase.⁷⁾ The reaction occurred in the present experiment seems to be the same as these reactions. The CS-0 powder heated at 500°C was amorphous, and the formation of CaCO₃ (calcite) was found.

Figure 5 shows the SEM micrographs of CS-0 and CS-1 samples heated 100°C for 2 hours. Although for both samples, the primary particles were fine, being below submicron, particles agglomerated to several microns were also observed. The 50% average diameter of powder obtained by the particle size analysis was 2.92 μm for CS-0 sample and 2.34 μm for CS-1 sample; there were not appreciable difference between them.

3.3. Preparation of Sintered Bodies

Figure 6 shows the bulk density and water absorption of CS-0 and CS-1 sintered bodies. For both CS-0 and CS-1 samples, the sintered bodies of nearly zero water absorption were obtained by firing at 1400°C. There has been no report that CaSiO₃ sintered bodies with zero water absorption have been obtained by the normal-pressure firing without any additive. The powder obtained in the present experiment seems to be fine and highly sinterable. However, its bulk density is about 90% of theoretical density, and considerable number of closed pores remain. At firing temperatures higher than 1400°C, the density did not increase. At temperatures between 1200° and 1350°C, CS-1 sample has higher bulk density than CS-0 sample. This may mainly reflect the difference in compact density. It is supposed that since the temperature range in which sintering mainly proceeds is over 1125°C, which is the transition temperature from β phase to α phase, though the material powder of CS-0 and CS-1 has different CaSiO₃ crystalline phase, the difference in crystalline phase did not affect the sintering behavior.

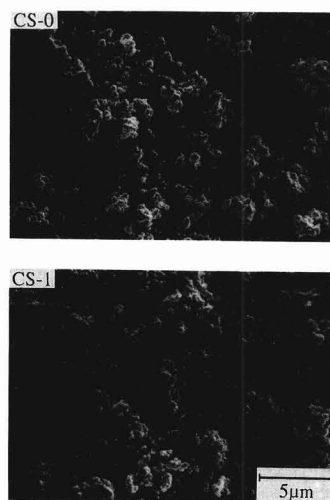


Fig. 5. SEM micrographs of CS-0 and CS-1 samples heated in air at 1000°C for 2 hours.

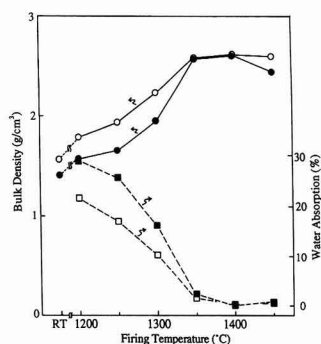


Fig. 6. Bulk density and water absorption of CS-0 and CS-1 sintered bodies: ●■: CS-0, ○□: CS-1.

Figure 7 shows the SEM micrographs of polished and thermally etched surface of CS-0 and CS-1 sintered bodies fired at 1400°C. The observation has revealed that the microstructure for both samples are bimodal; it is composed of large columnar particles over 100μm and particles of several microns filling the gap between them. For fine particles, low anisotropy of form was found. It is thought that unusual particle growth occurred in the course of densification for both samples, which hindered high densification. Pores were widely distributed in the particles and at the boundary of particles, and their size was several microns.

4. Conclusions

CaSiO₃ powders were prepared by the coprecipitation method using an ethanol solution of Ca(NO₃)₂·4H₂O and Si(OC₂H₅)₄ and the sinterability was studied. The conclusions were as follows:

- 1) β-CaSiO₃ single-phase powder was obtained by heating the coprecipitate, which is prepared by adding concentrated ammonia water to the material powder, at 1000°C for 2 hours.
- 2) The formation of β-CaSiO₃ was suppressed during heating by adding oxalic acid in addition to ammonia water in synthesis. It was revealed that the powder prepared by adding oxalic acid with the equal mole as that of Ca and by heating at 1000°C for 2 hours becomes α-CaSiO₃ single phase.
- 3) The primary particles of powder heated at 1000°C for 2 hours were fine, being below 1μm, but easily formed particles agglomerated to several microns.
- 4) The sintered bodies with bulk density of about 90% and water absorption of nearly 0% were obtained by grinding by means of a vibration mill the powder prepared by

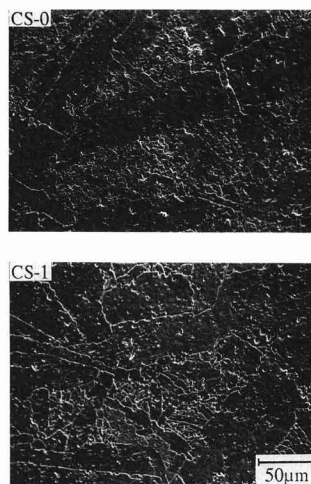


Fig. 7. SEM micrographs of thermally etched surface of CS-0 and CS-1 sintered bodies fired at 1400°C for 1 hour. They were polished and thermally etched at 1300°C for 30 minutes.

the above-described method and by firing it at 1400°C for 1 hour. These sintered bodies had a bimodal microstructure composed of unusually grown columnar particles over 100μm and fine particles of several microns. The difference in CaSiO₃ polymorph phase in material powder had almost no effect on sinterability.

References:

- 1) Y. Goto, H. Ishida and T. Fujisawa, *Fain Seramikkusu*, 10, 27-34 (1989).
- 2) K. Nagasawa and M. Kuzwart, *Mineral Resources for Industrial Material*, Shugakukan (1989) 80-82.
- 3) Millan Vukocich, Jr., *J. Am. Ceram. Soc.*, 39, 323-329 (1956).
- 4) M. Hattori and T. Ito, *Annual Report, Ceram. Res. Inst., Mie Pref.*, 17, 16-29 (1982).
- 5) N.H. Snyder, J.H. Koenig, *Am. Ceram. Soc. Bull.*, 31, 246-247 (1952).
- 6) H. Yasuda, *Research Report Ceram. Res. Inst., Fukui Pref.*, 16, 30-42 (1980).
- 7) K. Hayashi, M. Fukui and I. Uei, *Yogyo-Kyokai-Shi*, 89, 165-170 (1981).
- 8) T. Ishihara, Y. Watanabe, A. Sato and Y. Takida, *Proc. Ann. Mtg. Ceram. Soc. Jpn.* (1990) 432.
- 9) H. Imai, S. Takeuchi and Y. Fujimoto, *Kobutsu Kogaku, Asakura Shoten* (1976) pp.111-119.

This article is a full translation of the article which appeared in *Nippon Seramikkusu Kyokai Gakujutsu Ronbunshi* (Japanese version), Vol.99, No.12, 1991.

Influence of Powder Characteristics on Sinterability and Mechanical Properties of Silica-Alumina Ceramics (74wt% Al₂O₃)

Takeshi Kumazawa, Shigetoshi Ohta, Takaaki Nagaoka*,
Masaki Yasuoka* and Shuzo Kanzaki*

Mino Yogyo Co., Ltd.

1-46, Kamezakikitauro-cho, Handa-shi, 475 Japan

*Government Industrial Research Institute, Nagoya

1-1, Hirate-cho, Kita-ku, Nagoya-shi, 462 Japan

Influence of powder characteristics on mullitization, sinterability and mechanical properties was investigated for silica-alumina powders with 74wt% Al₂O₃ composition synthesized by various methods. Mullitization of the synthesized powders showed a difference depending on the degree of homogeneity of the starting powders. However, all the calcined powders, except for the specimen of oxide mixtures, showed a similar result for the sinterability and microstructure of the sintered bodies. The sinterability of the oxide mixed specimen, which contains unreacted corundum and cristobalite besides mullite, was poorer than those of the other specimens. This can be attributed to the co-existence of corundum, which inhibits sintering of mullite in a similar manner as observed in a solid phase sintering of various particulate composites. The powder processing routes for mullite synthesis do not affect their high temperature mechanical properties, when mullitization occurred fully prior to densification.

[Received June 28, 1991; Accepted September 19, 1991]

Key-words: Mullite ceramics, Mullitization, Homogeneity, Sinterability, Mechanical property

1. Introduction

High-purity mullite ceramics have recently been found to have superior high-temperature characteristics,¹⁾ and are expected to serve as structural materials at high temperatures. The synthesis of high-purity mullite powder was first performed by Mazdiyasi et al.²⁾ by using alkoxide as a starting material, and then performed by many researchers by using combinations of various starting materials.³⁻⁸⁾ All of the synthesized powders reported previously were mullite precursors. It is known that since the mullite precursors are crystallized into mullite by heating, the crystallization temperature and formation process depend on the synthesis method.⁹⁾

There are few reports on the influence of the method for synthesizing powder on the sinterability and mechanical properties of mullite. The authors investigated the sinterability, microstructure, and mechanical properties of mullite of 3:2 composition synthesized by different methods, and revealed that since the yield of glassy phase at the grain boundary depends on the microstructural inhomogeneity in

the starting powder, the powder that is less homogeneous has higher sinterability but has relatively large decrease in strength at high temperatures.¹⁰⁾ This indicates that for mullite of 3:2 composition, the sinterability and mechanical properties depend on the amount of liquid phase formed at high temperatures.

It is known that mullite forms a dissolving region at the alumina-excess side from the 3:2 composition.¹¹⁾ Even now, there are different opinions regarding the phase diagram of mullite at high temperatures. However, when the composition of solid solution is assumed to be stable as a single phase of mullite at high temperatures, the powder that has high microstructural homogeneity is sintered in solid phase, whereas the powder that has low homogeneity may produce liquid phase in the sintering. Therefore, it is expected that the microstructure and mechanical properties of sintered body differ depending on the method for synthesizing material powder even for the composition of solid solution.

In this work, the mullitization, sinterability, the microstructure and mechanical properties of the sintered body were investigated for mullite powder with 74wt% Al₂O₃ composition synthesized by various methods.

2. Experimental Procedure

The used starting powder were mullite precursor powders manufactured by Hokko Chemical Industry Co., Ltd., which were synthesized by methods A through E given in Table 1. To obtain powders A and B, aluminum isopropoxide and silicon methoxide were mixed and hydrolyzed with distilled water and ammonia water, respectively. To obtain powder C, aluminum nitrate and silicon ethoxide were mixed and coprecipitated with ammonia water. Powder D was prepared

Table 1. Synthesis method for various mullite precursors.

Powder	Synthesis Method	Al ₂ O ₃ Content
A	Al(OPr) ₃ + Si(OMe) ₄ → Hydrolysis (H ₂ O)	73.9 wt%
B	Al(OPr) ₃ + Si(OMe) ₄ → Hydrolysis (H ₂ O, NH ₄ OH)	74.6 wt%
C	Al(NO ₃) ₃ + Si(OEt) ₄ → Co-Precipitation (H ₂ O, NH ₄ OH)	73.6 wt%
D	Al(OPr) ₃ — Hydrolysis (H ₂ O, NH ₄ OH) —→ Mixing	74.0 wt%
E	Si(OMe) ₄ — Hydrolysis (H ₂ O, NH ₄ OH) —→ Mixing	73.8 wt%
	Al(OPr) ₃ — Hydrolysis —→ Mixing	
	Si(OMe) ₄ — Hydrolysis —→ Mixing	
	Calcination —→ Mixing	

by separately hydrolyzing the starting materials that were the same as those of A and B and by mixing the resultant gel. Powder E was prepared by hydrolyzing aluminum isopropoxide and silicon methoxide, calcining them at 800°C into oxides, and mixing in methanol for 8h with a ball mill. The alumina content of powders A, D and E agrees well with the target value of 74wt%, while that of powder B and C slightly deviates from the target value. To remove moisture, organic substances, and reaction products that had been adsorbed, the synthesized mullite precursor powders were heat treated at 800°C for 1h after synthesis. The change of crystalline phase caused by the heating of dried powder was investigated by the differential thermal analysis (DTA manufactured by Rigaku Corporation) and the powder X-ray diffraction (Rad-Ru manufactured by Rigaku Corporation). The chemical composition of powder was determined by fluorescent x-ray analysis (3070 manufactured by Rigaku Corporation). Since it is known that sudden volume shrinkage of mullite precursor powder occurs in crystallization by some synthesis methods, the powder calcined at 1450°C for 1h and then ground was used for the comparison of sinterability. The specific surface area of powder after grinding was determined by the BET method (Sorptomatic 1800 manufactured by Carlo Erba) due to N₂ adsorption.

After phase powders were prepressed, they were CIPed under 200MPa. The shrinking rate in heating in the air at a rate of 10°C/min and the change in the isothermal shrinking rate of 1650°C were measured continuously by the thermal expansion meter (TMA-HT manufactured by Rigaku Corporation). Also, a sintered body of about 40×30×5mm was prepared under the same condition as that of shrinking rate measurement. From the sintered body, columnar specimens were cut, ground with #600 diamond wheel on all faces, and rounded on the edges to finally prepare flexural strength test pieces of 3×4×36mm in accordance with JIS R1601. The strength test was performed by the three-point bending method in the air in the temperature range from room temperature to 1500°C, and at least four measurements were made. The microstructures of material powders and sintered bodies were observed by a transmission electron microscope (JEOL-400FX) and a scanning electron micro-

scope (JEOL-T300).

3. Results and Discussion

3.1. Characteristics of Starting Powders

Figure 1 shows the DTA curves for the starting powders. Powders A, B and C exhibit nearly the same change, having exothermic peaks near 980°C and at 1250°-1300°C. For powders D and E, exothermic peaks are found only near 1280°C and near 1350°C.

Figure 2 shows the thermal crystalline phase change for specimens quenched before and after the exothermal peak and for specimens quenched after being heat at 1650°C by varying the holding time. The exothermic reaction at 980°C for powder A is due to the formation of spinel phase and mullite, whereas the exothermic reaction at 980°C for powder B and C is due to the formation of spinel phase only. After the exothermic reaction at 1250°-1300°C, only mullite was identified for powders A, B and C. For the 3:2 composition mullite powder (synthesized by the same method as that of powder A) prepared by hydrolyzing alkoxide with distilled water in the previous paper, the exothermal peak near 980°C corresponded to the crystallization from amorphous phase to single phase of mullite,^{9,10} whereas in the mullite solid solution, spinel phase was remarkably found by X-rays analysis, and the change nearly the same as that of 3.2 composition powder (synthesized by the same method as that of powder B) hydrolyzed with ammonia was shown.^{9,10} For powder D, spinel phase was identified over 1000°C and mullite was found over 1300°C. For powder E prepared by mixing oxide powders, only γ phase and θ phase of alumina were found up to 1350°C, and corundum, cristobalite, and mullite were identified over 1350°C. The corundum found in powder E remained for 4h at 1650°C, whereas the cristobalite disappeared over 1600°C in terms of X-rays. The disappearance of cristobalite may be caused by the fact that the cristobalite is melted over 1600°C and vitrified in cooling, since the eutectic temperature is 1587 ±10°C from the phase diagram of alumina-silica,¹¹ and a wedge-shaped hole has been found in which a glassy phase (indicated by the arrow in Fig.3) may be present at the grain boundary in the specimen fired at 1650°C for 4h.

The change in crystalline phase up to mullite and the difference in temperature with the synthesis method suggest

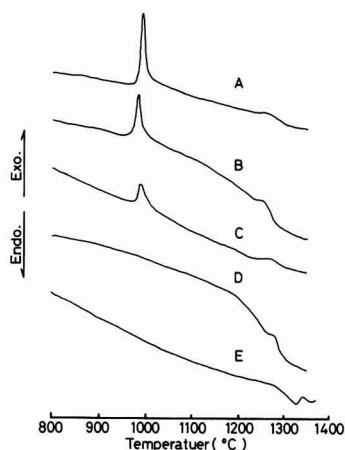


Fig. 1. DTA curves for the precursors prepared by different method.

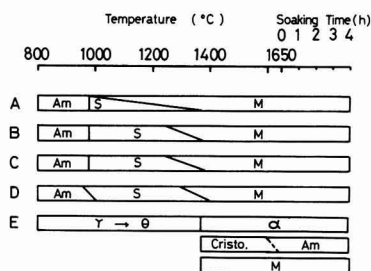


Fig. 2. Thermal crystalline phase change in the calcined specimens. Am : Amorphous phase, S : Al-Si spinel, M : Mullite, γ : γ -Al₂O₃, θ : θ -Al₂O₃, Cristo : Cristobalite

that the homogeneity of mixed alumina-silica in the starting powder is high in the descending order of powder A, powder B and C (nearly the same), powder D, and powder E.

3.2. Sinterability and Microstructure

Since the sinterability and microstructure of mullite differ depending on the alumina/silica ratio,¹²⁾ the subsequent experiments were performed by using powders A, D and E that had nearly the same composition. **Figure 4** shows the TEM micrographs and specific surface area for powders calcined at 1450°C for 1h and ground. For the crystalline phase of powder after being calcined, powders A and D were single phase of mullite, whereas corundum and cristabaltite were identified in addition to mullite for powder E. The particle diameters of powders A and D after being round were about 20-30nm and about 100nm, respectively. Powders A and D were good ones with a shape of clear profile and uniform diameter, but powder E had nonuniform columnar particles with a large diameter of about 200nm. The specific surface area of ground powder was 29.0 for powder A, 22.6 for powder D, and 18.9 for powder E; these values were relatively high though the powders were calcined at a temperature as high as 1450°C.

Figure 5 shows the change in shrinking rate for the powders fired at 1650°C for 4h after being pressed. For powders A and D, the shrinking rate begin increasing rapidly at about 1550°C, and the shrinkage was almost finished after a holding time of 20 minutes at 1650°C. The change in shrinking rate for powder E became rapid at about 1600°C, which was higher than the case with powders A and D, and the shrinkage proceeds slightly in holding at 1650°C.

Figure 6 shows the scanning electron micrographs (polished and thermally etched surface) and bulk density of

specimens obtained after their shrinking rate was measured (held for 4h at 1650°C). After firing, powder A had the highest bulk density of 3.15g/cm³. Powder D had a bulk density of 3.14g/cm³ and powder E 3.09g/cm³. The mullite grains were equi-axed irrespective of synthesis method; A and D had nearly the same grain size, whereas E had a slightly smaller grain size and had many pores in the grains and between the grains. The glassy phase was not found at the mullite grain boundary under the condition of TEM observation in this experiment (**Fig.7**). For E, as described above, corundum together with mullite was identified even when in fired synthesized powder compact was fired at 1650°C for 4h. However, as shown in **Fig.8**, calcination and grinding made corundum disappear in terms of X-rays by firing at 1650°C for 30 minutes or over.

However, it was thought that variations in composition between mullite grains occur even after firing at 1650°C for 4h because corundum was identified up to 1650°C for 30 minutes for E. Therefore, the chemical composition of sintered body prepared by using powders A and E was analyzed by the energy dispersive X-ray spectroscopy(EDS) to TEM.

The analysis was performed at nearly central position of each grain for 30 grains each. It is said that for the secondary X-rays from the thin-film specimen, unlike the bulk specimen, the spread in the specimen can be neglected. In

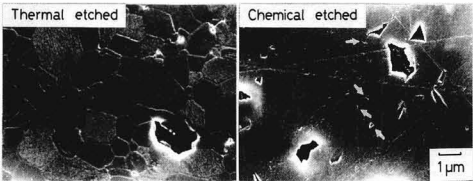


Fig. 3. Scanning electron micrographs of the E specimen calcinated at 1650°C for 4h.

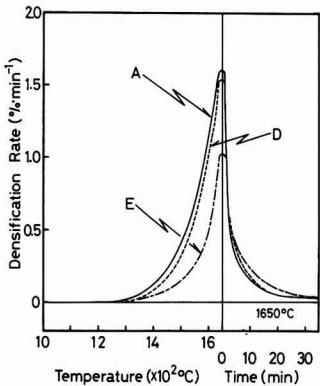


Fig. 5. Temperature dependence of shrinking rate of the A, D and E specimens. Heating rate: 10°C/min.

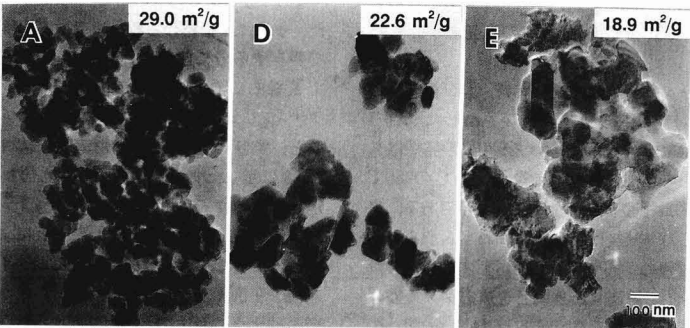


Fig. 4. Transmission electron micrographs and specific surface area of the calcinated and ground powders.

this experiment, therefore, the composition of mullite grain was calculated from the equation of Cliff et al.¹³⁾ **Figure 9** shows the distribution of alumina content in mullite grains in A and E specimens. The alumina contents in mullite grains in both A and E specimens show nearly the same composition distribution with the composition value of bulk

of about 74wt% of the center. This result shows that the influence of microstructural inhomogeneity of synthesized powder on the composition of solid solution is small under the condition that mullitization finishes completely. These results have revealed that for the mullite solid solution powder in the range of the condition of this experiment, the microstructural inhomogeneity of composition in the starting powder due to the synthesis method has an effect on the sinterability, but has little effect on the shape and constitutional phase of mullite grain in sintered body.

For powder E, which is an oxide mixture, however, the constitutional phase of sintered body differs depending on the presence of calcination, and the sinterability are inferior

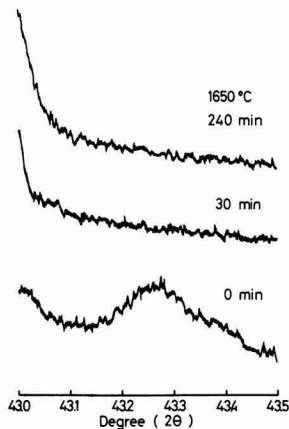


Fig. 8. X-ray diffraction patterns for the E specimen after calcinating at 1450°C and ground for 50h.

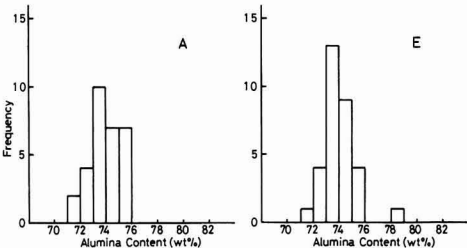


Fig. 9. Distribution of alumina content in mullite grains in the A and E specimens represented by histograms of frequency.

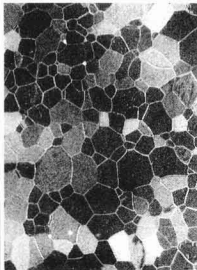
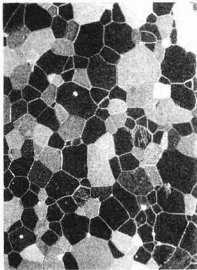
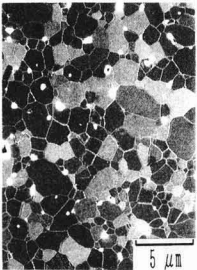
	A	D	E
			
Density (g/cm ³)	3.15	3.14	3.09

Fig. 6. Scanning electron micrographs and bulk density of the A, D and E specimens sintered at 1650°C for 4h.

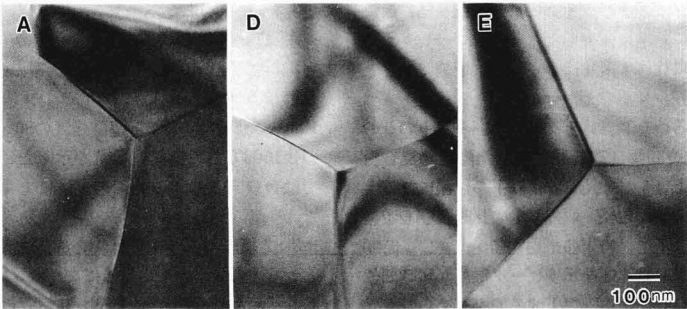


Fig. 7. Transmission electron micrographs of the A, D and E specimens sintered at 1650°C for 4h.

to that of other power. Next, we will consider the cause for this phenomenon.

Figure 10 shows the change in peak intensity of corundum and cristobalite for the oxide mixture powder calcined at 1500°C for 1-72h. The peak intensity was measured by X-ray diffraction. The peak intensity of cristobalite suddenly decreased with the calcination time. That of corundum also decreased, though slightly as compared with that of cristobalite.

Therefore, the oxide mixture powders calcined at 1500°C for 1h and 72h with different quantity of corundum and cristobalite remaining were ground and classified into 1 μ m or less diameter, and the average particle diameter of powder was measured and the shrinkage behavior was evaluated. The bulk density after measurement is shown in **Fig.11**. It was found that the peak temperature showing the maximum shrinking rate shifts slightly to the low temperature side for the specimen calcined for long time and having larger average particle diameter as compared with the specimen calcined for a short time. As shown in the figure, the bulk density after holding for 4h at 1650°C is higher for the specimen calcined for long time, being 3.12g/cm³. This means the specimen was densified to the degree of powders A and D described earlier. It is generally known that the presence of the liquid phase and the second phase particles produced in sintering affect the sinterability and that the

presence of liquid phase enhances the sinterability, while the presence of second phase particle against solid phase sintering inhibits the sintering.^{2,4-6)}

If cristobalite or corundum is present in sintering of mullite, cristobalite melts together with mullite as described above and produces liquid phase, which promotes densification. As shown in Fig.10, both cristobalite and corundum remain in the calcined powder in larger amounts when the powder is calcined for short time, but the density after sintering is higher when the powder is calcined for a long time. This indicates that the effect of corundum inhibiting densification is larger than the effect of cristobalite promoting densification.

It is therefore thought that the difference in sinterability between powders A, D and powder E depended on the quantity of corundum remaining after calcination. From the fact that the use of powder calcined for long time produced high-density sintered body, it was suggested that if fine powder was obtained by the full mullitization of oxide mixture by firing, excellent sinterability could be obtained as with the other synthesis method.

3.3. Mechanical Properties

Figure 12 shows the relationship between the flexural strength and the temperature in the range from room temperature to 1500°C for A, D, and E specimens. For the strength at room temperature, a small difference with the synthesis method was found. For all specimens, the strength decreased to about 220MPa, 50% of the strength at room temperature, at 1300°C, and was kept at that value up to 1500°C. Therefore, almost no difference with the synthesis method was found at high temperatures.

For the mullite of 3:2 composition, it was suggested that the quantity of glassy phase formed at the grain boundary due to inhomogeneous distribution of alumina and silica caused by the synthesis method differed and that the specimen having inhomogeneous distribution was vulnerable to time-dependent fracture, for example, having poor creep resistance.¹⁰⁾ For mullite solid solution containing 74wt% alumina, all of A, D and E specimens fractured without plastic deformation in the flexural test at 1500°C, and no difference was found on the stress-strain curve even when the loading rate was reduced from 0.5mm/min to 0.01mm/min at high temperatures.

From these results, the strength at room temperature

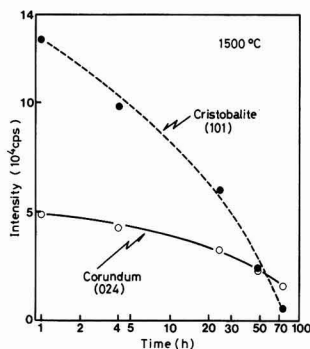


Fig. 10. Variation of peak intensities of cristobalite and corundum against calcination time at 1500°C.

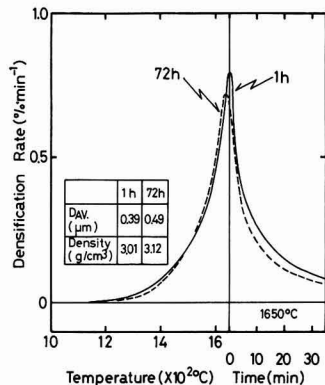


Fig. 11. Temperature dependence of shrinking rate of the specimens calcinated for 1 and 72h.

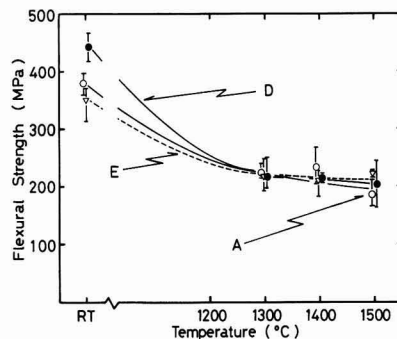


Fig. 12. Temperature dependence of the flexural strength of specimens.

probably differed slightly depending on the synthesis method because the homogeneity of powder affected the density of sintered body and the particle diameter of mullite powder. It is, however, thought that the effect of synthesis method on strength at high temperatures did not appear because of single phase of mullite in the process of sintering as shown in Figs. 7 and 8.

4. Conclusions

The influence of powder characteristics on sinterability and mechanical properties for mullite single-phase ceramics with 74wt% Al_2O_3 composition synthesized by using the powder prepared by hydrolyzing mixed alkoxide with distilled water (A), the powder hydrolyzed with ammonia water (B), the powder prepared by coprecipitating aluminum nitrate with ammonia water (C), the powder in which gel obtained by hydrolyzing alkoxide alone with ammonia water was added (D), and the powder in which oxide was mixed (E). The conclusions were as follows:

- 1) The mullitization temperature of synthesized powder was higher in the order of A; when powder E in which oxide was mixed was heated at 1650°C for 4h, corundum remained and mullitization was not completed. However, it was found that the sintered body with no remaining corundum and silica (glassy phase) was obtained by holding 30 minutes and over at 1650°C when powder E was calcined at a temperature below the eutectic point and ground.
- 2) When powders A, D and E having nearly the same composition were fired at 1650°C for 4h after being calcined and ground, the bulk density was higher in the order of $E < A = D$. This difference is caused by the fact that remaining unreacted corundum hinders the densification for the powder having poorer homogeneity.
- 3) The strength at high temperatures had nearly the same tendency irrespective of the synthesis method. It was therefore found that when mullite single-phase sintered body was obtained, the effect of the synthesis method of

material powder on the strength was small.

Acknowledgements

We wish to thank Mr. S. Mitachi at the Central Research Laboratory of Hokko Chemical Industry Co., Ltd. for supplying starting powders used in this experiment and Mr. Y. Ohashi at the Government Industrial Research Institute, Nagoya, for his cooperation in the analysis using an electron microscope.

References:

- 1) S. Kanzaki, H. Tabata, T. Kumazawa and S. Ohta, *J. Am. Ceram. Soc.*, 68, C6-7 (1985).
- 2) K.S. Mazdiyasi and L.M. Brown, *ibid.*, 55, 548-552 (1972).
- 3) B.R. Ghate, D.P.H. Hasselman and R.M. Spiggs, *Am. Ceram. Soc. Bull.*, 52, 670-672 (1973).
- 4) W.D. Sacks and J.A. Pask, *J. Am. Ceram. Soc.*, 65, 65-77 (1982).
- 5) Y. Hirata, K. Sakai, Y. Matsushita, and K. Shimada, *Yogyo kyokai shi*, 93, 577-580 (1985).
- 6) K. Okada and N. Otsuka, *J. Am. Ceram. Soc.*, 69, 652-656 (1986).
- 7) A.K. Chakravorty and D.K. Ghosh, *ibid.*, 71, 978-987 (1988).
- 8) K. Hamano, T. Sato, and Z. Nakagawa, *Yogyo kyokai shi*, 94, 818-822 (1986).
- 9) S. Mitati, N. Kaneko and S. Kanzaki, *Ceramic Transactions*, Vol.6, *Am. Ceram. Soc.* (1990) 275-228.
- 10) T. Kumazawa, S. Ohta, S. Kanzaki and H. Tabata, *ibid.*, Vol.6, *Am. Ceram. Soc.* (1990) 339-351.
- 11) I.A. Aksay and J.A. Pask, *J. Am. Ceram. Soc.*, 58, 507-512 (1975).
- 12) T. Kumazawa, S. Kanzaki, J. Asami, O. Abe and H. Tabata, *Yogyo Kyokai shi*, 94, 485-490 (1986).
- 13) G. Cliff and G.W. Lorimer, *J. Micros.*, 103, 203-205 (1975).
- 14) W.D. Kingery, H.K. Bowen, D.R. Uhlmann, *Introduction to Ceramics*, 2nd Ed., John Wiley & Son, New York (1975) 490-501.
- 15) C. Hsueh, A.G. Evans and R.W. McMeeking, *J. Am. Ceram. Soc.*, 69, C64-66 (1985).
- 16) G.W. Scherer, *ibid.*, 70, 719-725 (1987).

This article is a full translation of the article which appeared in *Nippon Seramikkusu Kyokai Gakujutsu Ronbunshi* (Japanese version), Vol.99, No.12, 1991.

Stability of Metastable Tetragonal Zirconia

Hirohiko Murakami and Hideo Ohno*

Planning Division, Ulvac Corporation

1-11-2, Kyobashi, Chuo-ku, Tokyo, 104 Japan

*Material Innovation Laboratory, Japan, Atomic Energy Research Institute,
Tokai-mura, Naka-gun, Ibaraki, 319-11 Japan

This research was undertaken to determine the reason for the occurrence of metastable tetragonal zirconia (ZrO_2). Metastable tetragonal ZrO_2 was prepared by low temperature calcination of zirconium oxychloride octahydrate $\text{ZrOCl}_2 \cdot 8\text{H}_2\text{O}$. The tetragonal-to-monoclinic (t-m) transformation in pure metastable tetragonal ZrO_2 powder was investigated with special reference to the isothermal annealing temperature, the variation of crystallite size and the annealing environment. The results indicate that the metastable tetragonal ZrO_2 is stabilized thermodynamically by surface free energy and there is a so-called "critical diameter (crystallite size)". Moreover, thermodynamic calculation showed that the t-m transformation temperature depends on the critical crystallite size.

[Received July 1, 1991; Accepted September 19, 1991]

Key-words: Metastable tetragonal zirconia, Phase transformation, Surface free energy, Thermodynamic stabilization.

1. Introduction

Since the paper titled "Ceramic Steel" was presented by Gavie et al.¹⁾ in 1975, the mechanical properties of partially stable zirconia have been studied, and the fact that the tetragonal-to-monoclinic (t-m) transformation is a stress-induced martensitic transformation that absorbs the fracture energy has been revealed. The study on the stabilization mechanism of zirconia is practically important, and many reports have been published. In these reports on zirconia, the formation of metastable tetragonal zirconia has been observed in the temperature range below the t-m transition temperature of pure zirconia.

Regarding the cause for the formation of metastable tetragonal zirconia, there are, broadly speaking, two views: the thermodynamic stabilization and dynamic formation. The former view can explain the experimental results quantitatively, but cannot satisfactorily explain all transformations. The latter view, on the other hand, cannot explain the experimental results quantitatively, but can satisfactorily explain various reported phenomena; however the phenomenon where no transformation occurs in vacuum annealing, which cannot be explained by only the view of dynamic formation, has been reported.²⁾ In a previous report,³⁾ we pointed out that the activation energy of this transformation is close to the activation energy of oxygen diffusion in zirconia and suggested that oxygen is an important factor for transformation.

In the present work, we (1) evaluated the two views on the formation of metastable tetragonal zirconia that have

been reported, and (2) investigated the effect of crystallite size, time, temperature, and environment on the transformation of pure zirconia to clarify the effect of oxygen on transformation.

2. Experimental Method

2.1. Preparation of Sample and Evaluation Method

The sample used in this experiment was metastable tetragonal zirconia prepared by pyrolytically decomposing commercially available zirconium oxychloride octahydrate $\text{ZrOCl}_2 \cdot 8\text{H}_2\text{O}$ in an oxygen atmosphere at 450°C for 14 hours and 45 minutes. The experiments were performed in the air and under vacuum. The transformation was traced by the high-temperature X-ray diffraction method as a function of temperature and time. In the X-ray measurement, a specified temperature was kept constant for about 1 minute in continuous heating and cooling.

For the determination of monoclinic zirconia produced by transformation, the molar fraction (f_M) of monoclinic zirconia was calculated by using the following equation:

$$f_M = \frac{I_M(111) + I_M(1\bar{1}\bar{1})}{I_M(111) + I_M(1\bar{1}\bar{1}) + I_T(111)} \quad \dots \dots (1)$$

where, I is the integrated intensity and the suffixes M and T denote monoclinic and tetragonal phases, respectively. The determination of tetragonal ZrO_2 was performed by using the relation of $f_T = 1 - f_M$.

The average crystallite size was calculated by using the following Sherrer's equation from the half value width of (111) diffraction of each phase.

$$D = 0.9\lambda / (\beta \cos \theta) \quad \dots \dots \dots (2)$$

where

- D : average crystallite size
- λ : $\text{CuK}\alpha = 0.15418 \text{ nm}$
- θ : angle of diffraction
- β : width of diffraction line

2.2. Isothermal Transformation Experiment

Regarding the experiment on transformation from metastable tetragonal ZrO_2 to stable monoclinic ZrO_2 by isothermal heating of pure zirconia, some reports, including Whitney's report⁴⁾ some time ago, have confirmed transformation at low temperatures of 500-600°C and for several hours. In our previous report³⁾, several dozen to several hundred hours were required for the completion of transformation at 650-750°C. This difference in experimental results may be ascribed to the fact that the X-ray diffraction method was used for tracing transformation in the former experiment, while the neutron diffraction method was used

in the latter. The result obtained by Whitney shows the information about the phenomena for the surface, while our result shows the information about the entire crystal. Therefore, it seems that an apparent difference in transformation rate was produced. Alternatively, this difference may be caused by the zirconia sample itself (for example, crystallite size or impurities) and not by the measuring method.

In this work, therefore, we observed the isothermal transformation at various temperatures by using the high-temperature X-ray diffractometer (the condition of meter was made equal to that of Whitney) and zirconia sample prepared by the same method as that in the previous report to clarify the difference between the two experimental results.

The outline of the view of thermodynamic stabilization is that since the tetragonal ZrO_2 has lower surface energy than the monoclinic ZrO_2 , the contribution of this surface energy compensates the energy of bulk and stabilizes the tetragonal ZrO_2 when the diameter of particle is below a certain critical value.

Therefore, in this work the following three experiments were performed to investigate the relationship between the transformation of zirconia and the crystallite size.

2.3. Transformation Experiment in Cooling

This experiment was intended to investigate the qualitative relationship between grain growth and transformation. In the experiment, the transformation in cooling was observed with the heating and cooling rate being set at $10^\circ\text{C}/\text{min}$ and $50^\circ\text{C}/\text{min}$, respectively and with the maximum attained temperature changing from 800°C to 850°C to 900°C . The grain growth was controlled by the change of the maximum attained temperature.

2.4. Experiment for Measuring Crystallite Size

This experiment was intended to investigate the actual relationship between transformation and crystallite size. In this experiment, the state of transformation in the entire course of heat treatment was investigated, and the crystallite size of monoclinic and tetragonal ZrO_2 at each temperature was measured with the heating and cooling rate being set at $10^\circ\text{C}/\text{min}$ and $50^\circ\text{C}/\text{min}$ respectively and with the maximum attained temperature being set at 900°C .

2.5. Transformation Experiment Under Vacuum

Regarding the oxygen effect on transformation, a report

presented by Kuroda et al.²⁾ discussing that "no transformation occurs in vacuum annealing; the oxygen in gas phase gives a change of transformation", and our previous report³⁾ discussing that "it is suggested that the activation energy of transformation is close to the activation energy of oxygen diffusion in zirconia; oxygen is an important factor for transformation." In this work, therefore, the following two experiments were performed to confirm that no transformation occurs under vacuum and to clarify the oxygen effect.

To confirm that no transformation occurs under vacuum, (1) transformation was observed by evacuating with an oil-sealed rotary vacuum pump throughout the test with the heating and cooling rate being set at $10^\circ\text{C}/\text{min}$ and $50^\circ\text{C}/\text{min}$, respectively.

To investigate the effect of atmosphere on crystalline grain growth, (2) the sample was heated in the air up to 600°C at a rate of $50^\circ\text{C}/\text{min}$ and then from 600°C to 850°C at a rate of $10^\circ\text{C}/\text{min}$. After 850°C was reached, the air was exhausted with an oil-sealed rotary vacuum pump. After evacuation, transformation was observed by cooling the sample at a rate of $10^\circ\text{C}/\text{min}$.

3. Experimental Results

3.1. Isothermal Transformation

Figure 1 shows the results of the isothermal transformation experiment. At temperatures below 650°C , which were reported by Whitney, transformation was hardly observed, and transformation proceeded at the temperature and time nearly the same as those reported by Ohno et al. This suggests that a rapid transformation reported by Whitney is not ascribed to the difference in measuring method as described in 2.2 but to the sample itself used in the experiment.

3.2. Effect of Crystallite Size on Transformation

3.2.1. Transformation in Cooling

Figure 2 shows the relationship between the proportion of tetragonal ZrO_2 and temperature in cooling after the sample was heated to a specified temperature. The Max. Temp. in the figure denotes the maximum attained temperature for each sample. The molar fraction in this figure was indicated by converting the molar fraction at the maximum attained

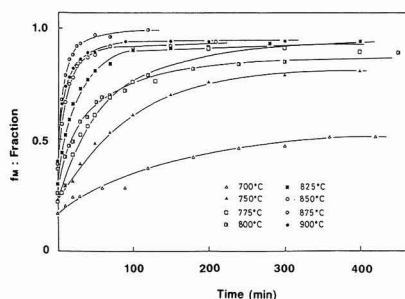


Fig. 1. Conversion of tetragonal ZrO_2 to monoclinic ZrO_2 as a function of time at different temperatures.

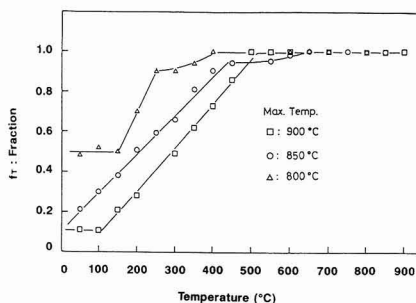


Fig. 2. Conversion of tetragonal ZrO_2 to monoclinic ZrO_2 with cooling.

temperature into 100% to eliminate the effect of transformation in heating. The result of Fig.2 showed various interesting facts which seem to apparently be in conflict with the result of the isothermal transformation experiment in 3.1.

- 1) No transformation occurred at high temperatures above 600°C.
- 2) Transformation occurred at low temperatures below 600°C despite of holding for a short time of about 1 minute necessary for measurement.
- 3) When the sample was heated to the maximum temperature of 900°C and 850°C, the tetragonal system hardly remained. When the sample was heated only to 800°C, about 50% of tetragonal system remained.
- 4) The molar fraction of tetragonal system decreased in approximate proportion to the decrease in temperature at temperatures below 600°C.

3.2.2. Change in Crystallite Size

Figure 3 shows the changes in intensity of tetragonal system and the crystallite size as a function of temperature for the sample heated to 900°C. The intensity of tetragonal ZrO_2 (●) decreased with the increase in temperature up to 900°C, and in the cooling process, it was almost unchanged down to 600°C and decreased again at temperatures below 600°C as indicated by (1) and (2) in 3.2.1. We emphasize that of prime importance is not the transformation in heating, but that at temperatures below 600°C indicated by (1) and (2) in 3.2.1. The crystallite size of tetragonal ZrO_2 (▲) was about 140Å at the starting material, and increased with the increase in temperature, reaching the maximum value of about 320Å. In the high temperature range where no transformation occurred in cooling, the crystallite size was unchanged, and in the temperature range below 600°C where transformation occurred, the crystallite size decreased again with the decrease in temperature.

Next, the result of monoclinic ZrO_2 will be described. Since this phase is produced by transformation, the intensity (○) changes in contrast to that of tetragonal ZrO_2 . Regarding the change in crystallite size (△), it should be noted that the size is several dozen angstroms larger than that of tetragonal ZrO_2 in any temperature range.

3.2.3. Transformation Under Vacuum

Figure 4 shows the result of transformation measurement

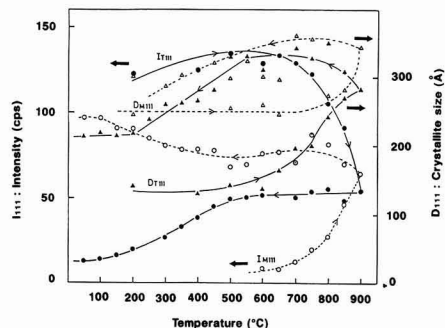


Fig. 3. Changes in intensity and crystallite size as a function of temperature.

made under vacuum in the heating and cooling processes (experiment (1); ○ and △) and the result of transformation measurement made in the air in the heating process and under vacuum in the cooling process (experiment (2); ●). As the result of experiment (1) (○ and △), no transformation occurred ($f_T=1$) when air was exhausted with an oil-sealed rotary vacuum pump throughout the heating and cooling processes. In this experiment, unlike the experiment in 3.2.2, the crystallite size did not increase, and the crystallite size of tetragonal ZrO_2 (D_{T111}) was nearly constant. It should be noted that the crystallite size was as small as 150Å or less. For the result of experiment (2) (the sample grain was grown in the air in heating), like the experiment in 3.2.1, almost complete transformation occurred despite of the vacuum atmosphere in cooling.

4. Discussion

4.1. Outline of Conventional View of Stabilization

The cause for formation of metastable tetragonal ZrO_2 has so far been explained by two views: thermodynamic stabilization and dynamic formation. The former view was proposed by Gavie^{5,6)} (non-restraint system) and has expanded to the restraint system by Lange.⁷⁾ The outline of this view is that the tetragonal ZrO_2 becomes more stable thermodynamically than the monoclinic ZrO_2 by the contribution of surface energy or strain energy; as a result, the tetragonal ZrO_2 is produced. Taking the free energy of monoclinic and tetragonal ZrO_2 as G_m and G_t , respectively, (suffixes m and t denote monoclinic and tetragonal phases), the difference in free energy accompanying transformation is expressed by the following equation:

$$\begin{aligned} G_{t \rightarrow m} &= G_m - G_t \\ &= G_m^c + U_m + V_m - (G_t^c + U_t + V_t) \\ &= G_m^c + S_m \gamma_m + V_m - (G_t^c + S_t \gamma_t + V_t) \end{aligned} \quad (3)$$

where

- G^c : chemical free energy
- U : surface free energy
- V : strain energy
- S : specific surface area per gram
- γ : surface energy per unit surface area

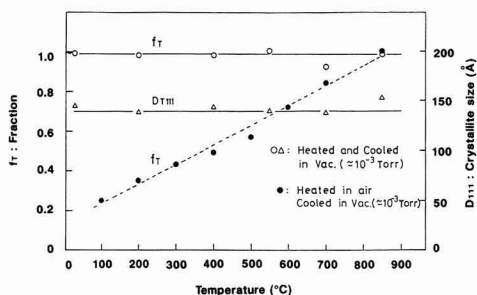


Fig. 4. Conversion of tetragonal ZrO_2 to monoclinic ZrO_2 heated in air and in vacuum.

Since the chemical free energy is $G_m^c < G_t^c$ in order to produce metastable tetragonal ZrO_2 , it is thought that $G_m > G_t$ holds due to the contribution of surface free energy and strain energy.

To hold this relation, the surface area must be sufficiently large, that is, the particle diameter must be sufficiently small and the condition of $\gamma_m > \gamma_t$ must be satisfied. This view of stabilization has been used by Murase⁸⁾ and Bailey et al.⁹⁾ To explain their experimental results. There are some reports in conflict with this view. The reason for the contradiction is that the critical particle diameter (the maximum particle diameter required to keep the metastable tetragonal ZrO_2 , meaning that the value of $G_{t \rightarrow m}$ becomes 0 in eq.(3)) was taken as 300Å. If this value of critical particle diameter proposed by Garvie is adopted, taking the value of $G_{t \rightarrow m}$ as 1130cal/mol at 300K, the value of γ_m should be about 1800 erg/cm² for the surface free energy to compensate the value. This value of about 1800 erg/cm² is too high considering the value of γ_t of 770 erg/cm². Considering that the surface free energy of oxide ceramics is usually about 1000erg/cm², a difference of about 100erg/cm² is unlikely produced by the difference in crystalline form.

In the view of dynamic formation, although the energy level of crystalline phase is in the order of amorphous tetragonal monoclinic, there is an energy barrier between transitions, and therefore amorphous and tetragonal ZrO_2 can exist as a metastable phase if sufficient activation energy is given. Accordingly, it is predicted that the tetragonal ZrO_2 is formed only from amorphous state, and this fact has actually been confirmed by several experimental results.¹⁰⁻¹²⁾ This view, however, has a disadvantage in that it cannot deal with problems quantitatively, though the view of thermodynamic stabilization can.

4.2. View of Thermodynamic Stabilization Viewed from the Result of This Study

The result of the isothermal transformation experiment (Section 3.1) indicated, as described in the section of experimental results, that the transformation rate depends largely on the sample used by the experimenter, not on the measuring method. The reason for this may be the existence of critical particle diameter described in the conventional view of thermodynamic stabilization. This fact will be clarified by the discussion of experimental results of 3.2.1-3.2.3.

To satisfy all results (1) through (4) of the transformation experiment in cooling (4.3.1), the existence of critical particle diameter is assumed, and additionally it should be assumed that the stable region of tetragonal ZrO_2 expands more to the low temperature as the crystallite size is small. These phase regions are shown in Fig.5. The results (1) through (4) will be discussed below by referring to this figure. The tetragonal ZrO_2 in which grain growth has occurred in heating and the crystallite size has increased (for example, about 250Å) lies in the stable region of tetragonal phase at high temperatures (above 600°C in this experiment). When the tetragonal ZrO_2 having grown grains is cooled, it enters the stable region of monoclinic phase at low temperatures, resulting in occurrence of transformation. Considered in this way, the crystallite size becomes larger at the maximum attained temperature of 850°C than that of 800°C, or at 900°C than 850°C; the transformation start temperature shifts to the high temperature side, and the fact that the quench amount is less can be explained. The result that the transformation does not occur in the high tempera-

ture region but does in the low temperature region cannot be explained only in terms of the activation energy of the view of dynamic formation.

In results (1) and (2) of crystallite size measurement experiment (3.2.2), the decrease in crystallite size at a temperature below 600°C at which transformation in cooling occurs suggests the expansion to the low temperature side due to the decrease in crystallite size in the stable region of tetragonal phase assumed earlier. With the decrease in temperature, the crystallite size that can stabilize the tetragonal ZrO_2 decreases. Therefore, the tetragonal ZrO_2 having greatly grown grains becomes unstable in the cooling process, and transforms into monoclinic phase. As a result, the tetragonal ZrO_2 of large crystallite size becomes monoclinic phase. Since the tetragonal ZrO_2 of small crystallite size is stable even at low temperatures, the crystallite size of tetragonal ZrO_2 being measured decreases due to the transformation. From the results of transformation experiment (3.2.3), it is suggested that the cause for no transformation under vacuum is not oxygen but the fact that the grain growth was inhibited under vacuum. The inhibition of grain growth due to vacuum annealing may be ascribed to the appearance of nonstoichiometry of zirconia. This result cannot also be explained in terms of the activation energy of the view of dynamic formation.

From the above discussion, it is supposed that the critical particle diameter proposed by Garvie exists, and that the diameter depends heavily on temperature. It is also revealed that the result of transformation experiment in cooling in which transformation occurred at a low temperature and the result of transformation experiment under vacuum in which no transformation occurs under vacuum cannot be explained in terms of the activation energy of transformation based on the view of dynamic formation. In the present study, however, there is no reason for denying the view of dynamic formation. We emphasize that the existence of critical particle diameter in the view of thermodynamic stabilization was suggested. It should also be noted that the two views do not conflict with each other. In the crystallization from the amorphous phase, the amorphous, tetragonal, and monoclinic ZrO_2 are probably formed in that order on the basis of the view of dynamic formation. Needless to

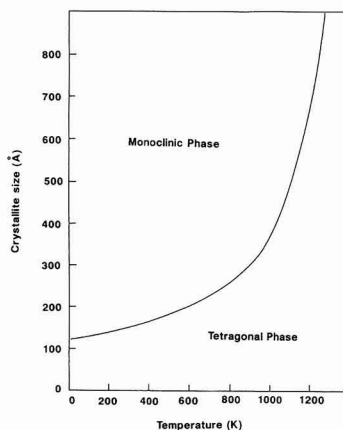


Fig. 5. Phase regions defined by $\Delta G_{t \rightarrow m} = 0$ as a function of crystallite size against temperature.

say, the tetragonal ZrO_2 below the critical particle diameter is formed irrespective of the applied energy. The view of dynamic formation has been known as Ostwald's Step Rule; unless sufficient activation energy is given, the amorphous and tetragonal ZrO_2 may exist in the metastable phase. Therefore as a contradiction of the view of thermodynamic stabilization, the tetragonal ZrO_2 of above the critical particle diameter is formed. However, thermodynamic stability is dominant for the tetragonal ZrO_2 once produced. If the crystallite size is small (about 150\AA), no transformation occurs even when activation energy is given (vacuum annealing experiment). If the crystallite size is large, transformation occurs irrespective of the applied activation energy (in the transformation experiment in cooling, stability is kept in the high temperature region, and transformation occurs in the low temperature range).

4.3. Determination of Stable Region of Metastable Tetragonal Zirconia

In this section, the stable region of metastable tetragonal zirconia is determined by considering the mechanism of its thermodynamic formation. The free energies of monoclinic and tetragonal ZrO_2 are taken as G_m and G_t , respectively. For free energy, chemical free energy is usually considered, but the terms of surface energy and strain energy are introduced in addition to chemical free energy in the equation. The difference in free energy accompanying transformation (4.1) is expressed as eq.(3). Assuming that the crystallite is spherical,

$$S=6/\rho D \quad \dots \dots \dots (4)$$

where

ρ : density

D : diameter of crystallite

Substituting eq.(4) into eq.(3),

$$G_{t \rightarrow m} = G_m^c + \frac{6\gamma_m}{\rho_m D} + V_m - \left(G_t^c + \frac{6\gamma_t}{\rho_t D} + V_t \right) \quad \dots \dots \dots (5)$$

Taking the critical particle diameter in which the monoclinic and tetragonal ZrO_2 has thermodynamically equal stability as D_c , because $G_{t \rightarrow m}=0$,

$$D_c = \frac{6}{[(G_t^c - G_m^c) + (V_t - V_m)]} \cdot (\gamma_m/\rho_m - \gamma_t/\rho_t) \quad \dots \dots \dots (6)$$

The values of strain energy (V_t , V_m) may be negligibly low, considering the tetragonal zirconia used in this experiment is powder. Therefore, eq.(6) can be approximated as follows:

$$D_c = \frac{6}{(G_t^c - G_m^c)} \cdot (\gamma_m/\rho_m - \gamma_t/\rho_t) \quad \dots \dots \dots (7)$$

Next, the values of parameters substituted into eq.(7) must be estimated. The particle diameter D_c for which the tetragonal ZrO_2 exists without the occurrence of transformation in Figs.3 and 4 may be taken as about 150\AA . The value of $G_t^c - G_m^c$ at 300K can be calculated by assuming that the transition heat and entropy do not depend on temperature. At a transition temperature $T=1478\text{K}$, the relation $\Delta G=0$ holds since the formation free energy is equal for monoclinic and tetragonal ZrO_2 .

$$\Delta G = \Delta H - T\Delta S \quad \dots \dots \dots (8)$$

Substituting $\Delta G=0$, $\Delta H=1420$ cal/mol, and $T=1478\text{K}$ into eq.(8),

$$\Delta S = 0.96 \text{ cal/deg-mol} \quad \dots \dots \dots (9)$$

Therefore, the value of $(G_t^c - G_m^c)$ at 300K is 1132 cal/mol. Substituting $\gamma_t=770\text{erg/cm}^2$, $\rho_t=6.10\text{g/cm}^3$, and $\rho_m=5.56\text{g/cm}^3$ into eq.(7), we obtain $\gamma_m=1236\text{erg/cm}^2$. This value is proper, considering other oxides MgO and UO_2 have values of 1040 and 1030erg/cm^2 , respectively.

Next, we wish to determine the critical particle diameter D_c at each temperature. In this case, the temperature dependence of γ must be found newly. The surface free energy at temperature T is expressed as

$$\gamma = \gamma_0 - T S_s \quad \dots \dots \dots (10)$$

Assuming that γ_0 and S_s (surface entropy) do not depend on temperature, differentiation of eq.(10) by temperature T gives

$$\frac{d\gamma}{dT} = -S_s \quad \dots \dots \dots (11)$$

However, since a reliable value of S_s is unknown for solids either theoretically or experimentally, a proper value should be assumed. Usually, a value of about 0.7 is used for MO_2 oxide, and for zirconia, a value of 0.1 is also used.¹³⁾ Therefore, this value is used in this study and eq.(12) is assumed.

$$\frac{d\gamma}{dT} = -0.1 \text{ erg/deg} \cdot \text{cm}^2 \quad \dots \dots \dots (12)$$

From eq.(12), $\gamma_m=1236-0.1(T-300)$, $\gamma_t=770-0.1(T-300)$ can be obtained. Substituting these values into eq.(7), Fig.5 can be obtained by expressing D_c as a parameter of temperature. Comparing Fig.5 derived theoretically and the experimental result (Fig.3), the following points of agreement and difference are found. In Fig.3, the crystallite size of tetragonal ZrO_2 increases up to about 320\AA at about 900°C in the heating process, and the decrease in crystallite size is observed below 600°C . This fact is in good agreement with the fact that the boundary between tetragonal and monoclinic phases is about 300\AA at about 600°C in Fig.5. On the other hand, the crystallite size of tetragonal ZrO_2 cooled to room temperature is about 200\AA , but this crystallite size lies in the stable region of monoclinic ZrO_2 . This difference may be caused by the fact that the low temperature decreases the driving force of transformation, so the tetragonal ZrO_2 remains as a metastable phase even if the grains of tetragonal ZrO_2 grows to an unstable size. In the future, to more accurately express the diagram of Fig.5, it is probably necessary to perform the measurement of crystallite size in the isothermal transformation at various temperatures and the SEM observation in the high-temperature transformation.

5. Conclusions

This report summarized the study to determine the reason for the occurrence of metastable tetragonal ZrO_2 that has been receiving attention as functional ceramics and to determine the stable region of tetragonal ZrO_2 .

Noticing that when pure zirconia is prepared by the liquid phase method, metastable tetragonal ZrO_2 is often formed

without stabilizing agent, the cause was thought to be the surface free energy of fine particles. From this viewpoint, the transformation mechanism of pure zirconia was clarified by measuring the transformation of pure zirconia and the crystallite size. Also, it was found that the reason why the transformation is inhibited under vacuum is because the grain growth is inhibited under vacuum.

The conclusions from this study are as follows:

- 1) For the isothermal transformation of pure zirconia, there is no appreciable difference in transformation rate between the measuring methods, namely, between the neutron diffraction method and the X-ray diffraction method.
- 2) To investigate the effect of crystallite size on transformation, the transformation in the cooling process was measured. As a result, the phenomenon where no transformation occurs in the high temperature region and transformation occurs in the low temperature region, which cannot be explained by the view of dynamic formation (view of activation energy), was confirmed, and the existence of critical particle diameter, which is used in the view of thermodynamic stabilization, was suggested. This result showed that the critical particle diameter increases with the increase in temperature.
- 3) As reported by Kuroda et al., the fact that no transformation occurs under vacuum was confirmed for pure zirconia as well. However, the increase in zirconia crystallite size was not found even in high-temperature annealing under vacuum. It was confirmed that the factor directly governing the transformation is not the atmosphere but the crystallite size. This result, like the result of (2), cannot be explained by the view of dynamic formation, and strongly supports the existence of critical particle

diameter.

- 4) From the thermodynamic calculation, the stable region of tetragonal ZrO_2 was defined as a function of crystallite size against temperature.

References:

- 1) R.C. Garvie, R.H.J. Hannink and R.T. Pascoe, *Nature* 258, 703-704 (1975).
- 2) a) K. Kuroda, H. Saka, S. Iio, M. Watanabe and T. Imura, *Proc. Int. Conf. Martensitic Transformations* (1986) 1161.
b) K. Kuroda, K. Saka, T. Imura, S. Iio and S. Watanabe, *Proc. Fall Mtg. Sympo. Jpn. Inst. Metals* (1985) 97, 105.
- 3) H. Ohno, Y. Morii, H. Murakami, T. Nagasaki, H. Katsuta, M. Izumi, H.R. Child and R.M. Nicklow, *JAERI-M* 87-166, 60-78 (1987).
- 4) E.D. Whitney, *Trans. Faraday Soc.* 61, 1981-2000 (1965).
- 5) R.C. Garvie, *J. Phys. Chem.* 69, 1238-1243 (1965).
- 6) R.C. Garvie, *ibid.*, 82, 218-224 (1978).
- 7) F.F. Lange, *J. Mater. Sci.* 17, 225-234 (1982).
- 8) Y. Murase and E. Kato, *J. Chem. Soc. Jpn.* 3, 425-430 (1976).
- 9) J.E. Bailey, D. Lewis, Z.M. Librant and L.J. Porter, *J. Br. Ceram. Soc.* 71, 25-30 (1972).
- 10) A. Clearfield, *Inorg. Chem.* 3, 146-148 (1964).
- 11) K.S. Mazdhyasni, C.T. Lynch and J.S. Smith, *J. Am. Ceram. Soc.* 49, 286-287 (1966).
- 12) M. Yoshimura and S. Somiya, *Jirukonia Seramikkusu, Uchida Rokakuho* (1983) 45-60.
- 13) D.T. Livey and P. Murray, *J. Am. Ceram. Soc.* 39, 363-372 (1956).

This article appeared in English in *Nippon Seramikkusu Kyokai Gakujutsu Ronbunshi* (Japanese version), Vol.99, No.12, 1991.

Micro-Shirasuballoons (Hollow Glass Microspheres) from the Milled Shirasu Refined by Hydrothermal Treatment

Kunio Kimura, Kazuhiko Jinnai and Hiroshi Tateyama

Government Industrial Research Institute, Kyushu,
Shuku-machi, Tosu-shi, 841 Japan

The hollow glass microspheres named "Shirasuballoons" can be produced from Shirasu, a kind of acidic volcanic ejecta. Weathered surface layers of the Shirasu particles have several good properties, keeping the shape of the Shirasuballoons and preventing sticking each other during heat treatment. However, they can not be produced from the particles milled under $10\mu\text{m}$, because of the insufficient amount of water for foaming; ground particles have no weathered surface layer. This paper describes the hydrothermal treatment of milled particles to form the surface layer having the same properties as weathered one and to increase structural water. The results obtained are as follows: (1) the weathered surface layer of the Shirasu particles milled under $10\mu\text{m}$ is destroyed almost completely by milling process. (2) Sodium and potassium ions are replaced with H^+ by the treatment in 2wt% HCl solution at 200°C and about 15atm. The structural water increase with increasing volume of the solution, pressure, and time. Other ions such as Ca^{++} and Fe^{++} were removed also. (3) the highest yield of the micro-Shirasuballoons obtained by hydrothermal treatment in HCl solution was 10 times than without treatment. Even if heat treatment is performed in oxidizing atmospheres, whiteness of the micro-Shirasuballoons was more than 85.

[Received July 20, 1991; Accepted September 19, 1991]

Key-words: Shirasu, Micro-Shirasuballoons, Hollow glass microspheres, Hydrothermal treatment

1. Introduction

The writers et al. found the way to produce, with comparative cease, fine follow glass microspheres (Shirasuballoons) from such volcanic glasses found in volcanic glassine sediments as Shirasu and other.¹⁾ Some firms have since then commercialized this method and carried out the development of their own manufacturing processes. This has resulted in many characteristic products.²⁾ The finest particles among these products, however, remains around $20\mu\text{m}$ in diameter, and products of finer particles have not yet been available under the current materials and production facility. The Shirasu which is naturally available contains less portion of fine particles. Accordingly, it inevitably calls for a crushing process to adjust the grain sizes if we want to produce Shirasuballoons of fine particles. A preliminary experiment enabled us to obtain Shirasuballoons from fine particles down to $10\mu\text{m}$, although the quan-

tity is limited. We could not, however, obtain balloons from fine particles crushed less than $10\mu\text{m}$. The reason may be attributed to the loss of water content which must remain during the softening of the glass. The loss is caused by the multiplied effects of the following two reasons. One reason is that by crushing the natural Shirasu we also destroy most of weathered surface layers³⁾ which serve to prevent the outside diffusion of water particles caused by heating. Another reason is that the finer the particles are, the faster becomes the speed of water diffusion toward particle outside.

Therefore, we tried to carry out the hydrothermal treatment in chloric acid solution of Shirasu milled less than $10\mu\text{m}$. The purposes was to increase the water content and to formulate the surface layer having similar effects as the weathered surface layer. We succeeded to obtain Shirasuballoons from these hydrothermally treated samples. And we report the result as follows.

2. Specimens and Experimental Procedures

2.1. Specimens

We used, as the materials for this experiment, Shirasu obtained in the town of Yoshida, Kagoshimagun, Kagoshima Prefecture (commonly known as Yoshida shirasu).

We crushed the materials dry on a ceramic ball mill of 13cm I.D. The crushing conditions were: about 200g of materials, about 500g of ceramic balls, revolution of about 90rpm and crushing time of 8h.

Table 1 shows the materials and the grain size distribution of crushed particles measured by wet screening with standard sieves and levigation (separation by the sedimentation speed of particles in the water). The table indicates that the natural materials contained 3.3wt% of particles less

Table 1. Particle size distribution (percentage undersize, wt%) of the natural material and milled particles.

	149 μm	74 μm	37 μm	20 μm	10 μm	5 μm
Raw material	93.1	77.2	26.5	9.7	3.3	1.7
Milled particles	100.0	100.0	92.4	61.9	31.4	15.9

Table 2. Chemical composition (wt%) of raw material.

SiO_2	TiO_2	Al_2O_3	Fe_2O_3	MgO	CaO	Na_2O	K_2O	lg. loss	Total
73.15	0.29	12.00	1.26	0.37	1.63	2.65	3.32	4.97	99.64

than 10 μ m. This points to the inevitable need for the particle size adjustment of materials by the crushing process, to produce fine Shirasuballoons. We collected the grains of 5–10 μ m by levigation from the crushed materials as the starting batch.

Table 2 indicates the chemical composition of the starting materials. We carried out the measurement of thermal balance and X-ray powder diffraction for the physical properties of the samples. The thermal balance was measured for 30°–1000°C under the conditions of 150–200mg of sample volume and rising speed of 20°C/min. The X-ray powder diffraction was measured on 30kV voltage, 20mA current, 0.05° of step width and 2sec/step of measuring time.

2.2. Hydrothermal Treatment

We used an enclosed container for the hydrothermal treatment. The container was made of TEFLON with stainless steel jacket and had the volume of 70ml. **Table 3** shows the conditions for the experiment, in which items with * marks were fixed, while changing values other items. The retention time covers the duration from the time when the samples were placed in a constant temperature bath kept at the required temperature until the time when the samples were taken out of the bath. After the samples were taken out of the bath, they were left to cool off in open air. The pressure was the steam vapor pressure at the required temperature (about 5atm at 150°C, about 10atm at 180°C and about 15atm at 200°C). The volume of the samples was changed in the range of 5–20g in solution/sample ratio, so that the total volume of samples and chloric acid solution becomes uniform. After cooled, the samples were washed until the pH on the top of the solution became more than 5, and then they were filtered and dried (at 50°C overnight).

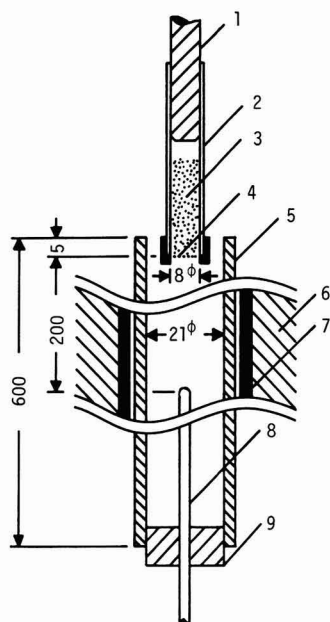


Fig. 1. Experimental apparatus for heat treatment. 1: Vibrator, 2: Teflon tube, 3: Sample, 4: 44 μ m mesh, 5: Ceramic tube, 6: Furnace (230 ϕ ×235h), 7: Heater, 8: Thermocouple, 9: Silicon rubber.

In order to know the physical properties of the samples before and after the hydrothermal treatment, we measured thermal balance and the whiteness of the samples heated upto 1000°C at the rising speed of 20°C/min. The whiteness was calculated⁴⁾ from the Lab value measured by colorimeter.

2.3. Heat Foaming

We used the apparatus as shown in **Fig.1** for the heat foaming. We placed samples in tube of 8mm I.D. with 44 μ m mesh of screen at the bottom. The electromagnetic vibration expelled the samples from the tube bottom, so that the samples were heat treated at the status of spontaneous fall. The maximum temperature was fixed at 1000°C inside the furnace, and the feed of the samples were 0.1–0.2g/min. The time to attain at the maximum temperature was calculated as 1min 50sec for grains of 5 μ m and 27sec for grains of 10 μ m, on the supposition that there was no air convection and the samples were completely dispersed. The heat treated samples were dispersed in water by ultrasonic device, and then separated by centrifugal separators into floating and sedimented substances. The floating substances were filtered, cleaned, dried (at 50° for overnight) and then weighed. We regarded these floating substances as Shirasuballoons,¹⁾ and calculated the yield. As the next step we observed the collected Shirasuballoons on a microscope. Then we measured the whiteness, tap filled bulk density,⁵⁾ air replaced particle density,⁵⁾ and the ratio of floating substance in water after applying hydrostatic pressure of 80kgf/cm² which is the indicator of the strength.⁵⁾

Table 3. Experimental conditions for hydrothermal treatment.

HCl content of sol. (wt%)	0.5, 1, 2*, 5, 10
Ratio of sol./sample (ml/g)	1.5, 4, 10*
Temperature (°C)	150, 180, 200*
Time (hr)	24, 48, 72, 120*, 168

*Fixed condition

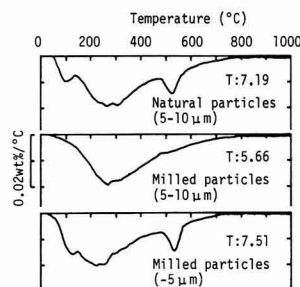


Fig. 2. DTG curves of the natural material and milled samples. T: Total weight loss (wt%).

3. Results and Observation

3.1. Difference between the Natural and Milled Grains

We carried out measurement on the starting batch of 5–10 μm collected from the above milled materials and on the grains of less than 5 μm , as well as on the natural grains of 5–10 μm for comparison. We show the DTG (differential value of the thermal weight loss) curves in Fig. 2 and the Powder X-ray diffraction patterns in Fig. 3. The thermal weight loss in Fig. 2 was mostly water content.¹⁾ The thermal foaming is greatly affected by the water content retained up to the high temperature, and this water content is of OH basis¹⁾ unevenly distributing within the meshed glass structure. The shoulder or the peak appearing around 500°–550°C in Figure 2 is related in size to the degree of the weathered clay (kaoline) formation from the surface of the glass grains.⁶⁾ The surface layer of unground natural grain has less Na^+ and more H^+ contents than its inside due to weathering.⁶⁾ This surface layer affects effectively on the thermal foaming, as in the model for the foaming mechanism proposed before.³⁾ In other words, the dissolving separation of Na^+ occurs from the grain surface layer in the weathering process. This causes softening at the surface layer of natural grains to take place at higher temperature than in its inside, and the hard layer is formed at the surface.

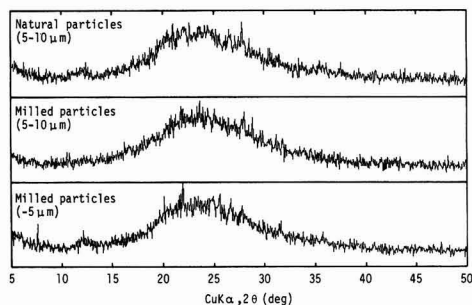


Fig. 3. X-ray powder diffraction patterns of the natural material and milled samples.

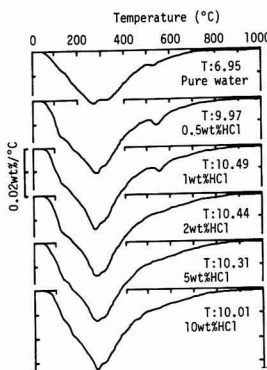


Fig. 4

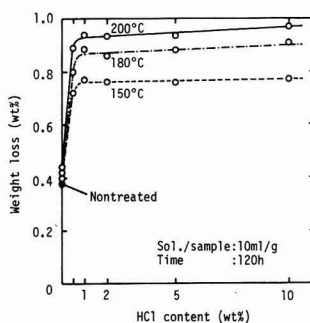


Fig. 5

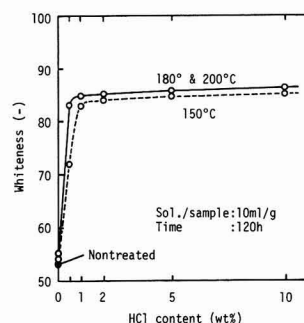


Fig. 6

Fig. 4. DTG curves of the samples obtained by hydrothermal treatment (10ml/g, 200°C and 120h). T: Total weight loss (wt%).

Fig. 5. Effect of HCl content of solution on weight loss (600–1000°C) of the samples obtained by hydrothermal treatment.

Fig. 6. Effect of HCl content of solution on whiteness after heated (1000°C) of the samples obtained by hydrothermal treatment.

This hard surface layer serves to inhibit the thermal dispersion of water out of the grain, to maintain the foams in spherical form, and at the same time, to prevent the interactive fusion of foams. When this weathered surface layer is destroyed, the grains become hard to foam, thus lowering the yield.³⁾

Figure 2 indicates that the size of shoulder or the peak appearing at 500°–550°C in the natural grains of 5–10 μm is larger than the starting batch but almost equal to milled grains below 5 μm . And the X-ray powder diffraction patterns in Fig. 3 shows, as in Fig. 2, that the profiles of the natural grain of 5–10 μm and milled grain below 5 μm are almost same. And we can slightly recognize the interlayer band of (hk) band neighboring the 4.5A(19.7°) and 7.2A(12.3°) which appears as the inclination toward forming clays. However, we fail to find the above band in the milled grain of 5–10 μm . This fact implies that weathered surface layers were mostly destroyed by crushing in the milled grains of 5–10 μm used as the starting batch. Therefore, the surface may have the same composition as in the inside, and most of the original weathered surface may have been condensed in the milled grain below 5 μm .

3.2. Hydrothermal Treatment

Figure 4 shows the DTG curves on the samples with hydrothermal treatment by changing the concentration of chloric acid. Here, we applied the factors other than the concentration of chloric acid set in the Table 3. The DTG curves of the starting batch was already shown in Fig. 2 as the mild grains (5–10 μm). The broad peak appearing in 200°–400°C became larger with the hydrothermal treatment, and total thermal reduction in weight also increased in proportion. This was thought to be the increase of the OH base which may have unevenly distributed in the meshed glass structure. The increase in the total thermal reduction in weight was remarkable, and we presumed that this increase was brought about by the reaction (hydrosis) with interchanging the H^+ ions, following the elution of such ions as Na^+ , K^+ and others which are easily separable. From the degree of the increase, this interchanging reaction seemed to have progressed well into the inside.

On the other hand, shoulder or peak appearing at

500°–550° became larger as the concentration of chloric acid was increased to 0.5 or 1wt%. This may have been caused by the formation of kaoline through the elution and hydrosis of Na^+ and K^+ ions out of the Shirasu glass, as was the case in the formation of kaoline through the hydrothermal treatment of feldspars contained in the low quality Amakusa claystone.⁷⁾ The small peak, however, appearing at the 500°–550°C implies a small formation of kaoline by progressing slightly from the surface. Whereas, with the above feldspars we did not recognize the formation of kaoline in the concentration of chlorine acid in excess of 2wt%.⁷⁰ Since this peak cannot be seen in Fig.4 in the concentration of chloric acid in excess of 2wt%, we can say that there was no formation of kaoline from the Shirasu glass. The figure, however, shows the dehydration pattern specific to natural glass. This implies to the progress of the delusion of delutable ions as Na^+ and K^+ and the likes from the grain surface, as well as the hydrolysis.

Figure 5 shows the relationship between the concentration of chloric acid during hydrothermal treatment and the thermal weight loss above 600°C which is thought to have effective action to foaming. As the temperature for the hydrothermal treatment becomes higher, the thermal weight loss increases. We also noted, though slightly, a tendency to increase the value of thermal weight reduction with the increase in the concentration of chloric acid.

In the samples changing the other factors, the value of thermal reduction in weight increased to almost the same extent in the hydrothermal treatment time of more than 48h, as in solution/sample ratio exceeding 4ml/g. The phenomenon to increase the value of thermal weight loss by the hydrothermal treatment may have been caused by the delusion of above Na^+ , K^+ and other ions which are apt to dissolve, and by their interchange reaction (hydrolysis) with H^+ ion. On the other hand, no increase was recognized in the value of thermal weight loss in the water bath treatment below 100°C in open air.

After the thermal weight measurement of the sample, we could notice marked difference in color between the starting batch and hydrothermally treated sample. Therefore, we measured the whiteness of the sample heated up to 1000°C at the rising speed of 20°C/min. Figure 6 shows the relationship between the concentration of chloric acid and the whiteness of heated samples in hydrothermal treatment. By the way, the whiteness of the starting batch was 85.2, but this decreased to 53.2 in the sample heated under the above conditions. This deterioration in whiteness may have been caused by Fe^{++} ion in the surface layer which turned to Fe^{+++} ion by oxidizing reaction. As Fig.6 indicates, the whiteness increased by about 30 to around 85 by the hydrothermal treatment. This indicates that we can obtain white Shirasuballoons without any deterioration in whiteness, even if we carried out the heat treatment in oxygen atmosphere, on the samples treated hydrothermally by chloric acid solution. In samples with other factors changed, the whiteness was almost unchanged with the hydrothermal treatment in excess of 48h and in solution/sample ratio of more than 4ml/g, as was the case in the value of thermal weight reduction above 600°C. On the other hand, the whiteness was less than 70 in the water bath treatment, and we recognized the effectiveness of this treatment to the whiteness.

By the way, we remilled the samples hydrothermally treated on the fixed conditions mentioned in Table 3, and carried out the similar heat treatment. The degrees of red

any yellow increased, while the whiteness decreased to 81.5. Even in the same powders, the finer the grains are, the larger the whiteness becomes. The content of grains below 5 μm which were not present before the remilling became 41.1wt%. It appears to us that the value of the whiteness may have become smaller in the same grain sizes. The fact that the decrease in whiteness was recognized in the samples milled after the hydrothermal treatment may point to higher Fe^{++} ion concentration in the grain from the outside toward inside. As such, it is conceivable in the sample hydrothermally treated by chloric acid solution that Na^+ , K^+ , Ca^{++} , Fe^{++} and other ions, which are easily dissolved in chloric acid solution, were diluted and the hydrogenated surface layer was formed.

3.3. Thermal Foaming

Figure 7(A) shows the relationship between the concentration of chloric acid in the hydrothermal treatment and the yield of fine Shirasuballoons collected as the floating substances in the water. When the concentration of chloric acid was 2wt%, the yield became maximum at 19wt%, about 10 times of the starting batch. We attribute the decrease in the yield in the hydrothermal treatment with high chloric acid concentration to the fact that Na^+ , K^+ , Ca^{++} , Fe^{++} and other ions diluted to increase the thickness of the hydrogenated surface layer too much. In other words, H^+ ions of the surface layer interchanged with Na^+ , K^+ and other ions dispersed to open air as H_2O gas at the start of heating, resulting in raising the softening temperature in the surface layer higher than in grain inside. If there is no surface layer of higher softening temperature, the H_2O gas generated from near the core of the glass grain dispersed outside the grain before softening, and no foaming would have taken place. With the adequate thickness in the surface layer, the surface layer of higher softening temperature will inhibit the H_2O gas to disperse to the outside of the grain before softening. In addition, too thick surface layer would have too much force to suppress the foaming. By the way, many samples in the starting batch and in hydrothermal treatment without chloric acid (chloric acid concentration of 0wt%), adhered to the furnace wall, and we had the difficulty in foaming treatment. While, we were able to carry out the foaming treatment without not much adhesion to the wall in samples hydrothermally treated with 1wt% or more concentration in the chloric acid solution.

Figure 7(B) indicates the relationship between the solution/sample ratio in the hydrothermal treatment and the yield. This figure shows that the higher the ratio is, the more the yield is. Figure 7(C) points to the relation of the

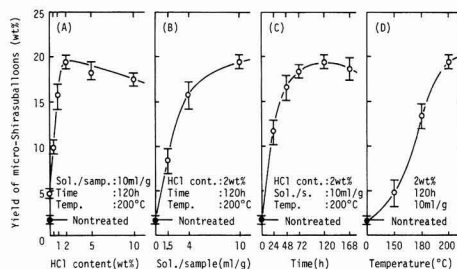


Fig. 7. Effect of experimental conditions for hydrothermal treatment on yield of micro-Shirasuballoons from the heated sample.

hydrothermal treatment time and the yield. The yield was maximum at 120h of treatment. In commercial production, it is advantageous that the volume is larger and the treatment time is shorter. Figure 7(B) points to the fact that the yield becomes larger at lower ratio of solution/sample. This means smaller volume of treatment at one time. There is a likelihood that the volume of treatment can be increased by the addition of such additives as metallic chlorides to chloric acid solution, or that the time can be cut in the hydrothermal treatment. These matters, however, must be studied in the future.

On the other hand, in the relationship between the temperature in the hydrothermal treatment and the yield, the yield becomes higher as the pressure increases in the treatment, as shown in Fig.7(D). It is, however, practically difficult in the industrial application to increase the treatment pressure to more than 15atm; that is, to raise the temperature to more than 200°C, because of the structure of the related equipment. Therefore, these figures may be the limit in the temperature and pressure.

3.4. Physical Properties of Fine Shirasuballoon

We carried out the measurements on the fine Shirasuballoons obtained from the hydrothermally treated samples under the fixed conditions in the Table 3, which indicated the highest yield. The measurements were done on the chemical analysis, microscopic observations, whiteness, density and strength (hydrostatically nondestructive ratio).

Table 4 shows the chemical analysis. Compared with the chemical analysis on the starting batch shown in Table 2, the contents of Na₂O and K₂O were very few, while Fe₂O₃ and CaO were somewhat small. The facts were explained in Section 3.2 that the hydrothermal treatment caused the dilution of the Na⁺, K⁺ and other ions which are easily dissolvable, to progress well into the grain inside, while the dilution of Fe⁺⁺ and other ions remained at the grain surface layer and not into its inside. The microscopic photographs are shown in Fig.8(B) and (C). We also show the milled grains of 5~10μm as the starting batch in Fig.8(A) and sedimented grains obtained by flotation after the heat treatment in Fig.8(C). The grain size were almost same as in the starting batch, although a little larger, and we also noticed many foamed sphericals in the sediment grains. The

density of these grains seemed to be slightly larger than 1g/cm³. This points to the likelihood that yield can be further increased by choosing the conditions for the heat treatment. The average grain size, density, strength and the whiteness are shown in Table 5. Wedilution included in the tale the value⁵⁾ of Shirasuballoons manufactured in 1981 for comparison. Shirasuballoons of almost same quality are being manufactured at present.

The grain density remained in the range of comparison, but the values for bulk density and strength (hydrostatically non-destructive ratio) are larger than the values of conventional products. This can be explained by the fact that they are finer than the conventional ones, so that the shell thickness becomes larger for the grain size. Furthermore, the whiteness value is larger than the comparison values. This points to the fact that white fine Shirasuballoons can be obtained by heat foaming in oxidizing atmosphere, and that the dilution of Fe⁺⁺ ion out of the surface layer only prevents the decrease in the whiteness value. by the way, the whiteness value in Table 5 is larger than that of Fig.6. This may be due to the fact that the rising speed in the heat foaming was extremely higher in this case than in the samples of Fig.6.

We may possibly increase the yield of fine Shirasuballoons and obtain fine Shirasuballoons of lesser density, by keeping the maximum furnace temperature higher than the current heating conditions, by accelerating the rising speed, by prolonging the maximum temperature, and the likes. Nonetheless, we may increase the yield by raising the maximum furnace temperature, but more samples will adhere to the furnace well, making the heat forming difficult. Therefore, this method is not advisable. On the other hand, as the mean to disperse the samples during the heat treatment, we passed them through a metal net of 44μm as mentioned in the Section 3.2. This screening method seems not to be uniform heating under the completely dispersed status. There is a possibility to raise the yield by uniform heating or by changing the rising speed, and these matters need further study.

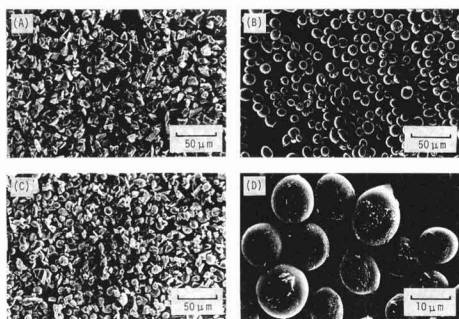


Fig. 8. SEM micrograph of samples. A : Milled particles (5~10μm). B : Micro-Shirasuballoons (floating part in water after hydrothermal and heat treatment). C : Sinking part in water after hydrothermal and heat treatment). D : The same samples as B.

Table 4. Chemical composition (wt%) of micro-Shirasuballoons.

SiO ₂	TiO ₂	Al ₂ O ₃	Fe ₂ O ₃	MgO	CaO	Na ₂ O	K ₂ O	lg. loss	Total
79.71	0.32	12.66	1.15	0.40	1.52	0.09	1.41	1.93	99.19

Table 5. Characteristics of Shirasuballoons.

Characteristics	Conventional Shirasuballoons	Micro-Shirasuballoons
Mean particle size (μm)	30-310	12.5
Bulk density (g/cm ³)	0.07-0.36	0.40
Particle density (g/cm ³)	0.65-1.20	0.84
Strength* (wt%)	5.21-49.1	93.5
Whiteness (-)	71.7-82.8	87.8

*Floating part in water after pressed under hydrostatic pressure: 80kgf/cm²

4. Conclusion

We examined the method to produce fine Shirasuballoons from the milled Shirasus, and we have learn the following points;

- 1) There are not much particles of less than 10 μ m in size contained in natural materials. It is, therefore, necessary to adjust the materials through crushing process in order to produce fine Shirasuballoons. When the grains are crushed below 10 μ m, most of the weathered surface layers, which effectively react in foaming, are destroyed, and making their surface layer to the same composition as their insides.
- 2) When the milled Shirasu was treated hydrothermally in the acid solution, the dilution of Na⁺, K⁺ and other ions which are easily dissolvable, progressed well into the inside from the surface, while the dilution of Ca⁺⁺, Fe⁺⁺ and other ions may have remained within the surface layer only, and not progressed to the inside.
- 3) We were able to obtain fine Shirasuballoons about 10 times more with the hydrothermal treatment, by adding 10ml of 2wt% chloric acid solution to every 1g of sample, and heated for 120h at 200°C (about 15atm).
- 4) If we use the hydrothermally treated samples, we can

obtain while fine Shirasuballoons. There was no deterioration in the whiteness, even under oxidizing atmosphere. And these fine Shirasuballoons had higher strength (hydrostatically non-destructive ratio) than conventional Shirasuballoons.

References:

- 1) K. Kimura, K. Jinnai and Y. Isayama, *Yogyo Kyokaishi*, 80, 84-91 (1972).
- 2) K. Jinnai and K. Kimura, *Kogyo Zairyo*, 29, 30-34 (1981).
- 3) K. Kimura and K. Hamano, *Yogyo Kyokaishi*, 84, 70-75 (1976).
- 4) For instance, *Yogyo Kyokai* (ed.), *Yogyo Keisoku* (1962) 234.
- 5) K. Kimura, K. Jinnai and Y. Isayama, *Funtai Kogaku Kenkyu Kaishi*, 12, 513-518 (1975).
- 6) K. Kimura, H. Tateyama, K. Jinnai and K. Tsunematsu, *Yogyo Kyokaishi*, 90, 504-510 (1982).
- 7) K. Kimura and H. Tateyama, *Seramikkusu Ronbunshi*, 97, 439-446 (1989).

This article is a full translation of the article which appeared in *Nippon Seramikkusu Kyokai Gakujutsu Ronbunshi* (Japanese version), Vol.99, No.12, 1991.

Nano Composite of PZT-PMN-MnO₂-NiO Ceramics-Alumina System

Kazumasa Ohnishi, Masaru Kawarada, Takaaki Ishii,
Yasuhiro Tanabe* and Eiichi Yasuda*

Nagaoka Plant, Niigata Division, Alps Electric Co., Ltd.,

1-3-5, Higashitakami, Nagaoka-shi, 940 Japan

*Research Laboratory of Engineering Materials, Tokyo Institute of Technology

4259, Nagatsuta-cho, Midori-ku, Yokohama-shi, 227 Japan

A nano-structure composite consisting of PZT-PMN-MnO₂-NiO ceramics and Alumina has been investigated. SEM observations of the composite revealed that particles of the dispersing phases were enclosed in the grain of matrix. The composition of one of disperse phases was analyzed by the X-ray method to be PbAl₁₂O₁₉. The composition of the other phase was analyzed by the TEM method and estimated to be a mixture of spinel structure compounds, such as MgAl₂O₄, NiAl₂O₄ and MnAl₂O₄. It was found that the bending strength, mechanical Q and electromechanical coupling factor (kr) were increased by 30–40%, 20% and 10%, respectively. As a result, properties of this composite have been improved.

[Received July 20, 1991; Accepted September 19, 1991]

Key-words: PZT, Al₂O₃, Nano composite, Spinel

1. Introduction

The electric performances of electronic ceramics have made marked advancements in recent years. Requirements on miniaturization, however, have increasingly been demanding, making the machining conditions further exacting. This trend has been placing more emphasis on the mechanical functions on top of the electrical performances. The writers et al. have focused on this trend and have been targeting on the improvements of the mechanical performances of electronic ceramics, centering around piezoelectric devices. We have been studying on the HIP treatment, addition of ceramic fibers, and composition of piezoelectric materials, improvements on firing methods and so on.¹⁻⁵⁾

Recently nano composite materials have extensively been studied, aiming at improving the mechanical performances of engineering ceramics. The conventional composite materials have particles of dispersing phase in micrometer order dispersed within the matrix grain. On the other hand, it is reported that nano composite materials using particles of dispersing phase in nanometer order have very interesting natures different from the conventional composite materials, and have attracted attention.⁶⁻⁷⁾ Some practical examples are reported that dispersion of SiC of nanometer order into Al₂O₃ raised the toughness to 7MPa·m^{1/2} from 5, and improves the bending strength to around 1500MPa from 400.^{8,9)} Fear on the reaction between the matrix and the dispersing phase has led studies to make the particles in the matrix themselves finer, instead of

making them composite. It is, however, difficult to maintain the electric performances by making particles of the matrix finer to improve the mechanical performances.

Under these circumstances, we hoped that we can expect to improve the mechanical performances, while keeping the electrical performances, if we can disperse the fine particles. That is nano composition, as the mean to improve the strength without making the particles of matrix finer. Further, it appears us possible in the case of nano composition to disperse the particles of dispersing phase within the particles of the matrix. We hoped that we can expect by this method both electrical and mechanical performances not found in the conventional composite materials.

This study used, as the matrix, PZT which is piezoelectric material, and dispersed alumina sol (Al₂O₃) on this. We expected the nano composition by dispersing Al₂O₃ of nanometer order. We also carried out various studies in our expectation for aluminum compounds of nanometer order, if a reaction should take place with the matrix. As the result, we succeeded to formulate the latter. And we report on the nano composite structure of the piezoelectric materials, as well as their mechanical and electric performances. We also clarified by this study that nano composition is very effective to electronic ceramics.

2. Experimental Procedures

2.1. Preparation of Samples

1) Preparation of PZT Matrix

We used as samples, first class reagents of PbO, ZrO₂, TiO₂, Nb₂O₅, MgO, NiO, MnO₂. We weighed these materials into the following molar ratio. 0.435PbTiO₃-0.44 PbZrO₃-0.125Pb (Mg_{1/3}Nb_{2/3})O₃. We added 0.5wt% each of NiO and MnO₂ as additives. We mixed these materials with pure water for 6hrs with zirconia balls in an urethane covered ball mill pot of 50l volume. Then the mixed materials were placed in a stainless container. After being dried, they were transferred into crucible of magnesia and calcined at 900°C for 1hr. After being left to cool, they were also crushed in the same ball mill with pure water for 24hrs, and then dried.

2) Addition of Alumina Sol

We measured out the alumina sol of 0.1, 0.5, 1.0, 3.0, 5.0 and 10.0wt% in terms of Al₂O₃ against 150g of above calcined sintered powders. We put these powders and required volume of alumina sol in an explosion-proof ball mill pot together with zirconia balls and mixed with acetone of 250 ml for 20hrs. (We also prepared the sample without the

alumina zol; that is 0wt%, going through the same process for comparison.) After mixed, they were dried in an explosion-proof drier.

3) Forming

We added 3wt% of water on the above powders and passed through a screen of mesh number 20, and formed into pellets of 14mm dia. and 3mm thick under the pressure of 10kg/cm². At the same time, we also formed blocks of 49×29×8mm as the samples for measuring the bending strength. In addition, both types of samples were CIP treated at the pressure of 2500kg/cm².

4) Sintering

The formed samples were placed on the zirconia setter and placed into a alumina crucible with the matrix powders as filler. Then the samples were fired at 1270°C for 2hrs under the oxygen atmosphere.

5) Machining and Treatment of Samples

After sintering, we machined the pellets for measuring electric characteristics into the thickness of 1mm, and silver electrode on both sides and fired at 700°C. Prior to polarization, the samples were measured according to the Denshi-Zairyou-Kogyoukai standard EMAS-6001, and then treated for the polarization by applying 2.0kV/mm of electric field for 60 minutes. The samples for the bending strength test were machined into 3×4×40mm, mirror finished, and chaffered according to JIS-R1601.

2.2. Measuring Methods

1) Electric Characteristics

Electric characters were measured at room temperatures in accordance with the Denshi-Zairyou-Kogyoukai's standard EMAS-6001 with the impedance analyzer (YHP-4192A) on dielectric and piezoelectric characteristics such as dielectric constant, dielectric loss, electromechanical coupling factor, mechanical quality factor and others.

2) Bending Strength

We prepared each 10 samples of 3mm thick, 4mm wide and 40mm long according to JIS-R1601, and carried out the 3-point bending test on DCS-50M of Shimazu Seisakusho.

3) Density was measured in water of 20°C by the Archimedes' Method

4) Observation and Analysis of Microstructures on SEM, TEM, and XRD (X-ray diffraction)

For SEM observation, we prepared the sample pellets of

15mm dia. by mirror-finishing. The thermal-etching was done at 1100°C for 5hrs in the O₂ atmosphere with unadded matrix at the bottom of Alumina crucible on the Zirconia setter. The surface of thermal-etched samples was plated with gold. TEM samples were ground to the thickness of 50μm, and then treated for ion milling by setting on the copper holder. We observed these samples on a TEM for qualitative analysis at each observation point by the Energy Dispersion X-ray Analyzer (EDAX).

3. Results and Discussions

3.1. Observation of Microstructure

We mirror finished the samples and then heat treated them to observe the microstructure of their inside on SEM. The result is shown in Fig.1. It is evident in these photographs that there are very few particles of dispersing phase of micrometer order up to the 1wt% of addition. We also noted the structures in which fine grains in several tens to several hundreds nm of dispersing phase were enclosed in the matrix grain. We observed in samples with more than 3wt% addition that particles of dispersing phase in micrometer order (several hundreds nm to several μm) having a uniform crystalline (hexagonal) structure suddenly

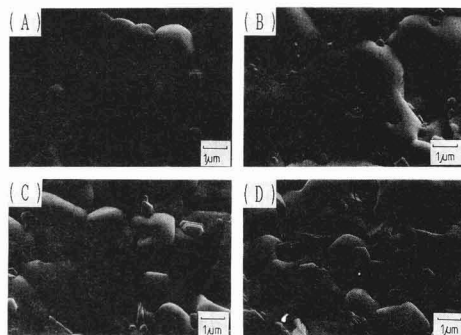


Fig. 1. SEM photographs of lapped and etched surfaces:

(A) Al₂O₃ 0wt%, (B) Al₂O₃ 1wt%,
(C) Al₂O₃ 3wt%, (D) Al₂O₃ 5wt%.

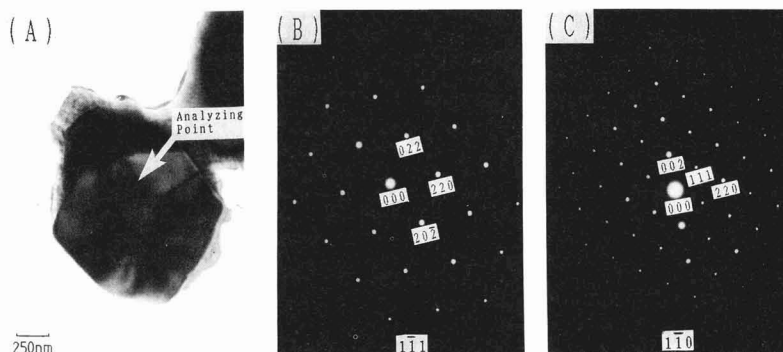


Fig. 2. TEM photographs of 1wt% Al₂O₃ added PZT composite: (A) Disperse phase, (B) Electron beam diffraction pattern at an analyzing point in (A), (C) Electron beam diffraction pattern at the same point as (B) by a different angle.

increased to penetrate into the grain of matrix, together with particles of dispersing phase of nanometer order. We also noted the structures by this sudden increase of particles of dispersing phase, in which needle like microstructures from other matrix grain were pinned to the matrix grain, or in which the shape of matrix grain became pronouncedly undulating. We presumed that such a structure affects on the mechanical characteristics. We carried out the TEM observation on the particles of dispersing phase confirmed by the SEM observation. We came to know that there is a difference in the composition of the samples with 1wt% and 5wt% in addition of the sol. We shall now explain on this difference.

3.2. Composition of the Disperse Phase with 1wt% Addition of Al₂O₃

We carried out a qualitative analysis (EDAX) with TEM on sample with 1wt% addition of Al₂O₃. And we detected Al, Ni, Mg and Mn among particles of the disperse phase. Figure 2 shows the particles of disperse phase and their electron beam diffraction patterns. We carried out similar checks in several locations of sample with 1wt% addition of Al₂O₃, and obtained the same results. This led us to believe that the metallic elements in the particles of disperse phase are the above 4 elements. This result in the qualitative analysis points to the likelihood of the spinel group of MgAl₂O₄, NiAl₂O₄, MnAl₂O₄ and the likes as the stable substances, even under the conditions of high temperature and Oxygen atmosphere. Therefore, we crushed the samples with 1wt% of Al₂O₃ well, and analyzed by the XRD. We could not, however, detect them, as the contents were very few. Then, we measured the interplanar spacing (d-value) on the typical one among clear electron beam

patterns at the location where the above qualitative analysis of the TEM detected Al, Ni, Mg and Mn. The Table 1 compares the actual d-values obtained from the electron beam analysis pattern and those of ASTM cards. The above 3 spinel group shows very close values of interplanar spact-ing and agrees quite well with the values of interplanar spacing measured from the analyzed pattern. Therefore, we were led to think that the disperse phase is the mixture of the 3 spinel group of MgAl₂O₄, NiAl₂O₄, and MgAl₂O₄.

3.3. Composition of Disperse Phase with 5wt% Addition of Al₂O₃

We also carried out similar TEM observation and qualitative analysis on samples with 5wt% addition of Al₂O₃ to those with 1wt%. The result showed us 2 types of disperse phases with different composition of constituent metallic elements. The one disperse phase had the exactly same result as seen in samples of 1wt%, pointing to the possible mixture of above spinel group. While, we detected the strong indication of Al in the other disperse phase, as well as Pb, Ti, Zr, Nb, Mg, Ni and Mn. We also checked on several locations with the same results. We milled the samples of 5wt% addition well, and analyzed by the XRD. We compared the values on the compounds having above metallic elements as the constituent elements with the ASTM cards, as shown in Fig.3. The result showed the good agreement between the peak of PbAl₂O₉ (hexagonal) and the peak other than that of the matrix phase. This clarified us that two disperse phases were formed by the reaction during firing between the Al₂O₃ and the matrix, when we added alumina sol to PZT used in this study. It also made clear to us that there was the precedence in the formation of these two phases. The mixed phase of such spinal group as MgAl₂O₄, NiAl₂O₄, MnAl₂O₄ and the likes was first formed upto the 1wt% addition of Al₂O₃, and the crystals of PbAl₂O₉ increased with more addition. From the analysis on the microstructure so far, we can explain well that the electrical and mechanical characteristics stated later vary with the volume of added alumina sol.

3.4. Density

As shown in Fig.4 , the density varies in proportion to the addition of Al₂O₃ up to 5wt%. We found, however, that the density suddenly decreased in the addition of 10wt%. Therefore, we observed the mirror finished samples on an optical microscope. The sample with 10wt% of addition

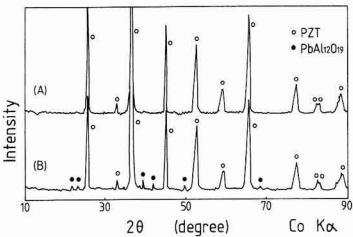


Fig. 3. X-ray diffraction patterns of (A) PZT 100wt% and (B) PZT-Al₂O₃ 5wt%.

Table 1. Comparison of values of ASTM cards and measured values.

Cited from ASTM cards				Measured value	
d-value(Å)			Miller index	d-value(Å)	
MgAl ₂ O ₄	NiAl ₂ O ₄	MnAl ₂ O ₄	(hkl)	Fig. 2 (B)	Fig. 2 (C)
4.66	4.65		(111)	4.61	
2.858	2.846	2.90	(220)	2.82	2.79
2.437	2.427	2.47	(311)	2.42	
2.020	2.013		(400)	2.01	
1.650	1.6415	1.585	(422)		1.63

was found to have extremely many pores compared with other samples. It appeared us that excess addition of Al_2O_3 formed many $\text{PbAl}_{12}\text{O}_{19}$, which adversely affect on sintering.

3.5. Electrical Characteristics

Figure 5 denotes the relationship between the relative dielectric constant before and after polarization and addition of 3wt% has the highest effect on the relative dielectric constant after the polarization. It also showed us that the values of $\tan\delta$ 0.5% for no addition of Al_2O_3 and 0.3% for 3wt% of addition, but no more reduction was noted for more addition. Then, we examined the effect of the addition of Al_2O_3 on the coefficient k_r of electromechanical coupling factor and mechanical quality factor Q_m . We showed the result in Fig.6. This chart indicates that both k_r and Q_m improve up to 3wt% addition, implying at the similar result to the change in the relative dielectric constant after polarization. From these results, we come to the conclusion that 3wt% addition of Al_2O_3 is the most effective to the electric characteristics.

3.6. Bending Strength

We show the change in the bending strength in Fig.7. The strength improved by more than 10% even with the addition of 0.1 or 0.5wt% from the matrix only, and with narrower distribution. In addition, the piezoelectric characteristics tend to improve by several % even with the addition of 0.1 or 0.5wt%. This showed us that our study so far has already attained our first target. Further examination clearly

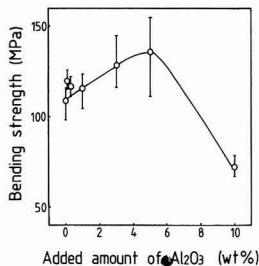


Fig. 7. Relationship between bending strength and added amount of Al_2O_3 .

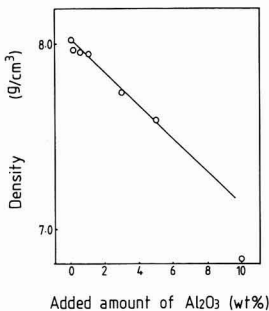


Fig. 4

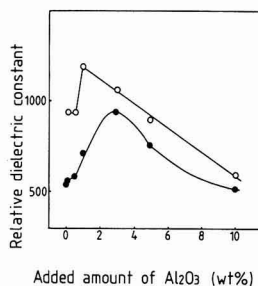


Fig. 5

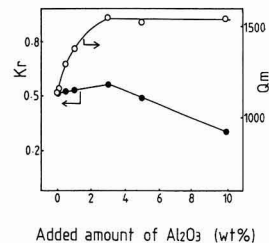


Fig. 6

Fig. 4. Relationship between density and added amount of Al_2O_3 .

Fig. 5. Relationship between relative dielectric constant and added amount of Al_2O_3 .

○ Before poling, ● After poling

Fig. 6. Effect of added amount of Al_2O_3 on k_r and Q_m .

showed that, while the strength tended to decrease between the addition of 0.1% to 1wt%, when the addition exceeds 1wt%, it improved up to 5wt%, although with a little wider in distribution. When considered that the TEM observation confirmed the formation of $\text{PbAl}_{12}\text{O}_{19}$ from 5wt%, we presume that the formation of the second disperse phase of $\text{PbAl}_{12}\text{O}_{19}$ becomes conspicuously evident from the addition of 1-3wt% of Al_2O_3 , and this formation brings about the marked effect on the improvement of the strength.

4. Conclusion

- 1) We have come to know that if we add alumina sol to PZT, a typical electric materials of electronic ceramics, in order to disperse Al_2O_3 of nanometer order, we can obtain nano composite having disperse phase of aluminum compound in nanometer order by the reaction.
- 2) The qualitative analysis confirmed that this nano composite formed disperse phase of different types by the addition of 1wt%. It also showed that it formed spinel mixtures of MgAl_2O_4 , NiAl_2O_4 and MnAl_2O_4 in less than 1wt% addition, and $\text{PbAl}_{12}\text{O}_{19}$ as well as these 3 spinel group with more than 1wt% addition.
- 3) We have come to know of the disperse phases that the strength suddenly improved when $\text{PbAl}_{12}\text{O}_{19}$ began to form, and that this compound has a great effect on the mechanical characteristics. (With 10wt% addition of Al_2O_3 , however, the sintering was adversely affected and the strength decreased, although the strength was improved up to 5wt% of addition.)
- 4) The most effective addition to the electric characteristics was 3wt%.

References:

- 1) K. Ohnishi, T. Morohashi and K. Uchino, *Seramikkusu Ronbunshi*, 97, 473-477 (1989).
- 2) K. Ohnishi, T. Morohashi and M. Kawarada, *Proc. 2nd Sympo. Ceram. Soc. Jpn.* (1989).
- 3) K. Ohnishi and T. Morohashi, *Proc. 7th Mtg. Ferroelectric Mater. and their Applications* (1989) 45-46.
- 4) K. Ohnishi, T. Morohashi and S. Tanaka, *Proc. 2nd Autumn Sympo. Ceram. Soc. Jpn.* (1989) 34.

- 5) K. Ohnishi, T. Morohashi and S. Tanaka, *ibid.*, (1989) 22.
- 6) T. Hirai, *Proc. Jpn. Soc. Powder and Powder Metallur.* (1987) 176-177.
- 7) T. Hirai and T. Goto, *Jpn. Inst. Metals*, 28, 960-967 (1989).
- 8) K. Niihara, *Electronic Ceramics*, 9, 44 (1988).
- 9) S. Saito, H. Suzuki and Y. Nakamura, *Ceramics Reinforced Composite Ceramics*, Sangyo Gijutsu Service Ctr., (1991) 127-148.

This article is a full translation of the article which appeared in *Nippon Seramikkusu Kyokai Gakujutsu Ronbunshi* (Japanese version), Vol.99, No.12, 1991.

Change of Surface Grinding Flaw of β -Sialon with Oxidation and Its Influence on Bending Strength

Kazushi Kishi and Seiki Umabayashi

Government Industrial Research Institute, Kyushu
Shuku-machi, Tosu-shi, 841 Japan

A β -sialon sintered body was fabricated from a spray dried mixture of α - Si_3N_4 and $\text{Al}(\text{Oi-Pr})_3$ solution by hot-pressing. Bending specimens with a size of $3\text{mm} \times 3\text{mm} \times 30\text{mm}$ were ground using a #600 diamond wheel. A change in grinding flaws by oxidation at 1400°C for 100hrs was observed with an optical microscope. The change in bending strength with oxidation and polishing after oxidation was examined. Grinding flaws consisted of surface flaws with depths of $5\mu\text{m}$ and cracks, which followed the flaws, with depths of more than $20\mu\text{m}$. By oxidation, the surface flaws changed to a smooth and dense oxide layer after oxidation. However, the cracks were supposed to retain the original size after oxidation, even though they were filled with the oxide. The strength of the sample after oxidation was approximately 1000MNm^{-2} and that after removing the oxide layer by polishing was approximately 1200MNm^{-2} . The strength of the sample after being heat treated at 1200°C for 2h in air after polishing was approximated 1400MNm^{-2} . The strength increased in comparison to the ground sample. This increase was supposed to result from a decrease in the depth of the cracks as fracture origins. To evaluate the essential strength of β -sialon, it is necessary to remove the cracks, at least those of more than $25\mu\text{m}$, by polishing or by milder machining.

[Received April 19, 1991; Accepted August 22, 1991]

Key-words: β -sialon, Aluminum-iso-propoxide, Oxidation, Grinding flaw, Bending strength

1. Introduction

Sintered β -sialon has a high oxidation resistance to and a high strength at high temperatures. Therefore, it is expected to be applied as a high temperature structural material, along with sintered bodies of silicon nitride (Si_3N_4) and silicon carbide (SiC).¹⁾ The authors previously demonstrated that surface grinding flaw has a marked effect on the strength on the hot pressed β -sialon with homogeneous microstructure, and that the strength was improved by heat treatment in air due to blunting the cracked tip of grinding flaws and covering the sample with an oxide layer.²⁻⁴⁾ However, there are many cases in which the cracks developed well into the sintered body were of fracture origin even after heat treatment. Furthermore, it was difficult to completely eliminate the effects of grinding flaws on the strength by heat treatment.⁵⁾

On the other hand, the oxidation of β -sialon progresses by diffusion of oxygen through the oxide layer formed on the surface of the sintered body.^{5,6)} Accordingly, it is sug-

gested that flaws, such as grinding flaws differ in the degree of oxidation from the crack developed to the inside of the sintered bodies. In other words, a grinding flaw near the surface may be covered with an oxide layer at a comparatively earlier stage, or the oxidation may progress well into the depth of the flaw to eliminate the flaw itself. And, it is probable that the crack may not be fully oxidized. We are not aware of any report which deals with changes in grinding flaw following oxidation, particularly with the changes in cracks developed inside sintered bodies which can be an origin of fracture origin.

This report summarizes the results of observation of the changes which follow the oxidation of surface grinding flaws of hot pressed β -sialon bodies. In addition, the bending strength of the oxidized sample, with the oxide layer removed by polishing, it examined because it is possible to minimize the effects of grinding flaw on strength.

2. Experimental Procedures

We prepared sintered β -sialon bodies with composition of $z=0.5$ from Si_3N_4 (α - Si_3N_4 , TS-7, 90% α -ratio, average particle size $0.6\mu\text{m}$, purchased from Toyo Soda Co., Ltd.) and aluminum iso-propoxide [$\text{Al}(\text{OC}_3\text{H}_7)_3$, 1st grade reagent,] purchased from Nakarai Chemicals Co., Ltd.). The conditions or preparation were the same as those in our previous report.²⁾ Pieces of approximately $4\text{mm} \times 4\text{mm} \times 30\text{mm}$ were cut from the hot pressed β -sialon and ground with a #600 diamond wheel into bending specimens of approximately $3\text{mm} \times 3\text{mm} \times 30\text{mm}$. Surface grinding was carried out at a table feeding speed of 0.6m/min , a grinding width of 2mm , and a cut depth of $2\mu\text{m}$. The specimens were then oxidized in air at 1400°C for 100h inside a Kanthal super furnace. After oxidation, the specimens were polished with a $6\mu\text{m}$ diamond disc (resin bond, made by 3M). While grinding the surface, the size was measured from time to timewith a micrometer and was observed using an optical microscope. A specimen with radial cracks of Vicker's indentation was also oxidized at 1400°C for 100h, and this specimen was observed during polishing using an optical microscope.

The bending strength of the specimens after oxidation and those of the specimens polished after oxidation was measured using a 3-point loading device with a span of 20mm and a cross-head speed of 0.5mm/min . The fractured surfaces were observed using an optical microscope and a scanning electron microscope (SEM).

3. Results and Discussion

The bulk density of the hot pressed bodies was 3.14gcm^{-3} . The crystalline phases were β -sialon and O' -sialon. The hardness was approximately 16GN^{-2} , and the K_{IC} measured by the IM method⁷⁾ was approximately $3\text{MNm}^{-3/2}$. This was almost the same as in the previous report.³⁾ The phase identified in the oxide layer was only α -cristobalite.

3.1. Observation of Sample Surface after Oxidation

The surface of oxidized specimens was covered by a uniform and smooth oxide layer of approximately $7\mu\text{m}$. No oxidation pits and cracks in the oxide layer, which reported conventional β -sialon fabricated from powders mixture^{5,6)} and Si_3N_4 , could be found using optical microscope and SEM observation.

Figure 1 shows the optical micrographs of (a) the ground surface, (b) the specimen surface polished to about $10\mu\text{m}$ after oxidation, and (c) the surface polished to about $15\mu\text{m}$. The oxide layer was removed by polishing the convex part of the surface in the plane polished to about $10\mu\text{m}$. However, it remained in the concave part, and the grinding flaws could be clearly observed. Furthermore, we noticed that the convex part of the grinding flaws, i.e. the oxide substrate interface of the concave part, was rather rounded. In addition, the sharp irregularity, which accompanied cracks ob-

served in the ground surface, was not found. This may indicate that the portion of grinding flaws turned to an oxide layer with the progress in oxidation, and it could be almost completely removed by polishing. However, there were many oxidized films extending widely across two or more grinding flaws, as shown by the arrow mark in the Fig.1. Such portions could be observed after removing the oxide layer by polishing to about $15\mu\text{m}$ as shown in Fig.1(c). This fact indicates the likelihood that the grinding flaws, including cracks are far larger than the average grinding flaws. In addition, it implies that the individual grinding flaw and the accompanying crack do not exist separately, but that cracks accompanying multiple grinding flaws may have landed on each other to form a larger grinding flaw. **Figure 2** shows a schematic illustration of an enlarged grinding flaw. It is considered that the size of the entire crack increases when cracks with multiple grinding flaws connect with each other in the sintered body, as shown into a' of the figure. Furthermore, there is a possibility that when a coarse flaw occurs during grinding due to a cause such as the detachment of grinding grain, the crack in this location may possibly continue to grow if the grinding work is continued. In addition, if a similar coarse flaw takes place nearby, then the cracks may join together for further growth. The local extension of the oxide layer observed on the surface of the polished sample is assumed to be attributed to this fact.

Figure 3 is the optical microscopic comparison of Vicker's indentations (indented at 10kgf , 15sec). **Figure 3** (a, b) shows an indentation before oxidation, and Fig.3 (c, d) shows an indentation after oxidation at 1400°C for 100h

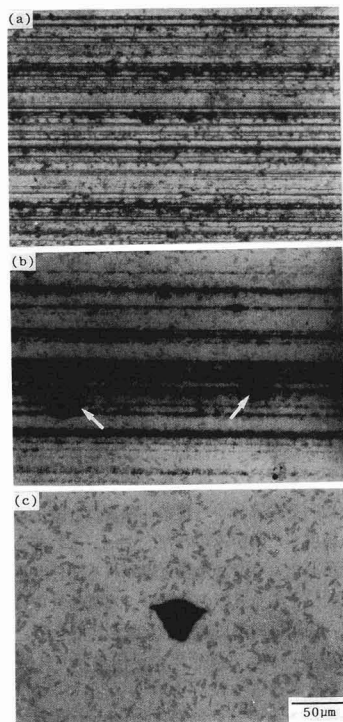


Fig. 1. Optical micrographs of specimen surfaces (a) As-ground, (b) Polished $10\mu\text{m}$ after oxidation at 1400°C for 100h , (arrows indicated wide spots of oxide layer), (c) Polished $15\mu\text{m}$ after oxidation at 1400°C for 100h .

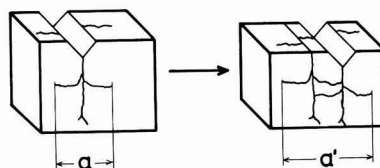


Fig. 2. Schematic illustration of grinding flaw.

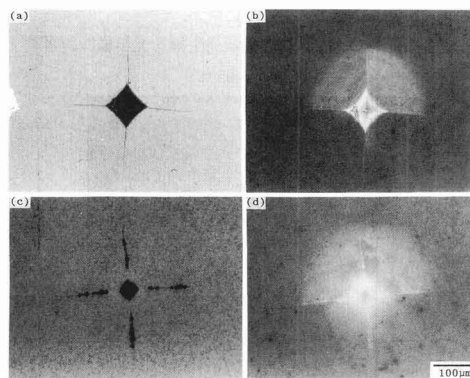


Fig. 3. Optical micrographs of Vicker's indentations (a) Before oxidation; bright field image, (b) Same as (a); dark field image, (c) Polished $15\mu\text{m}$ after oxidation at 1400°C for 100h ; bright field image, (d) Same as (c); dark field image.

and polishing to 15 μm . In specimens before oxidation, the radial cracks occurring from the four corners of indentation were clearly noted. Its dark field image (b) showed radial cracks in the direction parallel to the surface between the cracks. The bright field image (c) on samples polished after oxidation implied that these radial cracks may have disappeared at the four corners of the indentation, but the dark field image (d) clearly shows the existence of these cracks. The portions among these radial cracks, where the oxide layer became locally thick but did not accompany the foams, were observed. These portions are assumed to be result of the oxidation of the area around the foams, which were generated by oxides through air trapped in the opening of the cracks.

Figure 4 indicates the optical micrograph of the unchamfered corner of samples polished to 20 μm after oxidation. Although cracks developed in the sintered body were filled with oxides as shown by the arrow in the figure, they existed in almost the same state as before oxidation.

This fact indicated that oxidation does not progress smoothly in cracks developed inside the sintered body. Accordingly, when such cracks exist, the cracks will be filled with oxides even if oxidation progresses, and they will hardly change in size.

From these results it can be concluded that grinding flaws on the sample surface are oxidized and form a smooth oxide layer which can be removed by polishing. However, the cracks developed inside the sintered body remain in their original sizes, although they are filled with oxides.

3.2. Bending Strength of Samples

Figure 5 indicates the bending strength of (A) as ground specimens, (B) specimens oxidized in air at 1400°C for 100h, (C) specimens to approximately 25 μm after being oxidized at 1400°C for 100h, and (D) polished specimens heat treated in air at 1200°C for 2h after oxidation and polishing.

The strength of was approximately 850MNm⁻² for the ground sample, 1000MNm⁻² for the oxidized sample, 1200MNm⁻² for the polished sample after oxidation, and 1400MNm⁻² for the polished sample reheated at 1200°C for 2h.

Figure 6 shows the optical micrograph of an fracture origin of the ground specimen. The origins were all assumed to be cracks developed to the inside of the sintered body, and their depths were thought to exceed 20 μm . These

fracture origins appeared as flat surfaces by SEM observation, and the cracks shown in Fig.6 could not be clearly observed.

Figure 7 shows the optical micrograph of the fractured surface of the oxidized specimen. The surface of the sintered body was covered with a uniform oxide layer of 7-8 μm , and the formation of foams within the oxide layer or at the oxide substrate interface could not be observed.

The fracture origin of the oxidized specimen occurred at the substrate between the sintered body and oxide layer, the traces of radial fractures extending from this substrate toward both the sintered body and oxide layer, as shown in the figure, was observed. In addition, only a crack, as shown by the arrow in the figure, could be observed, no irregular structure such as coarse grains and, pores could be observed. From this observation, it is believed that the residual stress affected on the cracks developed inside the sintered body through the difference in the thermal expansion coefficient between the oxide layer and the substrate, resulting in the fracture origin. The strength of specimens polished after oxidation was approximately 1200MNm⁻², and one of the 3 specimens was fractured from the black spotted inside defect of about 10 μm . The remaining two were fractured from the surface. The strength of specimens heat treated after polishing was approximately 1400MNm⁻², and two of the 3 specimens were fractured from the inside defect like the polished specimens. The remaining one was

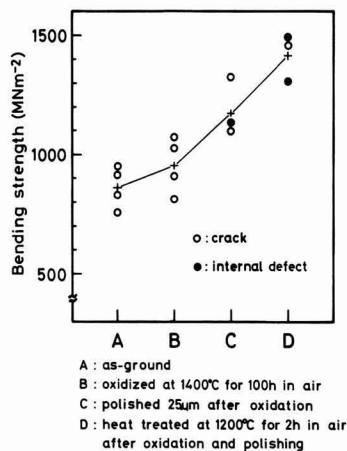


Fig. 5. Room temperature strength of specimens.

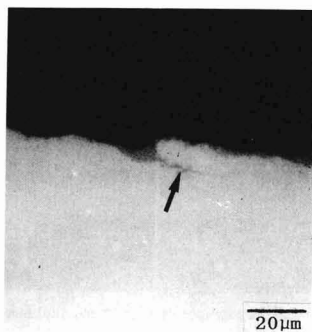


Fig. 4. Optical micrographs of a polished corner of oxidized specimen, (an arrow indicates a crack filled with oxide).

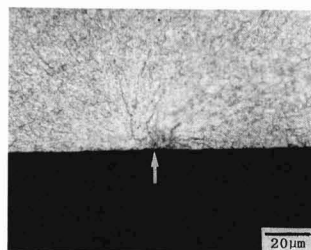


Fig. 6. Optical micrographs of fractured surface of as-ground specimen, (an arrow indicates a fracture origin, $\sigma_f=826\text{MNm}^{-2}$).

fractured from the surface. As reported in the last study,³⁾ the inside defect as a fracture origin may originate as a grain caused by the local growth of sialon crystals, having a large z value, from the spray dried particles, in which the content of Al_2O_3 increased. **Figure 8** shows optical micrographs for the fracture origin of the sample polished after oxidation and broken from the surface. The existence of cracks to the inside of the sintered body could not be clearly observed, as was the case with ground sample. The vertically-stepped-portion, as indicated by the arrow, is the fracture origin. This suggests the existence of cracks caused by grinding in this portion.

As stated in Section 3.1, it was observed that some coarse grinding flaws, which accompanied the cracks developed inside the sintered body of in the samples, were formed during grinding. These cracks were assumed to remain as being filled by oxides in the samples polished after oxidation at 1400°C for 100h. In addition, the K_{IC} of β -sialon was as small as 3MNm^{-2} , and the cracks caused by grinding seemed to have progress to the inside of the sintered body, as shown in Fig.6. The strength may have increased because the polishing after oxidization shortened the cracks in the specimens. However, these cracks could not be completely removed through polishing by $25\mu\text{m}$, as carried out in this experiment. Thus, the remaining cracks may be the fracture origin. In the specimen, which was heat-treated after polishing, the boundary between the crack and the polished plane may have been covered by oxides and become smooth, and the strength may have increased. However, the crack may still have remained to cause the fracture, as was the case in the ground specimen. In general, the surface of the bending specimen is evaluated by measuring surface roughness. However, it seems difficult to measure the depth and size of a sharp crack following the gaining flaw by the surface measurement with a stylus. In addition, even if the grinding work is carried out under the same condition, the size of an accompanying grinding flaw can not be fixed, as stated in Section 3.1. Accordingly, it seems

almost impossible for this method to measure the entire area of tensile plane in the bending specimen in order to confirm that the maximum grinding flaw is the fracture origin. Thus, it is difficult to precisely evaluate the intrinsic strength of a sintered body by investigating the relationship between surface roughness and the measured value of strength. In the case of ceramics, especially those materials which have a very small fracture toughness such as sintered β -sialon body, it may be necessary to remove a considerable volume of the roughly worked surface and to use of more moderate working method which would not cause deep cracks to extend inside the sintered body.

4. Conclusion

β -sialon sintered body was fabricated from a spray dried mixture of $\alpha\text{-Si}_3\text{N}_4$ and $\text{Al}(\text{O}i\text{-Pr})_3$ solution by hot-pressing. Bending specimens, with a size of $3\text{mm}\times 3\text{mm}\times 30\text{mm}$, were ground using a #600 diamond wheel. A change in grinding flaws by oxidation at 1400°C for 100h was observed using an optical microscope. A change in bending strength with oxidation and with polishing after oxidation was examined. Grinding flaws included surface flaws with depths of $5\mu\text{m}$ and cracks with depths of more than $20\mu\text{m}$. The surface flaws changed to a smooth and dense oxide layer after oxidation. However, the cracks were supposed to retain the original size after oxidation, even though they were filled with the oxide. The strength of the sample after oxidation was approximately 1000MNm^{-2} , and that after removing the oxide layer by polishing was approximately 1200MNm^{-2} . The strength of the specimen which was heat treated at 1200°C 2h in air after polishing was approximately 1400MNm^{-2} . These showed an increase in comparison to the ground specimen. This increase was supposed to result from a decrease in the depth of the cracks as fracture origins. To evaluate the essential strength of β -sialon, it is necessary to

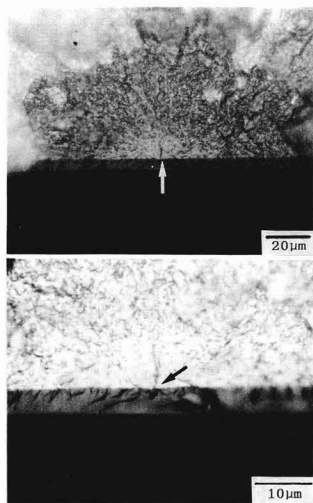


Fig. 7. Optical micrographs of fractured surface of the specimen oxidized at 1400°C for 100h in air, (arrows indicate fracture origins, $\sigma_f=1025\text{MNm}^{-2}$).

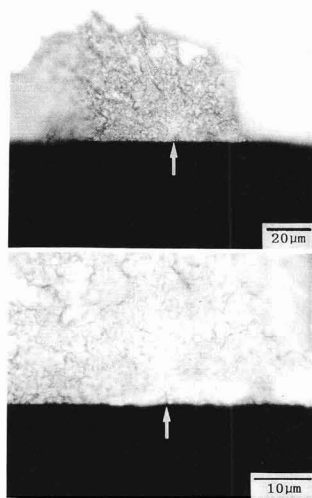


Fig. 8. Optical micrographs of fractured surface of the specimen polished after oxidation at 1400°C for 100h in air, (arrows indicate fracture origins, $\sigma_f=1326\text{MNm}^{-2}$).

remove the cracks, at least those of more than 25 μ m by polishing or by milder machining.

References:

- 1) K.H. Jack, J. Mat. Sci., 11, 1135-1158 (1976).
- 2) K.Kishi, S.Umebayashi, E.Tani and K. Kobayashi, Yogyo Kyokaishi, 94, 179-182 (1986).
- 3) K. Kishi, S. Umebayashi, E. Tani and K. Kobayashi, *ibid*, 95, 630-637 (1987).
- 4) K. Kishi, S. Umebayashi and E. Tani, J. Mat. Sci., 25, 2780-2784 (1990).
- 5) M.H. Lewis and P. Barnard, *ibid.*, 15, 443-448 (1980).
- 6) Y. Hasegawa, K. Hirota, N. Yamane, M. Mitomo and H. Suzuki, Yogyo Kyokaishi, 89, 148-155 (1981).
- 7) K. Niikara, Seramikkusu, 20, 12-18 (1985).
- 8) Y. Hasegawa, H. Tanaka, M. Tsutsumi and H. Suzuki, Yogyo Kyokaishi, 88, 292-297 (1980).
- 9) C.C. Wu, K.R. McKinney, R.W. Rice, W.J. McDonough and S.W. Freiman, J. Mat. Sci., 16, 3099-3104, (1981).

This article is a full translation of the article which appeared in Nippon Seramikkusu Kyokai Gakujutsu Ronbunshi (Japanese version), Vol.99, No.12, 1991.

Characterization of ZSM-5 Zeolite Synthesized from Silica Stone (Ioh Island, Kagoshima Prefecture)

Yoshihiro Hirata, Tadashi Kodama, Kinji Shimada and Yoshimi Ishihara

Department of Applied Chemistry and Chemical Engineering, Faculty of Engineering, Kagoshima University
1-21-40, Korimoto, Kagoshima-shi, 890 Japan

Tetrapropylammonium (TPA) - Na type, Na type, and H type of ZSM-5 zeolites were synthesized hydrothermally from natural siliceous stone containing Al_2O_3 of 1.40 wt% (produced in Ioh island, Kagoshima), TPABr, and NaOH solution, and their physicochemical properties (thermal stability, ion exchange, specific surface area, methanol to gasoline (MTG) test) were investigated. Thermal decomposition temperature of TPA ions in TPA-Na type ZSM-5 and that of Na type ZSM-5 increased with increasing amount of Al ions substituted for Si ions in the zeolite. H type ZSM-5 showed a higher thermal stability than Na type and was stable against heating at 1100°C for 3 hrs. More than 90% Na ions in ZSM-5 was replaced with proton in HCl solution through diffusion-controlled ion exchange at 45°-85°C for 24 hrs. H type ZSM-5 with specific surface areas of 360 to 420 m^2/g converted methanol into gasoline completely at 370°C with no degradation of conversion ratio until 5 hrs (the longest experimental time).

[Received April 22, 1991; Accepted July 18, 1991]

Key-words: ZSM-5 zeolite, Silica stone, Thermal stability, Ion exchange, Specific surface area, Methanol to gasoline test

1. Introduction

ZSM-5 zeolite of high SiO_2 content is highly evaluated as a strong proton acid catalyst in gasoline synthesis from methyl alcohol. For formation of ZSM-5 zeolite, much research is devoted to analyzing the hydrothermal reaction in the system of SiO_2 source - Al_2O_3 source - NaOH - organic compound such as tetrapropylammonium bromide (TPABr). We also reported a possibility of hydrothermal synthesis of ZSM-5 from silica stone (occurred in Ioh island, Kagoshima Prefecture; shorten as IIS) containing 1.40 wt% Al_2O_3 as an aluminum source of ZSM-5.¹⁾ The previous study revealed that (i) ZSM-5 with the molar ratios $\text{SiO}_2/\text{Al}_2\text{O}_3=61-75$ was formed hydrothermally at 220°C in the IIS-TPABr-NaOH- H_2O system, (ii) formation ratio, yield and morphology of TPA-Na type ZSM-5 were strongly affected by the concentration of NaOH solution, (iii) Al_2O_3 and Fe_2O_3 components (Al_2O_3 : 1.40wt%, Fe_2O_3 : 0.36wt%) remained in the formed ZSM-5, (iv) it was possible to control $\text{SiO}_2/\text{Al}_2\text{O}_3$ ratio of ZSM-5 by adding amorphous SiO_2 or NaAlO_2 to IIS, and (v) both Na and TPA ions compensate the charge with substitution of Al for Si ions in ZSM-5. In this paper, we report physicochemical properties (thermal stability, ion exchange, specific surface area, methanol to gasoline (MTG) test) of TPA-Na type, Na type, and H type ZSM-5 obtained hydro-

thermally from the IIS-TPABr-NaOH- H_2O system.

2. Experimental Procedure

ZSM-5 zeolite was hydrothermally synthesized from IIS, with TPABr and NaOH solution. The chemical composition (wt%) of IIS was 2.95 Ig.loss, 94.16 SiO_2 , 1.40 Al_2O_3 , 0.36 Fe_2O_3 , 0.81 TiO_2 , 0.17 CaO, 0.05 MgO, 99.80 Total (molar ratio $\text{SiO}_2/\text{Al}_2\text{O}_3=114$). Detailed synthesis procedure and physical or chemical properties of the as-produced TPA-Na type ZSM-5 were reported in the former paper.¹⁾ In this chapter, we describe mainly measurement procedures on thermal stability, ion exchange, specific surface area and MTG test. TG and DTA analysis of the as-produced TPA-Na type ZSM-5 were carried out up to 1000°C at a heating rate 10°C/min (PTC-10A Type, Rigaku Co., Tokyo, Japan). Phases in the powders after TG and DTA measurement or after heating at 540°-1200°C for 3 hrs were identified by X-ray diffraction (Cu K α , Model 2013, Rigaku Co., Tokyo, Japan). H type ZSM-5 was prepared through ion exchange of Na type ZSM-5 in 0.5 mol/l HCl solution. About 1 g of Na type ZSM-5, which was produced by heating as-produced TPA-Na type ZSM-5 at 540°C for 3 hrs, was immersed in 50 ml of 0.5 mol/l HCl solution and refluxed for 1-168 hrs at 45°-85°C. Ion exchange ratio was calculated by determining Na content in the HCl solution by atomic absorption analysis. Na content of Na type ZSM-5 decomposed by HF treatment was also determined by atomic absorption analysis. Specific surface areas of Na and H type ZSM-5 were measured by BET method using N_2 gas after drying at 300°-350°C for 16hrs in vacuum (<0.1mmHg, Type 2100E, Shimadzu Seisakusho, Kyoto, Japan). Acidic strength of H type ZSM-5 was investigated by measuring the weight of NH_3 gas absorbed on the sample as a function of heating temperature.²⁾ Before measurement, H type ZSM-5 was dried at 500°C in N_2 flow. MTG test was carried out using H type ZSM-5 of 1g at 2.0hr⁻¹ of WHSV (weight hourly space velocity, g feed/g catalyst per hour). The products after 1 and 5hrs of the test were analyzed by gas chromatography.

3. Results and Discussion

3.1. Structure Change of ZSM-5 with Heating

Figure 1 shows TG and DTA curves of TPA-Na type ZSM-5 with a $\text{SiO}_2/\text{Al}_2\text{O}_3$ ratio of 75, which was prepared by hydrothermal reaction at 220°C for 12 hrs in the system $9.30(\text{TPA})_2\text{O} \cdot 18.9\text{Na}_2\text{O} \cdot \text{Al}_2\text{O}_3 \cdot 114\text{SiO}_2 \cdot 1543\text{H}_2\text{O}$. A DTA curve of TPABr is also illustrated in Fig.1. Thermal decom-

position of TPABr, indicated by an exothermic peak of the DTA curve, occurred at around 260°C in air. On the other hand, small weight loss below 400°C and drastic weight loss above 400°C of TPA-Na type ZSM-5 correspond to evaporation of H₂O and thermal decomposition of (TPA)₂O, respectively.^{3,4)} Decomposition of (TPA)₂O was indicated by the exothermic peaks at 409°-443°C of the DTA curve. These data apparently suggest high thermal stability of TPA ions captured in the ZSM-5 framework.⁵⁾ **Figure 2** summarizes (TPA)₂O content and the exothermic peak temperatures indicating thermal decomposition of (TPA)₂O in ZSM-5 as a function of x value in the general formula for TPA-Na type ZSM-5, (TPA_yNa_{1-y})_xAl_{1-x}Si_{1-x}O₂. (TPA)₂O content was almost independent of x value and the formed ZSM-5 contained excess (TPA)₂O compared with x value.¹⁾ The temperatures of two exothermic peaks increased linearly

with increasing x value, indicating higher thermal stability of TPA-Na type ZSM-5 with higher content of substituted Al ions. These results imply that chemical interaction between negatively charged sites with substitution of Al for Si ions and positive TPA ions increased with increasing x value. In other words, increase in coordination number of negatively charged sites surrounding TPA ions increased the thermal stability of TPA ions. The ZSM-5 structure was maintained as determined by X-ray diffraction after decomposition of TPA ions by heating to 540°C, suggesting formation of Na type ZSM-5.

Table 1 shows phase change of Na-TPA and H type ZSM-5 with x value from 0 to 4.4×10⁻² with heating. H type ZSM-5 was produced by ion exchange of Na type zeolite in 0.5 mol/l HCl solution at 75°C. Detailed results of ion exchange are described in section 3.2. The H type ZSM-5 in Table 1 contained no Na ions as determined by X-ray fluorescence. Table 1 indicates that (i) thermal stability of Na type ZSM-5 increases with increasing x value, (ii) Na type ZSM-5 decomposes completely to cristobalite by heating for 3 hrs at 1100°C, and (iii) H type zeolite has a higher thermal stability than Na type zeolite and is stable against heating at 1100°C for 3 hrs. **Figure 3** shows x value dependence of lattice parameters (A) and unit cell volume (B) of Na type ZSM-5 (orthorhombic) formed by heating TPA-Na type at 540°C for 3hrs. Lattice parameters a and b were independent of x value but c parameter decreased at higher x value, indicating small unit cell volume at high x value. Therefore, rigid structure (small unit cell volume) of Na type ZSM-5 with high x value resulted in high thermal stability.

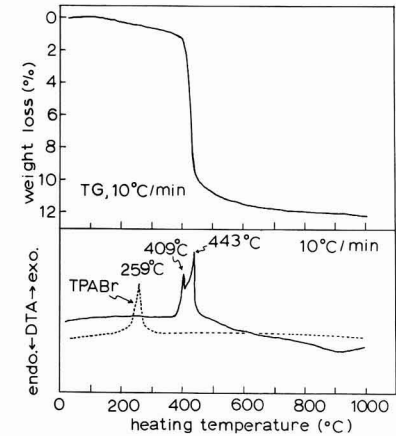


Fig. 1. TG and DTA curves of TPA-Na type ZSM-5 with the SiO₂/Al₂O₃ ratio of 75. A DTA curve of TPABr is also illustrated in Fig.1.

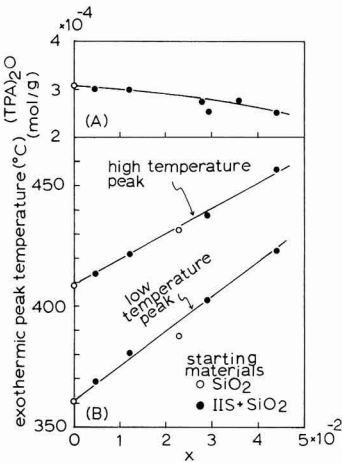


Fig. 2. (TPA)₂O content (A) and exothermic peak temperatures (B) in DTA curves of TPA-Na type ZSM-5 as a function of x in (TPA_yNa_{1-y})_xAl_{1-x}Si_{1-x}O₂.

3.2. Ion Exchange of Na-type ZSM-5

Figure 4(A) shows percent of Na ions exchanged by protons in 0.5 mol/l HCl solution at 70°C as a function of reaction time concerning Na type ZSM-5 containing Na₂O of 1.15 wt%. As seen in Fig.4(A), ion exchange ratio increased in proportion to square root of time, indicating a diffusion-controlled process. It took about 1 week to exchange more than 99% Na ions at 70°C, but 90% of Na ions in ZSM-5 zeolite was exchanged within 1 hr. Above results may suggest existence of two types of Na ions with different self-diffusion coefficients, which would be associated with the structure of ZSM-5. **Figure 4(B)** represents temperature

Table 1. Phase change of Na-TPA type and H type ZSM-5 with heating.

ZSM-5		heating temperature (°C)					
type	x ^{a)}	SiO ₂ /Al ₂ O ₃ ratio	540	600	800	1000	1100 1200
Na-TPA (0hr) ^{b)}	0 ^{c)}	∞				^{s)}	
	0.46×10 ⁻²	431				S	
	1.21×10 ⁻²	164				Z+S	
	2.60×10 ⁻²	75.0	^{z)}				Z+S
	2.89×10 ⁻²	67.1				Z	
Na-TPA (3hr)	4.39×10 ⁻²	43.6				Z	
	2.42×10 ⁻² ^{c)}	80.6	Z			S	S
	2.81×10 ⁻²	69.2		Z	Z	Z+S	S
	2.98×10 ⁻²	65.1	Z			Z+S	S
H (3hr)	2.67×10 ⁻²	72.9		Z	Z	Z	S

a) x in (TPA_yNa_{1-y})_xAl_{1-x}Si_{1-x}O₂ or H_xAl_{1-x}Si_{1-x}O₂, b) heating time
c) SiO₂ source : amorphous silica, other samples : IIS+amorphous silica
d) Z: ZSM-5, S: cristobalite

effect on ion exchange ratio of Na-type ZSM-5. Ion exchange ratio after 24 hrs was increased from 89.7% at 45°C to 99.0% at 85°C by increasing the solution temperature. By X-ray diffraction analysis, it was confirmed that ZSM-5 structure was stable against ion exchange using 0.5 mol/l HCl solution. Similar H type ZSM-5 was also prepared by heating NH_4 type ZSM-5 to 540°C after ion exchange of Na type ZSM-5 in 1-2 mol/l NH_4Cl solution.

3.3. Specific Surface Areas of Na and H Type ZSM-5

Figure 5 represents specific surface areas of the mixtures of Na or H type ZSM-5 and remaining IIS with the molar ratios $\text{SiO}_2/\text{Al}_2\text{O}_3=54-108$ as a function of formation ratio of TPA-Na type ZSM-5 ($f(z)=I_c(501)/(I_c(501)+I_c(101))$, $I_c(501)$, $I_c(101)$: X-ray diffraction intensity regarding (501) plane of ZSM-5 and (101) plane of cristobalite, respectively). Ion exchange of Na type ZSM-5 was done in 0.5mol/l HCl solution at 75°C for 70 hrs. Na content of H type ZSM-5-containing samples was less than 0.20 wt%. The specific surface areas of IIS and TPA-Na type ZSM-5 with $f(z)=1$ were 9.1 and 2.7-11.2 m^2/g , respectively. That

is, significant difference in the specific surface areas for both samples was not recognized. However, Na type ZSM-5-containing samples showed higher specific surface areas, which depended on the formation ratio of ZSM-5 as seen in Fig.5. This result is due to the formation of open space in TPA-Na type ZSM-5 with heating, which was occupied by $(\text{TPA})_2\text{O}$ before thermal decomposition. In addition, H type ZSM-5 showed higher specific surface area than Na type because size of proton can be ignored as compared with that of Na ion.

Specific surface areas of H type ZSM-5 ($f(z)=1$) with x values of 0 to 4.4×10^{-2} in the formula $\text{H}_x\text{Al}_n\text{Si}_{1-x}\text{O}_2$, were 360 - 420 m^2/g and tended to decrease with increasing x value. In addition, a good correlation was observed between unit cell volume of Na type ZSM-5 and specific surface area of corresponding H type ZSM-5. Above results can explain high specific surface area for H type ZSM-5 with small x value (Fig.3). Figure 6 shows change of specific surface area of H type ZSM-5 with x value of 2.7×10^{-2} as a function of heating temperature. Samples were heated for 3 hrs at each temperature. High specific surface area above 300 m^2/g was kept to 1100°C. High thermal stability of H type ZSM-5 evaluated from the specific surface area accorded with the experimental result analyzed by X-ray diffraction (Table 1).

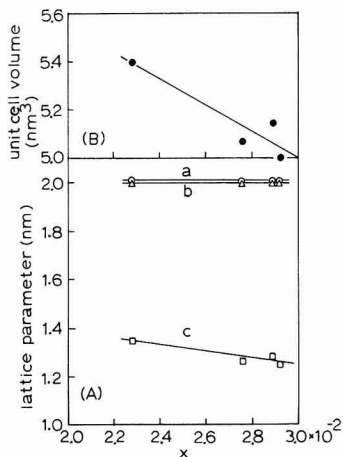


Fig. 3. Lattice parameters (A) and unit cell volume (B) of Na type ZSM-5 as a function of x value in $\text{Na}_x\text{Al}_n\text{Si}_{1-x}\text{O}_2$.

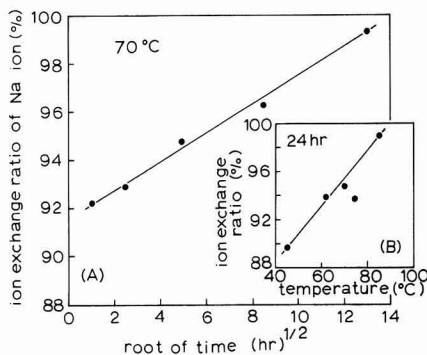


Fig. 4. Percent of ion exchange of Na ions by protons in 0.5 mol/l HCl solution concerning Na type ZSM-5 with Na_2O component of 1.15 wt% as a function of exchange time (A) and solution temperature (B).

3.4. Acidic Strength of H Type ZSM-5 and Gasoline Synthesis

Figure 7 shows a typical temperature dependence of acidic strength of H-type ZSM-5 with the $\text{SiO}_2/\text{Al}_2\text{O}_3$ ratio

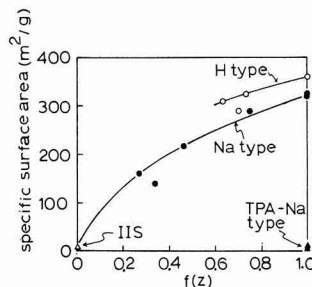


Fig. 5. Specific surface areas of the mixtures of Na or H type ZSM-5 and remaining IIS with the molar ratios of $\text{SiO}_2/\text{Al}_2\text{O}_3=54-108$ as a function of formation ratio of TPA-Na type ZSM-5. Formation ratio of ZSM-5, $f(z)$, means X-ray diffraction intensity ratio of ZSM-5 and cristobalite: $f(z)=I_c(501)/(I_c(501)+I_c(101))$.

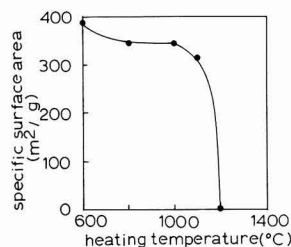


Fig. 6. Specific surface area of H type ZSM-5 with x value of 2.7×10^{-2} in $\text{H}_x\text{Al}_n\text{Si}_{1-x}\text{O}_2$ as a function of heating temperature.

of 78.4, evaluated by the amount of NH_3 gas adsorbed. The amount of NH_3 gas required for formation of NH_4 type ZSM-5 ($(\text{NH}_4)_x\text{Al}_x\text{Si}_{1-x}\text{O}_2$) was calculated to be 7.0 mg/1g H type ZSM-5 from the x value. This calculated amount of NH_3 gas was compared with the experimental result shown in Fig.7. The H type ZSM-5 absorbed more NH_3 gas than the calculated value at 100°-300°C. This comparison suggests that 2 or 3 molecules of NH_3 were adsorbed on 1 proton of H type ZSM-5 at 100°C. The NH_4 type ZSM-5 changes partially to H type ZSM-5 above 300°C.²⁾ A wide temperature range (100°-600°C) for desorption of NH_3 reflects a wide acidic strength distribution of the H type ZSM-5.

Table 2 summarizes the results of MTG test at 370°C using H type ZSM-5 with the $\text{SiO}_2/\text{Al}_2\text{O}_3$ ratios of 70.5 (No.1) and 66.4 (No.2). From Table 2, it was found that (i) methanol was completely converted to hydrocarbon of carbon numbers 1-10 until 5 hrs (the longest test time), (ii) about 60 wt% of produced hydrocarbon consisted of compounds of carbon numbers 6-10, and (iii) weight ratio of aliphatic compounds to aromatic compounds for hydrocarbon of carbon numbers 6-10 was about 40:60. Above results of MTG test were in accordance with the reported data,⁶⁻¹⁰⁾ indicating high quality of H type ZSM-5 catalyst synthesized from IIS.

4. Conclusions

Thermal stability of TPA ions in TPA-Na type ZSM-5 as indicated by exothermic peaks in the DTA curve increased with increasing amount of Al ions substituted for Si ions. Although thermal stability of Na type ZSM-5 also increased with increasing x value in $\text{Na}_x\text{Al}_x\text{Si}_{1-x}\text{O}_2$, Na type ZSM-5 decomposed completely to cristobalite by heating for 3 hrs at 1100°C. H type ZSM-5 showed a higher thermal stability than Na type and was stable against heating at 1100°C for 3 hrs. Na ions in ZSM-5 can be replaced by protons in HCl solution through diffusion-controlled ion exchange. Ion exchange ratio after 24 hrs was 90-100% at 45°-85°C. Specific surface areas of TPA-Na type ZSM-5 were in the range of 3 to 11 m^2/g , and increased greatly to 320 m^2 along with thermal decomposition of TPA ions. H type ZSM-5 showed higher specific surface areas (360-420 m^2/g) than Na type, and kept specific surface areas above 300 m^2/g after heating for 3 hrs at 1100°C. Methanol was completely converted to hydrocarbon of carbon numbers 1-10 over H type ZSM-5 with $\text{SiO}_2/\text{Al}_2\text{O}_3$ ratio of about 70 at 370°C with no degradation of conversion ratio until 5 hrs (the longest experimental time). About 60 wt% of produced hydrocarbon consisted for compounds of carbon numbers 6-10.

Acknowledgements

The authors gratefully thank Prof. T. Takahashi of Kagoshima University for conducting specific surface area measurement and acidic strength measurement of ZSM-5. The MTG test was carried out at the Research Laboratory of Idemitsu Kosan Co., Japan.

References:

- 1) Y. Hirata, T. Kodama, K. Shimada and Y. Ishihara, *J. Ceram. Soc. Jpn.*, 99, 1138-1143 (1991).
- 2) C.T.-W. Chu and C.D. Chang, *J. Phys. Chem.*, 89, 1569-1571 (1985).

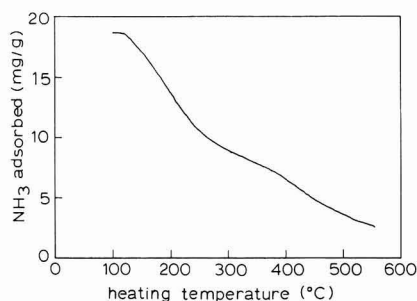


Fig. 7. The amount of NH_3 gas adsorbed on the H type ZSM-5 with x value of 2.5×10^{-2} in $\text{H}_x\text{Al}_x\text{Si}_{1-x}\text{O}_2$ as a function of heating temperature.

Table 2. Synthesis of gasoline from methanol using H type ZSM-5 formed hydrothermally from IIS.

H type ZSM-5	No.1	No.2
$\text{SiO}_2/\text{Al}_2\text{O}_3$ ratio	70.5	66.4
specific surface area (m^2/g)	369	358
temperature (°C)	370	370
WHSV (hr^{-1}) ^{a)}	2.0	2.0
time (hr)	1	5
conversion of methanol (%)	100	100
hydrocarbon distribution (%)	100	100
C ₁	0.4	0.5
C ₂	1.7	1.9
C ₃	17.1	16.8
C ₄	23.8	22.6
C ₅ ⁺	57.0	58.2
product distribution of C ₅ ⁺ (%)		
aliphatics	39.1	40.4
C ₆ aromatics	2.1	2.3
C ₇ aromatics	16.0	14.8
C ₈ aromatics	28.4	27.5
C ₉ aromatics	11.4	11.8
C ₁₀ aromatics	3.0	3.4
isomer distribution of xylene (%)		
p-xylene	24.5	34.2
m-xylene	52.8	46.6
o-xylene	22.7	19.2

a) weight hourly space velocity, g feed/ g catalyst per hour

- 3) S.G. Hill and D. Seddon, *Zeolites*, 5, 173-178 (1985).
- 4) A. Jentys, G. Waeckel, M. Derewinski and J.A. Lercher, *J. Phys. Chem.*, 93, 4837-4843 (1989).
- 5) J.B. Nagy, Z. Gabelica and E.G. Derouane, *Zeolites*, 3, 43-49 (1983).
- 6) T. Inui, T. Hagiwara and Y. Takegami, *J. Japan Petrol. Inst.*, 27(3), 228-235 (1984).
- 7) M. Koizumi and S. Ueda, *Syokubai*, 25(3), 211-224 (1983).
- 8) V.R. Choudhary, K.R. Srinivasan and A.P. Singh, *Zeolites*, 10(1), 16-20 (1990).
- 9) W.O. Haag, R.M. Lago and P.G. Rodewald, *J. Mol. Catal.*, 17, 161-169 (1982).
- 10) R.M. Dessau and R.B. LaPierre, *J. Catal.*, 78, 136-141 (1982).

Corrosion Behavior of Silicon Nitride Ceramics in Aqueous Solutions (Part 1) —Effects of Testing Condition and Various Corrosive Solutions—

Akira Okada, Satoshi Iio*, Tetsuo Asano**, Akira Kokaji***, Hideo Takahashi**** and Masahiro Yoshimura*****

Central Engineering Laboratories, Nissan Motor Co., Ltd.

1, Natsushima-cho, Yokosuka 237 Japan

*Research and Develop Center, NGK Spark Plug Co., Ltd.

2808, Iwasaki, Komaki-shi, 485 Japan

**SMI Techno-Research, Ltd.

1-8, Fuso-cho, Amagasaki-shi, 660 Japan

***Central Research laboratory, Kyocera Corp.

1-4, Yamashita-cho, Kokubu-shi, 899-43 Japan

****Research and Develop Division, Asahi Glass Co., Ltd.

1150, Hazuwa-cho, Kanagawa-ku, Yokohama-shi, 221 Japan

*****Research Laboratory of Engineering Materials, Tokyo Institute of Technology

4259, Nagatsuda-cho, Midori-ku, Yokohama-shi, 227 Japan

Corrosion test of gas-pressure sintered silicon nitride with the additions of yttria and alumina was carried out under various testing conditions. As a result compared with specimens sustained in 6N-H₂SO₄ and those placed at the bottom of glass containers, no significant differences were observed in weight and bending strength. Also, there was no distinctive observation in the test at 90°C and boiling sulfuric acid. Silicon nitride was found to be corroded more severely in H₂SO₄ and H₃PO₄ than NaOH and H₂O. In addition, the test in boiling water resulted in strength degradation of the specimens, while weight change was not detected through corrosion. Relationship between bending strength and weight loss indicated that the rapid decrease of the strength has taken place at below 0.05mg/cm² of weight loss.

[Received April 20, 1991; Accepted September 19, 1991]

Key-words: Corrosion, Sulfuric acid, Silicon nitride, Weight loss, Strength degradation

1. Introduction

Although no one can deny that steel is the representative structural material of today, ceramic materials are expanding their application to structural use due to the excellent properties such as high temperature durability, wear resistance, light weight and corrosion resistance. Taking automobile parts as an example, advantages in application to turbocharger rotors were the high temperature durability and light weight, and application to rocker arm pads was due to the excellent wear resistance.¹⁾ Although ceramics have ever been applied to crucible for melting metals and tools for chemical analysis due to the characteristics superior in corrosion resistance, it is noted that new application areas such as valves for transporting chemical liquids are now expanding.²⁾ It is necessary, however, to carefully select suitable materials and their purity for specific pur-

pose, because some chemical liquids corrode ceramics. Since many cases using ceramics as a substitute for steel would be featured under sever conditions, the material degradation in such environments must be fully understood.

Effects of high-temperature molten metals, corrosive gases and aqueous solutions on corrosion of ceramics have been extensively investigated. For example, molten salt corrosion of ceramics has been studied³⁻⁶⁾ because sodium sulfate formed by the reactions of sulfur compounds in the exhaust gas with splashed sea water may corrode ceramics when they are used for gas turbine engine of airplanes flying over sea. Another example is a corrosion test of ceramics in molten aluminum because the excellent corrosion resistance is required for the electrodes used in the electrolysis process for producing aluminum.⁷⁾ It is suggested that ceramics will be extensively used in the area where the corrosion resistance is strongly required. However, the standardization of methods for evaluating corrosion resistance of ceramics has not been fully established, and several methods such as a dissolution rate,⁸⁻¹⁵⁾ dimensional change¹⁶⁾ and bending strength change¹⁶⁾ are being used for specific purposes. To establish corrosion testing methods and databases of materials, it is thus necessary to develop methods for assessing corrosion resistance.

On the corrosion resistance of silicon nitride in aqueous solutions, corrosion tests in hydrofluoric and hydrochloric acids have been reported.^{9,10)} The specimen used in these experiments were sintered silicon nitride containing yttria and alumina as sintering aids. In the corrosion test in hydrochloric acid, it was reported that large pits were formed and the surface roughness increased as a result of selective dissolution of the silicon and aluminum ions.⁹⁾ On the other hand, the selective dissolution of yttrium and aluminum mainly existing at the grain boundaries was reported to occur in the corrosion test in hydrochloric acid.¹⁰⁾

In the present study, the corrosion resistance of silicon nitride is assessed in solutions where exhibiting the relatively small weight losses, and the effects of methods for the specimen-holding and conditions for heating specimens are investigated in several corrosive solutions to establish a test-

ing method for corrosion.

2. Experimental Procedure

Corrosion resistance of silicon nitride was assessed by measuring changes in weight and 3-point bending strength after immersing in acidic and alkaline solutions, in which each specimen was placed for a given time. The effects of the specimen-holding methods and boiling conditions in corrosive solutions were also investigated.

The specimen was gas-pressure sintered silicon nitride containing yittria and alumina as sintering aids, and it was cut into the dimensions of 4×3×40mm to adapt JIS R1601.

The solutions for corrosion test were 6N sulfuric acid, phosphoric acid, sodium hydroxide and distilled water, and three experimental conditions were chosen: room temperature for 24hrs, 90°C for 1hr, and boiling temperature for 1hr.

Prior to starting the corrosion tests, effects of specimen-holding methods were investigated. Using sulfuric acid as a corrosive solution, comparison was made between specimen placed on the bottom of a flat-bottomed glass vessel and those held 3 to 4cm from the bottom. Volume of the glass vessel was 1000ml, and it contained 500ml of 6N sulfuric acid. As a result, the tests solution level was approximately 6cm from the bottom. Three methods were compared for sustaining specimens from the bottom: holding by hand made spirally wound glass tube, suspended by platinum wire and Teflon string. In use of the would glass tube, the specimen was placed ont he tube in the tests conducted at room temperature and 90°C, while in the tests at the boiling temperature the specimen was fixed between the two glass tubes to prevent the specimen from moving.

Each specimen, which had been washed and dried was weighted and placed in the corrosion test solution for a

given time. It was then washed and dried again to be weighted.

The 3-point bending strength after being immersed in a corrosive solution was measured with a span of 30mm at a crosshead speed of 0.5mm/min to adapt JIS R1601. The fracture surface was observed by using a scanning electron microscope (SEM).

3. Results

Table 1 shows the weight loss and bending strength for the specimens after immersing in 6N sulfuric acid when employing the different placing methods. Three sets of corrosive conditions were used: room temperature for 24hrs, 90°C for 1hr and boiling temperature for 1hr. Total of 5 specimens were tested under each set of conditions, and average and standard deviation were calculated. Difference between suspended specimen and that placed on the bottom was hardly observed. **Figure 1(a)** shows the comparison of weight loss between suspended specimen and that placed on the bottom, and Fig.1(b) shows the comparison of the bending strength. Strong correlation was recognized for the measured results between suspended specimen and that placed on the bottom, while there are no significant difference in weight loss and bending strength due to the difference in settlement methods. No significant difference were observed in weight loss and bending strength resulting from the different conditions between 90°C and boiling temperature while there were the significant differences in the temperature by approximately 15°C and in fluidized conditions of the test solution.

Based on these results the corrosion behavior was evaluated with the specimens placed on the bottom of the glass vessel containing the test solution. The test solutions

Table 1. Weight loss during corrosion test and bending strenght after corrosion test under various suspending methods. (a) Pt wire, (b) teflon string, and (c) glass holder.

(a)

Conditions for Corrosion Test	Pt wire		at the bottom	
	Weight Loss (mg/cm ²)	Bending Strength (MPa)	Weight Loss (mg/cm ²)	Bending Strength (MPa)
R. T., 24hr	0.092±0.005	773±99	0.098±0.012	802±54
90°C, 1hr	0.622±0.012	727±53	0.591±0.021	736±61
boiling, 1hr	0.583±0.007	712±91	0.563±0.017	730±27

*Bending strength for the same lot of specimens before corrosion test was 1060±42MPa.

(b)

Conditions for Corrosion test	Teflon String		at the bottom	
	Weight Loss (mg/cm ²)	Bending Strength (MPa)	Weight Loss (mg/cm ²)	Bending Strength (MPa)
R. T., 24hr	0.065±0.019	816±88	0.059±0.019	860±44
90°C, 1hr	0.61±0.21	729±44	0.67±0.22	743±62
boiling, 1hr	0.99±0.06	717±60	1.18±0.10	742±68

*Bending strength for the same lot of specimens before corrosion test was 955±122MPa.

(c)

Conditions for Corrosion test	Glass Holder		at the bottom	
	Weight Loss (mg/cm ²)	Bending Strength (MPa)	Weight Loss (mg/cm ²)	Bending Strength (MPa)
R. T., 24hr	0.067±0.014	801±102	0.077±0.019	811±72
90°C, 1hr	0.632±0.027	761±49	0.659±0.024	815±75
boiling, 1hr	0.568±0.108	803±22	0.491±0.132	718±87

*Bending strength for the same lot of specimens before corrosion test was 1056±95MPa.

used were 6N sulfuric acid, phosphoric acid, sodium hydroxide and distilled water. After having been tested under the conditions of room temperature for 24hrs or boiling temperature for 1hr, each specimen was measured weight loss and bending strength. **Table 2** summarized the results. No significant weight loss were observed in any corrosive solutions tested at room temperature for 24hrs. In case of boiling solutions, however, sulfuric acid and phosphoric acid were found to cause the most sever corrosion, followed by sodium hydrate, and distilled water exhibited the least. Although there might be effect of temperature resulting from difference in boiling point of these solutions,

the result is considered to be mainly reflected by the difference in test solutions because there is little difference in the corrosive effects of sulfuric acid between 90°C and boiling temperature. For the order of boiling temperature of these test solutions, sodium hydroxide was the highest, followed by sulfuric acid, phosphoric acid and distilled water. **Figure 2(a)** and **(b)** show the plot of bending strength against weight loss, representing the data shown in Tables 1 and 2, respectively. In each case, bending strength rapidly decreased as weight loss increased in the small weight loss region (around 0.1mg/cm² or less), and decreased slowly thereafter. **Figure 3** shows scanning electron micrographs of typical fracture surfaces. It is observed that fracture origins for both tested and untested specimens are in the vicinity of the surface though it is difficult to detect any defects responsible for the fracture origin.

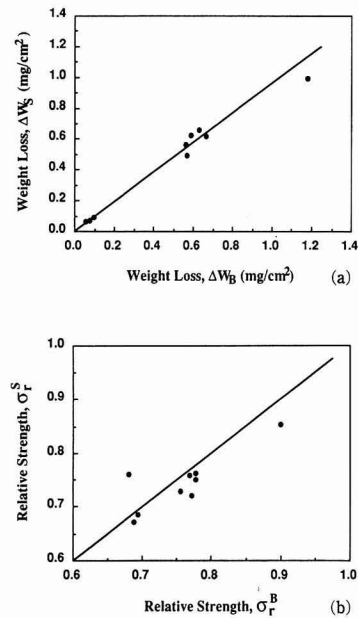


Fig. 1. Comparison of corrosion behavior of silicon nitride between suspended specimens and those placed at the bottom of glass containers; (a) results of weight loss; ΔW_s denotes weight loss for a suspending specimen and ΔW_b denotes weight loss for that placed at the bottom of a glass container, (b) results of bending strength; σ_r^S denotes relative bending strength of a specimen after corrosion in suspended state, and σ_r^B denotes relative bending strength of a specimen after corrosion placed at the bottom of a glass container. The bending strength was normalized by the strength before corrosion test.

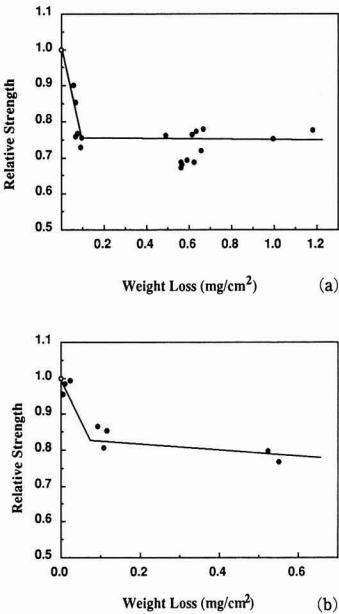


Fig. 2. Relationship between weight loss during corrosion test and bending strength after corrosion test. The bending strength was normalized by the strength before corrosion test. (a) Data from Table 1, (b) data from Table 2; ○: strength before corrosion test.

Table 2 Results of corrosion test for silicon nitride in various solutions.

Testing Conditions	Weight Loss (mg/cm ²)	Bending Strength (MPa)
6N-H ₂ SO ₄ , R. T., 24hr	0.108±0.031	749±85
6N-H ₂ SO ₄ , boiling, 1hr	0.524±0.036	740±67
6N-H ₃ PO ₄ , R. T., 24hr	0.115±0.034	795±68
6N-H ₃ PO ₄ , boiling, 1hr	0.551±0.051	714±40
6N-NaOH, R. T., 24hr	0.024±0.015	923±93
6N-NaOH, boiling, 1hr	0.092±0.017	804±95
H ₂ O, R. T., 24hr	0.010±0.017	914±116
H ₂ O, boiling, 1hr	0.005±0.007	889±148

*Bending strength before corrosion test was 927±68MPa.

4. Discussion

A number of work have been conducted regarding corrosion of ceramics, though they are mainly focused on the dimensional change caused by corrosion in view of the application to refractories. For example, the ASTM²¹⁾ for the assessment of corrosion resistance of refractories to the molten glass specifies to place half of the specimen in molten glass and to measure dimensional changes at the liquid level and in the portion soaked in the liquid.

The strength degradation caused by corrosion was reported for molten salt corrosion of silicon nitride.¹⁷⁾ Changes in 4-point bending strength and fracture toughness of the specimens were reported when exposed to molten NaCl and the eutectic composition of NaCl-Na₂SO₄ at 1000°C for 144hrs, while no relationship was reported with the corroded depth. In this investigation it was reported that a roughly 20% decrease in the fracture toughness from the original level of 4.95MPam^{1/2} occurred during corrosion, namely it was 3.95MPam^{1/2} in NaCl and 4.20MPam^{1/2} exposed in the eutectic composition of NaCl-Na₂SO₄. On the other hand, a decrease in 4-point bending strength was much more notably. The strength was decreased to 540MPa in NaCl and 305MPa in the eutectic composition, while that before the corrosion test was 820MPa. It is noteworthy that there are no tendency of convergence to a constant level. In other words, bending strength significantly decreases through corrosion while the fracture toughness, exhibiting a sudden decrease in the initial stage of corrosion, reaches a certain constant level. Smialek et al.⁶⁾ investigated the changes in weight and bending strength in the molten salt corrosion test of silicon carbide, and reported that the bending strength increase in proportion to 1/2th power of the pit depth. In other words, the bending strength decrease with an increase in the weight loss. Compared with such previous studies, the present study is characterized as investiga-

tion in the region of the much smaller corrosion, indicating that a sudden decrease in strength occurs in a small weight loss region. Similar phenomenon in which a small damage lead to a remarkable decrease in bending strength was reported for oxidation test.²²⁾ Figure 4 shows the plots of bending strength against weight gain for silicon nitride specimens exposed to 1200°C in air for 24hrs and 100hrs, indicating that a rapid decrease in bending strength occurs in a small weight gain region of 0.2mg/cm² or less. The corrosion test differs from the oxidation test in that the former is associated with weight loss whereas the latter with weight gain; nevertheless, they are common in that only a small weight change results in significant reduction in strength by more than 10%. It was reported that bending strength of silicon nitride monotonically decreased as a corrosion proceeded in hydrofluoric acid,¹⁰⁾ and that the decrease was more significantly in hydrofluoric acid.⁹⁾ It is, however, difficult to be compared with the present study because these previous investigations are focussed on the region where the specimens are greatly corroded.

The rapid reduction in bending strength during the initial stage of corrosion may result from the dissolution of the glassy phase in the grain boundaries on the corroded surface.^{9,23,24)} Modulus of elasticity decreases as porosity increases, which, in turn, decreases the fracture toughness. An increase in porosity by 4%, resulting from the formation of corrosion layer over the surface,²³⁾ is estimated to result in a decrease in fracture toughness and bending strength by 8%.²⁵⁻²⁷⁾ In case of non-oxide ceramics corroded in aqueous solutions, the weight gain due to the surface oxidation may lead to an additional increase in porosity and a decrease in bending strength. Another phenomenon to be considered is the selective corrosion of the second phase in the grain boundaries, by which part of the grain bridging effect to improve toughness can be lost.^{28,29)} It was also reported that a residual compressive stress of around 100MPa remains on the machined surface of ceramics,^{30,31)} which can cause degradation in strength being accelerated by stress corrosion cracking in the surface contacting with water. In any cases, the mechanisms proposed so far to explain the rapid reduction in bending strength during the initial stage of corrosion still remain postulative, and should be substantiated in the future.

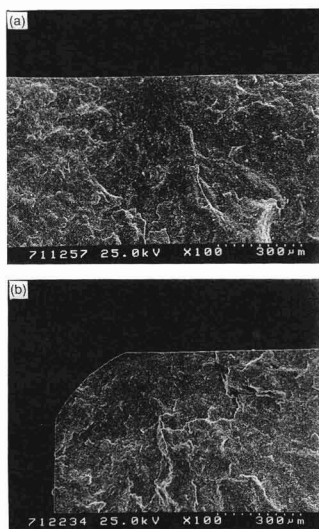


Fig. 3. Scanning electron micrographs for typical failure origins of silicon nitride; (a) after corrosion tested in boiling 6N-H₂SO₄ for 1hr, (b) before corrosion test.

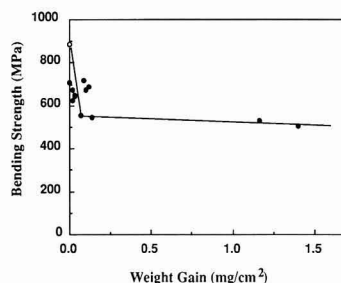


Fig. 4. Relationship between weight gain during oxidation test and bending strength after oxidation for silicon nitride at 1200°C in air.²²⁾ ○ : strength before oxidation test.

5. Conclusions

The effects of specimen-holding and solution heating (90°C and boiling point) procedures in the solution-corrosion of silicon nitride were investigated, while no significant effects were detected using 6N sulfuric acid under the condition of high temperature for 1hr and room temperature for 24hrs.

The silicon nitride corrosion tests were then conducted in various solutions, and the order of sever corrosion was found that sulfuric acid and phosphoric acid were the most, followed by sodium hydroxide and distilled water. The relationship between weight loss and bending strength indicates that the strength decreases rapidly in the small weight loss region (0.1mg/cm²), but slowly thereafter. The rapid reduction in bending strength during the initial stage of corrosion may result from mechanisms such as reduction in fracture toughness in the vicinity of the surface and water-induced stress-corrosion cracking.

Reference:

- 1) A. Okada and M. Andoh, *Jidosha Gijutsu*, 41, 710-715 (1987).
- 2) Y. Sonoda, *Kikai Sekkei*, 32, 41-46 (1988).
- 3) M. Levy and J.J. Falco, *Am. Ceram. Soc. Bull.*, 57, 457-458 (1978).
- 4) N.S. Jacobson and J.L. Smialek, *J. Am. Ceram. Soc.*, 68, 432-439 (1985).
- 5) N.S. Jacobson, *ibid.*, 69, 74-82 (1986).
- 6) J.L. Smialek and N.S. Jacobson, *ibid.*, 69, 741-752 (1986).
- 7) W.A. Zdaniewski, *ibid.*, 68, C309-312 (1985).
- 8) R.E. Tressler, M.D. Meiser and T. Yonushonis, *ibid.*, 59, 278-279 (1976).
- 9) T. Sato, Y. Tokunaga, T. Endo, M. Shimada, K. Komeya, K. Nishida, M. Komatsu and T. Kameda, *J. Mater. Sci.*, 23, 3440-3446 (1988).
- 10) T. Sato, Y. Tokunaga, T. Endo, M. Shimada, K. Komeya, K. Nishida, M. Komatsu and T. Kameda, *J. Am. Ceram. Soc.*, 71, 1074-1079 (1988).
- 11) T. Yoshio, K. Oda, K. Ohoka and K. Oda, *Yogyo Kyokaishi*, 94, 116-122 (1986).
- 12) T. Yoshio, K. Oda and K. Oda, *ibid.*, 95, 435-441 (1987).
- 13) T. Yoshio and K. Oda, *ibid.*, 95, 730-735 (1987).
- 14) T. Kawakubo, H. Hirayama, A. Gotoh and T. Kaneko, *Zairyo*, 38, 300-306 (1989).
- 15) H. Hirayama, T. Kawakubo, A. Goto and T. Kaneko, *J. Am. Ceram. Soc.*, 72, 2049-2053 (1989).
- 16) K. Terao, T. Suzuki and T. Arabori, *Yogyo Kyokaishi*, 94, 111-115 (1986).
- 17) W.C. Bourne and R.E. Tressler, *Am. Ceram. Soc. Bull.*, 59, 443-446 (1980).
- 18) P.F. Becher, *J. Mater. Sci.*, 19, 2805-2814 (1984).
- 19) M.K. Ferber, J. Ogle, V.J. Tennery and T. Henton, *J. Am. Ceram. Soc.*, 68, 191-197 (1985).
- 20) J.L. Smialek and N.S. Jacobson, *ibid.*, 69, 741-752 (1986).
- 21) ASTM C621-84.
- 22) Fine Ceramics Society of Japan, *Researches on standardization of Fine Ceramic Materials*, FY19, (1988) 5-56.
- 23) A. Okada, S. Iio, T. Asano and M. Yoshimura, *Seramikkusu Ronbunshi*, in printing.
- 24) S. Iio, A. Okada, T. Asano and M. Yoshimura, *ibid.*, unpublished.
- 25) K.K. Phiani, S.K. Niyogi, *J. Mater. Sci. Lett.*, 6, 511-515 (1987).
- 26) S.K. Dutta, A.K. Mukhopadhyay, D. Chakraborty, *J. Am. Ceram. Soc.*, 71, 942-947 (1988).
- 27) S.K. Dutta, A.K. Mukhopadhyay, D. Chakraborty, *Am. Ceram. Soc. Bull.*, 68, 2098-2102 (1989).
- 28) P.F. Becher, *J. Am. Ceram. Soc.*, 74, 255-269 (1991).
- 29) A. Okada, N. Hirotsaki, *J. Mater. Sci.*, 25, 1656-1661 (1990).
- 30) F.F. Lange, M.R. James and D.J. Green, *J. Am. Ceram. Soc.*, 66, C-16-17 (1983).
- 31) D. Johnson-Walls, A.G. Evans, D.B. Marshall, M.R. James, *ibid.*, 69, 44-47 (1986).

This article is a full translation of the article which appeared in Nippon Seramikkusu Kyokai Gakujutsu Ronbunshi (Japanese version), Vol.99, No.12, 1991.

Thermal and Mechanical Properties of SiC-p/Al₂O₃ Composite

Yoshio Akimune, Yasushi Katano, Tooru Akiba and Toshio Ogasawara

Nissan Motor Co., Ltd. Central Engineering Laboratories, Materials Research Laboratory
1, Natsushima-cho, Yokosuka-shi, 237 Japan

Thermal and mechanical properties of SiC-particle/Al₂O₃ composite produced by direct metal oxidation process were investigated. The composite shows similar level of bending strength (537MPa) and fracture toughness (4.8MPa√m) compared to monolith alumina and SiC. On the other hand, heat absorption at 578°C caused by Al-Si eutectic and exothermal peak at 960°-1140°C resulted from AlN formation were detected by DTA in N₂. Therefore, residual metallic phase from starting metal alloy influences the microstructure and properties of composite at elevated temperature.

[Received May 23, 1991; Accepted August 22, 1991]

Key-words: Direct metal oxidation, DTA, Nitridation, SiC-p/Al₂O₃, Mechanical properties.

1. Introduction

Techniques for compounding second-phase ceramics with matrix ceramics to toughen ceramics have been reported by many researchers. In these techniques, the characteristics and shapes of the second-phase ceramics are important factors. Two processes are well known: one process is to compound second-phase particles or whiskers having a higher Young's modulus than the matrix and to use crack bowing or crack deflection mechanism⁽¹⁻³⁾, and the other is to compound minute particles into the particles of matrix for subgraining⁽⁴⁻⁶⁾. However, these processes for sintering ceramics composites require a pressurized sintering process using a hot press which sinters coarse second-phase particles, needle-like particles, and ultrafine particles and a hot isostatic press (HIP) which promotes particle growth of matrix. Therefore, there are disadvantages that the shape of product is limited for hot press and that the sintering process is complex for HIP^(5,6).

For oxide matrix, a near-net production process by means of direct metal oxidation has recently been reported. This process is considered as one of the effective prices for producing ceramics. With this process, a preform is prepared from second-phase ceramics, and the matrix is oxidized in a high-temperature oxidation atmosphere after the matrix is infiltrated with metal.⁽⁷⁻¹⁰⁾ However, the thermal and mechanical properties of ceramics produced by such a chemical process are not yet known⁽¹¹⁾. In the present study, we investigate the thermal and mechanical properties of SiC-particle/Al₂O₃ composite produced by the direct metal oxidation process and clarified the relationship with the microstructure of ceramics composite produced by the chemical process.

2. Experimental Procedure

2.1. Material Procedure

The SiC-p/Al₂O₃ composite used in this experiment is a composite produced by the Direct Metal oxidation Process (DIMOXTM) from DuPont Lanxide Composite Co., Ltd. This material is prepared by the following process: SiC compact corresponding to 55vol% is prepared by the slip cast method, and is infiltrated with molten aluminum alloy for simultaneous oxidation. Thus, the SiC-p/Al₂O₃ composite is produced to near net shape.

2.2. Method for Evaluating Composite Microstructure and Mechanical Properties at Normal Temperature

Bending test pieces measuring 40mm×4mm×3.2mm were cut from a square plate of 150mm×150mm×3.2mm. The bending strength was measured at room temperature and the data was reduced by using the Weibull chart.⁽¹²⁾ After testing, the change of crystalline phase and microstructure of test piece was evaluated with X-ray diffraction, scanning electron microscopy (SEM), electron probe microanalysis (EPMA) and transmission electron microscopy (TEM).

2.3. Evaluation of Thermal Properties

The differential thermal analysis (DTA) and thermogravimetry (TG) were performed in a nitrogen atmosphere at temperatures from room temperature to 1400°C to investigate the thermal properties, focusing on the phase change and decomposition which are accompanied by heat generation/absorption in nitrogen.

3. Experimental Results and Discussion

3.1. Microstructure of Ceramics Composite

From the result of X-ray diffraction for SiC-p/Al₂O₃ composite (Fig.1), α-SiC and α-Al₂O₃ were detected on the surface layer, and Al and Si were detected in addition to α-SiC and α-Al₂O₃ inside the composite. Figure 2 shows the microstructure of composite obtained by an optical microscope. From the results of X-ray diffraction and EPMA, it is suggested that the composite surface is composed of preformed α-SiC (black) and α-Al₂O₃ formed by oxidation (gray), whereas the inside is composed of α-SiC (black), α-Al₂O₃ formed by oxidation (gray), and unreacted Al (white) and Si (grayish black).⁽⁷⁻¹¹⁾ The optical micrograph revealed that the crystalline grain was relatively large: the size of crystalline grain of α-SiC was 10–20μm, that of α-Al₂O₃ was 3–10μm, and Al and Si, which lay at the grain boundary, had a size of less than 5μm. Figure 3 shows the

observation results obtained by TEM. In the observation of microstructure in a light field, three forms were observed: black, grayish white, and dark gray. Putting together the above results of analysis, this material was found to be composed of four components of Al_2O_3 , SiC, Al, and Si.

3.2. Thermal Properties

As the result of cyclic differential thermal analysis in a nitrogen atmosphere (Fig. 4), an endothermal peak was detected at 578°C and exothermal peak accompanied by an expansion was detected between 960°C and 1140°C for the first analysis. The former peak was presumed to be a peak caused by Al-Si eutectic by combining with the result of X-ray diffraction,¹³⁾ and the latter was confirmed to result from a nitridation of $2\text{Al} + \text{N}_2 \rightarrow 2\text{AlN}$ by combining with the result of X-ray diffraction.¹⁴⁾ The aluminum with which the preform is infiltrated is an eutectic alloy of Al-Si and has a selected alloy composition that easily penetrates the preform. On heating further, a sharp exothermal peak was detected at 1260°C. Although it was presumed to be a crystallization peak of Al_2O_3 or a transition peak, a detailed study is needed on this peak. The formation of MgO ¹⁵⁾ and MgAl_2O_4 ¹⁰⁾ described in the references were not confirmed. These results indicate that the composite is changed by heat, being thermally unstable. For the peak at 840°C observed during cooling, the cause could not be confirmed.

In the second heating process, endothermal peaks were detected at 392°C and 578°C. The former was presumed to be caused by deposit due to the aging of aluminum alloy because a change of Al composition was caused by the nitrating reaction of Al in the first heating process,¹⁶⁾ whereas the latter was presumed to be caused by Al-Si eu-

tectic. For these peaks, however, a detailed analysis is needed. The exothermal peak at 960~1140°C, which was presumed to indicate the formation of AlN, was low; the surface layer was covered with AlN and the nitridation was inhibited. The exothermal peak at 1260°C was not detected, which suggests that crystallization was completed. Thus, there are many points about the thermal properties that are still unknown.

3.3. Mechanical Properties at Room Temperature (Table 1)

The hardness of $\text{SiC}_p/\text{Al}_2\text{O}_3$ composite in the vicinity of the surface was 9.7GPa. Although the presence of voids produced the low hardness, the entire Vickers impression was depressed, so it was presumed to be a fracture of material under point load. At the center of the specimen, the impression was clear, and the hardness was 12.3GPa, which showed an increase of about 30% and suggested that densification proceed inside the material. The Young's modulus was as low as 322GPa in relation to $\alpha\text{-SiC}$ and $\alpha\text{-Al}_2\text{O}_3$. This is probably due to residual aluminum.

The result of bending strength showed high mechanical properties; the strength was relatively high, being 537MPa, and Weibull coefficient was 20.1. After the bending test, the crystalline grains on the fracture surface were observed (Fig. 5). The size of primary grain of SiC was 3~10 μm ; it was found that fracture occurred within almost all grains. The reasons for relatively high bending strength despite the transgranular fracture are probably that the crystalline grains are small in size and that there is a crack blunting effect of residual Al with which the channels in microstructure are filled.⁹⁾

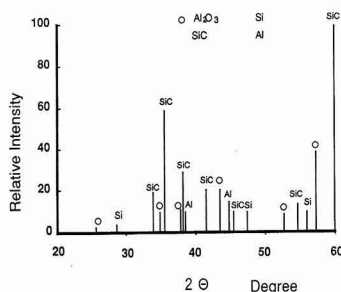


Fig. 1. X-ray diffraction result of $\text{SiC}_p/\text{Al}_2\text{O}_3$.

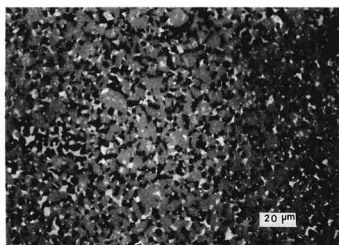


Fig. 2. Optical micrograph showing multiphase structure.

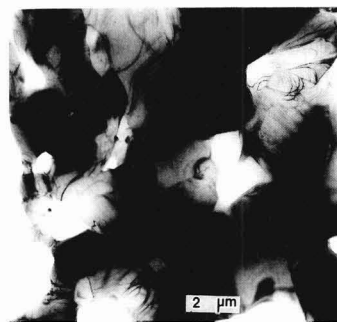


Fig. 3. TEM micrographs of $\text{SiC}_p/\text{Al}_2\text{O}_3$.

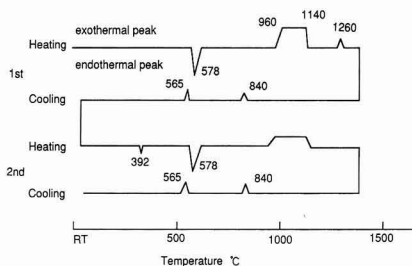


Fig. 4. The DTA result in N_2 with $\pm 10^\circ\text{C}/\text{min}$ heating and cooling speed.

Table 1. Properties of SiC-p/Al₂O₃.

SiC-p/Al ₂ O ₃		Mechanical properties	
Crystal Phase		α SiC, α Al ₂ O ₃ , Al, Si	
Density	(Mg/m ³)	3.42	
Young's Modulus	(GPa)	322	
Bending Strength	(MPa)	537 ± 31	
Fracture Toughness	(MPa√m)	4.8	
Hardness Hv-300	(GPa)	9.7	Surface
		12.3	inside

The value of fracture toughness was $4.8\text{MPa}\sqrt{\text{m}}$, which was fairly high as compared with that of alumina and SiC. On the cross section obtained by the SEPB method, a fracture surface due to transgranular fracture was found. The residual aluminum is thought to serve to enhance the resistance to fracture by the dislocation, slide, and bridging at the tip of crack.⁹⁾

4. Conclusions

In this work, we investigated the thermal and mechanical properties of SiC_p/Al₂O₃ composite produced by the direct metal oxidation process, and clarified the relationship with the microstructure of ceramics composite produced by the chemical process. The aggregate grain of composite had a size of 10–20μm (3–10μm for crystalline grain) for SiC, and 3–10μm for Al₂O₃. Al and Si exist at the grain boundary, whose size was less than 5μm. Regarding the thermal properties in a nitrogen atmosphere, a peak due to Al-Si eutectic was detected at 578°C, and an exothermal peak caused by a reaction of $2\text{Al} + \text{N}_2 \rightarrow 2\text{AlN}$ was detected at 960–1140°C. Thus, the effect of the phase change of residual metal and reaction was found. The mechanical properties (bending strength and fracture toughness) at normal temperature were at the same level as those of monolithic Al₂O₃ and SiO₂, which is thought to satisfy the expected value of materials for mechanical parts.

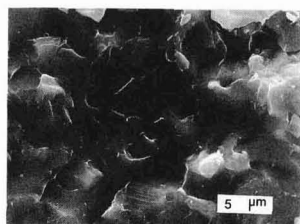


Fig. 5. SEM micrographs of fractured surface of SiC-p/Al₂O₃ composite.

Reference:

- 1) D.J. Green, J. Am. Ceram. Soc., 66, C4-C5 (1983).
- 2) P.F. Becher and G.C. Wei, *ibid.*, 67, C267-269 (1984).
- 3) K.T. Faber and A.G. Evans, Acta Metall., 31, 565-576 (1983).
- 4) Z. Li and R.C. Bradt, J. Am. Ceram. Soc., 71, 70-77 (1989).
- 5) K. Niihara and A. Nakahira, Proc. 3rd Int. Sympo. Ceramic Materials and Components for Engines ed. by V.J. Tannery, Am. Ceram. Soc., Ohio, (1989) 919-926.
- 6) Y. Akimune, J. Am. Ceram. Soc. 73, 3019-3025 (1990).
- 7) M.S. Newkirk, A.W. Urquhart, H.R. Zwicker and E. Breval, J. Mat. Res., 1, 81-89 (1986).
- 8) M.S. Newkirk, H.D. Leshner, D.R. White, C.R. Kennedy, A.W. Urquhart and T.D. Claar, Ceram. Eng. Sci. Proc. 8, 879-885 (1987).
- 9) M.K. Aghajanian, N.H. Macmillan, C.R. Kennedy, S.J. Luszcz and R. Roy, J. Mat. Res. 24, 658-670 (1989).
- 10) A.G. Gesing, G. Burger, E. Luce, N. Claussen, S. Wu and N.A. Travitzky, Ceramic. Eng. Sci. Proc. 11, 821-841 (1990).
- 11) E. Breval, M.K. Aghajanian and S.J. Luszcz, J. Am. Ceram. Soc. 73, 2610-2614 (1990).
- 12) W. Weibull, J. Appl. Mech., 18, 293-297 (1951).
- 13) Al-Si 164-165 Binary Alloy Phase Diagram (Vol1) ed. by T.B. Massalski, Am. Soc. Met., Metals Park, Ohio (1986).
- 14) D.K. Creber, S.D. Poste, M.K. Aghajanian and T.D. Claar, Ceram. Eng. Sci. Proc., 9, 975-982 (1988).
- 15) T. Cho, Y. Kagawa and S. Watanabe, Proc. Jpn. Inst. Metals Autumn Seminar (1990) 478.
- 16) S. Kokubo, Tohoku Univ. Science Reports 1st Ser. 20, 268 (1931).

This article is a full translation of the article which appeared in Nippon Seramikkusu Kyokai Gakujutsu Ronbunshi (Japanese version), Vol.99, No.12, 1991

β -Tricalcium Phosphate Coating on Titanium

Motohiro Toriyama, Yukari Kawamoto, Takahiro Suzuki, Yoshiyuki Yokogawa,
Kaori Nishizawa and Hajime Nagae

Government Industrial Research Institute, Nagoya
1-1, Hirate-cho, Kita-ku, Nagoya-shi, 462 Japan

Bioactive β -tricalcium phosphate (β -TCP) coating onto titanium was studied. It is shown that the β -TCP adhered to the surface of a titanium plate by the use of a frit, which was composed of CaO, TiO_2 , P_2O_5 and a few mol% Na_2O . The frit as a coated layer resulted in the formation of β -TCP and $\text{CaTi}_4(\text{PO}_4)_6$ phases by a thermal treatment at 800°C for 24h.

[Received July 28, 1991; Accepted September 19, 1991]

Key-words: β -Tricalcium phosphate, Titanium, Coating, Bioactive, Frit

1. Introduction

Calcium phosphate compounds have excellent affinity with biological tissue, and are expected to be used as biological materials. The authors have studied to provide high strength for the sintered bodies of β -tricalcium phosphate (β -TCP), aimed at its application to artificial tooth and bone materials. Achievements so far from this research¹⁻⁵⁾ include β -TCP sintered bodies with strength about 40% higher than human cortical bone. However, this is still insufficient for use as items such as artificial joint stems exposed to complicated and shock force.

In recent years, prospects have been using for cementless artificial joint systems, and research is flourishing on materials with bioactive calcium phosphate compounds coated onto the surfaces of titanium alloys. The major coating methods of calcium phosphate compounds under study are plasma spraying and coating by glass with dispersed calcium phosphate crystals. The coated layer formed by plasma spraying has high adhesion strength while temperatures as high as 10000°C by plasma tend to decompose calcium phosphate compounds. Moreover, the reliability of the glass method has not been proved yet.

The authors have studied β -TCP coating to titanium metal by a sintering reaction. However, the metal has a transition temperature at 882°C and oxidation was active on its surface with heat treatment in air over 900°C so that a coating layer could not be formed. Consequently, in order to lower heat treatment temperature as well as to form a coating layer with good adhesion, the presence of a liquid phase was considered to be necessary during a coating reaction. Hosono et al.⁶⁾ reported that $\text{CaO-TiO}_2\text{-P}_2\text{O}_5$ glass crystallizes into β -TCP and $\text{CaTi}_4(\text{PO}_4)_6$ by the addition of Na_2O along with heat treatment for a long period. The authors intended to apply this system to titanium metal coating.

2. Experimental Method

2.1. Coating

The raw materials of CaCO_3 , TiO_2 , H_3PO_4 and Na_2CO_3 were weighed out to provide composition showed in Table 1, and mixed with water. The mixtures were charged in a zirconia pot mill and ground for 4h. Dried at 200°C, they were placed in a platinum crucible and held at 1350°C for 1h. The resulting molten liquids were dropped into water for quenching to form frits, which were ground in wet, dried and watered again to prepare slurry with a solid matter content of 20wt%. The slurry was sprayed uniformly onto pure titanium plates (CP1) heated at 150°C. The slurry-applied pure titanium plates underwent heat treatment in air at 700-900°C.

2.2. Analyses

The crystal phases of synthesized substances and coating films were identified by X-ray diffraction. Moreover, the synthesized substances were subjected to thermal analysis using Samoflex 8112BH (Rigaku Denki). The surfaces and interfaces of coating layers were of served with a scanning electron microscope S-530 (SEM; Hitachi, Ltd.), and element analysis was conducted with an X-ray microanalyzer EMAX-2200 (Horiba, Ltd.).

3. Results and Discussion

Two kinds of slurry were prepared by applying water to the following samples: a ground sample with the same composition as the sample No.1 reported by Hosono et al.,⁶⁾ and a ground and fritted sample after melting at 1350°C. Each slurry sample was applied to titanium followed by heat

Table 1. Composition of frit for β -TCP coating.

Sample	Composition (mol%)				Phase
	CaO	P_2O_5	TiO_2	Na_2O	
No.1	45	30	25	2	amorphous
No.2	50	30	20	2	amorphous
No.3	55	30	15	2	amorphous
No.4	60	30	10	2	amorphous
No.5	65	30	5	2	amorphous
No.6	70	30	0	2	$\alpha\text{-Ca}_2\text{P}_2\text{O}_7$
No.7	45	30	25	-	amorphous
No.8	50	30	20	-	amorphous
No.9	55	30	15	-	amorphous
No.10	60	30	10	-	amorphous
No.11	65	30	5	-	$\alpha\text{-Ca}_2\text{P}_2\text{O}_7$

treatment at 760°C for 24h. The sample with only mixing and grinding did not react with titanium at all and peeled off from the face plate. When heat treatment temperature exceeded 900°C, titanium surfaces were strongly oxidized to form only brittle oxide layers and not coating layers with good adhesion. On the other hand, slurry from fritted samples after melting provided coatings adhering closely to titanium with heat treatment at 760°C.

Figure 1 shows the results of differential thermal analysis with granular glass having the composition of the sample No.1 and obtained by melting and quenching in water as well as its ground sample. The granular glass has a glass transition point at 650°C as reported earlier,⁶⁾ and crystallized at 821°C. The glass transition temperature of the ground sample was the same as that of the granular glass, but the crystallization temperature was lowered to 755°C by grinding. This temperature decrease was expected to offer a decrease in heat treatment temperature for the crystallization of coating layers and reduced heat treatment time, thus controlling the oxidation of titanium base plates.

Considering the results of differential thermal analysis, heat treatment after slurry application was conducted for 1h in the range of 700°-900°C (50°C higher than glass transition points, and the crystal phases of coating layers were examined by X-ray diffraction. As clearly shown in Fig.2, samples without heat treatment were amorphous only with halos near $2\theta=28^\circ$. Nevertheless, mere heat treatment at 700°C for 1h resulted in a distinct diffraction line by $\text{CaTi}_4(\text{PO}_4)_6$ and a light diffraction line by β -TCP. Moreover, the inten-

sity of the β -TCP diffraction line increased with a rise in heat treatment temperature. Over 850°C the β -TCP phase was no longer detected and β - $\text{Ca}_2\text{P}_2\text{O}_7$ was formed instead. Moreover, the effect of heat treatment time intended for crystallization was also studied, but the X-ray diffraction pattern of a coating layer indicated complete crystallization only by heat treatment for 1h, and no change was recognized in the diffraction pattern even with prolonged heat treatment time.

In order to heighten the concentration of β -TCP in coating layers as well as to investigate the possibility of the formation of apatite hydroxide, samples with different CaO content were prepared and underwent fritting as in Table 1. Each sample formed a uniform molten liquid at 1350°C. Out of ground samples, No.6 without TiO_2 at all and No.11 without Na_2O crystallized already into α - $\text{Ca}_2\text{P}_2\text{O}_7$ after quenching. The amorphous samples No.1-5 and 7-10 were applied to titanium followed by heat treatment at 800°C for 1h. Each coated titanium base plate has a coating layer on its surface. The cross sections of the coating layers were observed with SEM. The sample No.2 formed a uniform vitreous coating layer, while the other samples have independent crystallized particles the grain boundaries of which showed a sintered texture. Additionally, in the case of base plates coated with the samples No.1 and 3-5 containing Na_2O , intermediate layers 5-8 μm thick were noticed which exhibited different contrast in secondary electron images. The linear analysis of cross sections of the coating layers also proved that intermediate layers were formed different

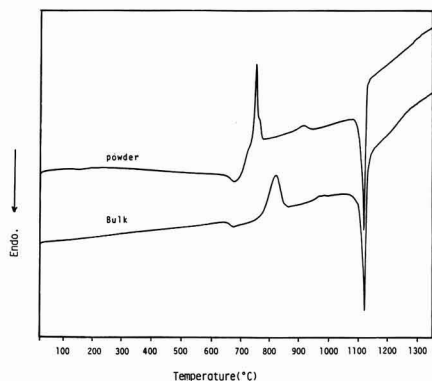


Fig. 1. DTA curves of Ca-Ti-P glass containing Na_2O and frit (sample No.1).

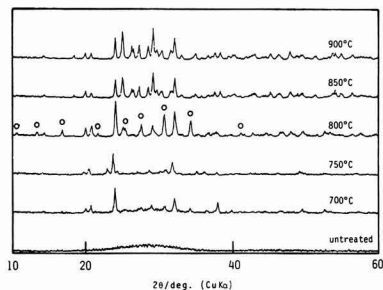


Fig. 2. X-ray diffraction patterns of heat treated Ca-Ti-P frit (sample No.1). (○): β -TCP

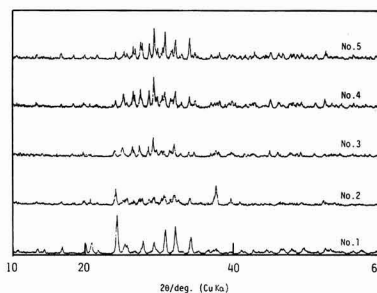


Fig. 3. X-ray diffraction patterns of heat treated titanium plate coated with Ca-Ti-P frit.

Table 2. Detected phases of titanium plate coated with Ca-Ti-P frit.

Sample	Phase
No.1	$\text{CaTi}_4(\text{PO}_4)_6$ β -TCP
No.2	$\text{CaTi}_4(\text{PO}_4)_6$ CaO
No.3	β - $\text{Ca}_2\text{P}_2\text{O}_7$
No.4	β - $\text{Ca}_2\text{P}_2\text{O}_7$ β -TCP
No.5	β - $\text{Ca}_2\text{P}_2\text{O}_7$ β -TCP
No.6	
No.7	α - $\text{Ca}_2\text{P}_2\text{O}_7$ $\text{CaTi}_4(\text{PO}_4)_6$
No.8	β - $\text{Ca}_2\text{P}_2\text{O}_7$ $\text{CaTi}_4(\text{PO}_4)_6$
No.9	α - $\text{Ca}_2\text{P}_2\text{O}_7$
No.10	α - $\text{Ca}_2\text{P}_2\text{O}_7$
No.11	

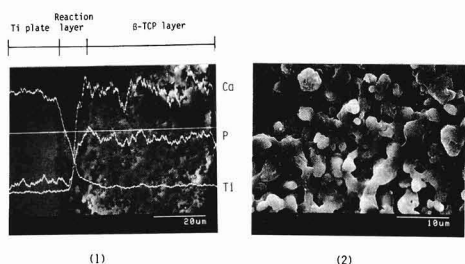


Fig. 4. Scanning electron micrograph of titanium plate coated with Ca-Ti-P frit. (1) cross section, (2) surface.

from the coating layers. The intermediate layers were mainly composed of Ti and P, but included little Ca.

By contrast, in base plates coated with the samples No.7-10 not containing Na_2O , such diffusion layers were not encountered at all, and coating layers were in indirect contact with the titanium base plates. The plate with No.2 developed a large crack at the interface of the titanium base and an intermediate layer while those with No.4 and 5 at the interface of the intermediate layer and coating layers.

Figure 3 gives X-ray diffraction patterns of coating layers and Table 2 the crystal phases identified from the X-ray diffraction patterns. β -TCP was not detected from the samples 7-10 without Na_2O . By contrast, distinct diffraction lines by β -TCP were noticed in the samples No.1, 4 and 5 with Na_2O added in frit synthesis. However, No.2 did not give the β -TCP diffraction line but formed CaO. Heightening the β -TCP content of coating layers was attempted by varying frit composition for coating, and yet conditions adopted this time did not provide better composition than No.1 reported by Hosono et al.

As described earlier, no change in the diffraction patterns of coating layer surfaces resulted from prolonged heat treatment time for the crystallization of coating layers. Nevertheless, qualitative scratching tests in which the surface of a coating layer is scratched with a metal needle showed that the extension of heat treatment time improves the adhesion of coating layers. Likewise, the linear analysis of cross sections of the coating layers revealed that prolonged heat treatment time leads to a decrease in Ca and an increase in Ti content intermediate layers formed at interfaces between titanium base plates and coating layers. The same heat treatment was performed in a vacuum furnace, but applied coating layers could be peeled off the base plates with ease. Consequently, the intermediate layer formed by a reaction

between a coating agent and the surface oxidation layer of the titanium base plate formed by heat treatment in air were considered to be important for improving the adhesion of the coating layer. Figure 4 shows SEM photos of the surface and cross section of a sample coated with No.1 and treated at 800°C for 24h. The coating layer had a porous surface with fine pores about $1\mu\text{m}$ in size. Materials coated by the method stated in this paper are expected to provide not only chemical adaptability by β -TCP but also surface structures suitable for mechanical bonding with bone tissue.

It is necessary as the next step to conduct evaluation of the biological adaptability of this material along with quantitative study of the adhesion strength of coating layers.

4. Conclusion

Research was carried out in an effort to coat β -TCP with excellent biological compatibility onto titanium surfaces. $\text{CaO-TiO}_2\text{-P}_2\text{O}_5$ frits containing a small amount of Na_2O were prepared, sprayed to titanium, dried, and subjected to heat treatment at 800°C in air for 24h, eventually to form a strong coating layer composed of β -TCP and $\text{CaTi}_4(\text{PO}_4)_6$. TiO_2 formed in the titanium surface during the heat treatment process was surmised to be important for the improved adhesion of coating layers. A single cycle of frit spraying and drying formed a coating layer about $100\mu\text{m}$ thick with a porous surface, so that the coating method was considered to be suitable for artificial bones.

References:

- 1) M. Toriyama and S. Kawamura, *Yogyo Kyokaishi*, 94, 1004-1008 (1986).
- 2) M. Toriyama, S. Kawamura, H. Nagae and K. Ishida, *Yogyo Kyokaishi*, 95, 822-824 (1987).
- 3) M. Toriyama, S. Kawamura, Y. Ito, H. Nagae and I. Toyama, *Seramikkusu Ronbunshi*, 96, 831-841 (1988).
- 4) M. Toriyama and S. Kawamura, *Yogyo Kyokaishi*, 95, 741-745 (1987).
- 5) M. Toriyama, S. Kawamura, Y. Ito and H. Nagae, *Seramikkusu-Ronbunshi*, 97, 554-558 (1989).
- 6) H. Hosono, Z. Zhang and Y. Abe, *J. Am. Ceram. Soc.*, 72, 1587-1590 (1989).

This article is a full translation of the article which appeared in *Nippon Seramikkusu Kyokai Gakujutsu Ronbunshi* (Japanese version), Vol.99, No.12, 1991.

Preparation of Heat and Water Vapor Resistant Composite Porous Glass Membrane Coated on Porous Alumina Tubing by Sol-Gel Method

Tetsuo Yazawa, Hiroshi Tanaka, Hiroshi Nakamichi, Kiyohisa Eguchi*
and Osamu Yamaguchi**

Government Industrial Research Institute, Osaka

1-8-31, Midorigaoka, Ikeda-shi, 563 Japan

*Consulting Engineer

2-1-72, Seiwadaini-shi, Kawanishi-shi, 666-01, Japan

**Central Research Laboratory, Nihon Cement Co., Ltd.

1-2-23, Kiyosumi, Koto-ku, Tokyo, 135 Japan

The composite porous glass membrane was prepared by coating on porous alumina tubing by the sol-gel method. The porous glass layer of the membrane contains 30 mol% of ZrO_2 . The permeation rate of hydrogen of this membrane is ca. 50 times higher than that of a symmetric porous glass membrane with a reasonable separation factor for H_2/N_2 mixture and this membrane shows no degradation by heating at 500°C . This membrane is also proved to be stable by water vapor exposing test at 350°C in an autoclave.

[Received June 25, 1991; Accepted September 19, 1991]

Key-words: Porous glass, Water vapor resistance, Sol-gel method, Composite membrane, Zirconium oxide

1. Introduction

Recently, research on porous glass membranes for the separation of gaseous mixtures has been actively carried out because of many advantages in their thermal and chemical stability. Separation of gaseous mixtures with symmetrical porous glass membranes has been widely investigated.¹⁻³⁾ However, these membranes have the following disadvantages: their membrane thickness is very large and consequently the permeation rate is very low, and in addition the composition of porous glass is restricted. The authors have prepared an asymmetric porous glass membrane, that is, thin porous glass layer coated on porous ceramics having high mechanical strength required for the phase separation method.⁴⁾ This membrane has sharp pore size distribution and the pore size could be changed fairly intentionally, but the porous glass layer was still thick and its adhesion to the base ceramics was not sufficiently tight.

In this work, composite porous silica glass membrane containing 30 mol% ZrO_2 was prepared by sol-gel method. This membrane has the following advantages: the membrane is very thin, the adhesion to the base ceramics is very tight and chemical durability is very large. The capability of this membrane to separate gaseous mixtures of hydrogen and nitrogen was tested.

2. Experimental

2.1. Membrane Preparation

A thin layer of porous glass was deposited on the surface of ceramic tubing, the pore size of which is $0.2\mu\text{m}$ (composition: Al_2O_3 99.9wt%, supplied by Toshiba Ceramics Co., Ltd.). The preparation procedure is shown schematically in Fig.1. The preparation of the coating sol was as follows.

$\text{Si}(\text{OC}_2\text{H}_5)_4$ (TEOS) was first hydrolyzed by dropping in a mixture of H_2O , $\text{C}_2\text{H}_5\text{OH}$ and HCl , the quantities of which were maintained at 1, 18 and 0.002 mol, respectively, per 1 mol of TEOS. After stirring this hydrolyzed TEOS solution for 1 hour at room temperature, $0.43\text{ mol Zr}(\text{On-C}_3\text{H}_7)_4$ was added, followed by stirring for 120 hours at room temperature to give a coating sol. The porous alumina substrate tubing was soaked in the sol with the sealed end down and pulled up at a speed of 2 mm/sec by the variable motor. The wet alumina tubing was put into an isothermal humidistat, keeping the temperature at 98°C and relative humidity 95% for 1 hour. After taking the tubing out, it was heated at 300°C in electric furnace for 10 min. The above described procedure, dipping, gelation and calcination, was repeated 4 times. For the final time, the calcination time was 20 min. From the composition of the coating sol, ZrO_2 content in the porous glass layer was 30 mol%.

2.2. Measurement of Pore Size of Porous Glass Layer

The sol solution was coated on a slide glass by the same procedure described above and the porous glass layer was stripped off from its surface. The pore size distribution and the specific surface area were measured by the nitrogen

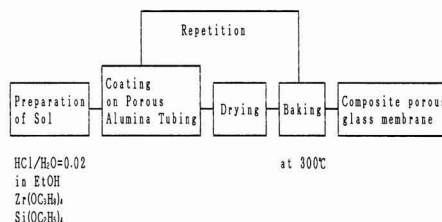


Fig. 1. Preparation process of composite porous glass membrane.

adsorption method. Prior to the measurement, the sample was heated at 150°C for 2 hours under a reduced pressure of 452 Pa.

2.3. Separation Test of Gaseous Mixtures of Hydrogen and Nitrogen

Cylindrical composite porous glass membranes (outer diameter: 10mm, inner diameter: 8 mm) were placed into a stainless module case as shown in Fig.2. The effective surface area of the membranes for a permeation test was in the range of 30 cm² to 50 cm². A schematic diagram of the apparatus used for separation is shown in Fig.3. The composition of the feed gaseous mixture of hydrogen and nitrogen was 50/50 mol%. The pressure of the feed gas was in the range of 150 abs. kPa to 400 abs. kPa. The composition of the permeate gas was analysed by gas chromatography. The separation test was performed at 30°C. The ratio, (volume of permeate gas)/(volume of feed gas), was 0.05.

2.4. Thermal Resistance Test

Membranes were baked in an electric furnace at 500°C for 1 hour to 21 hours, and then their separation factor and permeation rate of hydrogen were measured.

2.5. Water Vapor Resistance Test

Membranes were put into an autoclave saturated with water vapor. The employed pressure was 1 MPa and the test was performed at 250°C, 300°C and 350°C for 3 hours. After the exposure test the separation factor and permeation rate of hydrogen were measured.

3. Results and Discussions

3.1. Characterization of Membrane

The SEM photograph of a cross-section of the membrane is shown in Fig.4. The thickness of porous glass layer was ca. 2μm.

Figure 5 shows the pore size distribution of the porous

glass layer. The median pore radius is ca. 1nm. The pore size distribution is calculated from nitrogen adsorption isotherm based on Cranston-Inkley method. The specific surface area is 324 m²/g by BET equation.

3.2. Separation Factor and Permeation Rate of the Composite Membranes

Figure 6 shows the relation between the separation factor of hydrogen and the pressure difference across the membrane. The solid line indicates the separation obtained by the symmetric porous glass membrane (Median pore size: 4nm, Composition: SiO₂ 96wt%). The separation factor was calculated by the following equation by considering the effect of back diffusion.⁵⁾

$$f = \frac{X_1}{1 - X_1} \cdot \frac{(1 - X_h) - (1 - X_1) \cdot k}{X_h - k \cdot X_1}$$
$$k = \frac{P_1}{P_h} \dots \dots \dots$$

where
f : separation factor of H₂,
X₁ : H₂ concentration of permeate gas,
X_h : H₂ concentration of feed gas,
P₁ : pressure of permeate gas and
P_h : pressure of feed gas.
The separation factor decreases with increase of pressure

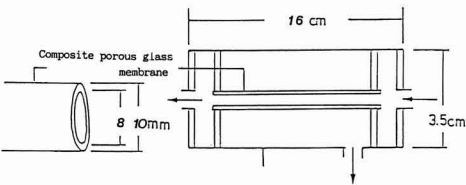


Fig. 2. Membrane module of composite porous glass membrane.

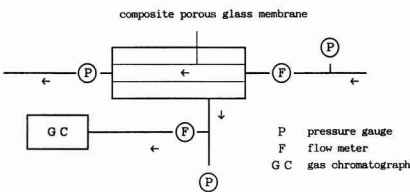


Fig. 3. Schematic diagram of apparatus for gas separation.

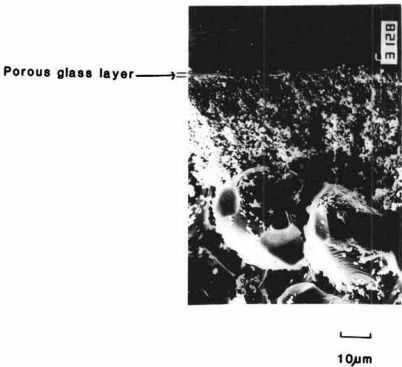


Fig. 4. SEM photograph of a cross-section of the composite porous glass membrane.

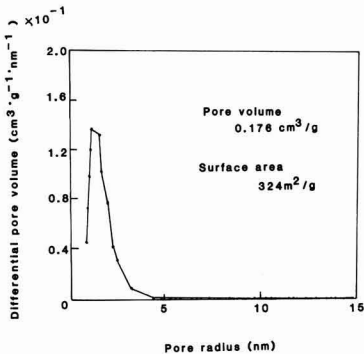


Fig. 5. Pore size distribution of porous glass layer.

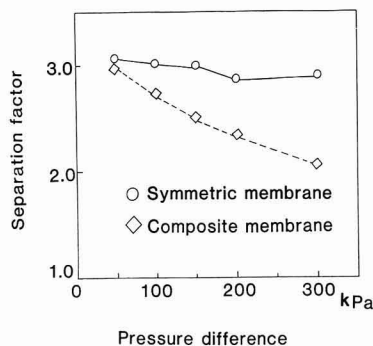


Fig. 6. Relation between separation factor and pressure difference.

difference, although that for the symmetric membrane remains unchanged. This is attributed to the concentration polarization because of the high permeation rate of the composite porous membrane.⁶⁾ Table 1 shows the hydrogen permeation rate of the composite porous glass membranes prepared by sol-gel method, phase separation method⁴⁾ and the symmetric porous glass membrane by sol-gel method is ca. 50 times higher than that of the symmetric porous glass membrane. This high permeation can be attributed to the thin porous glass layer of the composite porous glass membrane by the sol-gel method. As described in 3.1, the thickness of porous glass layer of the composite porous glass membrane is ca. 2 μm . On the other hand, the thickness of the symmetric porous glass membrane is ca. 500 μm .

3.3. Thermal Resistance

Table 2 shows the permeation rate and the separation factor of hydrogen of heat-treated membranes. It is clear that this membrane shows no degradation by heating at 500°C for 21 hours.

3.4. Water Vapor Resistance

Table 3 shows the permeation rate and the separation factor of hydrogen of the membrane exposed to water vapor for 3 hours at a temperature in the range of 250°C to 350°C. This membrane does not show the degradation. It is clear that the membrane has high water vapor resistance under such a condition. This may be attributed to the high content of ZrO_2 in the porous glass layer.

4. Conclusion

The composite porous glass membrane was prepared by

Table 1. Permeation rate of hydrogen

Membrane	Permeation rate $10^9 / \text{m}^2 (\text{STP}) \cdot \text{m}^{-2} \cdot \text{Pa}^{-1} \cdot \text{s}^{-1}$
Symmetric porous glass	5
Composite porous glass by phase separation method ⁴⁾	68
Composite porous glass by sol-gel method	230

Table 2. Thermal resistance of composite porous glass membrane at 500°C

Time h	Separation factor	Permeation rate $10^9 / \text{m}^2 (\text{STP}) \cdot \text{m}^{-2} \cdot \text{Pa}^{-1} \cdot \text{s}^{-1}$
1	2.9	231
5	2.9	229
21	2.8	230

Pressure difference across the membrane=50kPa

Table 3. Water vapor resistance of the composite porous glass membrane

Temp.	Separation factor	Permeation rate $10^9 / \text{m}^2 (\text{STP}) \cdot \text{m}^{-2} \cdot \text{Pa}^{-1} \cdot \text{s}^{-1}$
250°C	3.0	215
300°C	2.8	210
350°C	2.9	225

Pressure difference across the membrane=50kPa

sol-gel method. This membrane proved to have high permeation rate, large thermal stability and water vapor resistance. This membrane is expected to be applicable to the membrane reactor, etc.. Especially, the water vapor resistance is a noteworthy feature for application to the recovery of hydrogen and CO_2 from combustion waste gas and the recycling of CO_2 in molten carbonate fuel cells.⁷⁾

References:

- 1) S.T. Hwang and K. Kammermeyer, Can. J. Chem. Eng., 82-89 (1966).
- 2) K. Haraya, Y. Shindo, T. Hakuta and H. Yoshitome, J. Chem. Eng. Jpn., 19, 186-190 (1986).
- 3) T. Yazawa, H. Tanaka and K. Eguchi, J. Chem. Soc. Jpn., 201-207 (1986).
- 4) T. Yazawa, H. Nakamichi, K. Eguchi and O. Yamaguchi, Seramikkusu Ronbunshi, 96, 566-570 (1988).
- 5) R.W. Tock and K. Kammermeyer, AIChE J., 15, 715-718 (1969).
- 6) K. Haraya, MEMBRANE, 13, 88 (1988).
- 7) CRIEPI Report T86033 (1986).

This article appeared in English in Nippon Seramikkusu Kyokai Gakujutsu Ronbunshi (Japanese version), Vol.99, No.12, 1991.

Thermal Expansion Characteristics of Li-Replaced Type Pollucite ($\text{Cs}_{1-x}\text{Li}_x\text{AlSi}_2\text{O}_6$) Powder

Hidehiko Kobayashi, Toshihiro Terasaki, Toshiyuki Mori*, Hiroshi Yamamura* and Takashi Mitamura

Department of Applied Chemistry, Faculty of Engineering, Saitama University
255, Shimo-ohkubo, Urawa-shi, 338 Japan

*Tsukuba Research laboratory, TOSOH Co.
43, Miyukigaoka, Tsukuba-shi, 305 Japan

Pollucite ($\text{Cs}_{1-x}\text{Li}_x\text{AlSi}_2\text{O}_6$) powders of single phase have been synthesized by isomorphous replacement of part of the Cs^+ ion by Li^+ ion in the pollucite structure using sol-gel processing. Thermal expansion of the synthesized powders has also been investigated with a high-temperature XRD. The pollucite powders of single phase were synthesized in the case of the composition ($\text{Cs}_2\text{O}:\text{Li}_2\text{O}:\text{SiO}_2:\text{Al}_2\text{O}_3$ (molar ratio)=0.95~0.90:0.05~0.10:4.5:1). Thermal expansion was less than 0.2% (room temperature to 1200°C). In particular, the powders showed almost zero thermal expansion in the range of room temperature to 500°C.

[Received August 28, 1991; Accepted October 17, 1991]

Key-words: Pollucite, Sol-gel, Thermal expansion, Li, Isomorphous replacement

1. Introduction

Pollucite ($\text{CsAlSi}_2\text{O}_6$) has been known as a low thermal expansion ceramics, but literature^{1,2)} for its thermal expansion behavior is rather limited. The authors have prepared pollucite powders of single phase by sol-gel processing and examined thermal expansion behavior. An apt selection of pollucite composition and the heat treatment conditions were eventually effective in lowering the thermal expansion of the pollucite powders.^{3,4)} For the powder of excess SiO_2 (molar ratio of $\text{Cs}_2\text{O}:\text{SiO}_2:\text{Al}_2\text{O}_3=1:4.5\sim5:1$), the thermal expansion of the pollucite was particularly lowered in the range of room temperature to 200°C.⁴⁾ It is thought that this effect results in the transition to the 4-ring "spread structure"^{1,5)} which contains no Cs^+ ion configuration in the pollucite structure.

In this study, we prepared Li-replaced type pollucite powders, which replaced a part of Cs^+ ion in a pollucite structure by Li^+ ion isomorphously. The substitution of the Cs^+ and Li^+ ions is assumed to be very fast and proceeds almost quantitatively.²⁾ This should be feasible to synthesize pollucite powders with a lower thermal expansion. In the aluminosilicate system, a few examples^{2,6-9)} have been reported upon the lowering of thermal expansion by replacing part of the constituent atom by another atom or by adding another atom.

2. Experimental Procedure

Al_2O_3 sol and SiO_2 sol were adjusted to pH 5.5 with the addition of aqueous ammonia respectively, and then mixed. The mixture (molar ratio of $\text{SiO}_2/\text{Al}_2\text{O}_3=4.5/1$ or $5/1$) was evaporated to remove water, after being stirred for 20h. Trace amounts of water were then removed with ethanol, and the powder mixture was heated at 550°C for 2h. Powder samples were prepared by adding CsNO_3 and LiNO_3 at specified molar ratios ($\text{Cs}_2\text{O}:\text{Li}_2\text{O}:\text{SiO}_2:\text{Al}_2\text{O}_3=0.95\sim0.80:0.05\sim0.20:4.5:1$, hereinafter called Sample Cs-0.95, Sample Cs-0.90 and Sample Cs-0.80), wet mixing them together with ethanol and alumina balls in plastic pots for 24h and drying them. The powdered samples were calcined at 1000°C for 50h, after being heated at 600°C for 24h and at 750°C for 10h (so-called two-stage heat treatment).

The identification of a crystal phase and the measurement of lattice constants of the pollucite were performed by means of a powder X-ray diffractometer ($\text{CuK}\alpha$ ray, 40kV, 30mA). The lattice constants were calculated from 2θ by the least-squares method (utilizing application software made in Rigaku Denki), after the six peaks of (332), (431), (440), (611), (444) and (721) appearing at 2θ of 25°~55° were corrected using Si as the external standard. The thermal expansion of the pollucite powders of single phase was also calculated from the lattice constants at various temperatures with a high-temperature X-ray diffractometer; the same procedure as described above was followed to obtain the lattice constants. The measurements obtained were a scanning range of 2θ of 25°~55°, scanning speed of 10K/min, and step in temperature of every 50°C at room temperature-400°C and every 100°C at 400°-1200°C.

3. Results and Discussion

3.1. Synthesis of Pollucite Powder by Isomorphous Replacement of a Part of Cs by Li

The XRD patterns of the products (Sample Cs-0.95, Sample Cs-0.90 and Sample Cs-0.80 above calcined at 1000°C for 50h after heated at 600°C for 24h and at 750°C for 10h (two-stage heat treatment)) are shown in Fig.1. It was found that pollucite powders ($\text{Cs}_{1-x}\text{Li}_x\text{AlSi}_2\text{O}_6$) of single phase by isomorphous replacement of part of the Cs^+ ion by Li^+ ion were synthesized from Sample Cs-0.95 and Sample Cs-0.90. On the other hand, the pollucite phase and β -spodumene phase were identified concurrently in the products of Sample Cs-0.80. These phases have not

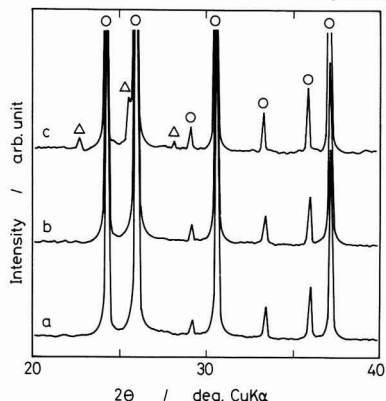


Fig. 1. X-ray powder diffraction patterns of the products calcined at 1000°C for 50h after heating at 600°C for 24h and at 750°C for 10h.

a: Sample Cs-0.95, b: Sample Cs-0.90, c: Sample Cs-0.80

○: CsAlSi₂O₆, △: LiAlSi₂O₆

changed for a recalcined powder at 1200°C for 2h. When the sample powders, of which the molar ratio of SiO₂ increased from 4.5 to 5, were treated under the conditions described above, a trace amount of CsAlSi₅O₁₂ phase was identified in all of them.

The lattice constants of Cs_{1-x}Li_xAlSi₂O₆ of single phase at room temperature were $a=13.657\pm0.003\text{\AA}$ and $a=13.655\pm0.003\text{\AA}$ in Cs-0.95 and Cs-0.90, respectively, and these values agreed with that of Li free ($a=13.651\pm0.004\text{\AA}$) in the cases of Sample Cs-0.95 and Sample Cs-0.90.

3.2. Thermal Expansion Behavior of the Cs_{1-x}Li_xAlSi₂O₆ Powder of Single Phase

The relationship between thermal expansion and the temperature of synthesis of the Cs_{1-x}Li_xAlSi₂O₆ powder from Sample Cs-0.95 and Sample Cs-0.90 is shown in Fig.2. The result with Sample Cs-1.0⁹⁾ (Cs₂O:SiO₂:Al₂O₃=1:4.5:1) is also shown for comparison. Similar trends were observed for Sample Cs-0.95 and Sample Cs-0.90, although the curves as a whole were shifted down to lower thermal expansion in the range of room temperature to 1200°C. These samples showed almost zero thermal expansion for the range from room temperature to 500°C, and the thermal expansion maintained was less than 0.2% up to 1200°C. Thus, the isomorphous replacement of part of the Cs⁺ ion in the pollucite structure by Li⁺ ion decreased the thermal expansion.

From these results, the difference in ionic radius of the alkaline metals replaced varies the proportion of "open space" (Li⁺ ion occupancy of the cavity of 4-ring is possible⁸⁾ in a continuous polyhedron made up of aluminosilicates in the pollucite structure. Exact control is possible in the range (lattice parameters do not change) of which a residual Cs⁺ ion can maintain the pollucite structure. It can therefore be that a proportion of "open space" affects a relaxation of heat motion in the lattice, and as a result the thermal expansion decreases when heat motion in the lattice is relaxed depending upon the isomorphous replacement of part of the Cs⁺ ion by Li⁺ ion.

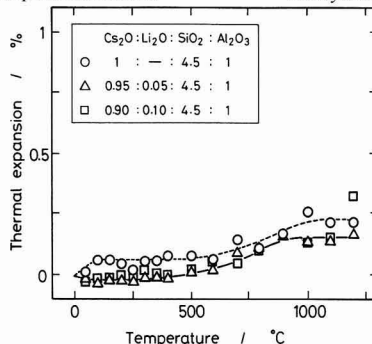


Fig. 2. Relation between temperature and thermal expansion of the pollucite powder obtained using various Cs₂O:Li₂O (molar ratio) compositions. Heat treatment conditions: 600°C for 24h, 750°C for 10h and 1000°C for 50h.

4. Conclusion

The pollucite powders by the isomorphous replacement of part of the Cs⁺ ion in the pollucite structure by Li⁺ ion were synthesized to produce lower thermal expansion. The influence of the isomorphous replacement on the thermal expansion behavior was studied. This resulted in the following:

- 1) In SiO₂ molar ratio=4.5, the Cs_{1-x}Li_xAl₂Si₂O₆ powder of single phase was synthesized in the case of the composition (Cs₂O:Li₂O:SiO₂:Al₂O₃=0.95~0.90:0.05~0.10:4.5:1). On the other hand, the CsAlSi₅O₁₂ phase and β-spodumene phase were formed in SiO₂ molar ratio=5 and Li₂O molar ratio=0.20 (Cs₂O=0.80) respectively.
- 2) The thermal expansion rate of the synthesized pollucite powders of single phase was maintained in an increase within 0.2% in the range of room temperature to 1200°C. In particular, these powders had almost zero thermal expansion in the range of room temperature to 500°C.

References:

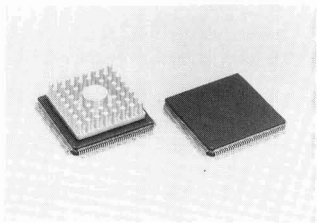
- 1) D. Taylor and C.M.B. Henderson, *Am. Mineral.*, 53, 1476-1489 (1968).
- 2) D.W. Richerson and F.W. Hummel, *J. Am. Ceram. Soc.*, 55, 269-273 (1972).
- 3) H. Kobayashi, T. Terasaki, T. Mori, C. Ishihara, S. Saito, H. Yamamura and T. Mitamura, *Seramikkusu Ronbunshi*, 99, 686-691 (1991).
- 4) H. Kobayashi, T. Terasaki, T. Mori, H. Yamamura and T. Mitamura, *J. Ceram. Soc. Jpn.*, 100, 91-93 (1992).
- 5) D. Taylor, *Mineral Mag.*, 38, 593-604 (1972).
- 6) H. Ikawa, T. Odagiri, O. Imai, K. Urabe and S. Udagawa, *Yogyo Kyokaishi*, 94, 344-350 (1986).
- 7) D.L. Evans, G.R. Fisher, J.E. Geiger and F.W. Martin, *J. Am. Ceram. Soc.*, 63, 629-634 (1980).
- 8) G. Bayer and O.W. Florke, *Naturwissen*, 60, 102-103 (1972).
- 9) K. Hirao, N. Soga and M. Kunugi, *J. Phys. Chem.*, 80, 1612-1616 (1976).

Information & Communications

News

IC Packing of Aluminum Nitride

Fujitsu Ltd. has developed a monolayer hood-type IC packing. It is characterized as having the black substrate of aluminum nitride, which directly carries the IC covered with mullite and sealed by low-melting glass. The substrate is deposited with lead frame finely etched iron-nickel alloy. Aluminum nitride has a high thermal conductivity, radiating heat 10 times faster than alumina. The new IC package radiates heat 2 to 2.5 times faster than plastic-base packages, and 30 to 50% faster than aluminum packages. It will radiate heat more efficiently when provided with fins. This thermal conducting package has been developed, in order to cope with increasing demands for more densely integrated, higher-speed packages which consume more electricity. The company plans to commercialize the IC's for high-definition TV's.



Mirror-Polishing of Cylindrical Ceramic Materials

Assist. Prof. K. Suzuki at Nihon University, Dept. of System Engineering and Assist. Prof. K. Kitajima at Kansai University, Faculty of Engineering, in cooperation with Yamaguchi Prefectural University, have successfully performed mirror-polishing of cylindrical silicon nitride. Assist. Prof. Suzuki has applied mechanical polishing to cylindrical surfaces. This method is preferably applied under constant pressure, and it uses a grinding film originally developed for polishing metals. The 50mm wide film of polyester base coated with chromium oxide is set on an ordinary lathe for polishing a silicon nitride cylinder, 20mm in diameter and 150mm long, which has been finished beforehand to surface roughness of 1 μ m. Cylinder rotation and film winding speeds were set at 10 to 100m/min and 90mm/min, respectively, to polish the surface to a roughness of 40nm in 1hr while the film was vibrated in the horizontal direction. Because it is polished by the soft substance, the surface can be mirror-polished without

scratches or formation of a degraded layer.

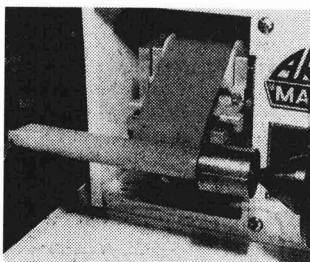
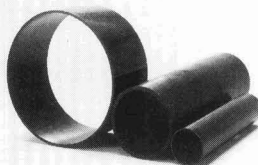


Fig. 1. Mirror polishing with film.

Development of Internal Pressure Forming Method

Yokohama Rubber Co., Ltd. has developed a new type of forming method, called internal pressure forming method (patent applied), to form a composite material, a super-engineering plastic of carbon fiber-reinforced matrix into pipes without damaging the inherent properties of the composite. The original composite is the prepreg of polyetheretherketone (PEEK) as the carbon fiber-reinforced matrix. It has been attracting much attention as the next-generation composite because of its high resistance to heat and ambient conditions and its high strength. The thermoplastic resin is used as the matrix for the composite, because of its high fabricability and controllability. It is the first method for forming a new material into a tubular shape which is one of the most difficult shapes to form uniformly.



Ultrafine Particles of Alumina

A research group at the Tokyo Institute of Technology's Faculty of Chemical Engineering, headed by Prof. J. Kamizawa, has prepared the fine particles of alumina by the reaction-plasma evaporation, and recovered

more than 80% of the particles produced. The plasma apparatus has a plasma torch (total length: 160mm) that produces a plasma, to which a cylindrical reaction tube (total length: 480mm, diameter: 160mm) is connected. The aluminum particles of several tens of microns, fed to the plasma apparatus at 0.5g/min, are molten at high temperature, reacting with oxygen to form the ultrafine particles of alumina. The new process is distinguished from the conventional one in that oxygen gas is supplied at 20 to 30l/min along the walls of the reaction tube connected to the torch at the bottom. It works to prevent the product particles from depositing on the walls, and, at the same time, oxidize unreacted aluminum. The apparatus will be applicable, in principle, to other oxides and nitrides. It will attract attention as a plasma-aided process to form ultrafine particles.

Optical Glass Harmless to Human Bodies

Ohara Co., Ltd. has developed optical glass completely free of toxic substances, such as lead oxide and arsenite. Lead oxide is an essential substance to form the crystals in glass and make the glass transparent. Glass containing a high proportion of lead has been used as a protector against radiation. Arsenite, on the other hand, is used as the deforming agent to improve transparency. The glass containing these substances is harmless, so long as it is. The glass dust generated during the grinding process, however, is toxic, causing various diseases, such as anemia, digestive troubles and protractor paralysis by lead oxide, and dermatitis and neurodermatitis by arsenite. This has led to development of the optical glass containing no lead oxide or arsenite. The titanium-base low-refractive glass contains 20 to 30wt% of lead oxide. The newly developed glass, on the other hand, uses titanium oxide and another substance in place of lead oxide for the low-refractive glass, and is produced by the improved melting method. It can be used for common camera lenses without causing any problem, though it is slightly inferior to the lead oxide glass in transparency, believes the company.

Laser-Aided Ceramic Surface Treatment

The Kanagawa Prefectural Industrial Research Institute has developed the new laser-aided treatment method to repair ceramic surfaces. Grinding ceramics, which are hard and fragile, tend to generate fine cracks, reducing ceramic strength to as low as 60%

of the inherent level, when left untreated. For this reason, they are ground by a diamond grindstone as the post-treatment. The newly developed method uses a YAG laser, in place of diamond grindstone, to treat the surfaces under heat. It requires only 20sec for treatment, versus 30 to 40min by the conventional method. The research group has tested the ceramic surfaces with 20, 50 and 100 μ m deep cracks, to confirm that these cracks are completely removed. It is also applicable to spherical and other complex surfaces, unlike the conventional method. The researchers are planning to clarify the advantages of the newly developed method. Release of residual stress is a possible advantage.

Correction of X-ray Stress Analyzer Using Thin Ceramic Film

Mechanical Engineering Laboratory has succeeded in fabrication of 40 μ m thick ceramic film using diamond abrasives, which enables to correct X-ray analyzer measuring non-destructively internal stress in the fabricated ceramic surfaces. The research group, headed by Chief Researcher Chisato Tsutsumi, has prepared the specimen of silicon nitride, which is thin enough to see colored paper through it, and its internal stress can be known from extent of its bending. The readings are compared with the computer-produced results, to correct the analyzer. The X-ray stress analysis is a method in which the specimen is irradiated with X-ray at different angles, and diffraction of the ray reflected from the specimen is used to estimate strains in the crystals. The ceramic thin film enables to measure internal stress directly, and compare the readings with the computer-produced results. This method is expected to accelerate development of new ceramic materials.

Prediction of the Future Technologies

The Fine Ceramic Society of Japan has started studying to predict the future technologies, and the results will be issued in March, 1992. This study is not based on the concept of ceramics as mere substitute materials but on (1) the new concepts, (2) the concept of fused materials, beyond composite, functional or structural materials, and (3) the recyclable, and light, thin, long and large materials. The society has organized the investigation committee within its structure, before starting the preliminary survey, to predict the future technologies related to fine ceramic materials. The committee consists of several sub-committees; the first sub-committee (chairman: K. Matsunaga, Science and Technology Agency) is responsible for the areas of aerospace, automobiles and vessels), the second sub-committee (chairman: Y. Okabe, the Tokyo University) for electric appliances, communications and information), the third sub-committee (chairman: H. Ishitani) for earth's environments, energy and resources, the fourth sub-committee (K. Hirano, Agency of Industrial Science and Technology) for construction, civil engineer-

ing and general industry), and fifth sub-committee (chairman: N. Nakajima, Tokyo University) for medicines, agriculture, forestry and fishery. The five sub-committees, each consisting of around 8 experts, cover all the industrial sectors. All of the chairmen are representatives of the users. The current status is analyzed and the future technologies are predicted from the angle of users, greatly departed from the traditional stance oriented to makers.

Needle-Shape Barium Ferrite

Kanto Denka Kogyo Co., Ltd. has developed the process for massively producing needle-shape barium ferrite particles as the starting material for vertical magnetic recording tapes. Needle-shape barium ferrite has been attracting attention as the next-generation magnetic recording material. Barium ferrite has two morphologies; plate and needle shapes. The latter was discovered by Prof. M. Sugimoto of Teikyo Technology and Science University, who also developed its production process. Kanto Denka, to which the new material was introduced by Research Development Corporation of Japan, has been studying the commercialization. The new process heats the mixture of needle-shape iron hydroxide, colloidal barium carbonate and boric acid. The flaky crystals will result, when operating temperature exceeds 800°C, which are difficult to spread uniformly over the magnetic tape. The company has developed special chemical substance, which can keep the crystals needle-shaped even when they are fired at 900°C or more. The magnetic tape has sufficiently high qualities, saturation density of 3,200 gauss or more and coercive force of 400 to 2,000 Oe, to find a variety of applications, such as audio and video equipments. The company is sending the samples to prospective users.

Utilization of Oxide Superconductor to be Focused by Materials

Use of oxide superconductor is focusing on specific use according to superconductor to be used, that is, Y system superconductor is to be used as bulk and thin film, and Bi system and Ta system superconductor as wire. Superconductor used for high performance element such as Josephson element is limited to Y system superconductor. The material used for element must have characteristics which permit microprocessing, therefore crystal of material should not have defects. Y system superconductor is sole one which satisfy such requirements as it does not contain compounds having different structure.

Bi system deteriorates with extraction of oxygen. This characteristic is regarded as disadvantage of the substance, however, another evaluation has appeared, that it Tc is controllable with control of supply of oxygen, which make it advantageous when compared with others. IBM, Shimadzu Corp., are studying application of Bi system supercon-

ductor with preparation of SQUID. Superconducting Sensor Laboratory which is a joint venture of 12 private companies is planning development of multi-channel SQUID.

As for bulky material, Nippon Steel Corp. has developed QMG process and PMMG process which is a advance method of PMG process, for preparation of bulky materials, Bi system prepared with this process is high in capacity to pinning magnetic force. When it is cooled in magnetic field, the bulk superconductor becomes highly strong magnet. When it is cooled being shielded from external magnetic field, it becomes highly strong diamagnet. NSC has succeeded in fabrication of a magnet which generated a magnetic field of 1 tesla. Mitsubishi Electric Corp. and Koyo Seiko Co., Ltd. are trying to develop a flywheel and a magnetic baring making use of Meissner effects.

Bi system oxide superconductor is a mixture of high Tc phase (110K) and low Tc phase (90K). As this superconductor has well arranged orientation of crystals, it can be used as wire. Sumitomo Electric Industries Ltd. is developing long superconducting wire of Bi system superconductor. At present, it does not allow large current at liquid nitrogen temperature under magnetic field impressed. But experiments showed that the superconductor wire could withstand 20T magnetic field.

The company succeeded in fabrication of a coil which generated a magnetic field of 0.225 tesla in external magnetic field of 23 tesla.

Toshiba Corp. is trying to find out pinning method aiming at application of oxide superconductor to electric power devices.

Ta system superconductor is highly toxins though its Tc is highest 138K. Few except Hitachi are studying the substance in Japan.

Synthesis of Oxide Superconductor with Complex Polymerization Process

Prof. M. Yoshimura and Assoc Prof. M. Kakihana, Tokyo Institute of Technology, have jointly with Prof. K. Mazaki, Defence Academy, developed a oxide superconductor synthesis process named complex polymerization process, which permit synthesis of high purity superconductor powder. The powder synthesized by the process permits to obtain very high quality superconductor by sintering under room atm, which only sintering under high pressure of 100 to 1,000 atm permits to obtain so far.

In this process, complex of metallic elements which compose a superconductor with citric acid is first synthesized, which is mixed with ethylenglicole of large volume. This is heated at 120°C. Viscous copolymer is produced. When the viscous copolymer is heated high quality powder is obtainable. When this powder is sintered with ordinary process.

This process is available for any type of oxide superconductor powder preparation, however, 1-2-4 type Y system superconductor

is obtained at room atm.

Generation of Argon Low Pressure Plasma using La, Sr, Co, O System Superconductor

Prof. T. Matsuda, Saitama University, has succeeded in generation of low temperature argon plasma at 1 atm. This was first report of this kind. Under normal atmospheric pressure, plasma at under 150°C was obtained stably. This plasma is expected to be applied for NO decomposition reaction, synthesis of inorganic substances, surface treatment, etc.

Plasma has generally been used for high temperature equipment as thermoplasma at temperature range from 10,000 to 1,00,000°C.

Low temperature plasma which use helium 1 atm has been used, but its usage is limited, as it employs electrode for generation. Newly developed low temperature plasma generation method generate plasma by means of irradiation of microwave on LaSrCoC system superconductor. When energy is accumulated, electron is discharged to activate argon so that plasma is generated stably.

When the low temperature argon plasma is applied for decomposition of NO, NO corrosion rate was 60% at 600cc/s of gas flow and 30W of microwave output. Temperature of reaction tube was 400K.

Withdrawal of Announcement of Success in Synthesis of C_{60} Superconductor

National Research Institute for Metals announced that the institute succeeded in synthesis of C_{60} superconductor which was added with halogen element on 19th August, but the institute withdraw the announcement. Many claimed against the announcement saying no Meissner effects was confirmed, and then the institute tested again to find no Meissner effect. According to the institute, such misunderstanding was made by erroneous confirmation of Meissner effect in measurement.

New Solid Electrolyte for Third-Generation Fuel Cells

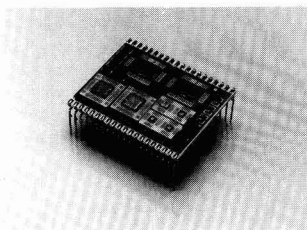
Matsushita Electric Industrial Co., Ltd. (ME) has developed a new solid electrolyte for third-generation fuel cells using barium-cerium-gadolinium oxide with a stable perovskite structure. R&D for the next-generation fuel cell have so far been focused on a zirconia series of a solid electrolyte (YSZ), having a high efficiency and no leakages of liquid. The operating temperature of YSZ is 1,000°C, and only ceramic with a high heat resistance is available as the electrode material. In contrast, the new oxide can reduce the operating temperature to 800°C, therefore, the electrode material ranks among metals, such as stainless steel, that are superior in functionality and durability.

Low-Temperature Glazed Ceramic Plate

Sumitomo Metal Industries, Ltd. has commenced production of low-temperature glazed ceramic plates within the Narumi Seito Co., an affiliate company of Sumitomo Kinzoku. The glazed ceramic plate has been studied by Narumi for possible applications in compact, high-performance electronic equipment, such as portable telephones, camcorders, ICs for HDTV. These are commercialized as Sumitomo products.

The LFC plates use glass and alumina rather than alumina only. The dielectric constant is low, and the thermal expansion coefficient is the same as that of silicon. Therefore, a chip and the substrate plate can be directly connected to the LFC plate without using a lead-frame, which is commonly used in IC wirings. Because of the direct connection, the physical dimensions can be reduced to one-third or one-fifth that of existing ICs using lead-frames.

A 2 billion yen sales value is expected in 1992, the first sales year; and a 5 billion yen sales value is projected for 1995.



Power Beam Machine

Sony Corp. has developed and begun sale of a powder beam machine. The HJ3700 machine operates by blowing out a beam of 1μm diameter ultra-hard ceramic grains at high speed. Processing materials are ferrite, glass, metal, and fine ceramics. The machine can even process three dimensional surfaces by altitude control of the injection nozzle. The machine can finish a mirror face of a metal mold and can also apply a photograph sculpture to pottery. The processing speed is 1μm/min toward depth which is equivalent to 10 to 100 times that of etching processing. Minimum processing width is 10μm, and processing depth is from 0.1μm to 100μm. The machine is capable of fine machining of ultra-hard material that is difficult to process conventionally. The machine plays an important role in the development of an ultra-small size part with sufficient durability. The company sells the machine primarily to the micro-machine field.

Mirror Finishing of Cylindrical Ceramic Applying Mechanochemical Polishing

Prof. K. Suzuki, Nippon Institute of Technology has developed a mechanochemical polishing process which permit mirror finish-

ing of ceramic cylindrical work. Mechanochemical polishing method was developed by Prof. O. Imanaka some 20 years ago, however, the method has permitted polishing of plane only, and has not been able to polish cylindrical work. Prof. Suzuki applied polishing film instead of plane disk now being used for mechanochemical polishing. The film is of polyester on which chrome oxide is coated. This film allows to polish SiN ceramics with surface roughness of 40μm.

Request for Joint Development of Ducted Rocket Engine with the U.S.A.

Defence Agency requested joint development of ducted rocket engine to the U.S.A. at S&TF. S&TF was established for exchange of technical information between Japan and the U.S.A., and meeting of it is opened once a year. At 12th meeting held in 1990, 5 items of (1) ducted rocket engine; (2) millimeter wave IR complex seeker; (3) magnetic field analysis and evaluation equipment; (4) ceramic engine for battle vehicle; and (5) advanced steel were discussed as favorable items. Technology necessary for these items are well advanced in Japan, so joint R&D would not permit one way flow of technology from the U.S.A. for which the U.S. had complain about it.

Pure Gold Clay That Handles Like Conventional Clay

Mitsubishi Material Co., Ltd. has developed a new material called "Pure Gold Clay" from which pure gold articles can be created through the same process as that for making ceramics from clay. The new material is a mixture of finely powdered gold with grain sizes of 20μm or smaller, water, and a special organic binder. Its weight composition is 90% powdered gold and 10% of water plus binder. Similar to clay used for ceramics, this clay is first mold into the desired shape and then burned at approximately 1000°C. In this process, the binder completely gasifies at the same time that the powdered gold grains bind to each other to create a pure gold product. This leaves the surface touch, which has been marked during forming process, intact.

The company has also been marketing pure silver clay and pure platinum clay. In addition, an 18K gold alloy clay and a platinum alloy clay are under development. With the new pure gold clay, the company plans to create a powerful series of new materials.

Abstracts of Articles on Ceramics and Superconductivity from the Selected Journals of the Academic Societies

Journal of The Physical Society
of Japan
Vol.60 No.7 July 1991
p.2122-2126

Magnetic and Superconducting Phase Diagram of Heavy Fermion Superconductors $Ce_{1-x}Th_xCu_{2.2}Si_2$ —Cu NMR and NQR Study—

Yoshio KITAOKA, Hiroyuki NAKAMURA, Taisuke IWAI,
Kunisuke ASAYAMA, Udo AHLHEIM,[†] Christoph GEIBEL,[†]
Christina SCHANK[†] and Frank STEGLICH[†]

Department of Material Physics, Faculty of Engineering Science,
Osaka University, Toyonaka 560

[†]Institut für Festkörperphysik, Technische Hochschule Darmstadt,
D-6100 Darmstadt, Fed. Rep. Germany

The magnetic and superconducting phase diagram of Th-doped $Ce_{1-x}Th_xCu_{2.2}Si_2$ has been established by Cu NMR and NQR technique and is compared with that of $CeCu_{2.2}Si_2$. Static magnetic ordering with $T_N=2.4$ K and 4.5 K for $x=0.08$ and 0.12, respectively, is evidenced by a pronounced broadening of the ^{63}Cu -NQR and -NMR spectra and a pronounced anomaly in the specific heat. In contrast, for the lightly Th-doped compounds with $x \leq 0.064$, there has been observed neither a signature of a broadening of the NQR and NMR spectra nor an anomaly of the specific heat, but a dramatic reduction of the NMR and NQR intensities below a temperature ranging from 0.9 K to 1.3 K upon increasing Th-content. It is emphasized that the unusual "magnetic transition" found in undoped and lightly Th-doped $CeCu_{2.2}Si_2$ should be distinguished from the static magnetic ordering in the heavily Th-doped systems.

[heavy fermion, superconductivity, magnetic phase, NMR, NQR]

Journal of The Physical Society
of Japan
Vol.60 No.7 July 1991
p.2311-2323

First Principles Investigation of the Electronic Structures of Copper Oxide Superconductors by the MCSCF Cluster Method

Mikio ETO and Hiroshi KAMIMURA*

Department of Physics, University of Tokyo, Bunkyo-ku, Tokyo 113

Electronic structures of La-Sr-Cu-O and Nd-Ce-Cu-O compounds are investigated from first principles, taking CuO_4 , CuO_4 , Cu_2O_{11} and Cu_2O_7 clusters, as a model. Many-body states are calculated in the presence of the correlation effect by the MCSCF-CI variational method. In the hole-doped CuO_4 cluster we have shown that the ground state changes from $^1A_{1g}$ to $^3B_{1g}$ near the doping concentration of the onset of superconductivity, owing to the effect of the apical oxygens. While in the electron-doped CuO_4 cluster the ground state is always $^3B_{1g}$, in which the dopant electron is accommodated in the Cu 4s orbital. The effects of the doped ions are also discussed. In the undoped Cu_2O_{11} and Cu_2O_7 clusters two electrons are localized at Cu sites, reflecting the strong correlation effect, and are coupled antiferromagnetically. The destruction mechanism of the antiferromagnetic ordering is shown to be different between in the hole-doped Cu_2O_{11} and in the electron-doped Cu_2O_7 clusters.

[high temperature superconductors, MCSCF, CI, cluster calculation, spin polaron mechanism]

Journal of The Physical Society
of Japan
Vol.60 No.7 July 1991
p.2324-2332

Temperature and Magnetic Field Dependences of Flux Pinning Force in High- T_c Superconductor $Tl_2Ba_2Ca_2Cu_3O_x$

Kenichi TENYA, Hideki MIYAJIMA, Shuetsu HASEYAMA,[†]
Yuuichi ISHIKAWA[†] and Shuji YOSHIZAWA[†]

Department of Physics, Faculty of Science and Technology,
Keio University, Hiyoshi 3-14-1, Kohoku, Yokohama 223

[†]Central Research Laboratory, Dowa Mining Co., Ltd.,
Tobuki, Hachioji, Tokyo 192

The magnetic flux pinning force in $Tl_2Ba_2Ca_2Cu_3O_x$ high- T_c superconductor ($T_c=120$ K) were measured as functions of temperature and magnetic field by using a torque magnetometry. The magnetic torque curves exhibit a large rotational hysteresis accompanied with a delayed angle for the rotation of applied magnetic fields. The number density of fluxoids and the pinning force acting on the fluxoids were estimated using a combined model with the Bean model and the Silcox-Rollins model for low and high magnetic field regions, respectively. The pinning force depends on the temperature as $(1-t^2)^{1/2}$, where t is a normalized temperature by 80 K. Above 80 K, the pinning force is too small to be observed, and it indicates that the fluxoids may become into a flux flow state.

[high- T_c superconductor, Tl-Ba-Ca-Cu-O system, flux pinning, pinning force, pinning potential, torque magnetometry, critical state model]

Journal of The Physical Society
of Japan
Vol.60 No.7 July 1991
p.2341-2350

Enforced Time-Reversal Breakdown in Unconventional Superconductors

Manfred SIGRIST, Nobuyuki OGAWA and Kazuo UEDA

*Institute of Materials Science, University of Tsukuba,
Tsukuba, Ibaraki 305*

In time-reversal symmetric unconventional superconductors time-reversal breaking structures can occur under certain conditions. This effect is demonstrated on two examples: a domain wall and a thin film for a superconductor with an order parameter consisting of two components. It is shown that the occurrence of time-reversal breaking states is compatible with the general stability conditions of a Ginzburg-Landau theory.

Journal of The Physical Society
of Japan
Vol.60 No.7 July 1991
p.2351-2360

Cu NQR Study of the Spin Dynamics in High- T_c Superconductor $\text{La}_{2-x}\text{Sr}_x\text{CuO}_4$

Shigeki OHSUGI, Yoshio KITAOKA, Kenji ISHIDA
and Kunisuke ASAYAMA

*Department of Material Physics, Faculty of Engineering Science,
Osaka University, Toyonaka, Osaka 560*

The nuclear spin-lattice relaxation time T_1 of ^{63}Cu in $\text{La}_{2-x}\text{Sr}_x\text{CuO}_4$ was measured in the concentration range of $x=0.075\sim 0.15$ near the magnetic phase boundary around $x=0.05$. At low Sr concentration and low temperature, $(T_1 T)^{-1}$ was found to increase markedly with a development of strong antiferromagnetic (AF) spin correlation among Cu spins. In normal state, $(T_1 T)^{-1}$ exhibits a temperature dependence of $C/(T+\theta)$ associated with the Curie-Weiss law of the staggered susceptibility $\chi_Q(T)$ at the zone boundary, $Q=(\pi/a, \pi/a)$, above 60 K and approaches a nearly constant value in a narrow T -region just above T_c . T_c decreases with decreasing θ , becoming zero at $x=0.05$ when θ is extrapolated to zero. The rapid decrease of $1/T_1$ below T_c has commonly been observed irrespectively of further development of the AF correlation with decreasing Sr content.

Japanese Journal of Applied
Physics
Vol. 30 No.7 July 1991
p.1390-1397

Preparation of $\text{YBa}_2\text{Cu}_3\text{O}_{7-x}$ (YBCO) Superconductive Film Using Sol-Gel Method

Yoshio MASUDA, Tsuyoshi TATEISHI¹, Kazuo MATSUBARA¹,
Rikuro OGAWA and Yoshio KAWATE

Kobe Steel, Ltd., 1-5-5, Takatukadai Nishi-ku, Kobe-shi 673-02
¹*Kobeeco Research Institute, Inc., 1-1-3, Wakinohana-cho, Chuou-ku, Kobe-shi 651*

Using alkoxides of Y and Ba and Cu-acetate as raw materials, $\text{YBa}_2\text{Cu}_3\text{O}_{7-x}$ (YBCO) superconductive films were produced through the sol-gel method. When the nonaqueous mixed solution was hydrolyzed under an appropriate condition, a pure and homogeneous YBCO powder could be prepared. Controlling the metal concentration and the temperature of the sol, precursor(gel) films were formed on YSZ substrate by dip-coating. And heating the films in the range of 200°–950°C, changes of the films morphologies, the generated phases and the film reactions with the substrates were studied using scanning electron microscopy and X-ray diffraction. It has been known that to improve the superconductivity of the film it is necessary to sinter it at as high as 950°C and increase its thickness over about 3 μm after sintering. A superconductive film with $T_{c,0K}=75$ K was obtained by adopting these conditions.

KEYWORDS: YBCO Superconductor, films, sol-gel, hydrolysis, dipping, coating, YSZ substrate

Japanese Journal of Applied
Physics
Vol. 30 No.7A July 1991
p.L1157-L1159

High Magnetic Flux Trapping by Melt-Grown YBaCuO Superconductors

Kiyoshi SAWANO, Mitsuru MORITA, Masamoto TANAKA,
Tsutomu SASAKI, Keiichi KIMURA, Seiki TAKEBAYASHI,
Masao KIMURA and Katsuyoshi MIYAMOTO

R&D Laboratories-1, Nippon Steel Corporation, 1618 Ida, Nakahara-ku, Kawasaki 211

Trapped magnetic flux density of melt-grown YBaCuO bulk superconductors was evaluated. A single-grained disc-shaped bulk sample with a size of 45 mm ϕ \times 15 mm trapped very high magnetic flux density after field cooling. One disc trapped a maximum surface flux density of 0.72 T, while the maximum of double-piled discs was 1.35 T after 100 seconds. A polycrystalline sample showed a much lower maximum. The pinning potential of this single-grained disc was 0.17 eV, and the overall critical current density estimated from the trapped flux density was about 7×10^3 A/cm². Since these values are lower than those of a small-sized sample, weak links are still expected to exist even in the single-grained sample. Domain structure within a grain is a strong candidate for this weak link.

KEYWORDS: superconductor, oxide, melt process, seeding, crystal growth, YBaCuO , grain boundary, magnetic flux density, critical current density, flux creep

**Japanese Journal of Applied
Physics**
Vol. 30 No.7A July 1991
p.L1160-L1162

**Microstructure and Superconducting Properties of
Bi-Sr-Ca-Cu-O System Prepared by a Melt Process**

Kunihiko EGAWA, Toshio UMEMURA, Shin-ichi KINOCHI,
Mitsunobu WAKATA and Shin UTSUNOMIYA

*Materials & Electronic Devices Laboratory, Mitsubishi Electric Corporation,
1-1-57 Miyashimo, Sagami-cho-shi, Kanagawa 229*

The microstructure and superconducting properties for samples with the nominal composition of $\text{Bi}_{1-x}\text{Sr}_x\text{Ca}_{1-x}\text{Cu}_2\text{O}_y$ ($x=0, 0.2, 1.0$) prepared by a melt process have been examined. The magnetic field dependence of the intragrain critical current density was improved by enriching the Ca and Cu contents. Such samples included two kinds of precipitates, $(\text{Ca}, \text{Sr})_2\text{CuO}_3$ and Sr-Pt-O compounds. The latter precipitates were much smaller in size than the former, and this suggests that they may be more effective in enhancing the pinning force.

KEYWORDS: melt process, Bi-Sr-Ca-Cu oxide superconductor, critical current density, susceptibility, precipitate, impurity, single crystal, quench

**Japanese Journal of Applied
Physics**
Vol. 30 No.7A July 1991
p.L1163-L1165

**Preparation of High- T_c Superconductor in the (BiPbSrCaCuO)
System by Hot-Pressing***

Anna TAMPIERI and Gian Nicola BABINI

*Research Institute for Ceramics Technology—CNR, via Granarolo 64,
48018 Faenza (Ra), Italy*

Superconducting Bi-Pb-Sr-Ca-Cu-O ceramics were sintered by the hot-pressing technique. The densification mechanism was investigated at 800°C and 850°C and a densification phenomenology has been proposed. Samples hot pressed at 850°C showed high density and $T_c \approx 110$ K.

KEYWORDS: high- T_c superconductor, Bi-Pb-Sr-Ca-Cu-O system, hot-pressing technique, high density, sintering mechanism

**Japanese Journal of Applied
Physics**
Vol. 30 No.7A July 1991
p.L1166-L1168

**Fabrication of Ag-Doped $\text{Y}_1\text{Ba}_2\text{Cu}_3\text{O}_{7-x}$ Superconducting Films
on Cu Substrates by Electrophoretic Deposition**

Hideo NOJIMA, Hidetaka SHINTAKU, Masaya NAGATA
and Masayoshi KOBAYASHI

Corporate R and D Group, SHARP CORPORATION, Ichinomoto-cho, Tenri, Nara 632

Ag-doped $\text{Y}_1\text{Ba}_2\text{Cu}_3\text{O}_{7-x}$ superconducting films were fabricated on Cu substrates by electrophoretic deposition. The electrophoretic deposition was carried out using presintered $\text{Y}_1\text{Ba}_2\text{Cu}_3\text{O}_{7-x}$ and Ag_2O powder dispersed in distilled acetone. The deposited films were heat-treated in air at 900°C. The Ag-doped $\text{Y}_1\text{Ba}_2\text{Cu}_3\text{O}_{7-x}$ films on Cu-coated YSZ exhibited a metallic temperature dependence of the resistance, and the zero-resistance state was obtained at 88 K. The critical current density and the grain growth were greatly improved by the Ag doping.

KEYWORDS: electrophoretic deposition, high- T_c oxide superconductor, $\text{Y}_1\text{Ba}_2\text{Cu}_3\text{O}_{7-x}$, Ag doping, Ag_2O , Cu substrate

**Japanese Journal of Applied
Physics**
Vol. 30 No.7B July 1991
p.L1250-L1252

**Effects of Electron Irradiation on the Structural Change in
Oriented $(\text{Bi}_{0.75}\text{Pb}_{0.25})_2\text{Sr}_2\text{Ca}_2\text{Cu}_3\text{O}_{10}$ Superconductors**

Teruo ISHIBASHI, Noriyuki INUISHI and Osamu YODA¹

*Department of Applied Physics, Hokkaido University, Sapporo 060
¹Takasaki Research Establishment, Japan Atomic Energy Research Institute,
Takasaki, Gunma 370-12*

Oriented sintered $(\text{Bi}_{0.75}\text{Pb}_{0.25})_2\text{Sr}_2\text{Ca}_2\text{Cu}_3\text{O}_{10}$ pellets have been irradiated up to $2 \times 10^{19}/\text{cm}^2$ with 3 MeV electrons at 370 K. By X-ray line broadening analyses, the amount of disordered portion in the c-axis direction increased by about 20% on irradiation of $2 \times 10^{19}/\text{cm}^2$. The intensity of Ca LMM Auger electrons decreased with increasing irradiation. The transition temperature onset remained unchanged at 110.1 K by irradiation, while the transition temperature offset decreased from 101.2 K to 94.7 K at the maximum irradiation dose. The above observations have been explained by the formation of the disordered portion in the grain surface by electron irradiation, which results in the reduction of the superconducting grain connection.

KEYWORDS: BPSCCO superconductor, electron irradiation, X-ray line broadening analysis, disordered portion

**Japanese Journal of Applied
Physics**
Vol. 30 No.7B July 1991
p.L1253-L1255

**High-Quality $\text{YBa}_2\text{Cu}_3\text{O}_{7-x}$ Ceramics Prepared from
Freeze-Dried Nitrates**

Toshimichi ITO, Yoshitaka KIMURA and Akio HIRAKI

Department of Electrical Engineering, Osaka University, Suita, Osaka 565

Using fine powders prepared by a freeze-drying process of a nitrate solution, a $\text{YBa}_2\text{Cu}_3\text{O}_{7-x}$ superconductor has been successfully formed in a ceramic plate. The other processes employed are two heat treatments, a flash decomposition of the freeze-dried nitrates and a subsequent calcination. It has been found that the formation of high-quality ceramics requires ~10% of the Cu nitrate to be added to the stoichiometric nitrate solution as a starting material of the freeze-drying process. The ceramics thus obtained have the characteristics of a very dense structure with large grains and exhibit magnetic properties as a high T_c superconductor as good as those of a monocrystalline $\text{YBa}_2\text{Cu}_3\text{O}_{7-x}$.

KEYWORDS: high T_c superconductor, $\text{YBa}_2\text{Cu}_3\text{O}_{7-x}$, freeze-drying, ceramics, nitrate solution

Japanese Journal of Applied
Physics
Vol. 30 No.7B July 1991
p.L1260-L1263

Gamma Irradiation Effect on a $\text{Bi}_{1.5}\text{Pb}_{0.5}\text{Sr}_2\text{Ca}_2\text{Cu}_3\text{O}_{10}$ Superconductor

Kensuke SHIRAIISHI, Koichi YANO¹* and Yasuo OTOGURO¹

Takasaki Radiation Chemistry Research Establishment, Japan Atomic Energy Research Institute,
Watanuki-machi, Takasaki, Gunma 370-12

¹Faculty of Engineering, Gunma University, Tenjin-cho, Kiryu, Gunma 376

A $\text{Bi}_{1.5}\text{Pb}_{0.5}\text{Sr}_2\text{Ca}_2\text{Cu}_3\text{O}_{10-x}$ ceramic was sequentially irradiated with ^{60}Co γ -rays of $1.5 \text{ MR} \cdot \text{h}^{-1}$ in dose rate up to a dose of about 50 MR at ambient temperature, and the electrical resistivity was measured as a function of temperature. The critical superconducting transition temperature of 103.4 K increased to 104.1 K at 20.25 MR, and then decreased at a rate of $2.0 \times 10^{-2} \text{ K/MR}$ on further irradiation. Concurrently, the electrical resistivity at 300 K increased almost linearly with a rate of $0.1 \mu\Omega \cdot \text{m/MR}$ in the dose range of about 2 to 20 MR, and the resistivity was little changed by the irradiation to about 37 MR.

KEYWORDS: superconductor, $(\text{Bi}, \text{Pb})_2\text{Sr}_2\text{Ca}_2\text{Cu}_3\text{O}_{10}$, ceramic, gamma irradiation, electrical resistivity, transition temperature

*Present address: Chiyoda Corporation, Tsurumi-cho, Tsurumi-ku,
Yokohama 230.

Japanese Journal of Applied
Physics
Vol. 30 No.7B July 1991
p.L1268-L1270

Preparation of Superconducting $\text{Ba}_2\text{YCu}_3\text{O}_{7-y}/\text{Ag}$ Composite Films by the Dipping-Pyrolysis Process Using Metal Naphthenates at 750°C

Toshiya KUMAGAI, Takaaki MANABE, Tatsuo TSUNODA,
Wakichi KONDO and Susumu MIZUTA

National Chemical Laboratory for Industry, Tsukuba, Ibaraki 305

Superconducting $\text{Ba}_2\text{YCu}_3\text{O}_{7-y}/\text{Ag}$ composite films were prepared on yttria-stabilized zirconia substrates by the dipping-pyrolysis process. Metal naphthenates were used as starting materials. Homogeneous $\text{Ba}-\text{Y}-\text{Cu}-\text{Ag}$ solutions with (Ag/BYCO) molar ratios of 0–1.0 were spin-coated onto the substrates and pyrolyzed at 500°C. Subsequently, these pre-fired films were heat-treated at 750°C under a low-oxygen partial pressure ($= 2 \times 10^{-4} \text{ atm}$) followed by higher- $p(\text{O}_2)$ annealing. High superconducting transition temperatures, $T_{c, \text{onset}}(s)$'s and $T_{c, \text{zero}}(r)$'s, of 88 K–90 K were obtained for the composite films with (Ag/BYCO) molar ratios of 0.1–0.5.

KEYWORDS: $\text{Ba}_2\text{YCu}_3\text{O}_{7-y}$ superconductor, Ag, composite, film, dipping-pyrolysis process, metal naphthenates, oxygen partial pressure, low temperature

Japanese Journal of Applied
Physics
Vol. 30 No.7B July 1991
p.L1271-L1272

Temperature-Dependent Irreversibility Magnetic Fields of High- T_c Superconducting BiPbSrCaCuO Tapes in the Magnetic Flux Densities up to 30 T in the Temperature Range from 33 to 90 K

Takeshi HIKATA, Ken-ichi SATO and Yukikazu IWASA¹

Osaka Research Laboratories, Sumitomo Electric Industries, Ltd.,
Shimaya 1-1-3, Konohana-Ku, Osaka 554

¹Francis Bitter National Magnet Laboratory Massachusetts Institute of Technology,
Cambridge, MA 02139, U.S.A.

Temperature-dependent irreversibility magnetic fields, $H_{ir}(T)$ were measured for four samples of silver-sheathed $\text{Bi}_{1-x}\text{Pb}_x\text{Sr}_2\text{Ca}_2\text{Cu}_3\text{O}_y$ tapes having 3 levels of zero-field, 77 K critical current density, J_{c0} , in magnetic flux densities up to 30 T and in the temperature range from 33 to 90 K. The measurements were performed for two orientations of the tape plane, the plane parallel to the applied magnetic field direction and that perpendicular to the applied field. The measurements show that H_{ir} increases with J_{c0} , implying that H_{ir} is strongly dependent on the morphology of the superconductors. H_{ir} was obtained at 27.9 T and 54.7 K for the sample with $J_{c0} = 298 \text{ A/mm}^2$ at 77.3 K.

KEYWORDS: irreversibility magnetic field, anisotropy, Bi-Pb-Sr-Ca-Cu-O, Ag-sheathed superconducting tape

Shigen to Sozai
Vol.107 No.8 (1991)
p.511-516

Estimation for Adhesion of Ceramics Film on Steel

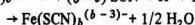
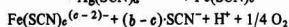
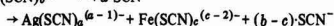
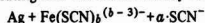
by Syuji YAMAMOTO¹ and Hiroshi ICHIMURA²

1. Sumitomo Metal Mining Co., Ltd. Central Research Laboratories, Ichikawa, Chiba 272

2. Nippon Rare Earths Co., Ltd.

A TiN film has been deposited on austenite stainless steel and high speed steel in arc ion plating system.

Adhesion between the coating film and the substrate was measured by scratch tester, and internal stress of the coating film was determined by X-ray diffraction.



KEY WORDS: Silver, Ammonium Thiocyanate, Dissolution, Acidic Solution, Oxidizing Agent, Fe(III) Solution

Zairyo
Vol.40 No.455 Aug. 1991
p.1049-1055

Fracture Behavior of Ceramics under Tensile Loading in High Purity Water at Room Temperature

Takeshi MIYAHARA*, Tetsuya CHIKARAISHI**, Mitsuo KIDO***
and Manabu UENO****

The characteristics of static or cyclic fatigue crack growth initiation of two ceramics (alumina (Al_2O_3) and partially stabilized zirconia (PSZ)) under tensile loading have been investigated in high purity water at room temperature. The time to crack growth initiation, t_k , at static and cyclic fatigue tests in water was shorter than that in air. In addition, it decreased markedly with increasing K_I or ΔK_I . From the observation of fracture surface for static and cyclic fatigue by SEM, it was shown that fracture surface was the mixed type of intergranular and transgranular cracking in alumina and intergranular cracking in PSZ. Fracture behavior under cyclic loading revealed the occurrence of time-dependent crack growth initiation in alumina and cyclic-dependent one in PSZ. The reason why the fracture time decreased by cyclic fatigue for PSZ is considered to result from the promotion of interaction between fatigue crack and microstructure, such as microcracking and phase transformation in the process zone, and the activation of hydration reaction at the crack tip.

Key words : Alumina, Partially stabilized zirconia, Static fatigue, Cyclic fatigue, High purity water

Zairyo-to-Kankyo
Vol.40 No.8 1991
p.533-539

Effect of Sintering Aids on Corrosion of Si_3N_4 Ceramics in Hot Water at 88°C*

Shoichi Ono**, Mami Yuki**, Mikio Kumagai** and Koji Hoashi**

** Institute of Research and Innovation

Corrosion and dissolution behaviors of hot-pressed Si_3N_4 ceramics at 88°C in lithiated and borated water that was prepared to simulate PWR primary coolant were studied using a small once-through type experimental loop. Experiments were carried out for two Si_3N_4 ceramics with different sintering aids composed of MgO and $\text{Y}_2\text{O}_3/\text{Al}_2\text{O}_3$, respectively, and also Al_2O_3 which is used as the component of the mechanical seals for PWR primary coolant pump. The weight loss of exposed Si_3N_4 specimen containing MgO was relatively large and reached to 2.1 mg/cm² after 1,000 h exposure. Mg was dissolved selectively into the test solution, but dissolution of Si_3N_4 grain itself was estimated to be negligibly small. The surface was deeply corroded with the depth of 70 μm , and changed to porous one. On the other hand, the weight loss of 1,000 h exposed specimen containing both Y_2O_3 and Al_2O_3 was very small at around 0.12 mg/cm². This value was nearly equal to that of Al_2O_3 ceramics. Similar to the case of Si_3N_4 containing MgO, Y was dissolved selectively and the surface was changed to porous. The corrosion depth, however, was small, of the order of 2 μm . It was thus estimated that the corrosion resistance of Si_3N_4 ceramics in hot water was largely dependent on the compositions of sintering aids.

Key words : Si_3N_4 ceramics, corrosion, elution, Al_2O_3 ceramics, aqueous solution, sintering aid, grain boundary, PWR primary coolant, mechanical seal

** 〒227 千葉県柏市高田 1201 (Takada, Kashiwa-shi, Chiba-ken, 277 Japan)

Funtai Kogaku Kaishi
Vol.28 No.8 1991
p.501-507

The Effect of Wet Ball Milling in the Production Process of YBaCu Composite Oxide on its Superconducting Properties

Toyokazu YOKOYAMA[†], Yoshifumi YOSHIDA[†], Akira KONDO[†]
Makio NAITO^{††}, Masahiro YOSHIKAWA^{††}, Hidehiro KAMIYA[†]
and Genji JIMBO[†]

The effects of wet milling of YBaCu oxide in ethanol and in n-hexane with a vibration ball mill on the superconducting properties of calcined powders and sintered pellets have been examined with a focus on first-stage milling before calcination in the preparation process. As a result, it was found that there is an optimum range of milling time in both cases.

In the wet milling in n-hexane, it was confirmed that the prolonged milling causes agglomeration of particles as in dry grinding, which is considered to be one of the reasons for the degradation of the superconductivity of calcined powder.

On the other hand, the elementary analysis by EPMA of the treated powder by wet milling in ethanol showed that the change in degree of mixing of each element agreed well with the tendency of variation in the superconducting props of the calcined powder and sintered pellet.

Key Words : Superconductivity, YBaCu Oxide, Wet Milling, Degree of Mixing, Vibration Ball Mill

Journal of The Physical Society
of Japan
Vol.60 No.8 Aug. 1991
p.2740-2747

Superconducting Correlation of Two-Dimensional Hubbard Model near Half-Filling

Masatoshi IMADA

*Institute for Solid State Physics, University of Tokyo,
Roppongi 7-22-1, Minato-ku, Tokyo 106*

Superconducting correlation of the Hubbard model on a square lattice is reinvestigated by quantum Monte Carlo method. Results from more than one order of magnitude larger Monte Carlo steps than before are presented to discuss the convergence of the data to the ground state. By examining the dependence on the choice of initial trial states as well as on the Trotter number in detail, the superconducting correlation in the ground state is reliably obtained up to 12×12 lattice away from the half-filling and up to 16×16 lattice at the half-filling, which substantially improve former results near the half-filling. Various channels of pairing in the ground state show no system size dependence and remain quite short ranged at any filling including the region close to the half-filling. Numerical data show further evidence that neither extended *s*- nor *d*-wave superconducting state is possible in the two-dimensional Hubbard model.

Journal of The Physical Society
of Japan
Vol.60 No.8 Aug. 1991
p.2748-2760

Self-Consistent Solution of the Bond-Asymmetric Two-Band Model for a Cu-O Based High- T_c Superconductor

Kosai TANABE and Masako KURAMOTO*

*Department of Physics, College of Liberal Arts, Saitama University,
Urawa, Saitama 338*

To describe high- T_c superconductivity the hole-occupation number-constrained BCS equation is self-consistently solved for the quasi-2D bond-asymmetric two-band model with weak coupling pairing interaction. The model is characterized by the split two oxygen bands and hole transfer interactions among nearest and next nearest neighbour O-sites. Since the self-consistent mean field induced by the Coulomb repulsion in the O-site is dependent on the hole-occupation numbers in the oxygen site $O(a)$ ($O(b)$), n_a (n_b), behaviour of the square-root singularities in the state density is determined by the total hole-occupation number, $x = n_a + n_b$. The self-consistent solution to the extended BCS equation describes x -dependence of physical properties and shows substantial quenching of the isotope effect in association with the superconducting phase realized only in a limited range of x . These results are displayed for some typical sets of interaction strengths.

[superconductivity, BCS equation, number-constrained HFB equation, self-consistent solution, bond-asymmetric model, two-dimensional lattice, phase transition, electronic properties of condensed matter, isotope effect, theory]

* Present address: Konica Corporation, No. 1
Sakura-machi, Hino-shi, Tokyo 191.

Japanese Journal of Applied
Physics
Vol. 30 No.8 Aug. 1991
p.1679-1684

Properties of Superconductive Strip-line Resonators Fabricated Using EuBaCuO Films on MgO (100)

Yasuhiro NAGAI, Makoto SATO¹, Hidefumi ASANO,
Shugo KUBO and Tuneso KONAKA¹

*NTT Applied Electronics Laboratories, Tokai, Ibaraki 319-11
¹NTT Transmission Systems Laboratories, Tokai, Ibaraki, 319-11*

This paper reports on the properties of superconductive strip-line resonators fabricated using EuBaCuO superconducting films on MgO (100) substrates. A high loaded-Q of 22000 and an unloaded-Q of 24000 are realized at 35.5 K and 5.55 GHz. The surface resistance is calculated as $160 \mu\Omega$ without any correction and $50 \mu\Omega$ with t/λ correction. In addition, a resonant frequency shift of 40 MHz occurs in the measurement range. This shift can be mainly explained by the reduction in penetration depth due to the decrease in temperature. From this shift, penetration depth at 0 K is estimated to be $0.75 \mu\text{m}$. Furthermore, there is no change in the unloaded-Q in the power region below -10 dBm , but then the unloaded-Q gradually decreases as the input power is increased although the penetration depth hardly varies. This limitation does not indicate that the whole superconductive phase is weakened. The influence of air spacing on resonant frequency is also discussed for MgO and LaAlO_3 substrates.

KEYWORDS: superconductive strip-line resonators, frequency shift, power dependency, surface resistance, penetration depth

Japanese Journal of Applied
Physics

Vol. 30 No.8 Aug. 1991

p.1685-1686

**Thermodynamic Estimation of Oxidation Ability of Various Gases
Used for the Preparation of Superconducting Films at High Vacuum**Takuya HASHIMOTO, Hideomi KOINUMA and Kohji KISHIO¹*Research Laboratory of Engineering Materials, Tokyo Institute of Technology, 4259 Nagatsuta, Midori-ku, Yokohama 227*¹*Department of Industrial Chemistry, University of Tokyo, 7-3-1 Hongo, Bunkyo-ku, Tokyo 113*

The oxidation ability of O₂, O₃, atomic oxygen, NO, N₂O, and NO₂ was estimated by thermodynamic calculation. The calculation was carried out on the equilibrium state of Cu₂O/CuO, considering the temperature dependence of Gibbs free energy of formation. Gases such as NO₂, O₃, and atomic oxygen were proven to have oxidation abilities higher than that of O₂, showing good agreement with the results of oxide film formation by molecular beam epitaxy.

KEYWORDS: thermodynamics, high-T_c superconducting film, NO₂, NO, N₂O, O₃, O₂, atomic oxygen

Japanese Journal of Applied
Physics

Vol. 30 No.8 Aug. 1991

p.1893-1898

NIJI-III Compact Superconducting Electron Storage Ring

Hiroshi TAKADA, Yasumitsu TSUTSUI, Katsuji EMURA,
Fujio MIURA, Chizuru SUZAWA, Takato MASUDA,
Toru OKAZAKI, Tomohiro KEISHI, Yoshikado HOSODA
and Takio TOMIMASU¹

*Sumitomo Electric Industries Ltd., Shimaya Konohama, Osaka 554*¹*Electrotechnical Laboratory, Umezono, Tsukuba, Ibaraki 305*

The NIJI-III is a compact superconducting electron storage ring for industrial applications. Features of the ring include four strongly curved large-bore superconducting bending magnets utilizing quadrupole coils with a circular cross section surrounded by an air core and a cold bore. The circumference of the ring is 15.54 m with a critical wavelength of 13 Å. Development of the NIJI-III is near completion. This report examines the design and performance of the NIJI-III.

KEYWORDS: synchrotron radiation, compact electron storage ring, superconducting magnet, cryogenic, electron-beam wobbling method

Japanese Journal of Applied
Physics

Vol. 30 No.8A Aug. 1991

p.L1381-L1383

**Bi₂Sr₂Ca₁Cu₂O₈/Bi₂Sr₂Cu₁O₆ Superconducting Superlattices:
Modulation of the Number of CuO₂ Plane between Bi₂O₂ Layers**

Ken HORIUCHI, Tomoji KAWAI, Masaki KANAI
and Shichio KAWAI

*The Institute of Scientific and Industrial Research, Osaka University,
Mihogaoka, Ibaraki, Osaka 567*

Superlattices with a combination of a superconductor and semiconductor have been formed by the periodic stacking of Bi₂Sr₂CaCu₂O₈ and Bi₂Sr₂CuO₆ layers. The observed X-ray diffraction patterns of the superlattices are consistent with those calculated from the ideal superstructures. The resistivity-temperature curve of the superlattices containing three unit layers (45 Å) of Bi₂Sr₂CaCu₂O₈ exhibits the same superconducting behavior as that of a Bi₂Sr₂CaCu₂O₈ film, indicating the Bi-Sr-Ca-Cu-O system has a strong two-dimensional nature.

KEYWORDS: Bi₂Sr₂CaCu₂O₈/Bi₂Sr₂CuO₆, oxide superconductor, laser ablation, thin film, superlattice

Japanese Journal of Applied
Physics

Vol. 30 No.8A Aug. 1991

p.L1384-L1386

**Microstructures and J_c-B Characteristics of Ag-Sheathed
Bi-Based Superconducting Wires**

Munetsugu UYEYAMA, Takeshi HIKATA, Takeshi KATO
and Ken-ichi SATO

*Osaka Research Laboratories, Sumitomo Electric Industries, Ltd.,
1-1-3 Shimaya, Konohananaku, Osaka 554*

We prepared silver-sheathed BiPbSrCaCuO wires by the powder-in-tube method. Maximum critical current densities at 77.3 K were 5.4×10^4 A · cm⁻² in a zero magnetic field, 4.2×10^4 A · cm⁻² at 0.1 T and 1.2×10^4 A · cm⁻² at 1 T. At 77.3 K, as the J_c improves, the history effects decrease. J_c and J_c-B enhancements are due to the decrease and dispersion of nonsuperconducting phases, and to grain boundary improvements.

KEYWORDS: Ag-sheathed superconducting wire, (Bi, Pb)-Sr-Ca-Cu-O, critical current density, microstructure, J_c-B characteristics

Japanese Journal of Applied
PhysicsVol. 30 No.8A Aug. 1991
p.L1390-L1392Comparison between Powder-Pressed and Melt-Processed Bulk
Superconductor Lenses (Supertrons) for Electron BeamsHidenori MATSUZAWA, Toshiyuki MIYAMOTO, Yukio CHINO,
Eiji FUKUTAKE, Tomoaki OSADA, Yoshiharu ISHIBASHI
and Tetsuya AKITSU

Faculty of Engineering, Yamanashi University, Kofu 400

To confirm a model for operation of powder-pressed bulk superconductor lenses (Supertrons), Y-based quench-melt-growth (QMG) bulk superconductors were used to focus intense electron beams (340 keV, ~1 kA, and 5~10 ns). The lens focused the beams much less effectively than any of the Y-, Bi-, and Tl-based powder-pressed bulk lenses and even worse than a copper-made lens. These facts support the validity of the model in which powder-pressed bulk superconductors behave like ferrite cores at frequencies of some hundred MHz.

KEYWORDS: high- T_c bulk superconductor lens, melt-processed superconductors, Y-based QMG superconductors, intense electron beams, supertrons

Japanese Journal of Applied
PhysicsVol. 30 No.8B Aug. 1991
p.L1462-L1464EXAFS Study on the Local Structure around Cu in the
Nitrogen-Annealed $\text{Bi}_{1.6}\text{Pb}_{0.4}\text{Sr}_2\text{Ca}_1\text{Cu}_2\text{O}_y$ Superconductor

Nobuya KURIYAMA, Hiroyuki NASU and Kanichi KAMIYA

Department of Chemistry for Materials, Faculty of Engineering, Mie University, Tsu 514

The effect of nitrogen-annealing on the local structure around Cu in the high- T_c superconductor- $\text{Bi}_{1.6}\text{Pb}_{0.4}\text{Sr}_2\text{Ca}_1\text{Cu}_2\text{O}_y$ has been studied using the extended X-ray absorption fine structure (EXAFS). In the CuO_2 plane, two Cu-O distances of 1.86 Å and 1.91 Å were observed for the nitrogen-annealed sample ($T_c=91$ K), while only one distance of 1.90 Å was observed for the untreated one ($T_c=71$ K). The coordination number of Cu was changed from about 5 to about 4 by the nitrogen annealing.

KEYWORDS: EXAFS, superconducting oxide, 2212 phase, Pb doping, nitrogen annealing, Cu-O bond

Japanese Journal of Applied
PhysicsVol. 30 No.8B Aug. 1991
p.L1468-L1470Nearly Untwinned Superconducting $\text{Bi}_2\text{Sr}_2\text{CuO}_y$ Thin Films
Grown on (Y, Nd) AlO_3 (001) Substrate

Ichiro TSUKADA and Kunimitsu UCHINOKURA

Department of Applied Physics, The University of Tokyo, 7-3-1 Hongo, Bunkyo-ku, Tokyo 113

Superconducting $\text{Bi}_2\text{Sr}_2\text{CuO}_y$ thin films were prepared *in situ* by molecular beam epitaxy with pure ozone gas. Films were deposited on SrTiO_3 (001) and (Y, Nd) AlO_3 (001) substrates, and their surface structures (Bi-O layer) were observed by reflection high-energy electron diffraction. While the film on the SrTiO_3 substrate had incommensurate modulated structures equivalently along both the SrTiO_3 [110] and SrTiO_3 [110] directions, the modulated structures of major domains of the film on the (Y, Nd) AlO_3 substrate ran along the (Y, Nd) AlO_3 [100] direction. The origin of the in-plane orientation is related to the in-plane lattice constants of (Y, Nd) AlO_3 and $\text{Bi}_2\text{Sr}_2\text{CuO}_y$.

KEYWORDS: superconductivity, $\text{Bi}_2\text{Sr}_2\text{CuO}_y$, ozone, molecular beam epitaxy, incommensurate modulated structure, untwinned structure

Japanese Journal of Applied
PhysicsVol. 30 No.8B Aug. 1991
p.L1474-L1476Superconducting $\text{YBa}_2\text{Cu}_3\text{O}_x$ Thin Film Growth on a
Vicinal Surface of NdGaO_3 Substrate

Masashi MUKAIDA, Shintaro MIYAZAWA and Masahiro SASAURA

NTT LSI Laboratories, 3-1, Morinosato Wakamiya, Atsugi-shi, Kanagawa 243-01
Tetsurō NAKAMURA, Masuhiro NATSUHARA, Hitoshi KAWAJI
and Mitsuru ITOHResearch Laboratory of Engineering Materials, Tokyo Institute of Technology,
4259 Nagatsuta, Midori-ku, Yokohama, Kanagawa 227

A new method for electrochemical synthesis of oxides in molten salt was developed. The following galvanic cell was assembled and electrolysis was carried out at 973 K between the electrodes LaB_6 vs Pt/O_2 and between Cu vs Pt/O_2 simultaneously.

Pt, LaB_6 $180\% \text{KCl} - 14\% \text{NaCl} - (6-x)\% \text{LaCl}_3 - x\% \text{CuCl}_2 \cdot (\text{ZrO}_2(\text{Y}_2\text{O}_3))\text{O}_2$, Pt

Pt, Cu

Formation of almost-single-phased La_2CuO_4 on the $\text{ZrO}_2(\text{Y}_2\text{O}_3)$ surface was confirmed when the ratio of electric currents passed through electrodes LaB_6 vs Pt/O_2 and Cu vs Pt/O_2 was controlled to 3:1.1 and the molten salt composition was fixed at 80%KCl-14%NaCl-6% LaCl_3 .

KEYWORDS: electrochemical synthesis, lanthanum copper oxide, zirconia, molten salt

Japanese Journal of Applied
Physics
Vol. 30 No.8B Aug. 1991
p.L1477-L1479

Influence of Ozone Concentration on the Preparation of Stoichiometric Superconducting Y-Ba-Cu-O Films by a Metalorganic Chemical Vapor Deposition Technique

Hiroshi OHNISHI, Hiroshi HARIMA¹, Yoshiyuki GOTO
and Kunihide TACHIBANA¹

*Manufacturing Development Laboratory, Mitsubishi Electric Corp.,
Tsukaguchi, Amagasaki, Hyogo 661*

¹*Department of Electronics and Information Science,
Kyoto Institute of Technology, Matsugasaki, Sakyo-ku, Kyoto 606*

As-grown, nearly stoichiometric YBa₂Cu₃O_{7-x} superconducting films were prepared by a metalorganic chemical vapor deposition technique on SrTiO₃(100) substrates at 650°C. This letter describes how the film characteristics change with the concentration of ozone in O₂ gas. It was found that the superconducting characters of nearly stoichiometric films can be improved by optimizing the ozone concentration. At 3% concentration of ozone, a film with the zero-resistive temperature of 85 K was obtained at a composition of Y:Ba:Cu=1.1:2:2.7. It had a smooth surface morphology and a good c-axis orientation.

KEYWORDS: superconductor, YBaCuO, MOCVD, as-grown film, ozone effect, stoichiometry

Japanese Journal of Applied
Physics
Vol. 30 No.8B Aug. 1991
p.L1535-L1537

A New Superconducting Gradiometer Complex for Vector Detection of Weak Magnetic Field

Kimisuke SHIRAE, Ayumu MATANI, Minoru YOSHIDA,
Shinjiro KIYONO and Hisao FURUKAWA

Faculty of Engineering Science, Osaka University, Toyonaka, Osaka 560

We have devised a superconducting gradiometer complex which enables the second-derivative detection of the vector components of the magnetic field at a point. Consisting of the orthogonal pairs of parallel first-derivative gradiometers, the gradiometer complex detects only two components of the magnetic field at its center, and synthesizes the last component using the former results.

KEYWORDS: gradiometer, coil, SQUID, magnetometer, biomagnetism, superconductivity

Kobunshi Ronbunshu
Vol.48 No.8 Aug. 1991
p.499-506

Use of Poly(glycidyl methacrylate) Used in Manufacturing on the Superconducting Properties of Ba-Cu-O Ceramics

Shinnosuke MIYAUCHI^{*1}, Yoshio SORIMACHI^{*1}, and Tatsuya IMAIZUMI^{*1}
^{*1}*Nagaoka University of Technology (Kamitomioka-cho, Nagaoka, 940-21 Japan)*

Y-Ba-Cu-O superconducting thick films were prepared with poly(glycidyl methacrylate) (PGMA) as a polymeric binder by a screen method. In this paper, influences of the binder on the superconducting properties are discussed. The superconducting ceramic thick film was obtained through very slow thermal decomposition of the binder. But T_c , where resistance becomes 0, was lowered with increasing the amount of the binder. SEM observations and X-ray analyses showed that the lowering of T_c was caused by structure strained due to the thermal decomposition of binder followed by the inhomogeneous sintering and by the thermal expansion difference between a substrate and the conducting layer. Moreover, XMA analyses suggested that the very slight amount of carbon, which remained even after the sintering was related to the lowering of T_c .

KEY WORDS Superconducting Ceramics / Poly(glycidyl methacrylate) / Binder / Thick Film /

Keyword Index of Volume 99 (1991)

- (Pb, La)TiO₃ 159
 2212 phase 758
²⁷Al-NMR 638
²⁹Si NMR 409
²⁹Si-NMR 638
 3C-SiC 363
 3D pore structure 1074
 6H-SiC 363
 α-Alumina 535
 a-axis orientation 514
 abrasive wear 797
 AC conductivity 265
 acid treatment 199
 activation energy 345
 active SiO₂ 305
 additives 72, 1140
 adhesion 412
 aerosols 1000
 Ag substrate 777
 Agglomeration factor 803
 Al-substitution 1174
 Al₂O₃ 51, 210, 1209
 Al₂O₃ abrasive 597
 Al₂O₃ coating 578
 Al₂O₃ compact 127
 Al₂O₃ sol 670
 Al₂O₃-SiC composites 797
 Al₂O₃-ZrO₂ system 261
 Al₂O₃/SiC nano-composites 510
 Al³⁺-substituted tobermorite 764
 AlB₂ addition 265
 ALC 409
 alkali durability 330
 alkali metal ions 137
 alkali passivation 531
 alkali resistance 1053
 alkali-earth metal oxide 330
 alkaline and alkaline
 earth salt additives 305, 693
 alkoxide 42, 179,
 290, 551
 alkoxide reaction 764
 alkylamine 14
 AlN 597, 819
 alumina 46, 92, 132,
 179, 233, 357,
 371, 491, 801, 100
 alumina layer 105
 alumina-zirconia 132
 aluminum 238
 aluminum nitrate 447, 735
 aluminum oxide 525
 aluminum
 polynuclear complexes 735
 aluminum-iso-propoxide 1214
 amakusa Pottery Clay 696
 ammonium Aluminum Carbonate
 Hydroxide (AACH) 535
 amorphous 102, 447
 amorphous carbon films 703
 amorphous phase 683
 anelastic relaxation 628
 anisotropy 458
 annealing 371
 anorthite 570
 apatite 2, 191,
 917, 937
 apparent cross
 sectional aspect ratio 793
 application 981, 1029
 aqueous solutions of
 slightly soluble electrolytes 227
 artificial bone 937
 autoclave 1110
 Avrami-Erofeev's equation 388
 β silicon nitride shisker 87
 β'-o' sialon 169, 644
 β-Alumina 551
 β-diketonate chelate 514
 β-sialon 1214
 β-SiC 429, 1136, 1140
 β-tricalcium phosphate 206, 1231
 B₄C addition 265
 Ba((Mg Co)_{1/3}Nb_{2/3})O₃ 633
 Ba(Mg_{1/3}, TA_{2/3})O₃ 466
 Ba₅Nb₄O₁₅ 633
 ball-on-ring test 558
 barium titanate 701
 basal spacing 1174
 BaTiO₃ 514
 beam-bending viscometer 164
 bending strength 23, 62, 77,
 120, 176, 182,
 186, 382, 458,
 483, 1214
 BeO 620, 699
 Bi-Pb-Sr-Ca-Cu-O film 217
 Bi-Pb-Sr-CA-Cu-O
 thin film 67, 1145
 Bi-Sr-Ca-Cu-O film 334
 Bi-substituted iron garnet 834
 Bi-system tape 825
 bimodal alumina powder 1150
 bioactive 1231
 bioactive and ferromagnetic
 glass-ceramic 937
 bioactive cement 937
 bioactive composite 937
 bioactive glass 937
 bioactive glass-ceramic 937
 bioactivity 2, 917, 937
 bioceramic material 19
 bioceramics 917
 biomaterials 917
 BN addition 265
 boehmite 169, 644
 bone implant material 927
 bone replacement 917
 boundary layer 1080
 breakdown voltage 772
 brittle matrix 953
 building materials 1074
 burn-out 1150
 C 77
 C/C composite 377
 C₂H₄ 1120
 Ca-addition 295
 CaCl₂-Si(OC₂H₅)₄-AlCl₃-
 C₂H₅OH-H₂ system 764
 calcium metaphosphate 206
 calcium phosphate 438
 calcium phosphate cement 927
 calcium phosphate ceramics 206
 calcium titanium phosphate 660
 Cao-SiO₂-P₂O₅ 937
 CaO-SiO₂-P₂O₅ glass 2
 capacitor 154
 capillary force 1150
 carbide 142
 carbon 1029, 735
 carbon composite 992
 carbon electrode 105
 carbon fiber 1029
 carbon rich layer 1090
 carbonation 409
 carbothermic
 reduction of silica 752
 CaSiO₃ 1187
 cation distribution 624
 cation exchange 764

cation exchanger	102	copper	412	dielectric relaxation	628, 812
CdS	609	copper oxide	420	dielectric semi-	
CeO ₂	339	coprecipitation	1187	conductive ceramic	1080
ceramic capacitor	1080	corrosion	1223	diffuse phase transition	812
ceramic capillary	199	Cr ₂ O ₃	127	diffusion	282, 649
ceramic coating	206	Cr ₂ O ₃ abrasive	597	diffusion layer	1182
ceramic composites	541	crack	715	dip-coating	843
ceramic nanocomposite	945	crack bridging	310, 962	dip-coating method	614
ceramic-matrix composites	1009	crack deflection	310	dipping-pyrolysis process	295
ceramics	142, 403,	crack growth	1009	direct current	82
660, 1009		crack healing	244	direct metal oxidation	1228
ceramics coating	665	crack model	371	dislocation	597
ceramics injection molding	438	cracking	665	disordered complex	
characterization		creep	282, 345	perovskite	812
thermal barrier	970	cristobalite	1099	dispersing media	525
charged state	137	critical current density	67	dissolution of Mg ion	578
chelate compound		CrO ₃	127	doped glass	609
of aluminum	578	crystal chemistry	420	doped silica	872
chemical bond	1029	crystal structure	367, 420, 825	double alkoxide	992
chemical reaction	715	crystalline intermediate	102	DTA	447, 570,
chemical sensors	858	crystallization	8, 210,	1104, 1228	
chemical spray pyrolysis	324	551, 570, 683		durability	1110
chemical vapor		crystallization behavior	1156	duty factory	398
deposition	176, 1024	crystallography	535, 710	dynamic fatigue	110
chevron notch	46, 176	CsNO ₃	670	ECR plasma CVD	703
chlorination	305, 693	cubic boron nitride	95	effect of shape of micropores	720
chlorosilanes	1120	cubic resonance method	584	effect of volume	
contact angle	1127	CuCl-doped glasses	257	fraction of micropores	720
coarse grains	1070	curing kinetics	501	effective fracture energy	51, 416
coarsening	244	current density	772	elastic anomaly	584
coating	19, 92,	cutting tool materials	142	elastic constant	584
1063, 1231		CVD	241, 377, 514,	elastic modulus	649
coating techniques	872	1046, 1130, 1136		elastic property	628
coherent length	257	CVD-coating	1090, 1168	electrical property	510
cold-wall type apparatus	1130	cyclic fatigue	286, 477,	electrical resistivity	324, 620, 1162
colloidal SiO ₂	222	520, 1009		electroconductive ceramics	398
cold-wall type apparatus	241	cyclic-CIP	182	electrolysis	105
color	1182	damage-tolerant design	1009	electrolytic etching	1080
columnar-like crystal	653	DC conductivity	265	electron spin resonance	899
columnar-like film	115	DEB test	452	electron-phonon interaction	889
complex impedance analysis	159	debinding	438	electrophoretic	
composite	51, 142,	debye peak	628	deposition	105, 447, 496
416, 1046		debye-Waller factor	889	electrostriction	812
composite ceramics	19, 87, 357	degree of c-axis orientation	30	emission spectra intensity	703
composite fine powder	1120	densification	77, 132, 665	emulsions	1000
composite material	1156	density	36, 169, 275	epitaxial film	241, 992
composite materials	72	deposition rate	115	epitaxial growth	514
composite membrane	1234	desification	525	epitaxial PLZT film	1130
composite piezo-		desorption	1162	equivalent inclusion method	720
electric ceramic	1096	diamagnetic glass	881	evaporated film	412
composites	676	diamond	653, 1024	excess Ca and Cu	334
composition	1090	diamond film	115	exciton	257
compositional grade film	970	diamond films	1162	external additive	1104
compression-prestress	149	diamond semiconductor	1024	F-doped silica glass	584
conductivity	353	diamond surface	1162	fabrication process	825
contact angle	227	dicalcium phosphate	927	Faraday rotator glass	881
content	238	dielectric constant	159, 319	fast response	592
controlled hydrolysis	1000	dielectric loss	30	fatigue	110
conversion efficiency	728	dielectric loss tangent	319	fatigue life distribution	477
conversion reaction	728	dielectric properties	614	fatigue threshold	1009
cooling rate	334	dielectric property	787	Fe ₂ O ₃ -CaO-SiO ₂ glass	8

Fe ₄ N	301	gold	412	222, 290, 992	
ferrimagnetic glass-ceramics	8	gradient structure	741	hydrolysis of	
ferroelectric films	819	grain boundary diffusion	132	tetraethylorthosilicate	58
ferroelectrics	154	grain boundary sliding	282, 345	hydrolysis precipitates	102
FET	1024	grain boundary	772	hydrothermal aging	120, 186, 382
fiber	992	grain diameter	238	hydrothermal corrosion	1110
fiber bridging	953	grain growth	132, 244, 310,	hydrothermal hot-pressing	58
fiber laser	881		394, 429,	hydrothermal reaction	728, 1099
fiber pullout	953		782, 1140	hydrothermal synthesis	271
fiber reinforced composite	953	grain size	149, 310, 1070	hydrothermal treatment	1203
figure of merit	30	grain size exponent	282	hydroxy-phlogopite	728
film	295, 1024	grain size dependence	604	hydroxyapatite	927, 438
films	843	granule	1124	hyperthermia	8, 937
flaw-size-distribution	349	graphite	1029	I-V characteristics	353, 772
flexural strength	699, 1113	graphite inter-		IF method	403
flexural test	46	calation compound	1029	image analysis	169, 1074
fluor-phlogopite	728	green body	1124	impregnation method	127
fluorite structure	420	green density	105	inclusion	199
flux cooling technique	353	grinding flaw	1214	indium	412
flux growth	327	groove	715	injection molding	199
fly ash	233	growth layers	653	inorganic polymer	174
foreign oxides	525	growth twins	710	insulating film	72
four-point bending strength	51	h-Boron Nitride	566	interfacereactions	917
four-point probe method	772	hardness	644, 797	interfaces	244
four-point shear bending test	558	hardness anisotropy	1039	interfacial bonding	1063
fractal analysis	1074	heat resistance	517	interfacial polarization	159
fractal dimension	545	heat transfer	471	internal friction	584, 628, 649
fracture	244, 434, 452	heat-treatment	102	ion	649
fracture criteria	558	heating rate	334	ion exchange	1219
fracture stress	110, 1113	heating temperature	578	IR sensing	592
fracture toughness	46, 51, 77,	heterocontact	807	iron nitride	301
	176, 310, 403,	heteronanocomposite powder	992	iron spinel	624
	416, 452, 458,	hexaaluminate	517	IS method	403
	604, 699, 720,	hexagonal ferrite	834	isolated grain	1145
	797, 981, 1063	high dielectric constant	154	isomorphous replacement	1237
free carbon	752	high pressure synthesis	810	ITO films	324
free Si	1136	high pressure polymorphs	810	J _c	825
free silicon	62	high purity ZrSiO ₄ powder	1058	K ₁ -V diagram	477
frit	1231	high T _c phase	1145	K ₂ Ti ₄ O ₉ crystals	102
frost durability	1074	high temperature		kaolin	706
FT-IR-PAS	693	bending strength	1058	kaolinite	271
Fulcher's equation	164	high temperature PHB	889	kinetics	244, 535
functionally		high toughness	310	K ₁ C	191
gradient materials	970, 1046	high-T _c phase	334	La ₂ O ₃	339
γ-alumina	624	high-temperature strength	1063	lamine	176
Ga-substitution	1174	high-temperature XRD	670	lanthanum oxide	701
gain growth	525	HIP	169, 191,	laser	491
gas deposition	777		644, 665	laser assisted	801
gas phase reaction	676	hole	889	laser flash method	471
gehlenite	570	hole concentration	758	laser glass	881
gelation	1000	hollow glass microspheres	1203	laser mirrors	872
glass	210	homogeneity	1191	lasers	858
glass phase	282	homogeneous width	889	lattice constant	624
glass substrate	531, 584	hot isostatic pressing	23, 186	lattice parameter	701
glass transition temperature	36		382	lattice strain	429, 1140
glass-ceramic dental crown	937	hot-press	275, 620	leach rate	1110
glass-ceramic		hot-press sintering	72	lead magnesium niobate	154
layered composite	434	hot-pressed Si ₃ N ₄	458	lead titanate	159
glass-like carbon	1029	hot-pressing	191	Li	1237
glaze	483	hybrid composite	945	Li ₂ O-SiO ₂ glass	1156
glaze of porcelain	1182	hydrolysi	23, 179,	life prediction	1009

- linkage of particles.....58
 LiOH aqueous solution.....728
 lithium niobate992
 lithography.....244
 low energy excitation modes.....889
 low porosity676
 low resistivity junction412
 low temperature sintering58
 low thermal expansion660
 luminescence858
 machining damage.....371
 machining rate.....398
 magnesium nitrate.....447
 magnesium triphosphate146
 magnetic materials72
 magnetic separation233
 magnetite8
 magnetization measurement683
 magneto-optical effect834
 Magneto-optical enhancement.....834
 magneto-optical thin film834
 manganese314
 mass-spectrometer1084
 material design420
 matrix cracking953
 mechanical
 properties.....87, 142, 644,
 962, 1228
 mechanical
 property275, 510,
 699, 1191
 mechanical strength1070
 mechanical strength149, 1156
 mechanochemical synthesis.....146
 melting.....801
 membrane.....571
 mesh.....1124
 metal alkoxide.....334, 992
 metal alkoxides1000
 metallization.....314
 metastable
 tetragonal zirconia1197
 methanol to gasoline test1219
 Meyer's law1038
 Mg.....496
 Mg-PSZ1009
 Mg₃(PO₄)₂·22H₂O146
 Mg₃(PO₄)₂·8H₂O146
 MgHPO₄·3H₂O146
 MgO particles.....578
 micro-Shirasuballoons1203
 microcrack137, 491
 microcrystal.....257, 609
 microindentation1038
 microstructural analysis458
 microstructure23, 2186, 244, 261,
 282, 310, 525, 566, 633,
 644, 782, 787, 843, 962,
 981, 1090, 1124
 microwave dielectric633
 mirror.....520
 mirror-like region.....520
 mixed solvent.....179
 mixed-mode fracture.....558
 Mn₆Si314
 MnSiN₂314
 model calculation.....793
 modified pore size545
 modulated structure367
 monodispersed particle179, 290
 montmorillonite.....14
 morphology653, 1090, 1136
 Mössbauer spectrum624
 mullite.....87, 233,
 282, 339, 345,
 452, 782, 992
 mullite ceramics1191
 mullite fiber638
 mullitization1191
 multi target67, 217, 1145
 multiaxial stress states558
 N₂ gas1084
 Na-mica1174
 NaGaTi₅O₁₂327
 nano composite1209
 nano-size dispersions945
 nanostructure-
 properties relationship945
 Na₂O-CaO-SiO₂ glass1156
 NaOH aqueous solution.....728
 natural polarization30
 near-net-shape sintering.....394, 676
 needle-like mullite706
 new carbon1029
 new tunnel structure327
 NH₃1120
 Ni77
 Ni/Cu970
 nicalon-SiC fiber1090, 1168
 nitridation676, 1228
 nitriding atmosphere301
 nitrogen429
 no additives275
 non-alkali glass36, 570, 1104
 non-destructive inspection349
 non-linear coefficient772
 non-stoichiometry154
 nonlinear glass materials881
 nonlinear optics858
 normal pressure sintering182
 NO_x807
 nozzle115
 O₂ gas.....752
 optical fibers872
 optical properties257, 899
 optical property1024, 1130
 optical storage889
 optical-fiber connector.....199
 opticalmicroscope1124
 organic polymer1053
 organometallic polymer992
 orientation992
 orthorhombic HfO₂.....810
 oxidation82, 37, 752,
 1084, 1214
 oxidation resistance541
 oxidation treatment.....501
 oxide683
 oxide matrix541
 oxide superconductor420, 825
 oxidizing gas.....807
 oxygen1162
 oxygen content.....758
 oxygen lattice diffusion.....99
 oxygen partial pressure624
 PAN-based carbon fiber592
 paramagnetic glass881
 partial hydrolysis174
 particle size62, 1058
 particles1000
 Pb doping.....758
 Pb, La)TiO159
 Pb(DPM)₂-La(DPM)₃-Zr(O-t-Bu)₄-
 Ti(O-i-Pr)₄-O₂ system1130
 Pb(Zr_{0.52}Ti_{0.48}O₃)507
 PbO-KF-PbCl₂ flux507
 PbTiO₃ single crystal353
 penetration1127
 penetration viscometer164
 permeability62, 545
 perovskite.....154
 perovskite structure420, 633
 phase diagram.....210
 phase separation.....210
 phase stability.....810
 phase transformation82, 120, 186,
 261, 382,
 491, 1197
 phonon-side band889
 photo acoustic spectra447
 photochemical
 hole burning (PHB).....889
 photochromics.....858
 photon-gated PHB889
 photonic materials858
 piezoelectric films819
 piezoelectric
 resonance method.....628
 pillared clay14
 plasma1024
 plasma activated
 (enhanced) CVD.....872
 plasma spraying.....491
 plasma-spray665
 plasmaspraying917
 plastic flow434
 point defects.....899
 pollucite1237
 pollucite powder670
 polycarbosilane92, 1117
 polycarbosilane fiber501
 polycrystalline alumina604

- polyethyleneglycol..... 1053, 1150
polytitanosiloxane..... 174
porcelain..... 483
porcelain body 149, 1070
pore drag 244
pore shape 545
porosity 62, 491,
665, 706, 1156
porosity fracture origin..... 483
porous ceramics 706
porous glass 330, 1053, 1234
porous glass-ceramics..... 747
porous material 14
post-sintering 191
potassium accelerator 305
powder preparation..... 1187
powder synthesis 1000
powders 735
precracked specimen 286
precursor 551
precursor gel 42
preferred orientation 1136
preparation 970
pressure drop..... 62
pressure pyrolysis 992
pressureless sintering..... 77, 566
properties..... 357
PSZ..... 95
PSZ/NiCrAlY..... 970
pull-out..... 51
pyroceram glass ceramics 471
pyrochlore 154
pyroelectric property 30
pyrolysis..... 388
pyrolytic-carbon
/graphite laminate 1009
PZT..... 241, 507,
614, 1209
PZT/Nb 970
PZT/Ni 970
 θ -Alumina..... 535
quantitative analysis 169
quantitative image analysis..... 1074
quantum size effect 609
quartz 149, 1070
R.F. plasma 1120
radiation damage 899
radio-frequency
thermal plasma CVD 653
radioactive glass sphere 937
raman spectroscopy 1024
rapid quenching 683
rapid sintering..... 466
rare earth oxide..... 339
rare earth doped glass 881
rate-determining step..... 501
rattling ion model 812
reaction kinetics..... 752
reaction mechanism..... 388, 501, 752
reaction-bonding 394, 676
reactive sputtering 1182
real threedimensional
aspect ratio 793
recovery..... 747
reduction 82
reflection 1182
regular array 1124
relative density 132
relative dielectric constant..... 30
relaxor ferroelectrics 812
residual stress 286, 371,
377, 434, 665
resistivity 275
rf magnetron
sputtering 67, 217, 1145
rice hull ash..... 305, 693
rice husk 741
Rietveld method 810
ring-on-ring test..... 558
rock salt structure..... 420
rod-like grain..... 793
role of water 58
rotary bending sintered Si_3N_4 520
rotating bending test 477
rutile 747
schottky contact 1024
sea water..... 747
second phase..... 1140
selective gas permeation..... 517
self-setting cement 927
semiconducting 701
semiconducting
ceramic monofiber 592
semiconductor doped glass 881
sensitivity in
weak magnetic field..... 217
sensor 807
SEPB method 403
serpentine 271
shirasu 1203
shrinkage..... 1127
 $\text{Si}(\text{OC}_2\text{H}_5)_4$ 42
Si-Ti-C-O fiber
(Tyranno fiber)..... 388
 Si_3N_4 169, 644,
1084, 1120
sialon 981
SiC 377, 620, 699,
1046, 1120
SiC ceramics..... 238, 715
SiC fiber 592, 741
SiC powder 688, 752, 803
SiC whisker 51, 416, 541,
688, 1063
 $\text{SiC-p}/\text{Al}_2\text{O}_3$ 1228
SiC-reinforced alumina..... 1009
SiC/C 970
SiC/TiC 970
 SiCl_4 305, 693
silica 992
silica/alumina ratio..... 1099
silica glass 899
silica stone 1099, 1219
silicate 339
silicate ion 409
silicon carbide..... 62, 92,
182, 363,
807, 1117, 1113
silicon carbide
/Alumina composite sheet 1117
silicon nitride 286, 310, 314,
477, 644,
981, 1009,
1063, 1223
silicon nitride
bonded aluminum oxide 394
silicon nitride
bonded ceramics 676
silicon nitride whisker 357
silver 412
simulated body fluid..... 2
single crystal 367, 507
single crystal growth 801
single edge
notched beam test 604
sinterability..... 787, 1187, 1191
sintered SiC..... 265
sintered silicon nitride 558
sintering..... 87, 105, 261,
301, 357, 438,
525, 660, 782,
981, 1150
sintering process 1058
sintering temperature 238
 SiO-TiO_2 sol 14
 SiO_2 210
 SiO_2 sol 670
 $\text{SiO}_2\text{-Al}_2\text{-O}_3$ ceramics 282, 345
 $\text{SiO}_2\text{-C}$ mixed powder 688, 803
 $\text{SiO}_2\text{-MgO-Al}_2\text{O}_3$ 1127
 $\text{SiO}_2\text{-TiO}_2$ fibers 174
 SiO_x fiber 741
 SiO_xC_y fiber..... 741
slice model 46
sliding face..... 715
slow crack growth 137, 452
 Sm_2O_3 339
small cracks 1009
smooth specimen 286
soda-lime-silica glass..... 137
sodium gallotitanate..... 327
sodium hydroxide solution 1099
softening temperature 36
sol-gel..... 517, 551,
843, 1000, 1237
sol-gel materials..... 858
sol-gel method 531, 638,
764, 1053, 1234
sol-gel process 42, 222, 609,
614, 660, 670
solid phase reaction 438
solid solution 701
solid state bonding..... 665

solvent.....	290	TEM	388	transformation	23, 363, 535, 962
sorption-desorption.....	758	temperature dependence	604	transmission	
speaker diaphragm	1024	tensile strength	1168	electron microscopy.....	597
specific surface area	1219	tetracalcium phosphate	927	transverse vibration	584
spherical coordinates.....	793	tetraethoxysilane	174, 1000	tricalcium phosphate.....	19
spherical silica particles.....	58	tetragonal		Tungsten	1127
spin-coating	843	zirconia polycrystals	110, 319	twinning	710
spinel	649, 1038, 1209	tetragonal ZrO ₂	99	twins	653
spinel ferrite	834	tetrahedral rotation angle.....	1174	TZP	110
spinnability	638	tetrapropyl-		ultrafine powder	777
spinodal decomposition	330	ammonium bromide	1099	uni-directional orientation	1063
spray pyrolysis	1000	TG.....	447	uranium adsorption capacity.....	747
sputtering method.....	834	Tg	164, 570	uranium solution.....	747
Sr/Ca ratio	758	thermal analysis	1150	vacancy	624, 649
SrO.....	353	thermal conductivity	620, 706	VAMAS project.....	403
SrSiO ₃ ceramics	787	thermal diffusivity.....	471	vapor phase reaction.....	741
stacking fault	429, 710, 1140	thermal expansion		vapor-diffusion.....	314
stacking layer structure	1145	coefficient	319, 1046	very high pressure sintering.....	95
stainless steel foil	715	thermal expansion	36, 1237, 1156	Vickers hardness.....	77, 127
standard reference materials	471	thermal hysteresis	324	Vickers microhardness	95
static fatigue	110, 286, 520	thermal plasma		viscosity	164
statistical analysis.....	477	chemical vapor deposition (CVD)		volume resistivity	319
stearic acid.....	1150	115, 1162	water vapor	1104
stoichiometry	1038	thermal shock behavior	1113	water vapor resistance.....	1234
strength	644, 696, 981	thermal shock fracture		water-quench	1113
strength degradation.....	1223	resistance parameter.....	1113	weathering resistance	531
stress corrosion cracking	403	thermal stability	1168, 1219	Weibull coefficient	1070
stress distribution	349	thermal stress relaxation.....	970	Weibull distribution	182
stress exponent	282, 345	thermite method	496	Weibull statistics.....	349
stress in glaze.....	483	thermodynamic stabilization	1197	weight gain	1084
structural analysis	810	thermodynamics	244, 777	weight loss	1223
structural ceramics	349	thermoelectric power	238	wet polishing	597
structural changes		thermogravimetry.....	388, 501	wettability	227
of SiO ₂ network	693	thick film.....	777	wetting	1127
structure	899, 1029	thin film.....	514, 614, 872	whisker reinforced ceramics	793
structure analysis.....	367	three point		willemite	570
substrate	683	bending strength.....	339	wire EDM	398
sulfuric acid.....	1223	TiB ₂	77	wollastonite	1104
superconductor	295, 334, 683, 758, 777	TiB ₂ /Cu	970	X-ray diffraction.....	82, 95, 447
surface area.....	466	TiC.....	377, 1046	XPS	1120
surface chemistry	137	TiC/Ti	970	YB ₂ Cu ₃ O ₇	295
surface crystallization	1104	TiN ceramics	275	YBa ₂ Cu ₃ O _{7-x}	412
surface damage.....	597	TiN film	1182	YBa ₂ Cu ₄ O ₈	295
surface dielectric layer	1080	TiN/Ti	970	(Y, Ce)-TAP/Al ₂ O ₃ substrate.....	319
surface diffusion	429	TiO ₂ addition	261	(Y, Ce)-TZP	23
surface energy	525	TiO ₂ -SiO ₂	747	(Y, Ce)-TZP/Al ₂ O ₃	
surface free energy	1197	Ti-OH	747	composites.....	120, 186, 382
surface modification.....	314, 992	titania-silica.....	531	Y ₂ O ₃	210, 339, 1110
surface morphology	703	titanite.....	570	Y-system film.....	825
surface roughness	67, 319, 398, 416, 1182	titanium	1231	Y-ZrO ₂	466
surface structure	2	titanium boride	142	Young's modulus	699, 1046
surface treatment	1162	titanium carbide	676	yttria-partially	
suspension.....	105	titanium carbo-nitride	142	stabilized zirconia.....	19, 82, 206
swelling.....	1174	titanium chelate.....	174	zero-phonon line	889
synchro-shear.....	535	titanium nitride.....	363	zinc	801
synthesis	179, 290, 735	tobermorite	409	zinc oxide.....	710, 807
tableware	483	tool	1024	zirconia.....	82, 110, 132, 191, 199, 290, 330, 345, 696, 782, 992
T _c	758, 825	topotaxial reaction	271		
TCP	438	toughening.....	953		
		toughness	696, 962		
		tracer diffusion	99		

zirconium oxide	1053, 1234	zone refining.....	801	ZrO ₂ /SUS.....	970
zirconium titanate	367	ZrN powder	496	ZrSiO ₄	42
ZnO	819	ZrO ₂	628	ZrSiO ₄ powder.....	222
ZnO varistor.....	772	Zr(O ⁱ C ₃ H ₂) ₄	42	ZrSiO ₄ precursor.....	222
Zn ₇ Sb ₂ O ₁₂ spinel.....	710	ZrOCl ₂	222	ZSM-5 zeolite	1099, 1219

Author Index of Volume 99 (1991)

Abe, Y.	174	Goda, S.	649	Ikuma, Y.	99, 466
Adachi, K.	324	Gomi, M.	834	Imai, A.	551
Akamatsu, K.	1182	Gotoh, K.	604	Imai, Y.	592
Akatsu, T.	51, 416	Griscom, D.	899	Imashita, K.	241, 1130
Akiba, Y.	339, 1228	Groot, K.	917	Inada, H.	23, 120, 186, 319, 382
Akimune, Y.	176, 477, 1228	Gunji, T.	174	Inoue, O.	72
Amakawa, K.	30	Hagio, T.	566	Inoue, T.	703
Arai, H.	517	Hamada, Y.	271	Ioku, K.	58, 191
Arai, T.	330	Hamano, K.	149, 1070	Iseki, T.	1038, 1096
Arai, Y.	764	Hangas, J.	676	Ishi, H.	416
Arakawa, M.	227	Harada, H.	132, 566	Ishibashi, N.	339
Arakida, T.	801	Harada, Y.	466	Ishida, S.	1084
Arato, T.	447	Hasegawa, A.	701	Ishihara, C.	670
Asahara, Y.	881	Hasegawa, H.	628	Ishihara, S.	1127
Asano, T.	1223	Hasegawa, M.	149, 1070	Ishihara, Y.	105, 1099, 1219
Ashizuka, M.	110, 282, 345	Hashimoto, N.	735	Ishii, M.	67, 217, 1145
Ashley, C.S.	843	Hatanaka, T.	620	Ishii, T.	1209
Awaji, H.	403	Hattori, M.	14	Ishikawa, K.	305
Bamberger, C.	1133	Hayakawa, H.	398	Ishikawa, M.	1084
Becher, P.	962	Hayashi, K.	99, 535, 604	Ishikawa, Y.	222, 665
Bradt, R.	710, 1038, 1096	Hayashi, N.	127	Ismail, M.	782
Brinker, C.J.	843	Hayashi, S.	787, 1187	Itatani, K.	660
Brynstad, J.	1133	Hayashi, T.	8	Ito, Y.	665
Chai, M.	517	Hino, M.	693	Iwasaki, H.	1134
Chiba, A.	394	Hirabayashi, H.	62, 715	Iwata, T.	92
Chigira, S.	1156	Hirai, T.	514, 970	Jinbo, K.	182
Chow, L.	927	Hirano, M.	23, 120, 186, 319, 382	Jinnai, K.	1203
Dauskardt, R.	1009	Hirao, K.	584	Jinno, H.	624
Deki, S.	735	Hirao, S.	14, 992	Kajiwarra, T.	592
Deshimaru, Y.	758	Hirata, Y.	105, 1099, 1219	Kakehi, Y.	388
Dunn, B.	858	Hirayama, T.	324	Kamata, K.	275, 703
Ebisawa, Y.	8	Hirosaki, N.	176	Kamino, M.	683
Eguchi, K.	330, 517, 1234	Hirota, K.	72	Kamitani, M.	1074
Endo, A.	227	Hiug, T.	466	Kamiya, K.	233, 257
Endoh, S.	801	Hokii, T.	545	Kamiya, N.	797
Frye, G.C.	843	Hon, M.H.	1136	Kamiyama, Y.	496
Fujii, S.	353, 507	Honda, T.	110, 282, 345	Kanaoka, C.	545
Fujiki, Y.	327, 638	Horie, K.	889	Kanda, H.	82
Fujimori, N.	1024	Hoshino, H.	222	Kaneko, S.	257
Fujimoto, Y.	458	Hurd, A.J.	843	Kaneko, Y.	438, 1134
Fujinuma, K.	238	Hwang, C.S.	261	Kani, A.	62, 715
Fujita, T.	728, 1127	Ichikawa, H.	592	Kanaka, Y.	438
Fujitsu, S.	701	Ichinose, A.	420	Kanzaki, S.	1191
Fujiwara, H.	507	Ichinose, H.	706, 1182	Kashiwaya, H.	665
Fukunaga, J.	36, 164, 570, 1104	Igarashi, T.	377	Katano, Y.	1228
Fukutomi, M.	825	Iguchi, Y.	551	Katayama, K.	782
Funakubo, H.	241, 1130	Iio, S.	541, 1223	Katayama, S.	62, 334, 531
Furuta, S.	706	Ikawa, H.	367	Kato, E.	483
Glaeser, A.	244	Ikazaki, F.	233	Kato, M.	179
Goda, K.	159	Ikeda, M.	179, 290, 409	Kato, Z.	1124

Katou, M.	496	Li, H.	1038, 1096	Nagasaka, K.	609
Katsuki, H.	706, 1182	Li, J.X.	1090, 1162	Nagashima, H.	77
Kawaguchi, Y.	452	Lin, W.H.	261	Nakada, S.	137
Kawahara, A.	706	Lu, Y.M.	1136	Nakagawa, Z.	149, 1070
Kawai, C.	377, 1046	Machida, M.	186, 382, 517	Nakajima, K.	301
Kawamoto, Y.	19, 146, 206, 1231	Maeda, H.	825	Nakajima, M.	688, 803
Kawamura, K.	92, 164, 633, 1117	Maeda, K.	154, 699, 1113	Nakamichi, H.	1234
Kawamura, M.	233	Maki, J.	624	Nakamura, K.	620
Kawamura, S.	19, 146, 206	Manabe, T.	295	Nakamura, M.	1074
Kawano, T.	584	Maruoka, K.	238	Nakamura, T.	649
Kawarada, M.	1209	Maruyama, K.	703	Nakamura, Y.	807
Kawasaki, H.	578	Masaki, T.	99	Nakanishi, S.	164
Kawashima, T.	310	Masuda, M.	558	Nakano, S.	683
Kersten, R.	827	Matsuba, T.	227	Nakasuji, Y.	558
Kieda, N.	241	Matsuda, A.	531	Nakata, H.	305
Kikuchi, M.	597	Matsuda, O.	696, 706	Nakata, Y.	693, 1120
Kikuta, K.	992	Matsui, M.	558	Nakayama, H.	30
Kimura, K.	1203	Matsui, T.	1063	Nakayama, M.	466
Kimura, S.	182, 349, 371, 443, 720, 1090, 1168	Matsuno, Y.	531	Nakazawa, H.	514, 728
Kimura, Y.	227	Matsuo, T.	398	Narisawa, T.	447
Kinoshita, M.	660	Matsuo, Y.	182, 371, 349, 443, 720, 1090, 1162	Narita, T.	314
Kinoshita, T.	793	Matsushita, J.	77	Nasu, H.	257
Kishi, K.	1214	Matsushita, K.	649	Niihara, K.	510, 945
Kishi, T.	452	Matsushita, Y.	154, 620	Nishikawa, T.	604
Kishioka, A.	660	Matsuura, S.	416	Nishimoto, A.	105
Kisuki, H.	458	Matsuyama, T.	186, 382, 747	Nishimura, T.	182
Kitajima, K.	1150, 1174	Messing, G.	1000	Nishio, H.	169, 644
Kitakami, K.	349, 443	Michiue, Y.	327	Nishio, T.	638
Kitamura, A.	310	Minami, T.	531	Nishioka, M.	58
Kitao, H.	398	Minehan, W.	1000	Nishizawa, K.	1231
Ko, H.N.	520	Misono, T.	174	Niwa, T.	286
Kobayashi, H.	42, 127, 222, 339, 496, 670, 1058, 1237	Mitamura, T.	42, 127, 222, 339, 496, 670, 1058, 1237	Noda, T.	777
Kobayashi, M.	633	Mitomo, M.	981	Nogami, M.	609
Kobayashi, T.	115, 653, 1162	Miura, N.	758	Nomura, K.	735
Kobayashi, Y.	275, 483	Miura, T.	633	Nonaka, Y.	447
Kobune, M.	30, 353	Miura, Y.	578	Nozu, T.	227
Kodama, T.	1099, 1219	Miyake, A.	1053	Oda, K.	1110
Kodama, Y.	46	Miyake, K.	1174	Ogasawara, T.	176, 371, 477, 1228
Koga, J.	92	Miyake, M.	1046, 1063	Ogura, G.	471
Koganezawa, N.	447	Miyamoto, Y.	660	Ohashi, Y.	483
Kokaji, A.	1223	Miyayama, M.	592	Ohira, O.	483
Kokubo, T.	2, 8, 747, 937	Miyazaki, Y.	566	Ohkubo, T.	233
Komura, O.	1063	Mizuta, S.	295	Ohnishi, K.	1209
Kondo, W.	295	Mizutani, N.	82, 179, 241, 290, 772, 1130	Ohnishi, T.	1074
Kondoh, I.	87, 357	Mori, T.	42, 222, 592, 670, 720, 1058, 1237	Ohno, H.	1197
Kose, S.	87, 357	Morinaga, K.	199, 535	Ohta, H.	471
Kosuge, K.	271	Moriyama, M.	275	Ohta, K.	696
Koumoto, K.	429, 701, 807, 1140	Munakata, M.	416	Ohta, S.	1191
Koyama, R.	807	Murakami, H.	777, 1197	Ohtaka, O.	810
Kubo, H.	793	Murakami, Y.	210	Ohtake, T.	233
Kubota, Y.	110, 282, 345	Murakawa, N.	688, 803	Ohtsuki, O.	2
Kuga, Y.	801	Murayama, N.	46	Ohura, K.	8
Kugimiya, K.	72	Muto, N.	592	Okada, A.	1223
Kumagai, T.	295	Nagae, H.	1231	Okada, K.	787, 1187, 1150
Kumazawa, T.	1191	Nagano, M.	1182	Okamoto, H.	310
Kume, S.	95, 810	Nagao, Y.	174	Okamoto, S.	301
Kuribayashi, H.	36, 570, 1104	Nagaoka, T.	1191	Okamoto, T.	649
Kuwabara, M.	159			Okamura, K.	388, 501
Lee, S.K.	179, 290			Okamura, O.	777
				Okano, K.	238, 265
				Okuda, H.	403

Okutani, T.	305, 693, 1120	Sugaya, Y.	72	Tsuchinari, A.	545
One, S.	115	Sugie, Y.	353, 507	Tsuchiya, F.	164
Ono, M.	92	Sugimori, K.	728	Tsukamoto, K.	67, 217, 1145
Onoda, M.	30	Sugimoto, M.	388, 501	Tsukida, T.	471
Osada, H.	62	Sugimoto, Y.	8	Tsunetomo, K.	257
Osaka, A.	578	Sumino, H.	772	Tsuno, T.	531
Oshima, E.	398	Sumita, S.	525, 633	Tsuruta, H.	558
Ota, R.	35, 164, 570, 1104	Suzuki, K.	186, 382, 633	Tsutumi, M.	363
Otani, T.	758	Suzuki, M.	1120	Tuchiya, T.	614
Otsuka, N.	787, 1150, 1187	Suzuki, N.	227	Uchida, K.	233
Otsuka, R.	271	Suzuki, S.	597	Uchino, K.	812
Otto, J.	827	Suzuki, T.	19, 146, 206, 1231	Ueda, Y.	741
Ozawa, M.	628	Suzuki, Y.	741	Uehara, M.	1080
Pai, C.H.	429, 1140	Tabuchi, M.	1134	Uematsu, K.	169, 644, 1124
Paquet, V.	827	Taguchi, T.	570, 1104	Ueno, A.	787
Ritchie, R.	1009	Tajima, Y.	286, 981	Umebayashi, S.	1214
Rödel, J.	244	Takahama, K.	14	Ura, A.	715
Saiki, A.	82	Takahashi, C.	491	Urabe, K.	367
Saito, H.	77	Takahashi, H.	1223	Urano, A.	592
Saito, S.	670	Takahashi, K.	683	Urashima, K.	286
Saitou, K.	438	Takahashi, Y.	353, 412, 507, 597	Utsugi, H.	227
Sakaguchi, S.	46	Takashima, T.	314	Wada, S.	797
Sakai, H.	614	Takashima, Y.	409	Wada, T.	420
Sakai, M.	953	Takata, M.	301	Wakabayashi, T.	793
Sakamaki, S.	566	Takatsuka, K.	2	Wakai, F.	46
Sakata, H.	324	Takebe, H.	535	Wakamatsu, M.	1084
Sakuma, T.	132	Takeda, K.	305	Wakiya, N.	772
Sakurai, Y.	102	Takeda, N.	452	Waseda, Y.	471
Sasaki, M.	970	Takeda, S.	137	Watabe, M.	609
Sasaki, T.	398	Takeda, Y.	620, 699, 1113	Watanabe, K.	1084, 1156
Satake, T.	458	Takekawa, S.	363	Watanabe, M.	286, 327, 541
Sato, H.	458	Takeuchi, K.	801	Watanabe, T.	142
Sato, S.	371	Takeuchi, N.	1084	Watari, T.	696
Sawaguchi, A.	510	Taki, K.	301	Wu, Y.H.	149, 1070
Schunk, P.R.	843	Takusagawa, N.	1150, 1174	Yabe, K.	741
Seki, A.	227	Tamari, N.	87, 357	Yabuta, K.	169, 644
Sekiguchi, I.	741	Tanabe, I.	703	Yamada, K.	609, 797
Sekine, M.	334	Tanabe, Y.	51, 416, 1024, 1209	Yamada, M.	416
Sekizawa, K.	517	Tanahashi, M.	1080	Yamada, N.	558
Senda, T.	491, 710	Tanaka, H.	330, 363, 1053, 1234	Yamada, T.	367, 403
Seo, W.S.	429, 1140	Tanaka, K.	584	Yamade, Y.	452
Shibata, H.	471	Tanaka, S.	154, 420, 777	Yamagishi, C.	67, 217, 1145
Shiga, H.	782	Tanaka, T.	87, 357	Yamaguchi, O.	1234
Shimada, K.	1099, 1219	Tanaka, Y.	825	Yamaguchi, S.	551
Shimizu, Y.	758	Tari, I.	137	Yamaguchi, T.	222
Shimobayashi, O.	545	Taruta, S.	1150	Yamamoto, Hide.	310
Shimojima, H.	67, 217, 367, 1145	Tateyama, H.	1203	Yamamoto, Hiro.	210
Shimokawa, K.	741	Tejima, Y.	715	Yamamoto, T.	314
Shimoo, T.	388, 501, 752	Terabe, K.	551	Yamamura, H.	42, 222,
Shinozaki, K.	82, 179, 772	Terasaki, M.	1182		670, 1058, 1237
Shinozaki, S.	676	Terasaki, T.	42, 670, 1237	Yamamuro, T.	2, 8
Shiohara, Y.	777	Tochigi, K.	447	Yamanaka, S.	14, 92
Shiosaki, T.	819	Toda, G.	1127	Yamanaka, T.	810
Shioya, Y.	764	Toda, K.	510	Yamane, H.	514
Sobue, M.	394, 676	Tohge, N.	531	Yamane, M.	747
Soga, N.	434, 584	Tomishige, S.	398	Yamasaki, N.	58
Somiya, S.	191	Tomota, Y.	471	Yamauchi, H.	420
Suematsu, H.	1038, 1096	Torikai, T.	696	Yamazoe, N.	758
Suga, T.	412, 597	Toriyama, M.	19, 146, 206, 1231	Yanagida, H.	429, 592,
Sugano, M.	458	Toyoda, S.	535		701, 807, 1140
Suganuma, E.	458	Tsubaki, Y.	99	Yanagisawa, K.	58

Yao, T.	624	Yazawa, T.	330, 1053, 1234	Yoshida, T.	102
Yasuda, E.	51, 371, 416, 1029, 1209	Yoden, H.	735	Yoshimatsu, H.	578
Yasuda, K.	182, 720	Yogo, T.	992	Yoshimura, M.	191, 1223
Yasue, T.	764	Yokogawa, Y.	19, 146, 206, 1231	Yoshimura, Y.	649
Yasuike, Y.	409	Yokoi, H.	541	Yoshio, T.	1110
Yasuoka, M.	1191	Yokoyama, M.	14	Yoshisato, Y.	683
Yasutomi, Y.	394, 676	Yoneda, K.	176, 477	Zhang, Z.	434
		Yoshida, H.	95, 186, 382	Zink, J.	858

Bibliographic Information

1. Title	Journal of Ceramic Society of Japan, International Edition	ISSN : 0912-9200
2. Frequency	Monthly	1 volume per year (No.1 Jan. - No.12 Dec.)
3. Volume No.	100	
4. Cover data of (Vol. 95, No1)	January 1987	Vol.95 No.1 is the first Issue of English version
5. Index of contents	Given annually	bound in
6. Size	21cm×29.7cm	1700 pages per annum
7. Subscription rates (Air speed)	¥200,000	(12 issues)

ORDER FORM

To: Circulation Div., the Journal of
Ceramic Society of Japan, Inter-
national Edition
c/o Fuji Technology Press Ltd.
Daini Bunsei Bldg., 1-11-7 Toranomon
Minato-ku, Tokyo 105, Japan

Date: _____

Please enter my subscription to the **Journal of Ceramic Society of Japan, International Edition**

(for _____ copy/ies)

Name: _____

Position: _____

Address: _____

Signature: _____

☐ Payment enclosed
(Payment by credit card is preferred)

☐ Bill me
Air speed ¥200,000

Attention: Please indicate our ref. No.(AUTO, TEC, TECJ, CER, ROB, ...) when you make the remittance.
All subscriptions can be paid in advance through any of the following methods.

1) Charge my:

☐ AmEx ☐ Visa ☐ MC

Card No. Exp. Date

Mr/Mrs./Ms.

Address City

Zip code Country

2) Transfer to Fuji Technology Press Ltd A/C No.10667 Fuji Bank Toranomon Branch, Minato-ku Tokyo

3) Bank Draft

4) Transfer to Fuji Gijyutsu Shuppan K.K.(Fuji Technology Press Ltd.) A/C No. Tokyo 7-145130, Postal Saving

Attention!!

You are now able to make remittance by credit card!

**You can enter subscriptions with only your name, card number and its
expiry date. No bank charge nor preparation of Japanese yen bank
draft is necessary.**

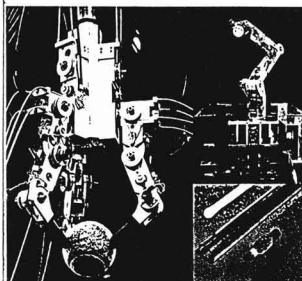
Journal of Robotics and Mechatronics

Vol.3 No.3 June 1991

Contents

**Journal of
Robotics and Mechatronics**
Vol.3 No.3 June 1991

Special Issue on Computer Architecture for Robotics



Special Issue on Spatial Information Sensing

- ☐ **Editorial on Special Issue on Spatial Information Sensing** . 135
Masanori Idesawa, Editor

Reviews:

- ☐ **Intelligent Robot Sensor System** 136
Masanori Idesawa
- ☐ **3-Dimensional Shape Measurement** 151
Yasuo Yamashita
- ☐ **The Recent Trend of Moire Metrology** 157
Toru Yoshizawa
- ☐ **Recent Holographic Interferometry** 163
Kiyofumi Matsuda

Papers:

- ☐ **3-Dimensional Shape Recognition by Active Vision** 170
Koichiro Deguchi
- ☐ **Automatic 3D Measurement System by the Grid Illumination Type Moire Method** 177
Yasuhiro Arai, Shunsuke Yokozeki and Tomoharu Yamada
- ☐ **Automatic Fringe Analysis of Moiré Interferometry** 184
Yasuhiro Arai, Tadao Kurata and Shunsuke Yokozeki
- ☐ **Three-Dimensional Curved Shape Measuring System Using Image Encoder** 190
Mitsuaki Uesugi
- ☐ **Setup Planning of Active Visual Sensing for Autonomous Robots** 196
Shigeyuki Sakane, Tomomasa Sato and Masayoshi Kakikura
- ☐ **A Study on a 3-Dimensional Expert Vision System Using the Fiber Grating Method (The Neural Network Applications for Recognition of Plant Pipeline Direction)** 201
Toshio Fukuda, Hidemi Hosokai, Fumihito Arai and Shusuke Mogi

Development Report:

- ☐ **Non-Contact, Real-Time, 3-Dimensional-Motion Analyzing System by Color Vision** 207
Shigeo Sasazawa

Letters:

- ☐ **Development of Long Span, High Precision Absolute Linear Scale by Moire Fringes** 211
Yasuhiro Arai, Shunsuke Yokozeki and Tomoharu Yamada
- ☐ **A Direction Sensing Technique of a Reference Point by Using Cross-Hair Diffraction Beam** 215
Masafumi Ito, Kazuhiro Hane, Fumio Matsuda, Yoshiki Uchikawa and Shuzou Hattori
- ☐ **The Measurement of 2-Dimensional Micro-Pattern Using Laserbeam Scanning** 218
Hiroo Fujita

Bibliographic Information

1. Title	Journal of Robotics and Mechatronics	ISSN : 0915-3934
2. Frequency	Bimonthly	1 volume per year (No.1 Feb. - No.6 Dec.)
3. Volume No.	4	
4. Cover data of (Vol. 1, No1)	June 1989	
5. Index of contents	Given annually	bound in
6. Size	21cm×30cm	700 pages per annum
7. Subscription rates (Air speed)	¥72,000	(6 issues)

ORDER FORM

To: Circulation Div., the Journal of
Robotics and Mechatronics
c/o Fuji Technology Press Ltd.
Daini Bunsei Bldg., 1-11-7 Toranomon
Minato-ku, Tokyo 105, Japan

Date: _____

Please enter my annual subscription to the **Journal of Robotics and Mechatronics**
(for _____ copy/ies)

Name: _____
Position: _____
Address: _____
Signature: _____

☐ Payment enclosed
(Payment by credit card is preferred)

☐ Bill me
Airmail ¥72,000

Attention: Please indicate our ref. No.(TEC, TECJ, CER, RB, ...) when you make the remittance.
All subscriptions can be paid in advance through any of the following methods.

1) Charge my:

☐ AmEx ☐ Visa ☐ MC

Card No. Exp. Date

Mr./Mrs./Ms.

Address City

Zip code Country

2) Transfer to Fuji Technology Press Ltd A/C No.10667 Fuji Bank Toranomon Branch, Minato-ku Tokyo

3) Bank Draft

4) Transfer to Fuji Gijyutsu Shuppan K.K.(Fuji Technology Press Ltd.) A/C No. Tokyo 7-145130, Postal Saving

Attention!!

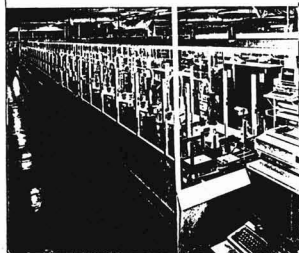
You are now able to make remittance by credit card!
You can enter subscriptions with only your name, card number and its
expiry date. No bank charge nor preparation of Japanese yen bank
draft is necessary.

Japanese Journal of Advanced Automation Technology

Vol.2 No.5 Sept.1990

**Japanese Journal of
Advanced Automation
Technology**

Vol.2 No.5 Sept. 1990



Contents

Reviews:

- **A Classifying Method for Automated Systems Through the Grading Index for Automatization** 239(3)
Takeo Haruyama
- **Machine Element Systematization for Sophisticated Automation** 242(6)
Latest Machine Element and Its Application Technology
Yoshimitsu Itoh

Research Papers:

- **Automatic Generation of Assembly Plans for Machines** . 246(10)
---Formalization of Problems---
Masatoshi Ito and Hiroshi Sobukawa
- **A Selecting Method of Tool Diameter and Depths of Cut in End Milling** 252(16)
Li Yong, Yoshiya Fujii and Hiroyasu Iwabe
- **A Scheduling Method for Multi-Product Assembly Process Capable of Adjusting Load Fluctuation According to Product Mix and Traffic Intensity** 258(22)
Yasuhiro Kajihara and Hirokazu Osaki
- **Development of an NC Machining Simulator - System Configuration -** 264(28)
Yasumasa Kawashima, Kumiko Itoh, Tomotoshi Ishida
Shiro Nonaka and Kazuhiko Ejiri

Development Report:

- **High Resolution Nanometer Stage Using a Linear Actuator** 269(33)
Yukitoshi Kobayashi and Toshimi Yamada
- **A XY-Table with Double Speed Through the Integration of a Cam and DD Motors** 274(38)
Masao Anma
- **Automation of Lip Seal Insertion** 279(43)
Masayuki Moriya
- **Flat Hollow Actuator and its Applications** 282(46)
Takashi Uchida

Tutorial:

- **Robotics for Beginners (I)** 286(50)
Hiroharu Suda

Bibliographic Information

1. Title	Japanese Journal of Advanced Automation Technology	ISSN : 0915-3942
2. Frequency	Bimonthly	1 volume per year (No.1 Jan. - No.6 Nov.)
3. Volume No.	4	
4. Cover data of (Vol. 1, No1)	September 1989	
5. Index of contents	Given annually	bound in
6. Size	21cm×30cm	700 pages per annum
7. Subscription rates (Air speed)	¥72,000	(6 issues)

ORDER FORM

To: Circulation Div., the Japanese Journal
of Advanced Automation Technology
c/o Fuji Technology Press Ltd.
Daini Bunsei Bldg., 1-11-7 Toranomom
Minato-ku, Tokyo 105, Japan

Date: _____

Please enter my subscription to the **Japanese Journal of Advanced Automation Technology**
(for _____ copy/ies)

Name: _____
Position: _____
Address: _____
Signature: _____

☐ Payment enclosed
(Payment by credit card is preferred)

☐ Bill me
Airmail ¥72,000

Attention: Please indicate our ref. No.(AUTO, TEC, TECJ, CER, ROB, ...) when you make the remittance.
All subscriptions can be paid in advance through any of the following methods.

1) Charge my:

☐ AmEx ☐ Visa ☐ MC

Card No.Exp. Date

Mr/Mrs./Ms.

AddressCity

Zip codeCountry

2) Transfer to Fuji Technology Press Ltd A/C No.10667 Fuji Bank Toranomom Branch, Minato-ku Tokyo

3) Bank Draft

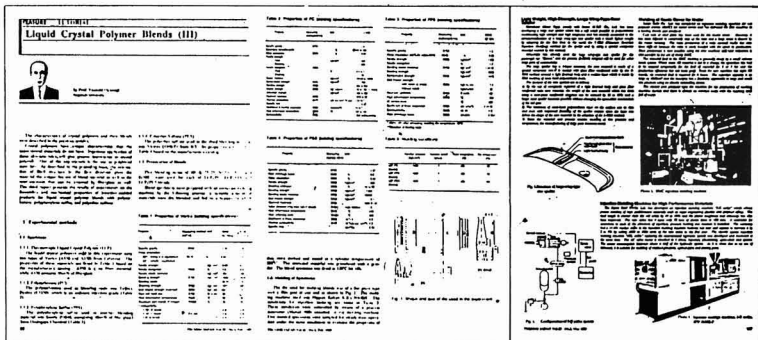
4) Transfer to Fuji Gijyutsu Shuppan K.K.(Fuji Technology Press Ltd.) A/C No. Tokyo 7-145130, Postal Saving

Attention!!

You are now able to make remittance by credit card!
You can enter subscriptions with only your name, card number and its
expiry date. No bank charge nor preparation of Japanese yen bank
draft is necessary.

What is the English Monthly Journal TECHNO JAPAN?

It is a professional international periodical designed to cater to people in a wide variety of key industrial and government positions. Its carefully selected contents, including complete reports, for example, on the current status and new developments in Japanese industry and technology, are tailored to meet the information needs of specialists all over the world. Each news article includes an expert's commentary based on in-depth data analysis and also incorporates sufficient data to enable readers to make their own independent judgements on various issues and topics. Techno Japan is a monthly journal whose reports contain information indispensable for those overseas specialists who keep track of current conditions and must project future Japanese and international economic and industrial trends. It is the most authoritative source of information about the most recent technological advances in virtually all fields of industry.



Contents of TECHNO JAPAN

Industrial & Technological News Articles

Every issue of Techno Japan contains more than 300 pieces of information.

News articles are classified as follows:

- Basic Industries:** Energy, Steels & Metals, Ceramics & Materials Science, Superconductivity
- Machinery Industries:** Miscellaneous Machines, Precision Engineering & Fine Finishing, Factory Automation, Transportation & Materials Handling
- Electronics Industries:** Electronic Devices, Telecommunications, Information Processing, Home Automation & Broadcasting, Electronics Instruments, Medical Engineering, Electronic Machine Manufacturing & Assembly
- Chemical Industries:** Chemicals, Polymers, Biotechnology

Systems Industries:

Feature Articles

Long, highly informative feature articles of crucial interest to overseas governments and industries appear each month. As many as 55 pages in one issue may be devoted to such important and fascinating articles which enlarge the depth and breadth of readers' knowledge about subjects of current interest. Such high news value feature articles are carried individually or in a series.

Economic Report and Statistics

Techno Japan's economic report and statistics is officially provided by the Economic Planning Agency. These reports help to promote mutual understanding among various nations.

Research Institutes in Japan

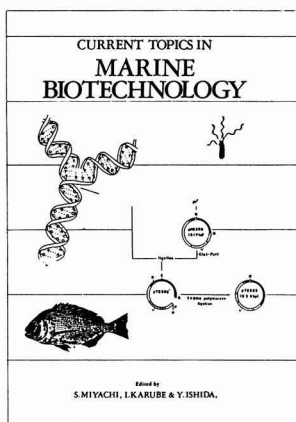
Disaster Prevention, Agribusiness

TECHNO JAPAN

FUJI TECHNOLOGY PRESS LTD.

Daini Bunsei Bldg., 11-7, Toranomon 1-chome, Minato-ku, Tokyo 105, Japan

CURRENT TOPICS IN MARINE BIOTECHNOLOGY



This is a collection of papers presented at the First International Conference on Marine Biotechnology held in Tokyo, from September 3 through 6, 1989. About 400 scientists from 23 different countries conferred about developments in marine biology, meeting in six sections: microorganisms, microalgae, macroalgae, fish, shellfish and other marine animals, and supporting technology and interfacial subjects. There were many very lively discussions and reports of exciting new findings in every area.

Many participants agreed that marine biology can develop only through multidisciplinary and international cooperation, and a committee meeting was held during the Conference to plan for future International Conferences. Considering the rapid progress in this field, it was unanimously decided that one should be held every two years. By vote, Washington, D.C., U.S.A. was chosen as the place for the second conference, as proposed by Dr. O.R. Zaborzky of National Research Council, National Academy of Sciences, U.S.A. The third meeting will be held in Norway, and the fourth in France. The organizers are happy that meeting sites have been fixed so long in advance, since we observe that marine biotechnology is growing so rapidly in many parts of the world.

This Conference was made possible by the advice, help and cooperation of many people, both in scientific and governmental organizations and in private companies. I would like to express our special thanks for the cooperation of government agencies including the Ministry of Agriculture, Forestry and Fisheries, the Ministry of Education, Science and Culture, the Ministry of Health and Welfare, the Ministry of International Trade and Industry, the Science and Technology Agency and the Ministry of Foreign Affairs. There was financial support from the Commemorative Association for the World Exposition (1970) and ninety private companies listed in the proceedings. Special thanks should be extended to the staff of Marine Biotechnology Institute Co., Ltd., for their devoted help in the organization of this Conference.

ORDER FORM

To: Circulation Div., Current Topics in
Marine Biotechnology,
c/o Fuji Technology Press Ltd.
Daini Bunsei Bldg., 1-11-17 Toranomon
Minato-ku, Tokyo 105, Japan

Date: _____

Please enter my subscription to **Current Topics in Marine Biotechnology** (for _____
copy/ies)

Name: _____

Position: _____

Address: _____

Signature: _____

☐ Payment enclosed

(Payment enclosed is preferred)

☐ Bill me

Airmail US\$250.00

